Universidad de Cantabria

CSIC - Universidad de Cantabria

Instituto de Física de Cantabria

La emisión infrarroja de galaxias activas

Memoria presentada por la Licenciada

Judit García González

para optar al título de Doctora en Ciencias, Tecnología y Computación

2017

Declaración de Autoría

Almudena Alonso Herrero, Doctora en Ciencias Físicas e Investigadora Científica en el Centro de Astrobiología, CSIC-INTA,

CERTIFICA que la presente memoria

La emisión infrarroja de galaxias activas

ha sido realizada por **Judit García González** bajo mi dirección.
Considero que esta memoria contiene aportaciones suficientes para construir la tesis Doctoral de la interesada.

En Santander, a 10 de Marzo de 2017

Almudena Alonso Herrero

A mi abuela…

Agradecimientos

Después de estos años de doctorado me gustaría expresar mi agradecimiento a todas las personas que han estado a mi lado y me han ayudado a finalizar esta tesis.

En primer lugar me gustaría agradecer a mi directora de tesis, Almudena, el haberme permitido realizar esta tesis doctoral. Su ayuda y comentarios científicos han sido imprescindibles para que esta tesis salga adelante. Agradecerle también su dedicación extra y accesibilidad a pesar de la distancia, y sus respuestas sin demora a todas mis dudas. También quiero agradecer a Silvia Mateos que haya aceptado ser mi tutora de tesis y sus atinadas correcciones, así como los buenos ratos pasados. Nunca olvidaré todas las anécdotas del último congreso en Canarias, y todo lo que nos pudimos reír.

También quisiera agradecer a Pablo el haberme dirigido el TFM y haberme animado a venir a Santander. Él consiguió que la asignatura de física extragaláctica fuera mi preferida entre todas las asignaturas de la especialidad. Si no fuera por él, yo no estaría aquí.

Debo agradecer también a Sebastian su hospitalidad y ayuda durante mi estancia en Southampton. Trabajar dos meses allí fue una experiencia enriquecedora en todos los aspectos. También a los estudiantes de doctorado de Southampton, por los divertidos desayunos de los viernes.

También quiero dar las gracias a Antonio por estar siempre disponible, tanto en persona mientras estuvo en el IFCA como por correo electrónico. No sé cómo aguantó tantas dudas y preguntas sin echarme de su despacho.

Mi agradecimiento también a todo el grupo de Galaxias y AGN del IFCA, tanto a los que han llegado hace poco, como a los que ya se fueron y los que todavía están, por hacerme sentir una más del grupo desde el primer día. ¡Voy a echar mucho de menos esos jueves gastronómicos! Muchas gracias a todos: Raquel, Nuria, Ángel, Maite, Ester, Pilar, Silvia Martínez, Bea, Francisco, Xavier. Y en especial, a mis compañeros de despacho, Anuar y Nacho, que se han convertido en muy buenos amigos y espero no perder el contacto con ellos.

Gracias en general a toda la gente del IFCA por crear un ambiente tan sano. Echaré de menos los miércoles de cine y las partidas de rol. Ha sido un placer pasar estos años allí. En especial gracias a David, Diego, Rosa y Belén por todos los momentos vividos y por su inestimable amistad. Toda la gente que he conocido y los lugares que he podido visitar durante mi doctorado han hecho de este mucho más que una mera experiencia académica.

También quiero agradecer a todos mis amigos que me han apoyado durante estos años. Una mención especial merecen Iván y Esther, que a pesar de la distancia siempre están ahí (aunque sea por *whatsapp*). ¡Me parece increíble que desde los 3 años no hayamos perdido la amistad! Además, quiero agradecer su amistad y apoyo a Cris, que es la que mejor entiende todo mi estrés de estos últimos meses. ¡Ánimo, ya nos queda poco para ser doctoras!

Durante mi estancia en Santander he conocido a mucha gente en clases de baile. Quiero agradecerles el buen ambiente creado y en especial dar las gracias a Estefanía, a quién conocí en clase de baile y se ha convertido en una buena amiga.

Por último, pero no menos importante, quiero agradecer todo el apoyo que me ha dado mi familia y en especial mi madre. Sin ella, no hubiera podido dedicarme a esto. Me gustaría dedicar un recuerdo a mi abuela Rufina, que por desgracia no me ha podido ver convertida en doctora. También quiero dar gracias a Carlos por estar a mi lado y apoyarme, sobre todo en los últimos meses de más estrés.

Resumen de la tesis en castellano

Actualmente se cree que existen agujeros negros supermasivos ($M_{SMBH}>10^6\,M_\odot$, SMBH del inglés *Super Massive Black Holes*) en el centro de todas las galaxias con un bulbo prominente. Este SMBH juega un papel importante en la formación de galaxias, compartiendo mecanismos de formación y crecimiento con el bulbo de las galaxias. En algunas galaxias el SMBH está inactivo mientras que en otras el SMBH está acretando material y creciendo. Este último fenómeno se conoce como núcleo galáctico activo (AGN, *Active Galactic Nucleus*) y es muy energético; la luminosidad de la región central puede llegar a ser miles de veces mayor que la de la galaxia anfitriona.

Según la versión más simple del modelo unificado, todos los AGN tienen la misma estructura: SMBH, disco de acreción, corona, región de emisión de líneas anchas (BLR, del inglés *Broad Line Region*), toro, región de emisión de líneas estrechas (NLR, del inglés *Narrow Line Region*) y algunos tipos de AGN presentan un chorro de partículas a velocidades relativistas. Los AGN emiten en todo el espectro electromagnético, desde radio a rayos γ, con una parte importante de su emisión en el infrarrojo (IR). Cada uno de los elementos del AGN tiene el pico de emisión en un rango diferente, por lo que el estudio de un rango en concreto del espectro electromagnético proporciona información de un elemento específico (por ejemplo, el disco de acreción, gas en la región de líneas anchas, el toro, etc). Las diferencias observadas entre los distintos tipos de AGN se explican mediante efectos de orientación, siendo el toro de polvo y gas el ingrediente clave para explicar esta dependencia. Como el toro reprocesa la radiación óptica y ultravioleta (UV) del disco de acreción y la reemite en el rango IR, es importante estudiar la emisión IR para entender las propiedades del toro de polvo que rodea al AGN.

La emisión IR de las galaxias activas no sólo se debe al AGN sino también a la galaxia anfitriona. En el caso de las galaxias Seyfert (las más comunes en esta tesis) la emisión IR se puede entender como una combinación de tres componentes espectrales principales: continuo y características espectrales debidas al polvo calentado por el AGN y formación estelar, así como líneas de emisión (atómicas, iónicas y moleculares) que pueden ser igualmente excitadas por el AGN y/o formación estelar. Mientras que la emisión nuclear en el IR cercano (NIR, del inglés *Near Infrared*) y en el IR medio (MIR, del inglés *Mid Infrared*) de las galaxias Seyfert está dominada por el AGN, la emisión en el IR lejano (FIR, del inglés *Far Infrared*) está normalmente dominada por la galaxia anfitriona.

En los últimos años se han presentado numerosos modelos de toro para reproducir las observaciones en el IR de los AGN. Estos modelos se pueden dividir en modelos hidrodinámicos y modelos de transferencia radiativa. Estos últimos han pasado en los últimos 15 años de configuraciones en las que el polvo está distribuido uniformemente a configuraciones más físicas donde el polvo se encuentra en nubes, también llamadas configuraciones de toro "grumoso" (clumpy torus). Estudios dinámicos e interferometría en el MIR favorecen una estructura grumosa en vez de un toro uniforme. Para delimitar los parámetros de los modelos de toro es necesario comparar predicciones de los modelos de toro grumoso con observaciones el el IR de los AGN hechas con alta resolución angular.

Existen diferentes métodos para seleccionar AGN tanto en el Universo Local como a distancias cosmológicas. No es posible tener una técnica de selección de AGN eficiente, fiable y completa, ya que no todos los AGN muestran las mismas características observacionales. Convencionalmente, el método más usado y directo para identificar AGN ha sido la espectroscopía óptica. Los AGN pueden ser identificados por la presencia de líneas de emisión anchas, por la detección de líneas estrechas características de la ionización de los AGN, o por cocientes de intensidades de líneas en diagramas de diagnóstico como [OIII]λ5007/Hβ vs [NII]λ6583/Hα. Los AGN en campos cosmológicos suelen ser identificados por su emisión en rayos X, su emisión IR, un exceso en la emisión en radio y por combinaciones de diferentes emisiones. Como la mayoría de AGN varía en escalas de tiempo de horas a millones de años, la variabilidad es otro método usado para seleccionar AGN. Este método selecciona preferentemente AGN de baja luminosidad porque se espera que muestren mayor variabilidad que los más luminosos. Todos estos métodos de selección de AGN son complementarios y pueden detectar fuentes que otros métodos pueden perder.

Objetivos de la investigación

Como se ha explicado anteriormente, al no haber una única técnica para identificar AGN es importante usar diferentes métodos ya que todos ellos presentan sesgos. Además, la banda IR es el rango espectral clave para entender el toro de polvo del AGN. Como la galaxia anfitriona también emite en el IR, es importante separar ambas emisiones.

El principal objetivo de esta tesis es el estudio de la emisión IR tanto en AGN de galaxias cercanas como de galaxias en campos cosmológicos. Esta tesis está dividida en dos partes diferentes. El principal propósito de la primera parte es la selección de AGN en campos cosmológicos por medio de la variabilidad en el IR, usando para ello datos de *Spitzer*/MIPS 24 μm (Capítulo 3). El objetivo de la segunda parte es el estudio del polvo calentado por el AGN en galaxias cercanas usando para ello datos de *Herschel* y de telescopios en tierra (Capítulos 4 y 5).

Seleccionar AGN por su variabilidad IR (24 μm) es un nuevo método que permite identificar AGN oscurecidos y de baja luminosidad que no son detectados por otros estudios. Además permite comparar

los AGN variables seleccionados con catálogos de AGN seleccionados por otros métodos, y estimar la fracción que suponen estos AGN oscurecidos respecto a la población general de AGN. También es posible calcular la contribución de estos AGN a la emisión en el MIR total para estas fuentes variables.

Por otra parte, el estudio de galaxias Seyfert cercanas permite separar la emisión nuclear en el IR debida al polvo calentado por el AGN de la debida al polvo calentado por formación estelar, y por tanto se pueden estudiar las propiedades en el IR de los AGN. También permite comparar estadísticamente las propiedades en el MIR de las galaxias Seyfert con las predicciones de los modelos de toro grumoso.

Los objetivos de la tesis se pueden resumir en los siguientes puntos:

1. Seleción de AGN por su variabilidad en 24 μm usando un método estadístico χ^2.
2. Caracterización de las propiedades de las fuentes variables en 24 μm, así como su comparación con otros estudios de variabilidad.
3. Mecanismos que dan lugar a la emisión nuclear e integrada en el FIR para galaxias Seyfert cercanas analizando para ello sus propiedades, como la emisión no resuelta en 70 μm, la distribución de colores en el FIR, las tasas de formación estelar (SFR, del inglés *Star Formation Rates*) nuclear y extranuclear y resultados de ajustar las distribuciones espectrales de energía FIR a un cuerpo gris.
4. Identificación de galaxias Seyfert cuya emisión en 70 μm es debida principalmente al polvo calentado por el AGN, usando para ello 4 criterios diferentes.
5. Estudio de la emisión en el MIR debida a polvo calentado por el AGN.
6. Comparación estadística entre las propiedades en el MIR de AGN y las predicciones de modelos de toro grumos, permitiendo delimitar algunos de los parámetros de los modelos.

Planteamiento y metodología

Para lograr los objetivos enumerados anteriormente se han usado principalmente dos estrategias diferentes: imágenes, usando para ello instrumentos en telescopios espaciales (como MIPS en *Spitzer* y PACS y SPIRE en *Herchel*) y espectroscopía usando instrumentos en telescopios terrestres (como T-ReCS en el telescopio de 8.1 m Gemini-South, VISIR en el telescopio de 8.2 m VLT UT3, CanariCam en el Gran Telescopio de Canarias de 10.4 m y Michelle en el telescopio de 8.1 m Gemini-North).

La estrategia adoptada para el primer estudio (selección de AGN mediante variabilidad en 24 μm) consiste en recopilar todos los datos tomados por el instrumento MIPS alrededor de los campos cosmológicos GOODS. Estos datos corresponden a diferentes propuestas de observación y pueden ser

recopilados mediante el archivo de *Spitzer* (*Spitzer* Heritage Archive). Se dividen los datos en diferentes épocas y se obtienen los flujos a 24 μm de las fuentes en cada época. Cruzando los datos de las distintas épocas se obtiene un catálogo con las fuentes comunes a todas las épocas. Con los datos de este catálogo se usa un método estadístico χ^2 que tiene en cuenta los diferentes errores fotométricos para seleccionar las fuentes variables. Se estudian las propiedades de las fuentes seleccionadas por su variabilidad y se compara con otros catálogos de AGN y estudios de variabilidad en otras longitudes de onda.

Para el segundo trabajo (emisión nuclear e integrada en el FIR de galaxias Seyfert cercanas) la estrategia utilizada ha sido diferente debido a que en este trabajo se estudian galaxias cercanas en lugar de galaxias en campos cosmológicos. Para este trabajo se han seleccionado 33 galaxias Seyfert con imágenes tomadas con PACS (70, 100 y 160 μm) y SPIRE (250, 350 y 500 μm) y con espectroscopía en el MIR de gran resolución espectral. Esto permite determinar si las galaxias poseen actividad de formación estelar en escalas de $50 - 60$ pc, lo cual es necesario para determinar si las galaxias tienen su emisión en el FIR dominada por el AGN. Se han realizado medidas fotométricas tanto para la zona nuclear como para la galaxia entera. Se definen 4 criterios diferentes para identificar las galaxias con una contribución importante en la emisión en 70 μm debida polvo calentado por el AGN. Estos criterios son: (1) elevados cocientes $f_\nu(70\,\mu\text{m})/f_\nu(160\,\mu\text{m})$ respecto a los típicos colores para galaxias con formación estelar, (2) gradiente de temperatura del polvo mayor que los valores típicos para las galaxias con formación estelar, (3) exceso de emisión en 70 μm respecto al ajuste de la emisión integrada a un cuerpo negro con valor de la emisividad del polvo de $\beta = 2$, y (4) exceso de la SFR nuclear obtenida a partir de la emisión en 70 μm respecto a la obtenida mediante indicadores en el MIR.

Para el tercer trabajo (investigación estadística de las predicciones de los modelos de toro grumoso en el MIR) se utiliza espectroscopía como estrategia principal, al contrario que en los anteriores trabajos en los que se usa la fotometría. Para ello se selecciona una muestra de 53 galaxias Seyfert cercanas con espectroscopía de alta resolución en el MIR (típicamente $7.5 - 13\,\mu$m) tomada con telescopios terrestres. Los espectros en el MIR de las galaxias se descomponen usando el programa DEBLENDIRS para obtener las distintas componentes y poder estudiar la contribución del AGN. Las propiedades obtenidas para las galaxias, en nuestro caso la fuerza de los silicatos en 9.7 μm y el índice espectral medido entre 8.1 y 12.5 μm, se comparan estadísticamente con las predicciones de los modelos de toro grumoso CAT3D de Hönig and Kishimoto (2010), así como con una nueva versión de los modelos que incluye una mejor representación física de las propiedades de sublimación del polvo. Comparando las predicciones de los modelos con las propiedades obtenidas para las galaxias se pueden delimitar algunos de los parámetros de los modelos de toro grumoso.

Aportaciones originales

La investigación presentada en esta tesis ha contribuido significativamente al conocimiento de la emisión en el IR de los AGN. Se han introducido varias novedades en este trabajo respecto a trabajos publicados anteriormente.

En el caso de los AGN seleccionados mediante variabilidad en 24 μm, se trata del primer estudio realizado en esa longitud de onda. Existen diversos estudios sobre variabilidad en los campos cosmológicos GOODS tanto en el óptico como en el rayos X y en radio. Pero no existe ningún estudio de variabilidad usando el MIR. Por tanto este trabajo ofrece un método novedoso para seleccionar AGN poco luminosos y oscurecidos que no son identificados con otras técnicas. Aparte de este trabajo, sólo existe un estudio de variabilidad en el IR en otro campo cosmológico. En ese trabajo usaron las bandas más sensibles de IRAC a 3.6 y 4.5 μm (NIR) para seleccionar fuentes variables.

En el caso de la emisión nuclear e integrada en el FIR de galaxias Seyfert cercanas, es el primer estudio estadístico de la contribución en el FIR del AGN. Existen diversos estudios de galaxias individuales para determinar la contribución del polvo calentado por el AGN a la emisión total en el FIR, pero ninguno para grandes muestras de galaxias. Por ello es importante encontrar un método para poder determinar estadísticamente si el AGN domina en el FIR sin necesidad de hacer ajustes individuales para cada galaxia. Los 4 criterios definidos en este trabajo proporcionan una novedosa forma de seleccionar estadísticamente galaxias Seyfert con una contribución significativa del AGN a 70 μm.

En el caso de la investigación estadística de las predicciones de los modelos de toro grumoso en el MIR, la nueva versión de los modelos CAT3D de Hönig and Kishimoto (2010) introducen un modelo diferencial de sublimación del polvo novedoso que es único y no está incluido en otros modelos de toro grumoso disponibles en la literatura. Los nuevos modelos producen distribuciones espectrales de energía más azules en el NIR y MIR y reproducen mejor las propiedades en el MIR de las galaxias Seyfert locales.

Los resultados obtenidos durante esta tesis han sido presentados en varios congresos y revistas internacionales (García-González et al. 2015, 2016). El último trabajo ha sido enviado a la revista MNRAS.

Conclusiones

La investigación realizada durante esta tesis está centrada en la emisión IR puesto que es la emisión clave para poder estudiar el toro de polvo que rodea el AGN.

El primer estudio realizado (Capítulo 3) ha permitido seleccionar AGN mediante su variabilidad en 24 μm (longitud de onda observada) en los campos cosmológicos GOODS usando para ello un método

estadístico χ^2. El principal resultado obtenido en este trabajo es que solo el ∼50% de las fuentes variables en 24 μm están identificadas como AGN por otros métodos. Además, la contribución estimada del AGN a la emisión en el MIR para las fuentes variables es pequeña (típicamente de menos del 20%). Por lo tanto, se espera que estas fuentes variables en 24 μm contengan AGN poco luminosos, donde se espera que la variabilidad sea mayor. De todas formas, la contribución de las fuentes variables en 24 μm a la población general de AGN es pequeña (∼13%).

El segundo trabajo (Capítulo 4) presenta un método basado en 4 criterios diferentes para seleccionar galaxias cuyo AGN tiene una contribución significativa en la emisión en 70 μm. El principal resultado de este trabajo es que a pesar de que en la mayoría de galaxias Seyfert la emisión en el FIR está dominada por la galaxia anfitriona, el 18% de la muestra inicial tiene una contribución significativa ($\sim 40-70\%$ de su emisión nuclear) debida al polvo calentado por el AGN. Por lo tanto, los criterios definidos en este trabajo proporcionan un buen método para seleccionar estadísticamente galaxias Seyfert con emisión significativa en 70 μm debida al AGN.

El tercer trabajo (Capítulo 5) presenta una comparación estadística de propiedades en el MIR de galaxias Seyfert con las predicciones de modelos de toro grumoso CAT3D de Hönig and Kishimoto (2010), así como con los nuevos modelos. El principal resultado obtenido en este trabajo es que en general los nuevos modelos reproducen mejor las propiedades en el MIR de los AGN locales. Además, aunque no es posible romper la degeneración en todos los parámetros de los modelos CAT3D (o de cualquier otro modelo de toro grumoso) usando únicamente espectroscopía en el MIR, se pueden descubrir diferentes tendencias entre galaxias Seyfert 1 y Seyfert 2.

Futuras líneas de investigación

Los resultados presentados en esta tesis se podrían extender a través de las siguientes líneas de actuación:

- Uso del método de variabilidad en 24 μm para seleccionar AGN de baja luminosidad en otros campos cosmológicos. El mismo método presentado en el Capítulo 3 puede ser utilizado en otros campos cosmológicos en los que haya observaciones en varias épocas tomadas con *Spitzer*. Además, las conclusiones de este trabajo se pueden fortalecer estudiando espectroscópicamente las fuentes variables que no son seleccionadas como AGN con otros métodos. Se podría usar, por ejemplo, el instrumento x-shooter en el VLT que permite tomar espectros de media resolución con longitudes de onda entre $300-2500$ nm. Esto permitiría probar si las fuentes variables no detectadas como AGN por otros métodos son realmente AGN.

- Estimación del flujo debido al AGN en 70 μm mediante predicciones de modelo de toro grumoso. Para fortalecer los resultados obtenidos en el Capítulo 4 se puede estimar individualmente el flujo

en 70 μm debido al AGN, según se hizo para IC 5063 y NGC 4151 (Alonso-Herrero et al. 2011; Ichikawa et al. 2015), para aquellas galaxias seleccionadas gracias a los 4 criterios definidos. Adicionalmente, se podría utilizar interferometría con ALMA para resolver el toro en el FIR (~450 μm) en otros AGN además de en NGC 1068 (García-Burillo et al. 2016).

- Introducción de emisión anisótropa del AGN en los nuevos modelos CAT3D. Los resultados del Capítulo 5 pueden ser extendidos explorando los efectos en las propiedades del MIR producidos al introducir emisión anisótropa del AGN. Esta emisión anisótropa tiene en cuenta la dependencia angular esperada para la emisión UV del AGN. Esta dependencia puede ser introducida como $cos(i)$ en la iluminación de las nubes del toro por el AGN, como una aproximación a la dependencia angular de la radiación UV en un disco de acreción $\propto 1/3cos(i) * (1 + 2cos(i))$ (Netzer 1987), también adoptada en otros trabajos (por ejemplo Hönig et al. 2006; Schartmann et al. 2005, 2008).

Universidad de Cantabria

Departamento de Física Moderna

CSIC - Universidad de Cantabria

Instituto de Física de Cantabria

Infrared emission of active galaxies

A dissertation submitted in partial fulfillment of the requirements
for the degree of Doctor of Philosophy in Physics

by

Judit García González

Summary

Nowadays it is accepted that all galaxies with a significant bulge component contain a supermassive black hole (SMBH) in their centres. This SMBH plays an important role in the formation of galaxies, sharing formation and growing mechanisms with the bulges of the galaxies. In some galaxies the SMBH is quiet, but in others the SMBH is accreting material and growing. The latter phenomenon is referred to as an active galactic nucleus (AGN) and it is very energetic, with the central region being able to reach luminosities as high as a few thousands that of the host galaxy.

AGN emit in all the electromagnetic spectrum, from radio to γ-ray, with a significant emission in the infrared (IR). Each AGN component peaks at a different range, so studying a particular electromagnetic range gives information about a specific component of the AGN. All AGN have the same components according to the simplest version of the unified model. The observational differences observed between different types of AGN are explained by orientation effects, with the obscuring dusty torus being the key ingredient to explain this orientation dependence. Since the torus reprocesses the optical/UV radiation from the accretion disk and re-emits in the IR range, it is important to study this IR emission to understand the dusty torus of the AGN.

The IR emission of active galaxies is not only due to the AGN but also to the host galaxy. Their IR emission of radio quiet AGN can be understood as a combination of three main spectral components: the thermal radiation from the dusty torus of the AGN, the thermal dust continuum and features due to star formation and line emission emanating from molecular, atomic, and ionic species. Whereas the nuclear near-IR (NIR) and mid-IR (MIR) emission of Seyfert galaxies (the most common galaxies in our study) is dominated by the AGN, the far-IR (FIR) emission is often dominated by the host galaxy.

To reproduce the IR observations of AGN, a large number of torus models have been developed in the last years. They can be divided into hydrodynamical models and radiative transfer models, with the latter moving from smooth to clumpy dust configurations. Dynamical studies and MIR interferometry tend to favour a clumpy structure rather than a uniform torus. To constrain the torus model parameters it is necessary to compare predictions of clumpy torus models with high angular resolution IR observations of AGN.

There are different methods to select AGN both in the Local Universe and at cosmological distances. As not all AGN show the same observational features, having an efficient, reliable and complete AGN selection technique is not possible, all of the methods present their own bias. Conventionally, the most direct and used method to identify AGN has been optical spectroscopy. AGN can be identified through the presence of broad emission lines, the detection of narrow emission lines characteristic of AGN ionization, or by line intensity ratios in diagnostic diagrams, such as [OIII]λ5007/Hβ vs [NII]λ6583/Hα. AGN in cosmological fields are routinely identified by their X-ray emission, MIR emission, excess radio emission and combinations of different emissions. Since the majority of AGN vary on time-scales from hours to millions of years, variability is another method used to select AGN. It selects preferentially low-luminosity AGN because they are expected to show stronger variability than the luminous ones. All these methods of AGN selection are complementary and each one can detect sources that other methods may miss.

The main goal of this thesis is to study the IR emission of AGN in nearby galaxies as well as active galaxies in cosmological fields. This thesis is divided into two different parts. The main objective of the first part is to select AGN in cosmological fields by their IR variability using *Spitzer*/MIPS 24 μm data (Chapter 3) while the objective of the second part is to study the dust heated by the AGN in nearby Seyfert galaxies using data from *Herschel* and from ground-based telescopes (Chapters 4 and 5).

This dissertation begins with an introduction to the AGN phenomenon (Chapter 1) and provides background information about AGN, their classification, and the unified model. This chapter also gives background information about the AGN identification, the IR emission, and the clumpy torus models, to understand the motivation for the research presented in this thesis. The main instruments used to obtain the data analysed during this work are presented in Chapter 2.

Chapter 3 focuses on MIR variability as a method to select AGN in the GOODS cosmological fields, using MIPS 24 μm (observed wavelength) data and a χ^2-statistics method. There are several studies of variability in other spectral ranges in these cosmological fields, such as optical, X-rays, and radio, but none of them has used MIR variability to select AGN. Therefore, this work provides a new way to select low-luminosity and obscured AGN. The main finding of this work is that only ~50% if the MIPS 24 μm variable sources are identified as AGN by other methods. Moreover, the estimated AGN contribution to the MIR emission for the variable sources is low (typically less than 20%). Therefore, these 24 μm variable sources are likely to host low-luminosity AGN, where the variability is expected to be stronger. However, the contribution of the 24 μm variable sources to the entire AGN population is small (~13%).

Chapter 4 presents a study of the nuclear and integrated FIR emission of Seyfert galaxies using images obtained with the *Herschel* telescope. Up until now there have been no statistical studies of the AGN contribution in the FIR using data obtained with the *Herschel* telescope. This works presents a method based on four different criteria to select galaxies whose nuclear 70 μm emission has a significant AGN contribution. The main finding of this work is that, although the majority of the FIR emission of Seyfert

galaxies is dominated by the host galaxy, 18% of the initial sample have a significant contribution ($\sim 40-70\%$ of their nuclear emission) from dust heated by the AGN. Therefore, the criteria defined in this chapter provide a good way to select statistically Seyfert galaxies with significant 70 μm emission due to the AGN.

Chapter 5 presents a statistical comparison of the MIR properties of Seyfert galaxies derived from high angular resolution spectroscopy and outputs from the CAT3D clumpy torus models (Hönig and Kishimoto 2010). The latter include previously published models as well as new runs of the models with an improved dust sublimation physics. The main finding of this chapter is that the new models reproduce better the overall MIR properties of local AGN. Moreover, although it is not possible to break fully the degeneracy in all parameters of the CAT3D models (or any other clumpy torus models) by using MIR spectroscopy alone, some different trends between Seyfert 1 and Seyfert 2 galaxies can be uncovered.

Finally, Chapter 6 summarizes the results obtained during this thesis and presents how this work can be extended in the future.

Contents

List of Figures

List of Tables

Chapter 1

Introduction

1.1 Active Galactic Nuclei

Supermassive black holes (SMBH, $M_{SMBH}>10^6\,M_\odot$) are believed to exist in the centre of all galaxies containing a significant bulge component (Kormendy and Richstone 1995). Furthermore, the bulge properties, such as the stellar mass and the velocity dispersion, are correlated with the black hole mass (Magorrian et al. 1998; Marconi and Hunt 2003; Häring and Rix 2004). From these relations one may deduce that the bulges of the galaxies and the SMBH evolve together, probably mutually regulating each other, or at least, sharing formation and growing mechanisms (see Alexander and Hickox 2012 for a review).

The first piece of evidence that some galaxies host a strongly emitting component in their centre was found by Seyfert (1943). He studied spectra of six galaxies showing nuclear emission lines superposed on a normal star-like spectrum. He also noticed that some galaxies showed broad emission lines (Full Width at Half Maximum, FWHM $\gtrsim 1000\,\mathrm{km\,s^{-1}}$) while others only showed narrow emission lines (FWHM $\lesssim 1000\,\mathrm{km\,s^{-1}}$). Since then, the study of active galaxies started.

In some galaxies, the SMBH is quiet, but in some of them the SMBH is growing. The latter phenomenon is revealed in a variety of ways and it is generally referred to as active galactic nucleus or AGN. It is a very energetic phenomenon that occurs in the central region of the galaxies and cannot be due to star formation. The luminosity in the central region can be thousands of times higher than the host galaxy, with the bolometric luminosity for the AGN ranging from 10^{41} to $10^{48}\,\mathrm{erg\,s^{-1}}$. The AGN luminosity is emitted in all the electromagnetic spectrum, often peaking in the ultraviolet, but with significant emission in X-rays and infrared (IR). For comparison, a *normal* galaxy has a bolometric luminosity of $\leqslant 10^{42}\,\mathrm{erg\,s^{-1}}$, with a large fraction of their luminosity being emitted in the visible and/or IR. The only exception are luminous and ultraluminous IR galaxies (LIRGs and ULIRGs, $L_{IR} = 10^{11} - 10^{12}\,L_\odot$ and $10^{12} - 10^{13}\,L_\odot$). The majority of these galaxies in the local Universe contains an AGN but at least in the case of LIRGs the AGN does not dominate the bolometric

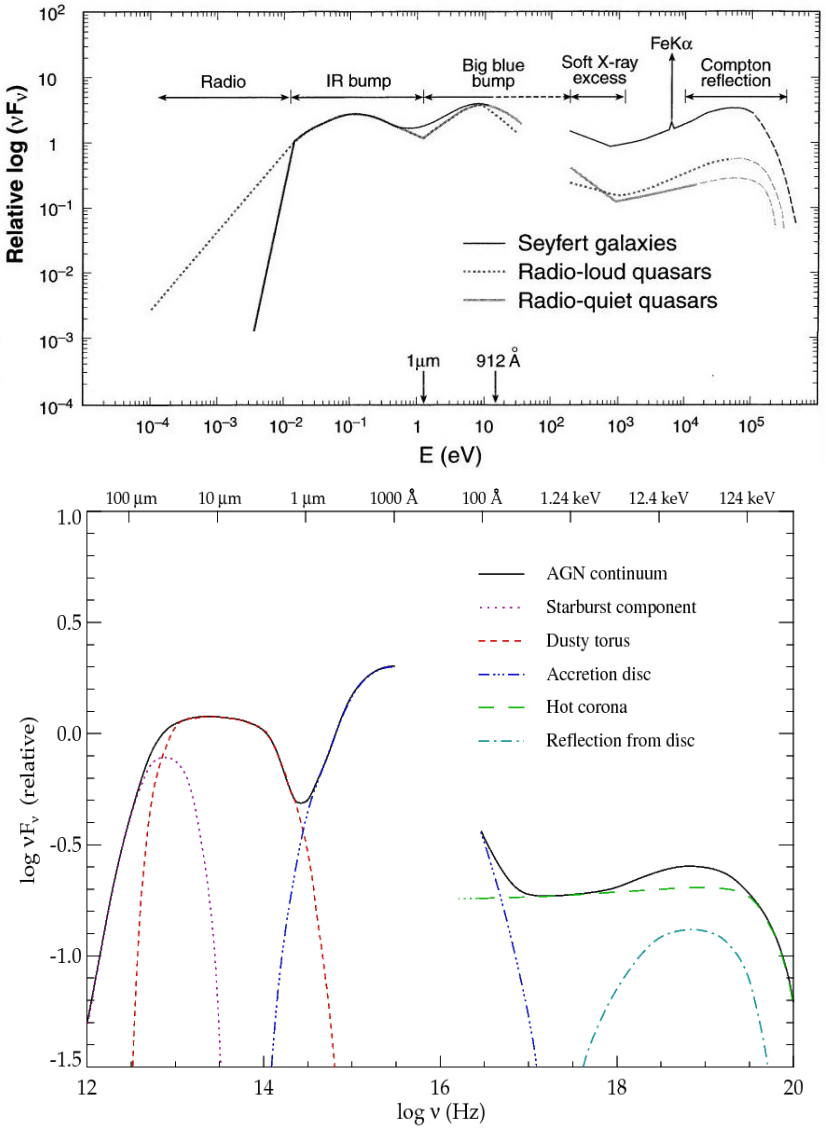

FIGURE 1.1: Top: Average SED for three different types of AGN. Bottom: Schematic representation of the SED of a AGN with a possible source for each emission component. Credit: Koratkar and Blaes (1999) and Manners PhD thesis (2002).

luminosity (Alonso-Herrero et al. 2012a). The focus of this thesis is the IR emission of AGN, which is discussed in more detail in Section 1.5. In this Section we only give a brief description of the continuum emission for every wavelength range, from radio to gamma rays. A schematic representation of the Spectral Energy Distribution (SED) of a AGN with a possible source for each emission component is shown in Fig. 1.1. The main wavelength ranges are:

1. **Radio emission:** Only about 10% of the AGN are radio loud (RL), i.e., the radio to optical flux ratio is high (>10). The radio quiet (RQ) AGN can have radio emission 100 to 1000 times weaker than the RL AGN (see top of Fig. 1.1). The radio emission is a small fraction of the bolometric luminosity for both, the RL and RQ AGN. The radio emission from AGN consists of compact

and extended components. For the RL AGN the radio emitting regions are relativistic jets and extended lobes with scales of kpc and Mpc. In the case of the RQ AGN the radio emission comes from the central radio cores with scales of pc. The radio emission can be well described with a power law coming from synchrotron radiation. The radio spectrum is flatter for the radio core emission than for the radio emission of jets.

2. **IR emission:** The integrated emission of all the IR range ($1 - 1000\,\mu$m) is typically 30% of the bolometric luminosity. The IR continuum shows a broad IR bump (see top of Fig. 1.1) between $\sim 1 - 200\,\mu$m with the minimum around $1\,\mu$m. The IR emission can be thermal and/or non-thermal depending on the AGN type and the spectral range. In RL AGN, the same synchrotron emission process producing the radio continuum is the predominant source of IR emission. For the RQ AGN there are multiple thermal components, such as thermal radiation from the nuclear material obscuring the AGN central engine, the so-called dusty torus (see Section 1.3 and dashed red line of Fig. 1.1), thermal dust continuum and features associated with star formation as well as additional line emission emanating from molecular, atomic, and ionic species (see Section 1.5 for more details).

3. **Optical/UV emission:** The most noticeable feature in this range mostly seen in type 1 AGN (see below for a definition) is the big blue bump (BBB) in the optical/UV spectra of AGN. This BBB peaks at around 1000 Å, and dominates the spectra at wavelengths shorter than ∼4000 Å. The BBB usually corresponds to the peak of AGN luminosity and can account for up to ∼50% of the bolometric luminosity. The relative strengths of the IR bump and the BBB vary from galaxy to galaxy but they are generally comparable. This BBB feature is attributed to some kind of thermal emission in the range around $10^4 - 10^6$ K, believed to be emission from a heated accretion disk surrounding the SMBH (dot-dot-dashed blue line of Fig. 1.1). The optical spectrum shows strong broad permitted emission lines in type 1 AGN as well as narrow forbidden and permitted emission lines superposed on the continuum.

4. **X-ray emission:** The accretion disk surrounding the black hole is believed to produce a thermal spectrum in X-rays. Inverse Compton scattering of the low-energy disk photons by the relativistic electrons located in the inner part of the accretion disk (corona, see Section 1.3) produces the X-ray emission (dashed green line of Fig. 1.1). It can be approximated to a power law with spectral index of $0.8 - 1$ from energies of ∼1 keV to over 100 keV. There is also a bump above the power-law continuum between $\sim 7 - 60$ keV, peaking at ∼30 keV. This bump is explained as reflection of the X-ray continuum in the accretion disk (dot-dashed blue line of Fig. 1.1).

5. **γ-ray emission:** γ-ray emission has not been detected in the majority of the AGN, but some RL AGN, known as Blazars, emit most of their bolometric luminosity above 100 MeV. They are characterised by a non-thermal continuum spectrum, a flat radio spectrum, strong variability and optical polarisation.

TABLE 1.1: Classification of AGN.

Radio classification	AGN type	Subtype	X-ray obscured?	Broad Balmer lines?	Narrow Balmer lines?	γ-rays?
RQ	Seyfert	Seyfert 1	<10%	✓	✓	x
		Seyfert 2	>90%	x	✓	x
		NLS1	<10%	✓	✓	Few
	LINER	type 1	x	✓	✓	x
		type 2	✓	x	✓	x
	Quasar	type 1	x	✓	✓	x
		type 2	✓	x	✓	x
RL	Radio galaxy	FR I	x	Some	✓	x
		FR II	x	Some	✓	x
	Quasar	type 1	x	✓	✓	Some
		type 2	✓	x	✓	x
	Blazar	FSRQ	x	✓	✓	✓
		BL Lacs	x	x	x	✓

1.2 AGN classification

The classification of AGN is very complex because the physical differences between different types of AGN are not clear. Historically, RL and RQ AGN have been classified in a different way. Whereas the RL AGN are classified according to their optical spectral properties and their radio morphology, the RQ AGN are classified according to their optical spectral properties and their luminosity. Therefore, the first main AGN classification depends on the radio emission. The parameter used to divide the galaxies into RL and RQ is called radio-loudness and is defined as:

$$R = \left(\frac{f_{5\,\mathrm{GHz}}}{f_{4400\,\text{Å}}} \right) \tag{1.1}$$

where $f_{5\,\mathrm{GHz}}$ is the monochromatic radio flux at 5 GHz and $f_{4400\,\text{Å}}$ is the monochromatic optical flux centred at 4400 Å. An object is classified as RL when $R > 10$, and RQ when $R < 10$. Thus, an object which is radio-quiet is not necessary radio-silent, it can show radio emission. RL sources represent only about ~10% of all the AGN. Here, we describe briefly some of the most relevant AGN types as they are usually classified in the literature, and we summarize their main properties in Table 1.1.

- **RQ AGN:**
  - **Seyfert galaxies**

    Seyfert galaxies were the first AGN identified as active. The host galaxy has a typical galactic spectrum while the central region has highly ionized emission lines, including

forbidden lines. This is the criterion used nowadays to identify Seyfert galaxies, if the spectrum shows these highly ionised emission lines, it qualifies it as Seyfert.

Khachikian and Weedman (1974) studied the spectra of Seyfert galaxies and found two different types of optical spectra. Whereas all spectra showed narrow highly ionized emission lines, only some of them showed broad lines. They separated the Seyfert galaxies into two classes (Seyfert 1 and Seyfert 2) depending on the relative widths of narrow (forbidden) lines and Balmer lines (FWHM $\gtrsim 1000\,\mathrm{km\,s^{-1}}$ for type 1 AGN and FWHM $\lesssim 1000\,\mathrm{km\,s^{-1}}$ for type 2 AGN). Seyfert 1 galaxies have broader Balmer lines (Hα, Hβ, Hγ) than the forbidden lines, like the [OII]λ3727, [OIII]$\lambda\lambda$4959,5007, [NII]$\lambda\lambda$6548,6584, [NeIII]λ3869, [NeIV]λ2439 lines. Furthermore, the Balmer lines have a broad and a narrow component. Conversely, Seyfert 2 galaxies show both, the Balmer and the forbidden lines with the same narrow width. Osterbrock (1977) introduced the intermediate types of Seyfert according to the Balmer lines characteristics. Seyfert 1.2 galaxies have typical broad Balmer lines, as Seyfert 1, but the Hβ line is slightly less broad. Seyfert 1.5 galaxies have Hβ lines in which the broad and the narrow component are equally strong. Seyfert 1.8 galaxies show some broad component in the Balmer lines and Seyfert 1.9 galaxies only show a broad Hα line while the Hβ line is narrow. There is another subset of Seyfert 1 galaxies, called narrow-line Seyfert 1 galaxies (NLS1). They are strong X-ray emitters with broad Hα lines and narrow Hβ lines (FWHM(Hβ) $< 2000\,\mathrm{km\,s^{-1}}$), similar to Seyfert 1.9 galaxies. The NLS1 also have a ratio ([FeII]λ4570/Hβ) twice as high as the other Seyfert types.

For Seyfert galaxies a combination of emission from the host galaxy and the active nucleus is observed. In general, in Seyfert 2 galaxies the AGN nucleus is less dominant with respect to the host galaxy than for Seyfert 1 galaxies. For this reason it is more difficult to find Seyfert 2 galaxies based on their optical spectra (Moran et al. 2002). Conversely, Seyfert 1 galaxies show in general a strong continuum, without the characteristic stellar absorption lines, which cannot be attributed to the host galaxy.

– LINER

LINERSs (Low-Ionisation Nuclear Emission-line Region) are low-luminosity AGN. They are the most numerous type of AGN in the local Universe (Ho et al. 1997). They were first identified by Heckman (1980), who arbitrarily defined a LINER as an object in which [OII]λ3727 is at least as strong as [OIII]λ5007 and [OI]λ6300 is at least one third as strong as [OIII]λ5007. This definition is nearly equivalent to those of Veilleux and Osterbrock (1987), who defined the division between Seyferts and LINERS at [OIII]λ5007/Hβ = 3. Therefore, LINERs can show [OIII]λ5007/Hβ < 3, unlike Seyfert galaxies. González-Martín et al. (2009) found that about 60% of the LINERs could host AGN cores emitting in the 4.5 − 8 keV band. Adding multiwavelength information they showed that about 80% of the objects have evidence of harbouring an AGN. In LINERs it is often difficult to detect the AGN because the host galaxy contributes a large amount to the observed

emission (González-Martín et al. 2014). However, González-Martín et al. (2015) showed that about 60% of the LINERs have their mid-IR (MIR, $\sim 5-50\,\mu$m) spectra not dominated by starburst. They also found that the average spectrum of AGN-dominated LINERs is different from the other optical classes, showing a rather flat continuum in the range 6 – 28 μm.

– **Quasars**

Quasars were discovered in the late 1950s and early 1960s in large radio surveys (Schmidt 1963). Many of the strong radio sources appeared in optical images like blue stars, so they were called quasi stellar objects (QSO) or quasars. Although the first quasars were found in radio surveys, the majority of the quasars found in optical surveys do not present strong radio emission, with approximately 90% of quasars being RQ AGN. Quasars have spectra similar to those of Seyfert galaxies, therefore they are divided into type 1 and type 2 depending of the presence (or absence) of broad emission lines. Quasars are brighter than Seyfert galaxies and are at higher redshifts. The division between quasars and Seyfert galaxies is arbitrary and depends on the luminosity. Seyfert galaxies with absolute B-magnitude $M_B < -23$ mag are referred to as quasars (Schmidt and Green 1983).

- **RL AGN:**

– **Radio galaxies**

Radio galaxies are RL AGN in which the central region is hidden but show bright radio jets and large radio luminosities. They can be divided in two groups according to their radio morphology and luminosity: the low-luminosity Fanaroff-Riley class I (FR-I) and the high-luminosity Fanaroff-Riley class II (FR-II). The FR-I galaxies show compact radio emission and their radio surface brightness profiles decrease outwards, while FR-II galaxies are dominated by radio lobes and their radio surface brightness profiles increase outwards as they reach the end of the extended structures (Fanaroff and Riley 1974). Both, FR-I and FR-II optical spectra are similar to those of Seyfert galaxies. Those with a Seyfert 2 optical spectrum are called narrow-line radio galaxies (NLRG) and those with broad optical-UV lines are called broad-line radio galaxies (BLRG).

– **RL Quasars**

The RL quasars were the first quasars to be discovered. Although they are only about 10% of the quasars, they are easier to detect due to their strong radio emission. As RQ quasars, their optical spectrum is similar to those of Seyfert galaxies and are therefore divided into type 1 and type 2.

– **Blazars**

Blazars are a special subclass of RL quasars, in which a relativistic jet is pointing very close to the line of sight of the observer. They have high variability and emit from radio

frequencies to very high energies. Their emission is variable in all the electromagnetic spectrum in time scales from years to hours. Blazars are divided into BL Lac objects and Flat Spectrum Radio Quasars (FSRQ). BL Lac objects do not have prominent features in the optical spectrum, so the equivalent width (EW) of emission lines is used as an arbitrary dividing line between the two types of Blazars.

1.3 The Unified Model

In the previous section a great variety of AGN types have been presented, but all of them are believed to share the same basic phenomena at their centres. To explain this diversity of AGN, Antonucci (1993) proposed the first unification model. In the most simplified picture, there are basically two types of AGN: RL and RQ. A range of luminosities is observed for each type, allowing the distinction between Seyferts and quasars. All other observational differences are explained by orientation effects. Therefore, the differences between type 1 and type 2 AGN and the intermediate types are explained as a continuum transition in the viewing angle from 0° to 90°.

The unification between RQ and RL AGN was made by Urry and Padovani (1995). They included the relativistic jet, so the AGN radio emission depends on the inclination angle between the observer to the jet. Fig. 1.2 represents the AGN unified model, with the principal components and the type of AGN depending on the viewing angle. The principal components of the AGN unified model are:

- **SMBH**

  It is accepted that the main engine of an AGN is an accreting SMBH with mass $> 10^6\,M_\odot$ at the centre of the host galaxy. As AGN are compact, extremely luminous and often variable, the only plausible mechanism that can provide a highly efficient conversion of potential and kinetic energy to radiation is accretion of material onto a SMBH.

- **Accretion disk**

  The matter orbiting and falling onto the SMBH forms a geometrically thin and optical thick accretion disk. The matter falls converting the potential and kinetic energy to radiation via viscous dissipation. The accretion disk emits thermal radiation in the optical/UV range, producing the BBB. The approximate inner radius of the accretion disk is at $\sim 0.01 - 60$ astronomical units (AU) from the SMBH centre and the outer disk radius is at $\sim 1 - 1000$ AU.

- **Corona**

  Over the inner parts of the accretion disk, there is a corona of very energetic electrons that is responsible for the inverse Compton scattering of the thermal photons emitted from the disk. This results in the X-ray power law emission (see Section 1.1).

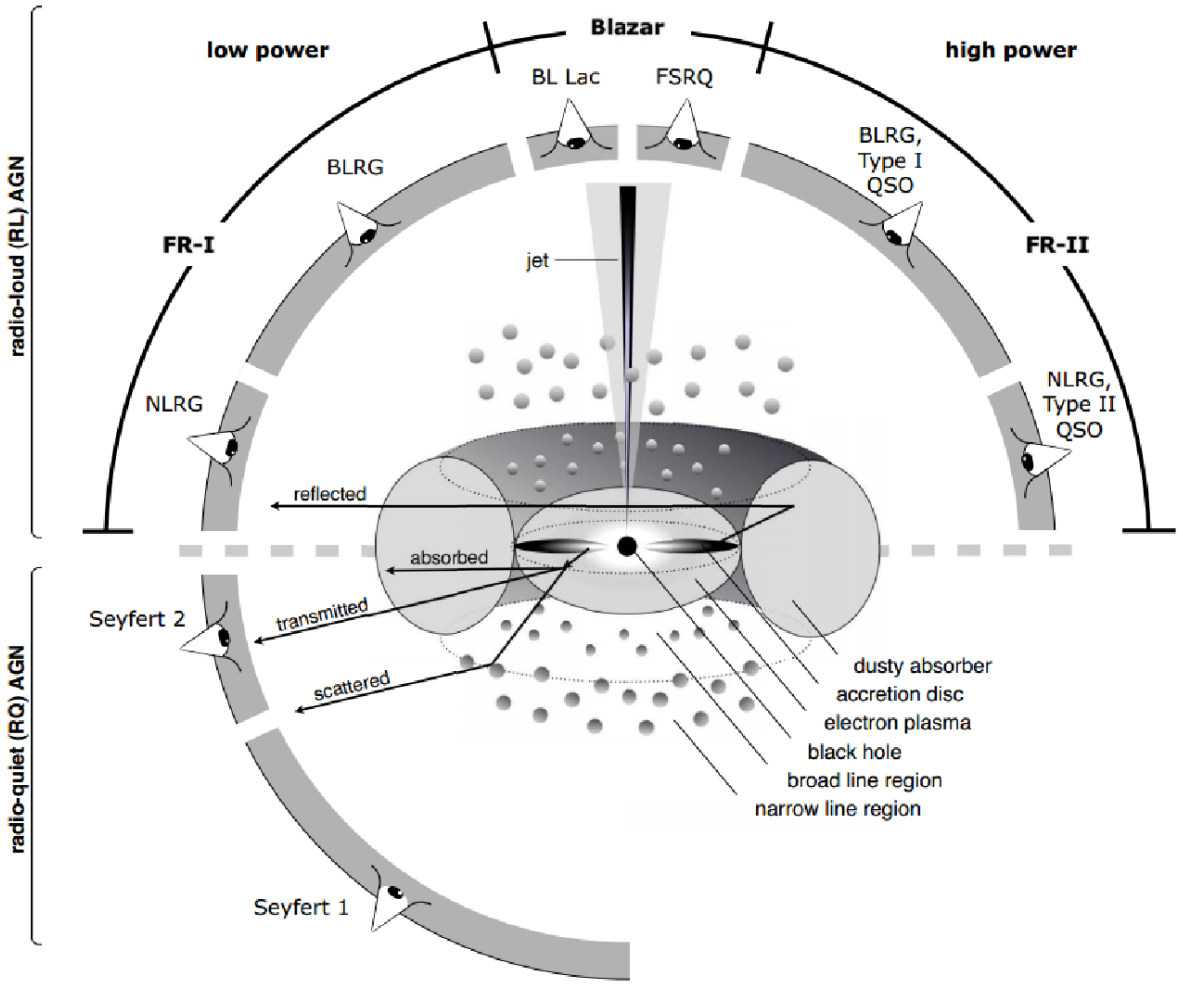

FIGURE 1.2: Schematic representation of the AGN unified model. The type of AGN depends on the viewing angle, whether or not the AGN produces a significant jet emission, and how powerful the central engine is. Credit: Marie-Luise Menzel.

- **Broad line region (BLR)**

  The BLR is the region where broad permitted emission lines observed in the optical/UV and near-IR (NIR, $\sim 1 - 5\,\mu$m) ranges arise from. It is formed of clouds of gas in photoionization equilibrium, with turbulent motions. The large Doppler broadening observed in the permitted lines is due to the deep gravitational potential of the SMBH, with gas velocities of order of 10^3 to a few $10^4\,\mathrm{km\,s^{-1}}$. The size of the BLR can be estimated by reverberation mapping of the broad lines, with typical sizes of $\sim 0.01 - 1$ pc. The absence of broad forbidden lines indicates that the gas density has to be $> 10^9\,\mathrm{cm^{-3}}$.

- **Torus**

  Outside the BLR there is an obscuring dust structure with a toroidal geometry that extends from 1 to 100 pc, in a similar plane as the accretion disk. It contains both, cold gas and dust. The torus provides anisotropic obscuration of the central engine, blocking the BLR and the accretion

disk for high viewing angles (directions close to the equatorial plane of the torus), whereas for low inclinations (close to the polar direction of the torus) the observer has an unobscured view of the central engine. The dust reprocesses the optical/UV radiation from the accretion disk via absorption and re-emission, and it is responsible for the major part of the nuclear MIR emission and for part of the far-IR (FIR, $\sim 50 - 1000\,\mu$m) continuum observed in AGN. In Chapter 4 we investigate the AGN contribution to the FIR. See Section 1.6 for information about the different torus models available in the literature.

- **Narrow line region**

  The NLR is the region where the narrow permitted and forbidden lines in the optical/UV NIR and MIR ranges come from. The gas clouds have less turbulence than those in the BLR. The velocities of the clouds are $\sim 400 - 500\,\mathrm{km\,s^{-1}}$. The presence of forbidden and permitted lines is indicative of lower densities than the BLR ($10^3 - 10^5\,\mathrm{cm^{-3}}$). The narrower widths and the lack of variability of the emission lines indicates that they arise from a region that is much larger and kinematically separate from that of the broad lines ($\sim 10^2 - 10^4$ pc).

- **Relativistic jet**

  Certain subclasses of AGN present relativistic jets emanating from the sub-parsec scales of the AGN. They are believed to be extremely energetic and collimated outflowing plasma structures launched from the accretion disk that can extend up to hundreds of kpc. These jets occur in about 10% of the AGN (the RL AGN), and are responsible for the radio emission in the RL AGN.

The dusty torus is the essential component to explain the orientation dependence on the unified model. Its first direct detection was made with ALMA in the Seyfert 2 NGC 1068 (García-Burillo et al. 2016). In type 1 AGN the viewing angle is near to the polar direction of the torus, so the central engine is directly visible and the BLR can be seen (see Fig. 1.2). On the other hand, type 2 AGN are viewed edge-on, so the torus hides the central engine and the BLR, and therefore only narrow lines are present in the optical spectrum. The relativistic jet explains the differences between RQ and RL AGN. Those AGN with jet emission are RL AGN, while those with no jet are RQ AGN.

The first hint of the unified model was given by Antonucci and Miller (1985). They studied NGC 1068 and discovered that although in the direct optical light it only showed narrow emission lines when observed in polarized light it also showed broad Balmer lines. The proposed explanation is that although the BLR is hidden by the torus, the light can be scattered towards the line of sight of the observer, and these scattered photons are polarized. Other studies have confirmed the presence of hidden broad lines in type 2 AGN (see Moran et al. 2000; Ramos Almeida et al. 2016 and references therein). The IR band is another way to find hidden broad lines in type 2 AGN, as this spectral range is less affected by obscuration. The inferred optical depths from the IR correspond to the expected optical extinction (Ward et al. 1991).

However, there are observations that deviate from this unified model. Not all Seyfert 2 galaxies show a hidden type 1 nucleus even when observed in polarized light (Bianchi et al. 2008; Tran 2001, 2003). Studies with 8 m telescopes and good S/N have reduced significantly the number of Seyfert 2 galaxies without a hidden Seyfert 1 nucleus (Ramos Almeida et al. 2016). One explanation for Seyfert 2 galaxies without hidden broad lines is that the central engine has a low power, so it cannot illuminate sufficiently the BLR. This also can be used as explanation of why BL Lac objects do not show emission lines.

According to the unified model, type 2 AGN should be X-ray absorbed, but there are examples of type 2 AGN with no absorption in X-rays, like NGC 3147 and NGC 4698 (Pappa et al. 2001), and for example the works of Corral et al. (2011) and Mateos et al. (2005). They can be due to the same effect as the Seyfert 2 galaxies without a hidden type 1 nucleus. The intrinsic power of the AGN is low so there might be only a weak BLR.

Another challenge for the unified model is the anticorrelation between the fraction of absorbed sources and the luminosity in hard X-rays surveys (Beckmann et al. 2009). This can be explained introducing the luminosity as a parameter in the unified model.

All these examples that deviate from the simplest unified model highlight the importance of adding the AGN intrinsic properties, such as the SMBH mass, its spin, the accretion rate, and the host-galaxy morphological type.

1.4 AGN identification

AGN present a large range of observational features, such as emission lines, variability, IR excess, strong X-ray emission, and strong radio emission. Not all AGN show all the features, so having an efficient, reliable and complete AGN selection technique is very difficult. The methods are also different for local AGN, where it is possible to have nuclear images and spectroscopy, than from those in cosmological fields, where most AGN appear unresolved. We describe briefly the different methods to select AGN.

Conventionally, the most direct and used method to identify AGN has been optical spectroscopy. As explained previously, AGN can be identified through the presence of broad emission lines (FWHM $\gtrsim 1000\,\mathrm{km\,s^{-1}}$, type 1 AGN) or the detection of narrow emission lines characteristic of AGN ionization (FWHM $\lesssim 1000\,\mathrm{km\,s^{-1}}$, type 2 AGN). Another method is by line intensity ratios in diagnostic diagrams, such as [OIII]λ5007/Hβ vs [NII]λ6583/Hα. Baldwin et al. (1981) demonstrated that it is possible to distinguish type 2 AGN from normal star-forming galaxies using line intensity ratios. Veilleux and Osterbrock (1987) also used line diagnostics based on emission line ratios to derive a semi-empirical classification between AGN and star-forming galaxies. Using the same diagnostic diagrams Kewley et al. (2001) derived new theoretical boundary regions to classify LINERs and to separate AGN from starburst. Later Kauffmann et al. (2003) defined an empirical dividing

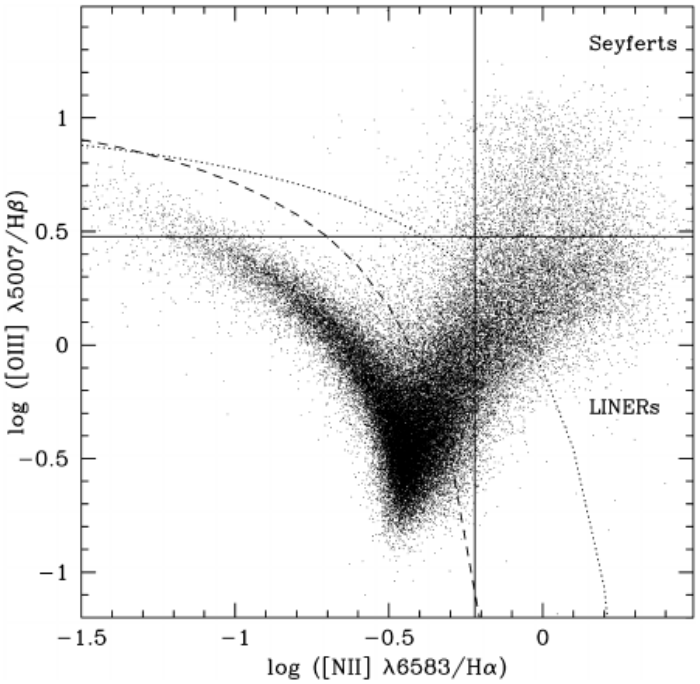

FIGURE 1.3: An example of a spectroscopic diagnostic diagram using the [OIII]/Hβ ratio versus [NII]/Hα ratio. The dashed curve shows the dividing line of Kauffmann et al. (2003) while the dotted line is the dividing line defined by Kewley et al. (2001). Seyfert galaxies are often defined to have [OIII]λ5007/Hβ > 3 and [NII]λ6583/Hα > 0.6, while LINERs are defined to have [OIII]λ5007/Hβ < 3 and [NII]λ6583/Hα > 0.6. Credit: Kauffmann et al. (2003)

line below the line drawn by Kewley et al. (2001) and Stasińska et al. (2006) proposed other division line between the AGN and the star-forming galaxies, close to the one defined by Kauffmann et al. (2003) and proposed a new diagnostic diagram for the galaxies up to z = 1.3. The underlying idea of these diagrams is that the emission lines in normal star-forming galaxies are emitted by HII regions, ionized by massive stars, while AGN are ionized by a harder radiation field. Therefore, for a given [OIII]λ5007/Hβ or [OIII]λ5007/[OII]λ3727 ratio, galaxies containing an AGN will show higher [OII]λ3727/Hβ, [NII]λ6583/Hα, [SII]$\lambda\lambda$6717,6731/Hα, or [OI]λ6300/Hα ratios than normal star-forming galaxies. Fig. 1.3 shows an example of a line ratio diagnostic diagram where it is plotted the emission line flux ratio [OIII]λ5007/Hβ versus [NII]λ6583/Hα. The dashed and dotted curves show the dividing lines of Kauffmann et al. (2003) and Kewley et al. (2001), respectively. Unfortunately, spectroscopy of a large number of objects is very expensive in terms of observing time, especially for faint sources in cosmological fields. Furthermore, AGN lines can be obscured and/or swamped by emission from the host galaxy (Moran et al. 2002).

AGN in cosmological fields are routinely identified by their X-ray emission (Alexander et al. 2003; Brandt and Hasinger 2005). The standard threshold used to select AGN is a hard X-ray luminosity $L_{2-10\,\mathrm{keV}} > 10^{42}\,\mathrm{erg\,s^{-1}}$. This is based on the fact that the X-ray spectra of star-forming galaxies are typically softer than those of AGN. Therefore, luminous X-ray emission is a indicator of the existence

of an AGN and does not need additional observations at other wavelengths to confirm it. Although X-ray surveys provide the most complete AGN samples, they miss the most obscured AGN needed to fit the cosmic X-ray background integrated energy density (Gilli et al. 2007). Another method to identify AGN in cosmological fields is by their radio emission. It is known that a tight correlation exists between FIR and radio emission for star-forming galaxies (Helou et al. 1985; Appleton et al. 2004). Thus, an excess of radio emission over the expected relation is produced by an AGN, often obscured by large amounts of dust and gas (Donley et al. 2005; Del Moro et al. 2013). As this method depends only of the FIR and radio emission, AGN that are missed at other wavelengths can be detected. The AGN detection through radio emission also presents biases, as only about 10% of the AGN are RL, and in general there is little overlap between radio and IR/X-ray selected AGN (Hickox et al. 2009). In the last years many AGN searches have been done in the NIR and MIR, allowing to identify AGN whose optical emission is obscured by dust. Whereas star-forming galaxies have their NIR SEDs dominated by the 1.6 μm stellar bump, galaxies containing an AGN have a power-law emission in the NIR. For this reason the *Spitzer* IRAC NIR and MIR bands (3.6, 4.5, 5.8, and 8.0 μm) have been used to identify AGN (Lacy et al. 2004, 2013; Stern et al. 2005; Alonso-Herrero et al. 2006; Donley et al. 2007, 2008, 2012). The Wide-field IR Survey Explorer (WISE) bands (3.4, 4.6, and 12 μm) have also been used to select AGN (Mateos et al. 2012; Stern et al. 2012; Assef et al. 2013). These IR selection methods are only complete for the most luminous AGN (e.g., Donley et al. 2012), but they are likely to select obscured AGN not detected in X-rays (Mateos et al. 2013).

Variability can also be used to select AGN. Practically all AGN vary on time-scales from hours to millions of years (Ulrich et al. 1997; Hickox et al. 2014). Any variability detected in galaxies on human time-scales must originate in the nuclear region, because the typical timescale for star formation variability is ≥ 100 Myr (Hickox et al. 2014). In particular low-luminosity AGN are expected to show stronger variability than the luminous ones (Trevese et al. 1994). Therefore, variability is likely to be an effective method to select low-luminosity AGN. Although the mechanisms that produce variability are not well understood, the main explanations involve disk instabilities (Pereyra et al. 2006) or changes in the amount of accreting material (Hopkins and Beacom 2006).

All these methods of AGN selection are complementary and each one can detect sources other methods miss. It is therefore important to study the same region of the sky with different methods of AGN selection. In Chapter 3 we use MIR 24 μm variability as a method to identify AGN in a cosmological field.

1.5 IR emission of active galaxies

The IR emission of active galaxies not only is due to the AGN but also to the host galaxy. In RL AGN the predominant source of IR emission is the synchrotron emission process, which occurs when

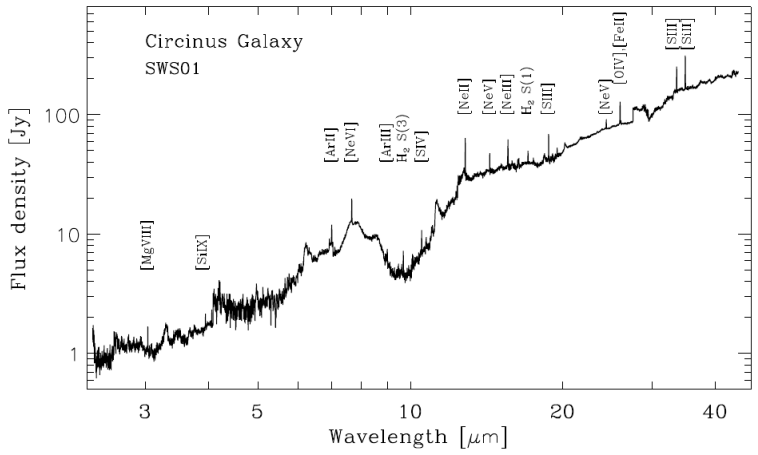

FIGURE 1.4: IR spectrum of the Circinus galaxy, taken by ISO. It shows PAH features between $5 - 12\,\mu$m, ionic emission lines resulting from star formation, and higher excitation lines from gas photoionized by the AGN. Credit: Moorwood et al. (1996)

charged particles are accelerated in a magnetic field. For RQ AGN the origin of the IR emission is different than in the RL AGN, and involves multiple thermal components.

In Seyfert galaxies, the most common galaxies studied during this thesis, the IR emission dominates their SEDS (Rieke 1978; Spinoglio et al. 1995). This emission is due to dust grains that re-radiate the absorbed optical and ultraviolet photons emitted by the AGN as well as by stars in their host galaxies. Therefore, their IR emission can be understood as a combination of three spectral components. The fist one is a thermal radiation from the dusty torus of the AGN. Another component is thermal dust continuum associated with star formation, consisting in line emission from polycyclic aromatic hydrocarbons (PAH) and continuum features form heated dust. The last component consists of line emission emanating from molecular, atomic, and ionic species. Fig. 1.4 shows an example of a IR spectrum for a Seyfert 2 galaxy, the Circinus galaxy, taken by the *Infrared Space Observatory (ISO)*. It shows PAH features between $5 - 12\,\mu$m, ionic emission lines resulting from star formation (e.g. [FeII]$\lambda 5.34\,\mu$m, [NeII]$\lambda 12.81\,\mu$m), and higher excitation lines from gas photoionized by the AGN (e.g. [MgVIII]$\lambda 3.03\,\mu$m, [SiIX]$\lambda 3.94\,\mu$m, [NeV]$\lambda\lambda 14.32,24.32\,\mu$m).

Using *ISO* observations, Perez Garcia et al. (1998) proved the composite nature of the IR emission of Seyfert galaxies. They showed that the integrated MIR and FIR thermal emission of Seyferts can be modelled with a combination of three different components: warm, cold, and very cold dust. The warm component is due to dust heated by the AGN and/or circumnuclear star formation ($T \sim 150\,K$), the cold component comes from dust heated by stars in the disc of the galaxy ($T \sim 40 - 50\,K$) and the very cold component arises from dust heated by the general interstellar radiation field of the galaxy ($T \sim 10 - 20\,K$).

Whereas the nuclear NIR and MIR emission of Seyfert galaxies is dominated by the AGN, the FIR emission is often dominated by the host galaxy. Rodríguez Espinosa and Pérez García (1997) found

that the MIR emission correlates with the compact optical emission whereas the FIR emission correlates with the extended optical emission from the galaxy disk. There are several studies determining that the majority of the FIR emission of Seyfert galaxies is due to the host galaxy. For example, Rodriguez Espinosa et al. (1987) studied the FIR emission of a sample of optically selected Seyfert galaxies using observations taken with the *Infrared Astronomical Satellite (IRAS)*. They found that the distribution of the integrated FIR luminosities and 60 μm to 100 μm colours of Seyfert and starburst galaxies were indistinguishable and concluded that most of the FIR emission of Seyfert galaxies must be due to star formation processes. Spinoglio et al. (2002) also found, using *ISO* imaging data, that the integrated FIR emission of Seyfert galaxies is dominated by emission from the host galaxy.

This thesis focuses on the IR emission of active galaxies. In Chapter 3 we study the emission at 24 μm to select variable sources in the MIR. In Chapter 4 we study the FIR ($70-500\,\mu$m) emission of Seyfert galaxies to disentangle their FIR emission due to dust heated by the AGN from that due to dust heated by star formation. In Chapter 5 we analyse the MIR spectrum of Seyfert galaxies to compare it with the predictions of clumpy torus models.

1.6 Torus models

As explained above, the dusty torus is the essential component to explain the orientation dependence on the unified model. There are some constraints for the torus that can be inferred from indirect evidence. It has to be optically thick (optical depth > 1), dusty and geometrically thick to explain the difference between type 1 and type 2 AGN and the IR bump.

A large number of torus models have been presented in the literature to explain the IR observations. They can be divided into radiative transfer models and hydrodynamical models. The radiative transfer models have gained complexity over the years, beginning with smooth dust configurations (see e.g., Pier and Krolik 1992; Granato and Danese 1994; Efstathiou and Rowan-Robinson 1995; Fritz et al. 2006) and moving to clumpy dust distributions (see e.g., Hönig et al. 2006; Nenkova et al. 2008a,b; Schartmann et al. 2008; Hönig and Kishimoto 2010). Dynamical studies tend to favour a clumpy structure rather than a uniform torus (Elitzur and Shlosman 2006), but the first models used smooth dust distributions due to the lack of suitable computing power. In this Section we only give a brief description of the radiative transfer models, as the clumpy models are the ones used during this thesis.

1.6.1 Radiative transfer models

All radiative transfer models of the AGN torus have similarities in the torus geometry and some of the parameters used to define the models. The torus is characterized by a inner radius R_d (dust sublimation radius) and a outer radius R_{out}, that is defined in physical units or relative to R_d. R_{out} does not correspond to the observed size, it is only an outer boundary definition of the model space.

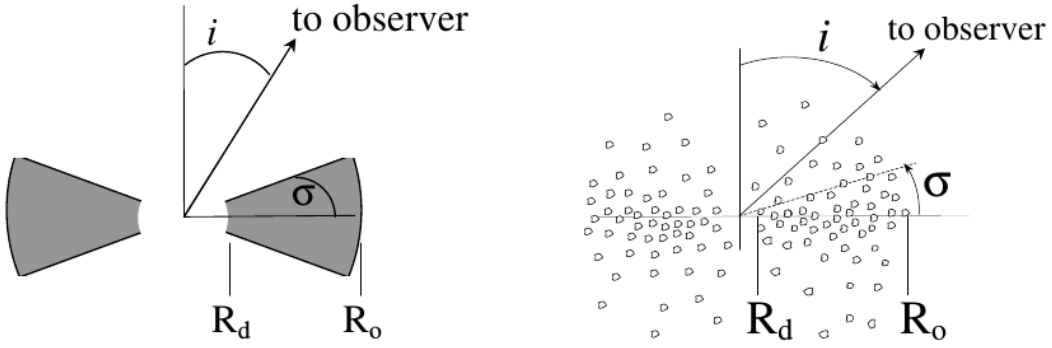

FIGURE 1.5: Schematic representation of the AGN smooth torus configuration (left) and a clumpy torus configuration (right). Credit: Elitzur (2007)

The distribution of the dust is different in smooth and clumpy models. In the case of smooth models, the dust is homogeneously distributed, whereas in clumpy torus the dust is distributed in clouds. This cloud distribution is commonly parametrized with a radial power law $n(r) \propto r^a$ where the power-law index, a, defines the compactness of the cloud distribution. For high negative values of a the dust is concentrated near R_d, for small negative values of a (near zero) the dust mass is distributed over a wide range of distances from the AGN, and for positive values of a the dust is concentrated near R_{out}. The mean number of clouds, normally defined along the equatorial line of sight, is a fundamental parameter in the clumpy models.

Another important parameter in both, the smooth and clumpy torus models, is the angular size of the torus or half-opening angle represented with the σ symbol in Fig. 1.5. The optical depth is another important parameter. It is defined along any line of sight and depends on the dust mass and density in the model space. In clumpy models the optical depth is usually a combination of the optical depth of an individual cloud and the number of clouds along the preferred line of sight.

Fig. 1.5 shows a schematic view of a smooth torus configuration (left) and a clumpy torus configuration (right). For the smooth model, the relation between the viewing angle (i) and the torus angular size (σ) determines the classification between type 1 ($90 - i > \sigma$) and type 2 AGN ($90 - i \leqslant \sigma$). For the clumpy model, the delimitation between type 1 and type 2 is not strictly due to orientation but to the probability of observing directly the AGN nucleus which in turn is a function of i, σ (or θ_0 in the Hönig and Kishimoto (2010) notation) and N_0 (see eq. 5.1).

One of the arguments for clumpy torus instead of smooth models is the velocity dispersion observed in the centres of galaxies (Krolik and Begelman 1988). If the torus were homogeneous, the temperatures corresponding to that velocity dispersion would be too large for dust to survive. Conversely, if the dust is distributed in clouds, the velocity dispersions reflect the random motion of the clouds. Another evidence of clumpy torus is the long-term variability of the column density of type 2 AGN (Risaliti et al. 2002). The interpretation of the MIR interferometry also favours the clumpy models. Furthermore, the

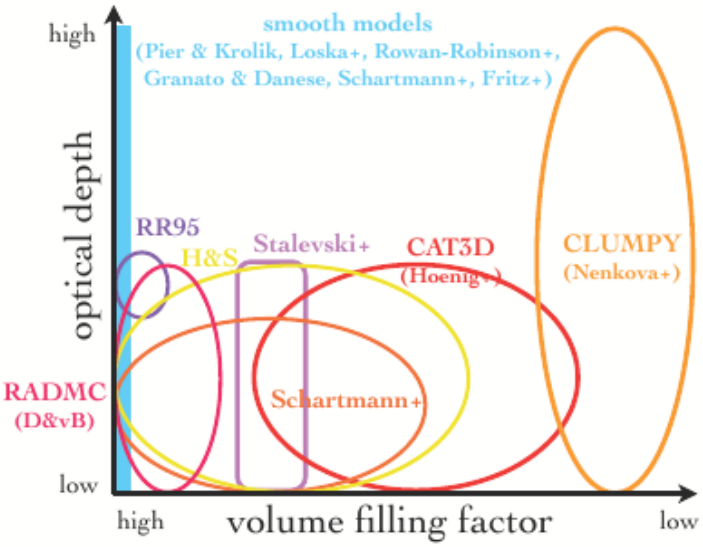

FIGURE 1.6: Volume filling factor vs. optical depth for clumpy torus models. Smooth models are shown for reference. Credit: Hoenig (2013)

smooth models predict deeper 9.7 μm silicate features than observed in Seyfert galaxies, and have very abrupt division between the shape of the SEDs of Seyfert 1 and Seyfert 2, without SEDs for intermediate Seyfert galaxies (see Alonso-Herrero et al. 2003). However, Feltre et al. (2012) argued that the differences in the predictions of the smooth and clumpy models were due to different hypothesis in the dust chemical composition and the primary sources.

Nowadays, the advancements in computational power allow Monte Carlo simulations of clumpy torus to predict SEDs and images. It is also possible to simulate a inter-cloud medium, formed by optically thin dust, between the clouds (Stalevski et al. 2012; Siebenmorgen et al. 2015).

There are significant differences between clumpy torus models. Fig. 1.6 shows the volume filling factor and the optical depth for various clumpy torus models (Hoenig 2013). Therefore, the clumpiness depends on the model used, and differences in the shape of the SEDs are expected, as the cloud size and density and the global optical depth dominate the shape of the SED. Another difference among the models is the way the cloud density profile is treated. Depending on the model, when the optical depth increases, the emission region of the cloud (the directly AGN-heated surface) can transit toward a steep density gradient (e.g., Nenkova et al. 2008a,b) or toward a smooth density gradient (e.g., Hönig and Kishimoto 2010). In the first case the hot emission becomes a black-body in the NIR and MIR, while in the second case the hot surface is dominated by optically thin emission in the IR and is independent of the total density of the cloud.

In Chapter 5 we use Hönig and Kishimoto (2010) clumpy torus models, including new models with improved physics and compare them with the nuclear MIR properties of AGN. A description of Hönig

and Kishimoto (2010) models is given in Section 5.5.1.

1.7 Aims of this thesis

As discussed above, since there is not a unique technique to identify AGN, it is important to use different methods as all of them present biases. Moreover, the IR band is a key spectral range to understand the dusty torus of the AGN. Not only the AGN emits in the IR but also the host galaxy, so it is important to disentangle both emissions.

The main objective of this thesis is to study the IR emission of AGN in nearby galaxies as well as active galaxies in cosmological fields. This thesis is divided into two different parts. The main goal of the first part is to select AGN in cosmological fields by their IR variability using *Spitzer*/MIPS 24 μm data (Chapter 3) while the objective of the second part is to study the dust heated by the AGN in nearby Seyfert galaxies using data from *Herschel* and from ground-based telescopes (Chapters 4 and 5).

Selecting AGN by their IR (24 μm) variability is a new method that can allow us to identify obscured and low-luminosity AGN that are missing in other wavelengths surveys. It also allows us to compare the selected variable AGN with catalogues of AGN detected by other methods and to estimate the fraction of these obscured AGN to the general AGN population. We are also able to calculate the AGN contribution to the MIR emission of these 24 μm variable sources.

On the other hand, the study of nearby Seyfert galaxies allows us to disentangle the nuclear IR emission due to dust heated by the AGN from that due to dust heated by star formation, and to study the IR properties of AGN. It also permits to make statistical comparisons of the MIR properties of Seyfert nuclei with predictions from clumpy dusty torus models.

Summarizing, along this work we will tackle the following issues to understand better the IR emission of active galaxies:

1. Selection of AGN by their 24 μm variability using a χ^2-statistics method.
2. Characterization of the properties of the 24 μm variable sources, as well as a comparison them with other variability studies.
3. Mechanisms giving rise to the nuclear and integrated FIR emission of nearby Seyfert galaxies by analysing their properties, such as the unresolved 70 μm emission, FIR colour distributions, nuclear and extranuclear star formation rates (SFR), and results from fitting the data to a grey body.
4. Identification of Seyfert galaxies whose 70 μm emission is mostly due to dust heated by the AGN, using four different criteria.

5. Study of the MIR emission due to dust heated by the AGN.

6. Statistical comparison between the MIR properties of AGN and the predictions of clumpy dusty torus models. This will allow us to constrain some of the torus model parameters.

Chapter 2

The instruments

In this Chapter we present the main instruments used to obtain the data analysed in this thesis. We used archival data obtained by instruments on space telescopes (such as MIPS on *Spitzer* and PACS and SPIRE on *Herschel*) and on ground-based telescopes (such as T-ReCS on the 8.1 m Gemini-South Telescope, VISIR on the 8.2 m VLT UT3 telescope, the CanariCam instrument on the 10.4 m Gran Telescopio Canarias, and Michelle on the 8.1 m Gemini-North Telescope).

2.1 *Spitzer*

Spitzer, an IR space telescope, is the NASA's Great Observatory for IR astronomy (Werner et al. 2004). It was launched in August 2003. It has two main components: the Cryogenic Telescope Assembly (CTA) where the telescope and instruments are contained and the Spacecraft which controls the telescope, provides power to the instruments, and has data and telecommunications functions. The Spacecraft operates at ambient temperatures whereas the CTA is cooled by helium. The CTA contains the telescope with a primary mirror diameter of 85 cm, cooled to 5.5 K, and three science instruments: the InfraRed Array Camera (IRAC, Fazio et al. 2004); the InfraRed Spectrograph (IRS, Houck et al. 2004); and the Multiband Imaging Photometer for *Spitzer* (MIPS, Rieke et al. 2004). These instruments provide a wavelength coverage of $3 - 180\,\mu$m. For the purpose of this thesis, we will refer only to the MIPS instrument.

Spitzer was planned to last for a minimum of 2.5 years in the cryogenic mission, but it lasted until May 2009 ($\sim$ 5.5 years) when the helium was depleted. The warm mission began in July 2009, at 28 K. Only the shortest wavelength IRAC channels are still operating. It is planned that the warm mission lasts until late in this decade, providing a science mission of more than 15 years. In Fig. 2.1 we show the *Spitzer* telescope diagram.

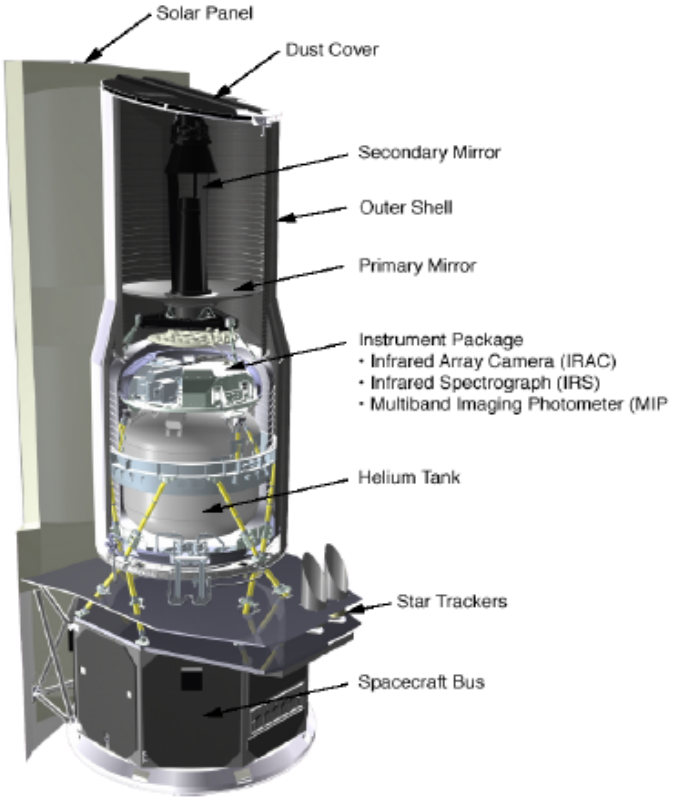

FIGURE 2.1: *Spitzer* telescope diagram. Credit: *Spitzer* Space Telescope Handbook.

2.1.1 *Spitzer*/MIPS

MIPS is the long-wavelength imager on board of the *Spitzer* Space Telescope. It observes at three broad spectral bands (24, 70, and 160 μm) and also provides low-resolution spectroscopy between 55 and 95 μm. It has three detectors, one for each imaging band. In Chapter 3 we used MIPS images at 24 μm to select AGN candidates through variability at this wavelength.

The 24 μm detector is an Si:As array with 128×128 pixels and a pixel size of 2.49×2.60 arcsec^2. It has a pointed field of view (FoV) of 5.4×5.4 arcmin^2. The 24 μm detector is read in a non-destructive mode every ~0.5 seconds with a integration time of 3, 4, 10, or 30 seconds, depending of the observing mode. The 24 μm detector is diffraction limited, as well as the other two detectors. The FWHM of the PSF is 6 arcsec and is dominated by the telescope optics, not by the instrument optics. In Fig. 2.2 we show an example of the 24 μm PSF.

The four observing modes of MIPS are: scan map, photometry, SED and total power mode. The scan map mode is used to map large areas on the sky, as done for the majority of the observations of the

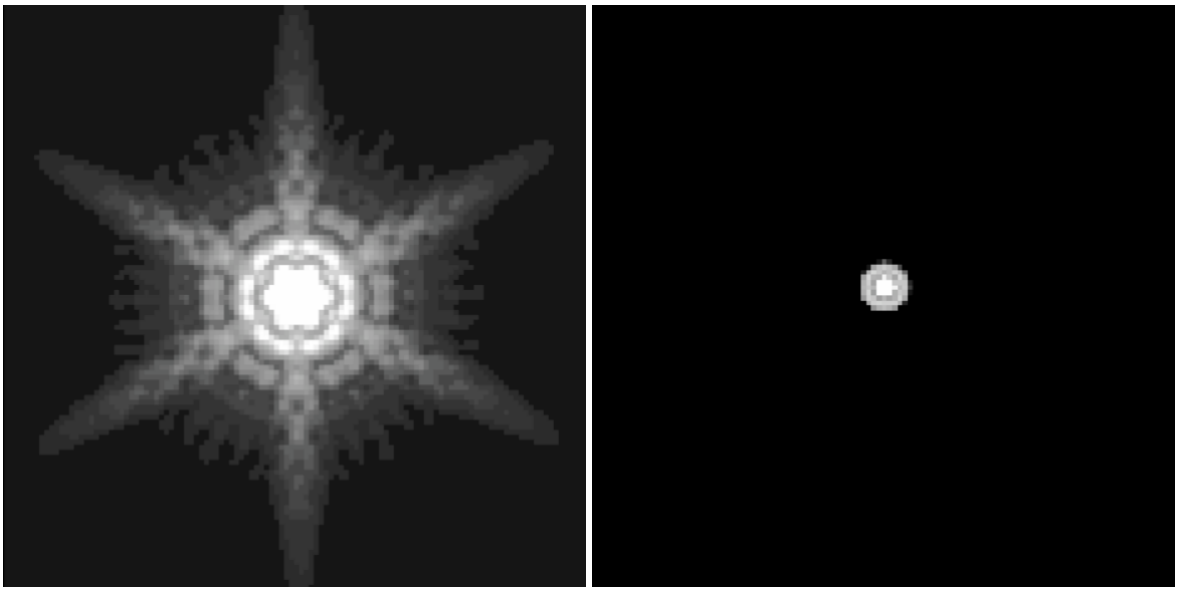

FIGURE 2.2: Left: Example of the MIPS 24 μm PSF with the parameters stretched to show the central peak and the first Airy ring. Right: The same PSF with the parameters stretched to show all the PSF in the FoV of the detector (5.4×5.4 arcmin^2). Credit: MIPS Instrument Handbook.

cosmological fields in Chapter 3. In this mode, the scan mirror freezes the images on the arrays to compensate the constant movement of the telescope. The photometry mode is used to obtain observations of compact sources. The telescope points at the source and integrates, with a small dithering. The SED mode is only applied in the 70 μm detector. It provides long-slit, low-resolution spectra between 55 and 95 μm. The total power mode is used with highly extended sources to obtain absolute brightness measurements.

2.2 *Herschel*

Herschel (Pilbratt et al. 2010) is a FIR and submillimetre ($55-625\,\mu$m) space telescope of the European Space Agency. It was launched in May 2009 and the mission lasted until April 2013, when the liquid helium ran out. It has two main components: the Herschel Extended Payload Module (HEPM), where the telescope, cryostat, and the three instruments are contained and the Service Module which provides power to the instruments, attitude and orbit control, and has data and telecommunications functions. In Fig. 2.3 we show the *Herschel* telescope diagram. The telescope has a primary mirror diameter of 3.5 m (the largest ever sent to space). The cryostat provides a temperature of 1.7 K to the instruments, reaching a temperature of 0.3 K with ^{3}He absorption coolers. The three instruments contained in the HEPM are the Heterodyne Instrument for the Far Infrared (HIFI, de Graauw et al. 2010), the Photodetector Array Camera and Spectometer (PACS, Poglitsch et al. 2010), and the Spectral and Photometric Imaging Receiver (SPIRE, Griffin et al. 2010). In Chapter 4 we use images from PACS

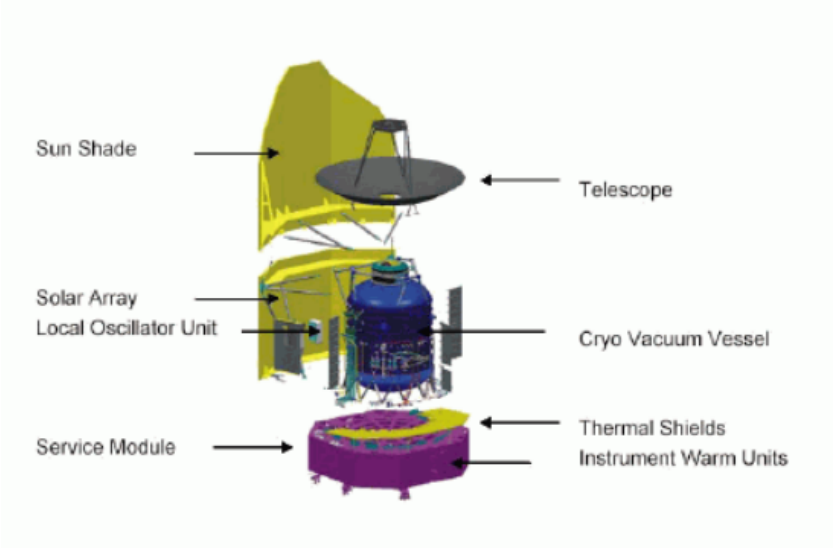

FIGURE 2.3: *Herschel* telescope diagram. Credit: *Herschel* Observers' Manual.

and SPIRE to study the nuclear and integrated FIR emission of Seyfert galaxies. Therefore, we will refer only to PACS and SPIRE.

2.2.1 *Herschel*/PACS

The PACS instrument comprises two sub-instruments, a photometer and a integral-field spectrometer. As we only use images of PACS, we will refer to the photometer. The PACS photometer has three bands referred to as blue, green, and red with central wavelengths of 70, 100, and 160 μm, respectively. The blue and green channels have 32×64 pixel arrays whereas the red channel has a 16×32 pixel array. All of them have a FoV of 1.75×3.5 arcmin^2. The nominal angular resolutions are 5.6, 6.8, and 11.3 arcsec (FWHM). The red band can be combined with the blue or the green band, for simultaneous observations. In Fig. 2.4 we show an example of the PSF for the three bands of PACS.

PACS has three observing modes: point-source photometry mode, scan map mode (for point-sources, small and large fields) and scan map mode with the PACS/SPIRE in parallel mode. The galaxies in Chapter 4 were observed with the point-source photometry mode. This mode uses a chop-nod technique. It uses the PACS chopper to move the source along the Y spacecraft axis with a chopper frequency of 1.25 Hz. The nodding is performed along the Z spacecraft axis with the same amplitude than the chooping, about 50 arcsec.

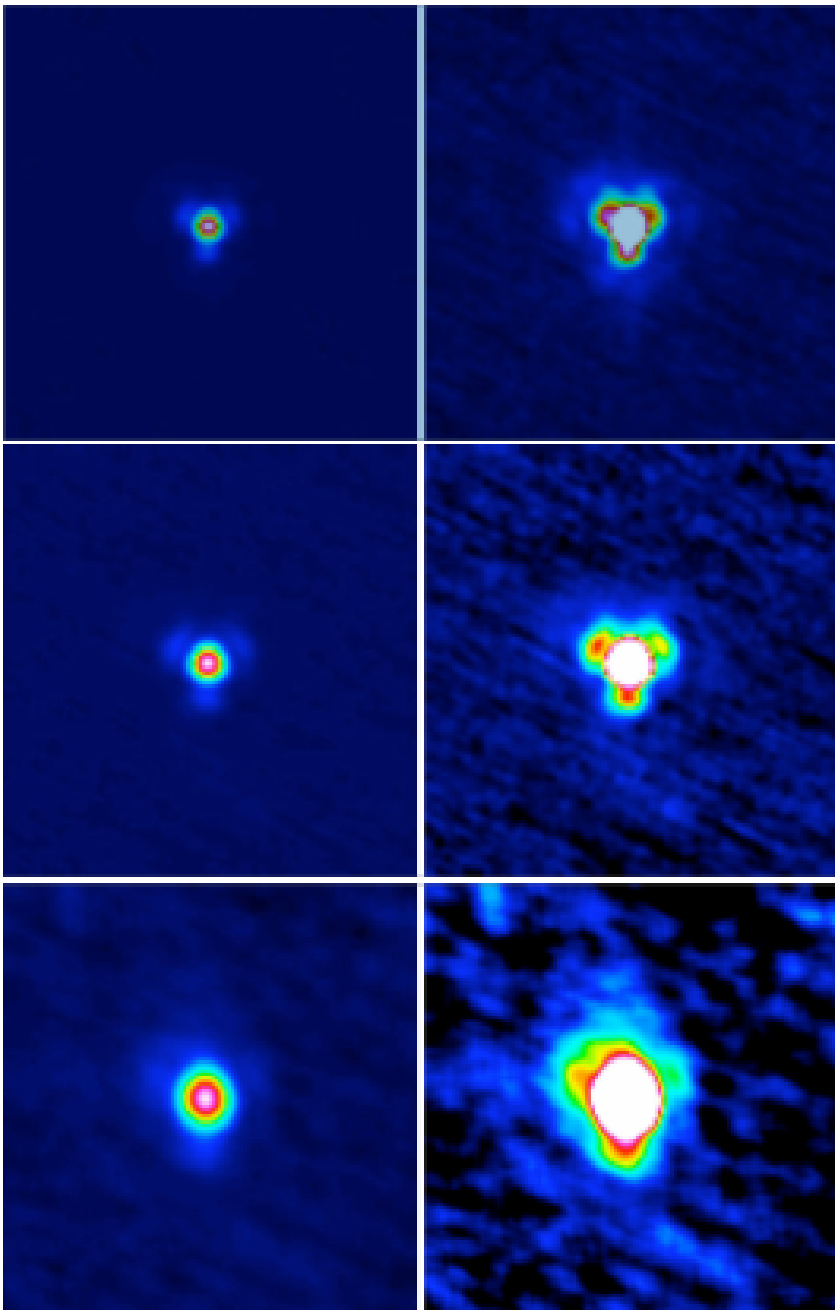

FIGURE 2.4: Example of the PACS PSF for the blue (top), green (middle) and red (bottom) channels. The left panels show the image in a linear scale up to the peak and the right ones show up to 10% of the peak. Credit: PACS Observer's Manual.

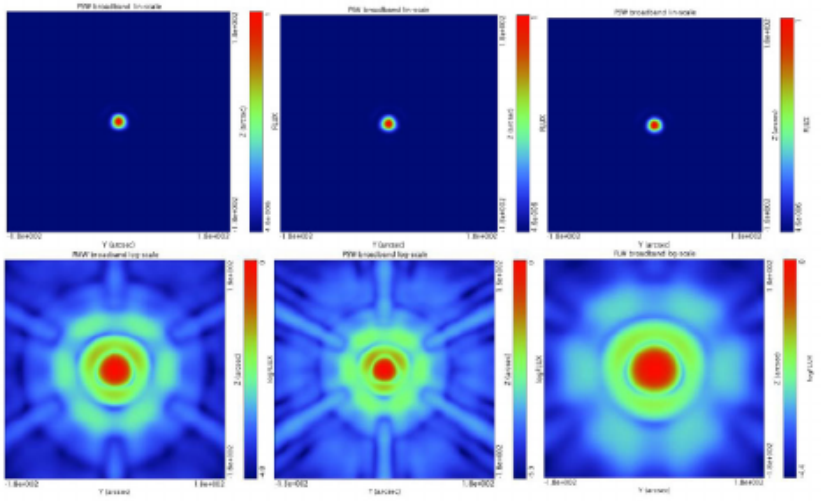

FIGURE 2.5: Theoretical photometer beams for 250 (left), 350 (middle) and 500 μm (right) of the SPIRE photometer. The top row shows a linear scaling and the bottom row a logarithmic scaling. Credit: SPIRE Handbook.

2.2.2 *Herschel*/SPIRE

The SPIRE instrument consists of a three-band imaging photometer and a imaging Fourier Transform Spectrometer. As we only use images from SPIRE, we will refer only to the photometer. The SPIRE photometer has three bands centred at 250 (PSW), 350 (PMW), and 500 μm (PLW), with beam sizes of 17.6, 23.9, and 35.32 arcsec (FWHM), respectively. The three arrays are composed of 139, 88 and 43 bolometers, respectively. All of them have a FoV of 4×8 arcmin^2. The three bands are observed simultaneously. In Fig. 2.5 we show the theoretical beams for SPIRE photometer.

SPIRE photometer has three observing modes: large area maps, small area maps, and point source photometry. The last was never used for science observations. The large area maps is used to cover large areas of the sky (> 5 arcmin diameter) and the map is made by scanning the telescope. The small area maps is used to sources or areas of less than 5 arcmin diameter. The telescope makes two short cross-scans to make the map. Of the 33 galaxies of Chapter 4, 23 were observed with the small area maps mode and the other 10 with the large area maps mode.

2.3 Ground MIR instruments

In Chapter 5 we use MIR spectra obtained on ground 8 – 10 m class telescopes. We use observations taken with four different instruments covering the N-band atmospheric window, approximately between 7.5 and 13.5 μm. This N-band atmospheric window can be seen in Fig. 2.6. The instruments used are: the Thermal-Region Camera Spectrograph (T-ReCS; Telesco et al. 1998; De Buizer

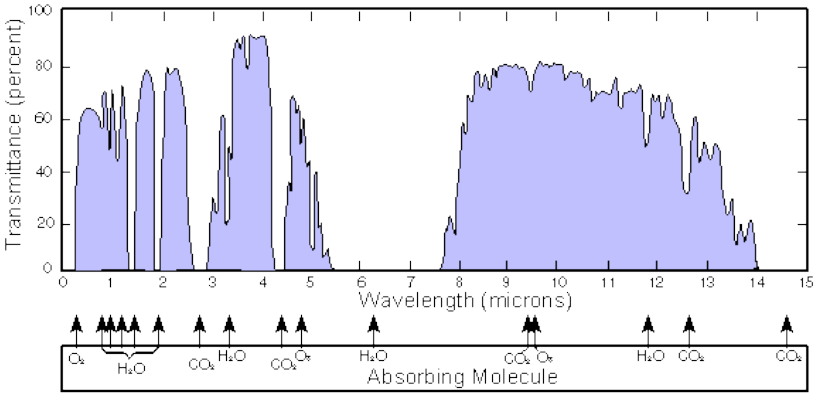

FIGURE 2.6: Atmospheric IR windows. The window between approximately 7.5 and 14 μm is the one used for the observations of Chapter 5 and is usually referred to as N-band.

and Fisher 2005) on the 8.1 m Gemini-South Telescope; the Very Large Telescope (VLT) spectrometer and imager for the mid-infrared (VISIR; Lagage et al. 2004) on the 8.2 m VLT UT3 telescope at ESO/Paranal observatory; the CanariCam instrument (Telesco et al. 2003; Packham et al. 2005) on the 10.4 m Gran Telescopio CANARIAS (GTC) in El Roque de los Muchachos Observatory, and Michelle (Glasse et al. 1997; De Buizer and Fisher 2005) on the 8.1 m Gemini-North Telescope.

2.3.1 T-ReCS

T-ReCS is a MIR imager and long-slit spectrograph. It is capable of spectroscopy with R = $\lambda/\Delta\lambda \sim 100-1000$ in the $8-26\,\mu$m range. The slit length is 21.6 arcsec and the slit width is in the range 0.21 – 1.32 arcsec. T-ReCS can work in different modes. The principal spectroscopy modes are: 10 μm low-resolution spectroscopy, 20 μm low-resolution spectroscopy, and 10 μm high-resolution spectroscopy. The low-resolution modes were commissioned in 2003 and the high-resolution mode in 2004. The background from the sky and the telescope is removed by chopping (moving the secondary mirror of the telescope) and nodding (moving the telescope itself). The observations used in Chapter 5 were obtained with the 10 μm low-resolution spectroscopy mode.

2.3.2 VISIR

VISIR has two sub-instruments, the imager and the spectrograph. It provides imaging and long-slit spectroscopy between $5-24\,\mu$m. It performs differential measurements by chopping and nodding to remove the background from the atmosphere and the telescope. The spectrometer has two arms, one for the low and medium spectral resolution, with a prism and low order gratings, and the other arm to the high spectral resolution, with large echelle gratings. The slits have selectable widths of 0.4, 0.75, and 1 arcsec, and a length of 32.3 arcsec except for the high-resolution mode, which has a slit length

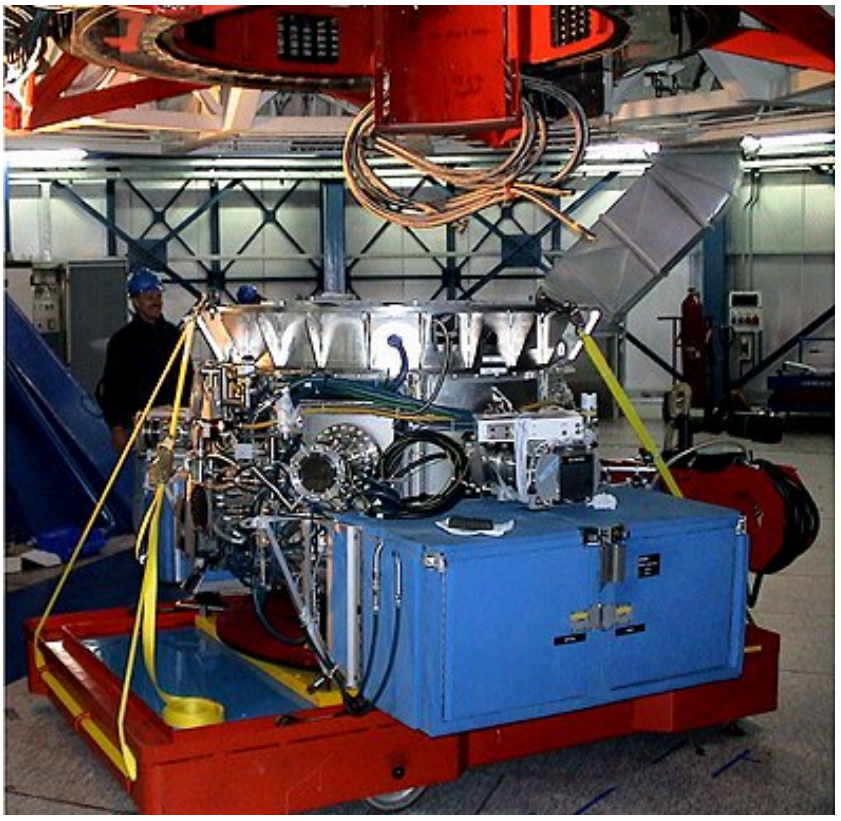

FIGURE 2.7: The VISIR instrument. Credit: ESO

of 4.1 arcsec. The observations used in Chapter 5 were obtained with the low spectral resolution mode (R $\sim$ 300) and a slit width of 0.75 arcsec. Four different spectral settings were used to cover all the N-band. In Fig. 2.7 we show the VISIR instrument.

2.3.3 CanariCam

CanariCam is a MIR (7.1 – 25 μm) imager with low and moderate spectral resolution spectroscopic, coronagraphic, and polarimetric capabilities. It works in two atmospherics windows, one centred at approximately 10 μm and the other near 20 μm. It allows to obtain low and high spectral resolution spectroscopy in each range. In the spectroscopy mode it has a slit length of 19.2 arcsec and different widths in the range 0.17 – 1.04 arcsec. The values of R are $\sim$ 175 in the 8 – 14 μm range and $\sim$ 121 in the 16 – 26 μm range for the low spectral resolution mode, that was the one used for the galaxies of Chapter 5. The technique used to subtract the background is the combination of chopping and nodding. In Fig. 2.8 we show the CanariCam instrument.

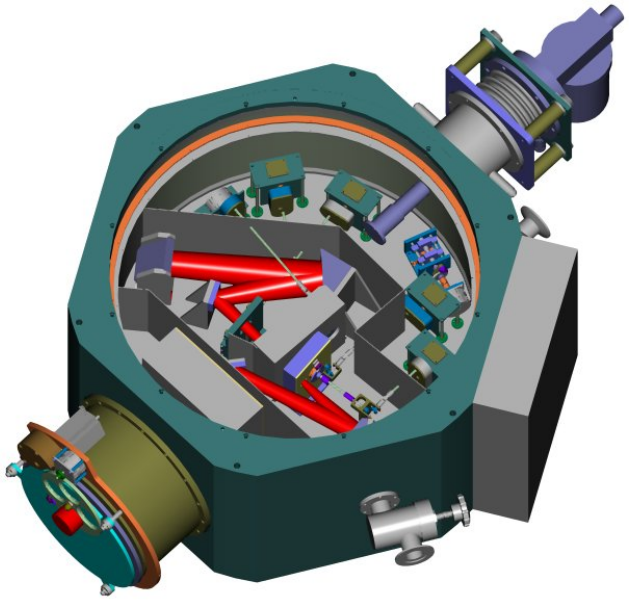

FIGURE 2.8: The CanariCam instrument. Credit: CanariCam Science Web page.

2.3.4 Michelle

Michelle is a MIR imager and log-slit spectrometer. It is capable of spectroscopy with R$\sim$ 100 – 30000 in the 7 – 25 μm range. It can observe at low, medium and high resolution. The slit length is 43.2 arcsec and the slit width is in the range 0.37 – 1.30 arcsec. The narrowest slit is used for point sources and the 0.55 arcsec width slit is used in the 20 μm region. The cancellation of the sky and the telescope background is done by chopping and nodding. The observations of NGC 4151, used in Chapter 5, were obtained using the low resolution and a slit width of 0.37 arcsec, giving R $\sim$ 200.

Chapter 3

AGN candidates selected by 24 μm variability

3.1 Motivation

In the last decade a number of studies have identified AGN in the Great Observatory Origins Deep Survey (GOODS; Giavalisco et al. 2004) fields, which are one of the most commonly observed cosmological fields. The GOODS fields are two fields of 150 arcmin^2 centered around of the Hubble Deep Field North (HDFN; Williams et al. 1996) and the Chandra Deep Field South (CDFS; Giacconi et al. 2001). The observations in the GOODS fields are amongst the deepest at all wavelengths, from X-rays to radio. In particular, these fields have observations from *Spitzer*, *Hubble Space Telescope* (*HST*), *Chandra*, *Herschel*, *XMM-Newton* and many ground-based facilities.

As we discussed in the Introduction there are a number of techniques to identify AGN in cosmological fields although none of them provide a complete census of AGN. In this Chapter we focus on variability. There are a number of variability studies in the GOODS fields, most of them using optical data. The first one was made by Sarajedini et al. (2003) using *V*-band data (λ_c = 550 nm) from *HST* in two epochs separated by five years. They found nuclear variability evidence in 16 of 217 galaxies (7% of the sample) with magnitudes down to 27.5. Cohen et al. (2006) conducted a similar study using the *HST i*-band (λ_c = 775 nm) data from the Hubble Ultra Deep Field (HUDF; Beckwith et al. 2006). They determined that 1% of the sources (45 sources) presented significant variability. Klesman and Sarajedini (2007) conducted a study of five epoch *V*-band data in the GOODS South field. They selected a sample of 22 MIR power-law sources (using the criteria of Alonso-Herrero et al. 2006) and 102 X-ray sources and found that 26% of the sample were variable in the optical. Trevese et al. (2008) used ground-based data, also in the *V*-band and obtained 132 variable AGN candidates (2.6% of the sample). Villforth et al. (2010) selected all the objects in the *z*-band (λ_c = 850 nm) catalogue in the GOODS fields in five epochs. They found 139 variable AGN candidates (~1.3% of the sample) in the

North and South fields. Sarajedini et al. (2011) identified 85 variable galaxies (~2% of the sample) in the North and South fields using five epochs *V*-band images from the *Hubble Space Telescope* Advanced Camera for Surveys.

X-ray variability of low luminosity X-ray sources has also been used to identify additional AGN in the CDFS. Paolillo et al. (2004) studied 346 sources and found that 45% of the sources with more than 100 counts presented X-ray variability. Young et al. (2012) found that 185 of 369 AGN and 20 of 92 galaxies (i.e., low-luminosity AGN with $L_{0.5-8\mathrm{keV}} < 10^{42}\,\mathrm{erg\,s^{-1}}$) presented X-ray variability.

Mooley et al. (2013) studied radio variability in the Extended-CDFS. They found that 1.2% of the point sources presented radio variability associated with the central regions of AGN or star-forming galaxies.

The aim of this Chapter is to identify AGN through MIR variability in the GOODS cosmological fields using 24 μm observations taken with the instrument MIPS on board the *Spitzer* Space Telescope (see Chapter 2). The NIR and MIR nuclear emission of AGN, once the stellar component is subtracted, is believed to be due to hot and warm dust (200 − 2000 K) in the dusty torus of the AGN, according to the Unified Model (Antonucci 1993). In this context, variability in the accretion disk emission would cause delayed variability in the NIR and MIR as the hot and warm dust, respectively, in the torus react to this change (see Hönig and Kishimoto 2011 and references therein).

Our choice of using MIR variability allows a novel way to select low luminosity and possibly obscured AGN that might be otherwise missed by other techniques. Apart from this work, there is only other IR variability study in the Boötes cosmological field using Infrared Array Camera (IRAC) data (Kozłowski et al. 2010). They used the most sensitive IRAC bands at 3.6 and 4.5 μm and found that 1.1% of the sources satisfied their variability criteria.

The Chapter is organized as follows: in Section 3.2 we present the MIR data used to detect variable sources. In Section 3.3 we explain the procedures followed to get photometry of the data. In Section 3.4 we present the statistical method used to select the variable candidates. In Section 3.5 we present the general properties of these candidates, as well as their IRAC properties. In Section 3.6 we present the candidates in the Extended Chandra Deep Field South (E-CDFS), their properties, and a cross-correlation with other AGN catalogues in the same field. The discussion and conclusions are given in Section 3.7. Throughout this Chapter we use a cosmology with $\mathrm{H_0} = 70\,\mathrm{km\,s^{-1}\,Mpc^{-1}}$, $\Omega_\mathrm{m} = 0.3$ and $\Omega_\Lambda = 0.7$.

TABLE 3.1: MIPS 24 μm observing programmes in GOODS cosmological fields.

Epoch	PI	Programme ID	Programme name	Initial date	Final date	AORs[1]	BCDs[2]	t_{exp}^{3} (s)	Area (arcmin^2)
			GOODS-South						
1	Rieke, G.	81	The Deep Infrared Sky	29-01-2004	01-02-2004	12	7660	10	2653
2	Dickinson, M.	194	Great Observatories Origins	19-08-2004	23-08-2004	24	14974	30	255
3	Rieke, G.	81	The Deep Infrared Sky	26-08-2005	28-08-2005	12	6660	10	1706
4	Frayer, D. T.	20147	Ultra-Deep MIPS-70 Imaging of GOODS CDF-S	24-02-2006	26-02-2006	12	19968	10	226
5	Dickinson, M.	30948	A deep-Wide Far-Infrared Survey of Cosmological Star Formation and AGN Activity	01-09-2006	05-09-2006	24	39633	10	756
6	Dickinson, M.	30948	A deep-Wide Far-Infrared Survey of Cosmological Star Formation and AGN Activity	22-01-2007	23-01-2007	8	6216	10	2293
7	Dickinson, M.	30948	A deep-Wide Far-Infrared Survey of Cosmological Star Formation and AGN Activity	01-03-2007	07-03-2007	32	44274	10	2265
			GOODS-North						
1	Dickinson, M.	169	Great Observatories Origins Deep Survey (GOODS)	27-05-2004	01-06-2004	24	15173	30	249
2	Rieke, G.	81	The Deep Infrared Sky	01-06-2004	03-06-2004	12	2174	10	2657
3	Frayer, D. T.	3325	Confusion-Limited 70 μm Imaging of the GOODS Hubble Deep Field North	28-11-2004	03-04-2005	12	8234	10	491
4	Dickinson, M.	30948	A Deep-Wide Far-Infrared Survey of Cosmological Star Formation and AGN Activity	04-12-2006	06-12-2006	12	9984	10	285

[1] AOR: Astronomical Observation Request.
[2] BCD: Basic Calibrated Data.
[3] t_{exp}: Exposure time per BCD.

3.2 The data

We compiled all the data taken around the GOODS cosmological fields with the MIPS instrument at 24 μm by querying the *Spitzer* Heritage Archive[1]. The GOODS-South field was observed by *Spitzer* during several campaigns from January 2004 to March 2007 and is located around RA = $3^h32^m36^s$ (J2000) and DEC = $-27°48'39''$ (J2000). The GOODS-North field was observed by *Spitzer* during four campaigns from May 2004 to December 2006 and is located around RA = $12^h36^m49^s$ (J2000) and DEC = $62°12'58''$ (J2000). These data correspond to different observing proposals from different PI, including the Guaranteed Time Observations programme (GTO, PI: G. Rieke) and the GOODS programme (PI: M. Dickinson). We refer the reader to Table 3.1 for a detailed description of all the MIPS 24 μm observing programmes in the GOODS cosmological fields. We obtained 151 AORs (Astronomical Observation Request) for the GOODS-South field but only downloaded 127 because the others were from the SWIRE (*Spitzer* Wide-area InfraRed Extragalactic) survey and were not sufficiently deep.

We divided the GOODS-South data sets into 7 different epochs (see Fig. 3.1) and the GOODS-North data sets into 4 different epochs in order to detect variable sources. Epochs 5 and 7 in the GOODS-South field, which have the longest durations, can also be divided into subepochs to detect short term variability in time scales of days and even of hours. For each epoch and subepoch, we built a mosaic

[1] http://sha.ipac.caltech.edu/applicatio ns/Spitzer/SHA

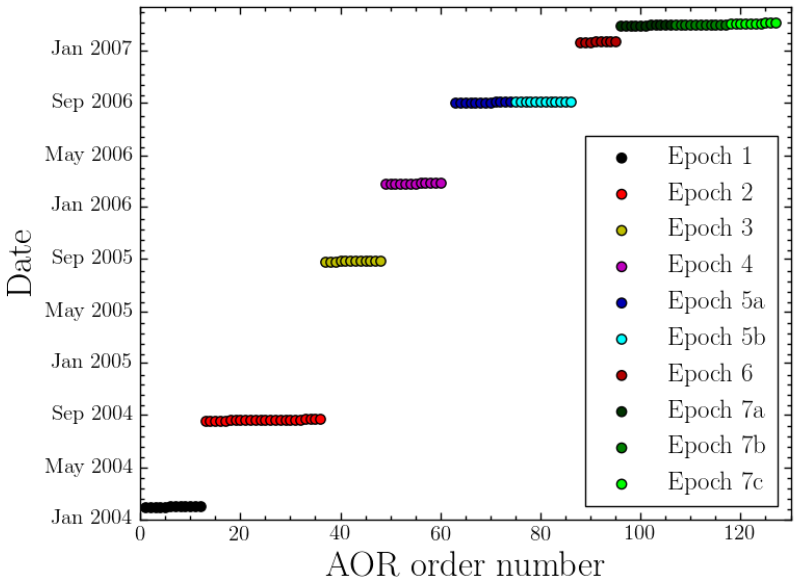

FIGURE 3.1: Summary of the different epochs available in the GOODS-South field with deep *Spitzer*/MIPS 24 μm observations. The epochs with the longest durations can also be divided in subepochs to study short-term variability (time scales of days). The number of AORs per epoch and the exposure time per BCD are given in Table 3.1.

with the AORs using the software MOPEX[2] provided by the *Spitzer* Science Center (SSC). In Table 3.1 we list the main information about the epochs. Each epoch has both a different field of view (FoV) and a different depth. As can be seen from Table 3.1, Epoch 2 (GOODS-South) and Epoch 1 (GOODS-North) have the longest exposure time per Basic Calibrated Data (BCD), resulting in the deepest MIPS 24 μm exposure in our data sets (see below).

For this study we decided to exclude Epochs 2, 4, and 5 in the GOODS-South field because their FoV is small when compared to the other epochs (see Table 3.1). Fig. 3.2 shows the FoV of Epochs 1, 3, 6, and 7 and how they overlap in the GOODS-South field. The common area for the four epochs is $\sim$1360 arcmin^2. They probe time scales of months up to three years, and henceforth are used to study the long-term variability covering a period of over three years. We also subdivided Epoch 7 in three epochs, namely Epochs 7a, 7b, and 7c to study the short-term variability. The short-term variability epochs have a common area of $\sim$1960 arcmin^2 and probe time scales of days, covering a period of 7 days. Fig. 3.3 shows the overlap of the 4 epochs of the GOODS-North field. As can be seen from this figure, the overlap between regions is smaller than for the GOODS-South field (common area of less than 100 arcmin^2).

[2]http://ssc.spitzer.caltech.edu

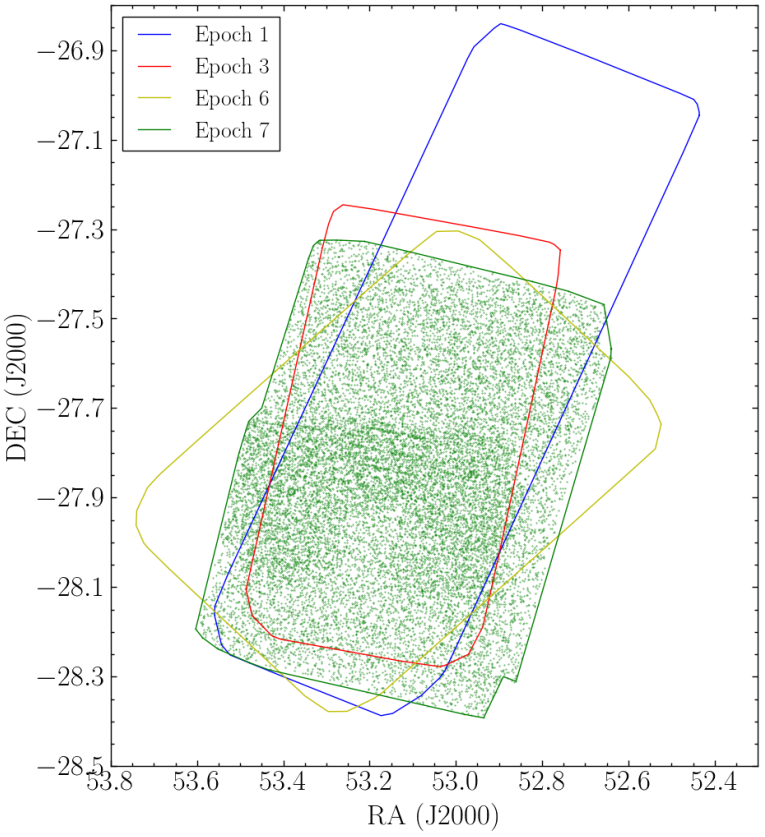

FIGURE 3.2: FoV of Epochs 1, 3, 6, and 7, and their overlap region in the GOODS-South field. These four epochs are used to study the long-term variability. Epoch 7 is subdivided in three epochs to study the short-term variability. The filled dots indicate the MIPS 24 μm sources detected in epoch 7. This epoch is deeper in the central region.

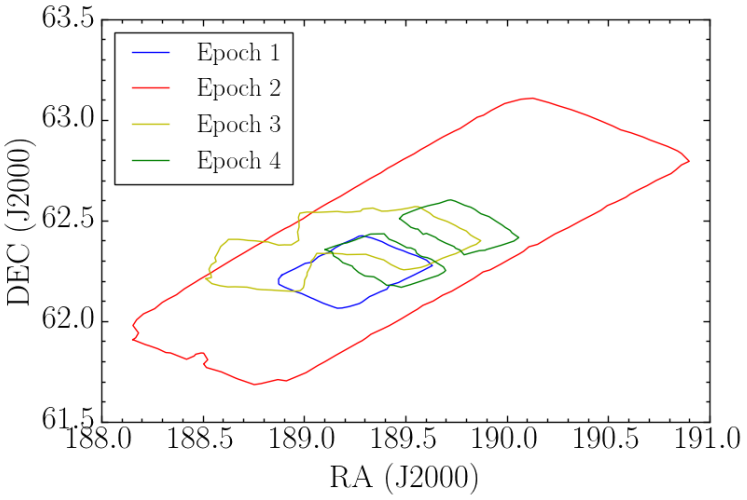

FIGURE 3.3: FoV of Epochs 1, 2, 3, and 4 in the GOODS-North field, and their overlap region.

TABLE 3.2: MIPS 24 μm source counts for the different epochs.

Epoch	$N_{\rm detections}$	$N_{\rm detections}$ F>5σ	$N_{\rm detections}$ F>5σ without neighbours	Area (arcmin^2)	Density (objects/arcmin^2)
Long-term variability (5σ = 80 μJy)					
1	19742	11467	8017	2653	3.02
3	11843	7116	5041	1706	2.95
6	15707	9697	6870	2293	3.00
7	18406	9320	6605	2265	2.92
Short-term variability (5σ = 100 μJy)					
7a	14453	7607	5715	2027	2.82
7b	15629	7348	5551	2107	2.63
7c	14659	7673	5789	2046	2.83

3.3 MIPS 24 μm photometry

3.3.1 GOODS-South field

To study the temporal variability of MIPS 24 μm sources detected in the common regions of the GOODS-South field we built a source catalogue for each epoch and subepoch. We used SExtractor (Source-Extractor, Bertin and Arnouts 1996) to detect sources and the Image Reduction and Analysis Facility (IRAF)[3] to perform the photometry following the procedure explained in Pérez-González et al. (2005, 2008). Sources were detected in five passes to recover the faintest ones, possibly hidden (i.e., more difficult to detect) by brighter sources. All the measurements were made by PSF fitting. To obtain the photometry, we used a circular aperture of radius ∼12 arcsec and then applied an aperture correction of 17% as in Pérez-González et al. (2005) to obtain the total flux. We calculated the uncertainties in the flux taking into account the correlation of the pixel-to-pixel noise introduced by the reduction method and mosaic construction, as described in appendix A.3 of Pérez-González et al. (2008). We obtained a 24 μm source catalogue for each epoch. In our analysis we restricted to sources above the 5σ detection limit in the shallowest data in the mosaics. This corresponds to MIPS 24 μm fluxes of 80 μJy and 100 μJy for the long-term and the short-term epochs, respectively. We also discarded sources with neighbours at distances of less than 10 arcsec to minimize crowding effects in the photometry that could affect the flux measurements and produce false variability positives. In Table 3.2 we list for each epoch the total number of detections, the number of $> 5\sigma$ detections, the number of $> 5\sigma$ detections without neighbours, the area covered, and the density of objects. The positional accuracy of our catalogues is better than 0.7 arcsec.

To identify the common sources in all the epochs we cross-matched the catalogues using a 2 arcsec radius, imposing additionally that the 2 arcsec criterion was fulfilled in each pair of epochs. Due to this criterion, we missed 316 sources cross-matching Epochs 1, 3, 6, and 7 and 282 sources cross-matching

[3]IRAF is distributed by the National Optical Astronomy Observatory, which is operated by the Association of Universities for Research in Astronomy (AURA), Ibc., under cooperative agreement with the National Science Foundation.

Epochs 7a, 7b, and 7c. For the long-term variability (Epochs 1, 3, 6, and 7) there are 2277 sources (1.67 objects × arcmin^{-2}) in common with 24 μm flux >80 μJy (5σ detection) without neighbours within 10 arcsec and satisfying the 2 arcsec criterion. For the short-term variability (Epochs 7a, 7b, and 7c) there are 2452 sources (1.25 objects × arcmin^{-2}) in common with 24 μm flux >100 μJy (5σ detection) without neighbours within 10 arcsec and satisfying the 2 arcsec criterion. Our final catalogues contain 2277 MIPS 24 μm sources detected in Epochs 1, 3, 6, and 7 and 2452 MIPS 24 μm sources in Epochs 7a, 7b, and 7c, covering an area of 1360 and 1960 arcmin^2, respectively.

3.3.2 GOODS-North field

As for the GOODS-South field, we built a source catalogue for each epoch. We restricted the analysis to sources above the 5σ detection limit for each catalogue and discarded sources with neighbours at distances of less than 10 arcsec to minimize crowding effects in the photometry. Then we cross-matched the catalogues using a 2 arcsec radius, imposing additionally that the 2 arcsec criterion was fulfilled in each pair of epochs, as for the catalogues of the GOODS-South field. Using these criteria, there are only 118 sources detected in Epochs 1, 2, 3, and 4. As the overlap is so small, the number of sources detected in the four epochs is not sufficiently large to conduct a statistically study of variability. In the rest of the Chapter we focus only in the GOODS-South field, as it is the only where we can perform a statistically study of variability.

3.4 Selection of MIPS 24 μm variable sources

In this section we describe the method used to select the 24 μm variable sources. To do so we used a χ^2-statistics method to account for the variations of intrinsic flux uncertainties of each epoch (related to differences in depth). This is the case for our study as different epochs have different depths and within a given mosaic there are some variations in depth. The latter effect is most prominent in epoch 7, which is deeper in the centre.

This method associates each flux with its error. The χ^2-statistics is defined as follows:

$$\chi^2 = \sum_{i=1}^{n} \frac{(F_i - \bar{F})^2}{\sigma_i^2} \tag{3.1}$$

where n is the number of epochs, F_i is the flux in a given epoch, σ_i is the associated error in the i^{th} epoch, and $\bar{F}$ is the mean flux.

As errors are essential in this method, we checked them for each epoch. Errors in the parent photometric catalogue could be affected by correlation of the noise due to the reduction method. We compared our estimated errors with the uncertainties resulting from the scatter of points with the fluxes estimated

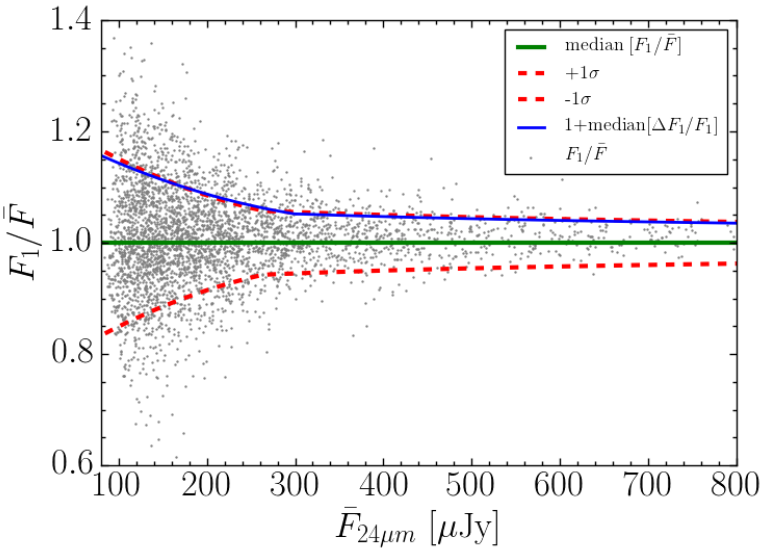

FIGURE 3.4: Scatter of the fluxes of the sources in epoch 1 (grey points). The black line represents the fit of the median in each bin and the red lines represent the fit of the $\pm 1\sigma$ (26^{th} and 84^{th} percentiles). The fit of the median of the photometric errors for each bin is plotted with the blue line.

in images from different epochs. As fluxes in different epochs are measured independently, the scatter must account for the real uncertainties of the measured fluxes. To do this we calculated the ratio $F_{\rm epoch}/\bar{F}$ and $\Delta F_{\rm epoch}/F_{\rm epoch}$ for every source in each epoch, where $F_{\rm epoch}$ is the flux in each epoch, $\bar{F}$ is the mean flux for the source from measurements in all epochs, and $\Delta F_{\rm epoch}$ is the error of the flux in each epoch. We separated the values in bins according to their mean flux value, so each bin contained 200 sources. For each bin we calculated the median of the $F_i/\bar{F}$ values and $+1\sigma$ and -1σ (26^{th} and 84^{th} percentiles) so that between the median and $\sigma+$ there were the 34% of the data in the bin, and the same between the median and $\sigma-$. This is a measure of the scatter of the fluxes and should be consistent with the photometric errors. We also calculated the median of the $\Delta F_{\rm epoch}/F_{\rm epoch}$ for the sources of each bin.

Fig. 3.4 plots the scatter in fluxes as a function of the 24 μm median flux for Epoch 1, as an example. As can be seen from the figure, the median of the errors (blue line) is consistent with the dispersion of the fluxes (red line). This confirms the validity of the estimated photometric errors used to calculate the χ^2 value. For all the epochs and subepochs these figures are similar and the photometric errors are consistent with the dispersion of the fluxes.

We calculated the χ^2 value for each source without neighbours. We selected as variable candidates those sources above the 99^{th} percentile of the χ^2 distribution expected from photometric errors alone. That is, only 1% of non-variable sources satisfy the selection criteria. This value corresponds to $\chi^2 \geq 11.34$ for the 4 epochs sample (3 degrees of freedom) and $\chi^2 \geq 9.21$ for the 3 epochs one (2 degrees of freedom). In Fig. 3.5 we show the observed χ^2 distribution (filled histograms), the theoretical distribution (black line), and the threshold (red dashed line) for the four epochs (left panel) and three

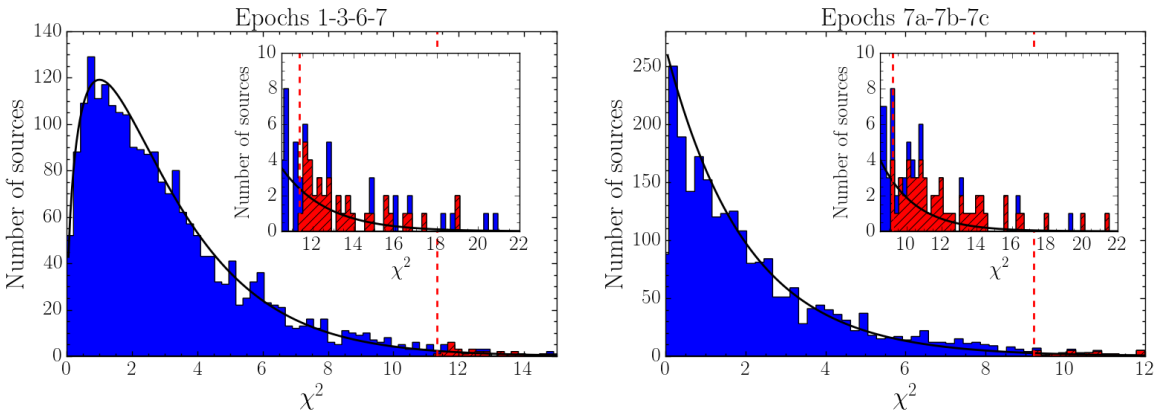

FIGURE 3.5: Observed χ^2 distributions (filled histograms) for all sources without neighbours within 10 arcsec. The left panel is the distribution for the four epochs used for the long-term variability, whereas the right panel is for the three epochs used for the short-term variability. The black line is the theoretical χ^2 distribution for 3 degrees of freedom and 2 degrees of freedom, respectively. The dashed red line marks the 99^{th} percentile for χ^2 due to random photometric errors alone. In the insets we zoom on the high χ^2 region. The red histograms show the χ^2 distribution for the final candidates after discarding problematic sources visually.

epochs (right panel). As can be seen from these figures, the calculated values of χ^2 follow well the expected theoretical distribution for Gaussian photometric errors, indicating that our estimates of the flux uncertainties are accurate.

We performed a Kolmogorov-Smirnov test (hereafter KS-test) in order to determine whether our observed distributions of χ^2 values differ significantly from the theoretical distribution based on the assumption of Gaussian photometric errors. We did the test for the data used to study both the long-term and short-term variability at 24 μm.

Fig. 3.6 shows the cumulative distribution function, CDF, for the long-term data. As can be seen from the figure (and confirmed by a KS-test), the theoretical χ^2 distribution for 3 degrees of freedom (dashed line) is incompatible with the CDF of the data (blue line). This is because the tail of objects with high χ^2 is more populated than expected from the photometric errors alone. This is shown with the magenta symbols which are the ratio between the theoretical distribution of χ^2 and the number of sources in the sample, in intervals of $\Delta\chi^2 = 1$. This ratio presents a small deficit of sources in the range $\chi^2 = 1-2$ and an increasing excess at higher χ^2 values. We truncated and rescaled the CDF at $\chi^2 = 9$ (red line). The rescaled CDF follows well the theoretical distribution for $\chi^2 < 9$. There is a small depression around $\chi^2 = 5$, but it is not significant. The KS-test found no significant differences between the theoretical and the observed distributions below $\chi^2 < 9$. Cutting the CDF in $\chi^2 = 10$ the differences start to be significant. This indicates there is an excess of $\chi^2 > 9$ sources, which is evidence for variability.

Fig. 3.7 shows the CDF for the short-term data. The theoretical distribution corresponds to a χ^2 distribution with 2 degrees of freedom. The rescaled CDF follows well the theoretical distribution for

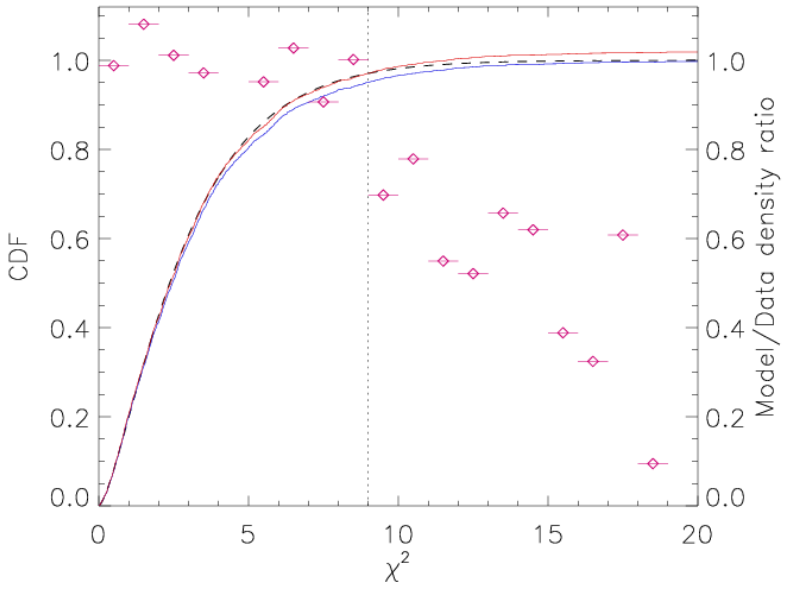

FIGURE 3.6: KS-test for the long-term data. The dashed line is the theoretical χ^2 distribution for 3 degrees of freedom corresponding to long-term variability. The blue line is the CDF of the data and the red line is the scaled and truncated CDF in $\chi^2 = 9$ (vertical dotted line). The magenta symbols (right axis) represent the ratio between the theoretical distribution of χ^2 and the number of sources in the sample, in intervals of $\Delta\chi^2 = 1$.

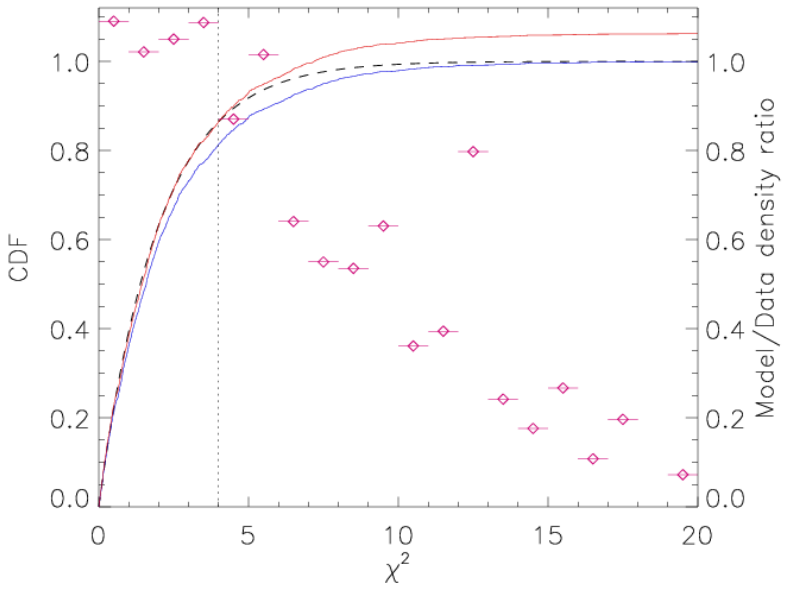

FIGURE 3.7: KS-test for the short-term data. The symbols are the same as Fig. 3.6. In this case the dashed line corresponds to the theoretical χ^2 distribution for 2 degrees of freedom corresponding to short-term variability. The dotted line is the truncation of the CDF in $\chi^2 = 4$

$\chi^2 < 4$. For higher values of χ^2 the difference between the theoretical and the observed distribution is significant, again indicating that our criterion is valid for selecting variable sources.

Every object with a χ^2 value higher than the threshold was visually inspected to remove artefacts. We also discarded objects that fell close to the edge of the mosaic. We also compared the candidates with the supernova (SN) catalogue of Strolger et al. (2004) and found that none of our candidates was in the SN catalogue. The original number of selected variable sources before the removal of artefacts/objects close to the edge of mosaics was 52 and 64 for long-term and short-term variable sources. In the insets of Fig. 3.5 the red histogram shows the distribution for the final candidates. After discarding problematic objects, our final sample contains 39 MIPS 24 μm long-term variable sources (0.03 sources $\times$ arcmin^{-2}) and 55 MIPS 24 μm short-term variable sources (0.03 sources $\times$ arcmin^{-2}). Only two sources are identified as having both, long and short-term variability. The spatial distribution of the MIPS 24 μm variable sources in the GOODS-South field is shown in Fig. 3.8.

The χ^2 cut means that we would expect that 1% of the parent samples of MIPS 24 μm sources would be incorrectly identified as variable (i.e., false positives). The expected numbers of false positives are then 23 and 25 sources for long and short-term variable sources. Taking the original number of selected variable sources before the removal into account we expect that the fraction of false positives in our final sample of variable sources would be ~44% for long-term and ~39% for short-term. We detect many more variable source candidates than expected by random errors, so our selection is statistically meaningful.

The selected MIPS 24 μm long-term and short-term variable sources represent 1.7% and 2.2% of the original parent samples, respectively. After removing the expected number of false positives, the estimated percentages are 1.0% and 1.4%. These fractions of variable sources at 24 μm are similar to those found in the same cosmological field at other wavelengths, mostly optical and NIR (e.g. Cohen et al. 2006; Villforth et al. 2010; Sarajedini et al. 2011; Kozłowski et al. 2010). The higher fraction of short-term variable sources is due to the presence of a deeper region in Subepochs 7a, 7b, and 7c (shown as the area enclosed by the solid line in Fig. 3.8). This means that the photometric errors of sources in this region are smaller and then if variable, they present higher values of χ^2 than sources in shallower areas.

We note that the presence of intense (obscured) star-formation in the host galaxy would impair the detection of AGN variability at 24 μm, so only sources with the highest variability might be detected. We refer the reader to Sections 3.6.1 and 3.6.3 for further discussion on this issue.

In Figs. 3.9, 3.10, 3.11, and 3.12 we show examples of the MIPS 24 μm images of four variable sources, two long-term and two short-term, in each of the epochs of our study. In Tables 3.3 and 3.4 we list the flux and corresponding error at each epoch, median flux, and χ^2 value, for the long-term and short-term MIPS 24 μm variable sources, respectively.

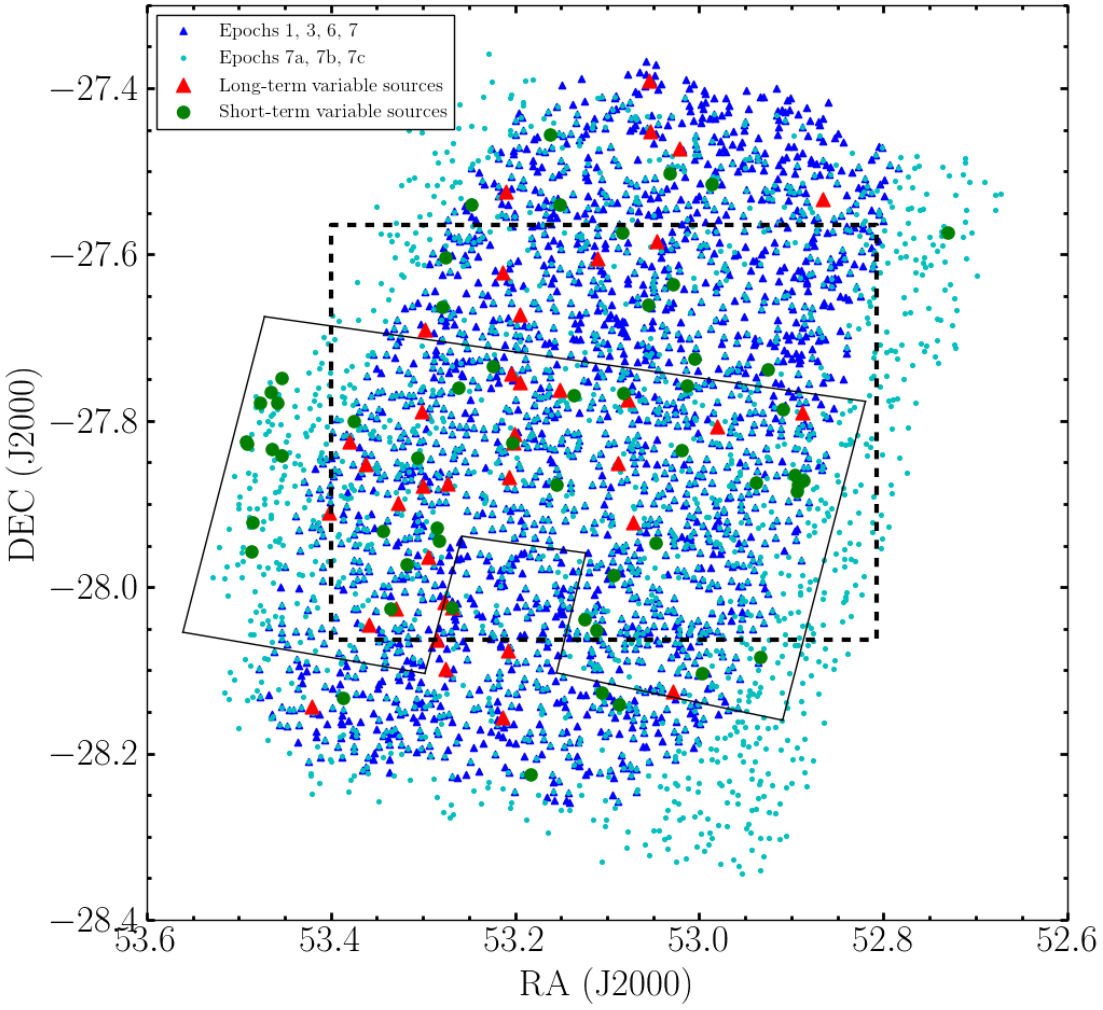

FIGURE 3.8: Location of the MIPS 24 μm long-term variable sources (red large triangles) and the short-term variable sources (green large circles) in GOODS-South. The black dashed line encloses the E-CDFS (see Section 3.5 for more details). The small blue triangles and the small cyan circles are all the MIPS 24 μm common sources to Epochs 1, 3, 6, and 7 and to Epochs 7a, 7b, and 7c, respectively. The solid line encloses the deepest region in Epochs 7a, 7b, and 7c.

3.5 Properties of the MIPS 24 μm variable sources

In this section we analyse the different properties of the 24 μm variable sources, such as their median 24 μm fluxes, variability properties, and their IRAC colours.

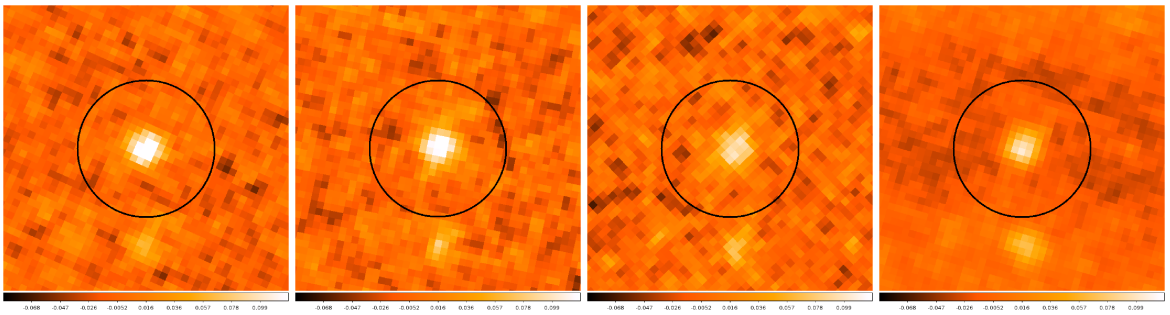

(a) Epoch 1 (b) Epoch 3 (c) Epoch 6 (d) Epoch 7

FIGURE 3.9: MIPS 24 μm images of the four epochs of the long-term variable candidate ID:5109. The FoV of the images is 50 arcsec $\times$ 50 arcsec. The black circle represents the source and has a radius of 12 arcsec.

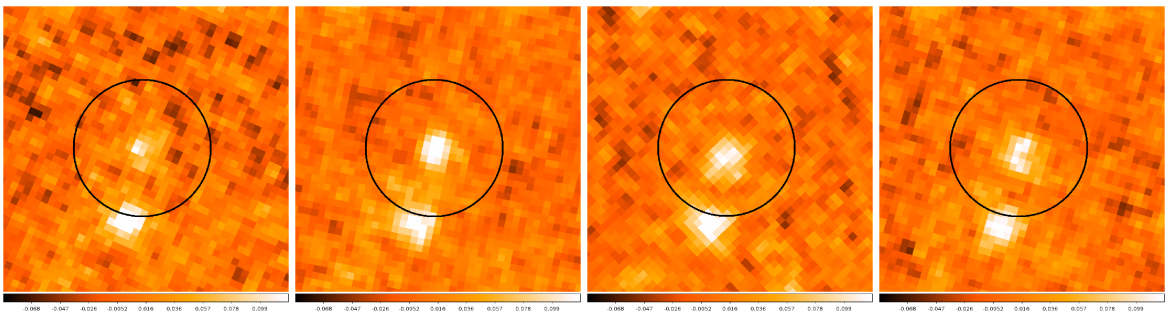

(a) Epoch 1 (b) Epoch 3 (c) Epoch 6 (d) Epoch 7

FIGURE 3.10: Same as Fig. 3.9 for the long-term variable candidate ID:5086

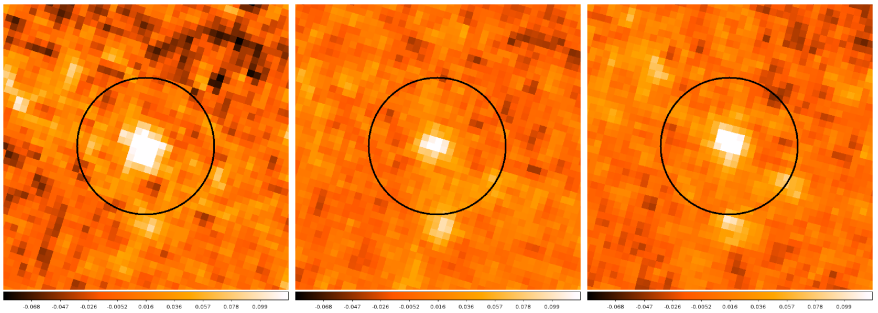

(a) Epoch 7a (b) Epoch 7b (c) Epoch 7c

FIGURE 3.11: Same as Fig. 3.9 for the short-term variable candidate ID:7513

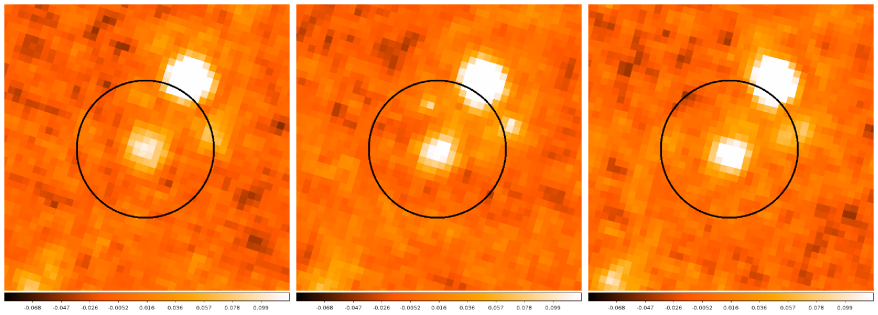

(a) Epoch 7a (b) Epoch 7b (c) Epoch 7c

FIGURE 3.12: Same as Fig. 3.9 for the short-term variable candidate ID:7921

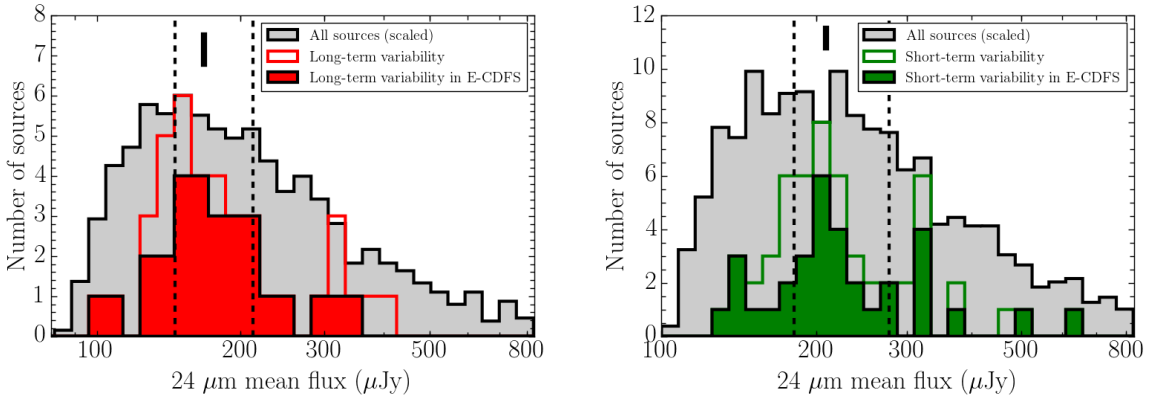

FIGURE 3.13: Distribution of the 24 μm mean flux. The empty histograms are the distribution of the mean flux at 24 μm for long-term variable sources (left panel) and short-term variable sources (right panel) for the full sample, whereas the filled histogram are for sources in the E-CDFS (see Section 3.6). The black lines are the median and the dashed lines the first and third quartiles for the variable sources. The grey histograms shows the scaled distributions of all the sources detected in the four epochs (top) and three epochs (bottom) without neighbours within 10 arcsec.

3.5.1 MIPS 24 μm properties

In Fig. 3.13 we show the distribution of the mean flux (over the 3 or 4 different epochs) at 24 μm for the long-term variable sources (left panel) and short-term variable sources (right panel) compared with the corresponding flux distribution of the parent sample for $> 5\sigma$ detections. In both cases, the 24 μm fluxes of the variable sources are dominated by sources with mean fluxes below 300 μJy. The median 24 μm flux is 168 μJy for the long-term variable sources and 209 μJy for the short-term variable sources (see Table 3.5). This slight difference in the median values of the 24 μm fluxes for long and short-term variability is likely reflecting the different depths (i.e., 5σ detection limits) of the epochs rather than different intrinsic properties of the sources (see Section 3.6).

TABLE 3.3: Catalog of the long-term variable candidates.

ID	RA	DEC	Flux [epoch 1]	Flux [epoch 3]	Flux [epoch 6]	Flux [epoch 7]	$\bar{F}$	χ^2	Var	$R_{\max}$	z^+	R	X-ray?	Radio?
	(J2000)	(J2000)	(μJy)	(μJy)	(μJy)	(μJy)	(μJy)		(%)					
7348	52.8655903	-27.5329591	410±16	410±24	416±20	342±17	395	12.23	18.9	1.22	0.71	-	NO	NO
13441*[1,2]	52.8882698	-27.7897526	144±14	156±20	148±18	99±11	137	12.48	41.4	1.57	0.57	20.98	NO	NO
5071*	52.9801950	-27.8067295	129±13	83±14	104±21	127±7	111	11.39	41.8	1.56	0.75	23.08	NO	NO
11519	53.0214235	-27.4722517	178±16	191±15	128±15	124±21	155	13.61	43.2	1.54	1.07	-	NO	NO
12269	53.0288333	-28.1259252	114±19	174±15	163±19	118±13	142	11.71	42.4	1.53	0.29	-	NO	NO
14622*[2]	53.0467505	-27.5834456	201±14	225±14	177±16	269±18	218	16.75	42.5	1.52	1.43	25.22	NO	NO
9579	53.0534834	-27.4522969	403±17	418±17	341±19	369±21	383	11.63	20.3	1.23	0.19	-	NO	NO
16416	53.0543385	-27.3906117	159±17	151±15	163±19	251±31	180	11.87	55.5	1.67	0.57	-	NO	NO
5359*	53.0719302	-27.9225433	112±14	169±18	139±21	116±7	134	12.39	42.6	1.51	1.27	24.98	NO	NO
5080*[1,2]	53.0779999	-27.7740151	247±17	260±16	196±20	208±10	228	11.73	28.3	1.33	1.729	24.08	NO	NO
11976*	53.0885467	-27.8504550	134±17	161±14	126±19	182±8	151	18.92	36.6	1.44	1.78	23.28	YES	NO
9796*[1,2]	53.1110983	-27.6040756	185±13	172±16	234±16	152±15	186	14.77	43.7	1.53	1.24	24.79	NO	YES
5109*[2]	53.1515045	-27.7620615	224±13	214±19	162±17	143±10	186	30.41	43.6	1.57	0.426	22.16	NO	NO
7742*[1,2]	53.1942822	-27.6723954	333±15	358±25	373±17	277±16	335	19.00	28.8	1.35	0.668	21.84	NO	NO
10015*[1,2]	53.1948840	-27.7538449	172±13	146±16	184±17	133±9	159	11.67	31.6	1.38	0.838	22.96	YES	NO
2226*[1,2]	53.2001248	-27.8155580	146±13	155±17	180±22	191±8	168	12.37	26.4	1.30	0.233	20.78	YES	NO
13601*[2]	53.2022070	-27.8263358	149±19	174±16	144±16	196±8	166	17.41	31.1	1.36	1.117	25.08	YES	YES
14779*[1,2]	53.2047528	-27.7432269	100±13	81±17	94±15	141±10	104	15.46	57.0	1.73	0.216	19.75	YES	NO
2324*[2]	53.2064728	-27.8675984	174±16	135±13	135±19	177±8	155	11.94	27.2	1.31	0.414	21.38	NO	NO
10402	53.2076102	-28.0760407	345±14	335±19	312±15	265±18	314	13.35	25.5	1.30	1.95	-	NO	NO
4679	53.2103280	-27.5243703	340±23	269±17	341±19	274±18	306	13.33	23.4	1.27	0.98	-	NO	NO
5930	53.2134267	-28.1566425	136±14	178±16	95±20	164±16	143	12.72	57.4	1.86	-	-	NO	NO
4878*	53.2139709	-27.6210732	212±14	273±15	166±15	212±16	207	11.88	34.5	1.43	1.88	-	NO	NO
10377*[1]	53.2681253	-28.0246684	198±19	169±16	171±25	241±17	195	11.58	37.4	1.43	0.92	22.83	NO	NO
2380*[1,2]	53.2730602	-27.8755176	179±18	111±15	165±15	140±8	149	12.01	46.0	1.62	0.50	20.99	NO	NO
12354	53.2756206	-28.0988060	149±13	122±17	153±15	81±15	126	16.58	57.6	1.90	1.86	-	NO	NO
8295*	53.2766409	-28.0183704	174±13	190±16	217±15	91±17	168	34.06	75.1	2.39	1.57	24.21	NO	NO
13829*[1,2]	53.2853000	-28.0627180	137±13	161±18	140±16	94±13	133	12.01	50.9	1.72	0.76	22.88	NO	NO
2552*[1,2]	53.2943522	-27.9635147	250±14	314±17	361±16	348±12	330	13.59	20.2	1.23	1.26	21.21	YES	NO
5086*[1,2]	53.2980525	-27.6902849	130±19	215±14	185±18	171±23	175	13.65	48.4	1.65	0.90	22.95	NO	NO
5451*	53.3000223	-27.8779051	283±18	345±16	275±15	298±10	300	11.82	23.1	1.25	0.81	22.52	NO	NO
2253*[1,2]	53.3011532	-27.7885025	220±17	182±15	239±16	184±10	206	12.90	27.4	1.31	1.45	23.98	NO	NO
12132*[1]	53.3266480	-27.8986874	149±15	208±15	231±15	201±10	197	15.46	41.4	1.55	0.63	21.31	NO	NO
5766*[2]	53.3296181	-28.0256251	241±13	201±13	274±16	252±11	242	14.64	30.0	1.36	0.30	21.58	NO	NO
8379*[1]	53.3585985	-28.0450788	203±15	158±13	230±17	192±9	196	12.77	37.0	1.46	1.08	22.63	NO	NO
12099*[1,2]	53.3617713	-27.8518082	100±16	119±21	152±16	153±8	131	12.56	40.1	1.53	0.94	22.31	YES	NO
5403*[1,2]	53.3798560	-27.8245098	145±26	178±20	166±18	129±8	154	13.92	32.0	1.38	0.70	22.14	NO	NO
5582	53.4022377	-27.9101321	133±27	150±24	156±18	106±8	136	15.81	36.4	1.47	1.93	-	NO	NO
6061	53.4205850	-28.1435063	163±15	217±21	101±16	130±17	153	22.74	76.5	2.16	0.81	-	NO	NO

[+] Redshifts with three decimal points are spectroscopic redshifts.
[*] In the E-CDFS.
[1] In COMBO-17 catalogue and only one counterpart in 2.5 arcsec in Rainbow catalogue.
[2] Only one counterpart in 2.5 arcsec in COMBO-17 catalogue.
The references for the spectroscopic redshifts are: ID 5080: Grazian et al. (2006); ID 5109: Mignoli et al. (2005); ID 7742, 10015, 14779, 2324: Le Fèvre et al. (2004); ID 2226: Balestra et al. (2010); ID 13601: Mainieri et al. (2008).

We cross-correlated our parent MIPS 24 μm catalogues with the Xue et al. (2011) deep X-ray catalogue of AGN and galaxies using a search radius of 2.5 arcsec (see Section 3.6.2). There are 211 X-ray sources that are not stars in Xue et al. (2011) catalogue detected in 24 μm satisfying our criteria, that is, they have 24 μm fluxes over our 5σ limit and have no neighbours within 10 arcsec. Of the 211 sources, 149 are classified as AGN in the Xue et al. (2011) catalogue. These X-ray selected AGN in our parent catalogues have a 24 μm median flux of $\sim$240 μJy. This implies that our selected 24 μm variable sources are typically fainter at 24 μm than X-ray selected AGN. Since the redshift distributions are similar (see Section 3.6.1), this may indicate that the 24 μm variable sources, if they were AGN, are less luminous, as predicted by Trevese et al. (1994).

TABLE 3.4: Catalog of the short-term variable candidates.

ID	RA (J2000)	DEC (J2000)	Flux [epoch7a] (μJy)	Flux [epoch7b] (μJy)	Flux [epoch7c] (μJy)	$\bar{F}$ (μJy)	χ^2	Var (%)	$R_{\rm max}$	z$^+$	R	X-ray?	Radio?
13	52.7297992	-27.5739281	298±30	216±33	156±33	223	10.80	63.8	1.92	-	-	NO	NO
2634^{*1,2}	52.8866973	-27.8719379	211±15	229±15	155±17	198	11.81	37.5	1.48	0.65	20.30	NO	NO
6314^{*1,2}	52.8931060	-27.8764410	200±14	194±15	128±21	174	10.12	41.0	1.56	0.74	21.20	NO	NO
937*	52.8942467	-27.8840075	326±14	281±14	346±16	318	10.15	20.5	1.23	1.16	-	NO	NO
2625^{*2}	52.8962139	-27.8649395	119±14	103±18	190±16	137	16.43	63.5	1.85	1.28	23.94	NO	NO
763*	52.9090009	-27.7866579	339±20	291±15	363±21	331	9.37	21.7	1.25	1.05	22.07	NO	NO
2356^{*1,2}	52.9251368	-27.7383352	231±26	162±20	152±24	215	12.52	50.8	1.72	1.02	22.38	NO	NO
6827	52.9338732	-28.0834027	406±17	325±16	380±19	370	13.22	21.8	1.25	0.44	-	YES	NO
4648^{*1,2}	52.9379937	-27.8746505	163±11	104±11	133±17	133	14.29	44.1	1.56	0.734	23.49	NO	YES
1947	52.9862313	-27.5157096	346±31	208±25	200±48	251	13.67	58.1	1.73	0.81	-	NO	NO
8181	52.9972222	-28.1038541	222±15	178±15	143±17	181	12.25	43.4	1.55	-	-	NO	NO
718^{*1,2}	53.0047558	-27.7255025	243±26	149±20	235±31	209	11.87	44.9	1.63	1.001	22.29	NO	NO
7513^{*1,2}	53.0134300	-27.7581000	272±19	165±18	227±18	221	16.47	48.3	1.65	0.534	21.01	NO	NO
917^{*1,2}	53.0192273	-27.8352082	228±12	197±13	181±10	202	9.23	23.2	1.26	0.23	19.93	YES	NO
8613^{*1,2}	53.0286682	-27.6356610	217±37	158±20	262±28	212	10.48	49.2	1.66	0.50	20.92	NO	NO
1943	53.0316927	-27.5017437	389±32	258±22	271±29	306	12.61	42.8	1.51	1.91	-	NO	NO
7921^{*2}	53.0476619	-27.9473127	173±15	212±12	254±16	213	13.81	38.1	1.47	1.11	22.21	NO	NO
2277*	53.0555289	-27.6597959	238±40	230±21	356±32	275	11.85	45.9	1.55	1.49	-	NO	YES
8766*	53.0819932	-27.7672103	369±17	321±18	277±22	322	11.94	28.5	1.33	0.62	-	YES	YES
517^{*1,2}	53.0839618	-27.5734177	179±29	286±21	225±28	230	10.60	46.6	1.60	1.12	21.08	NO	YES
1503	53.0869545	-28.1404091	197±32	142±19	234±26	191	9.59	48.0	1.65	0.69	-	NO	NO
10885*	53.0925557	-27.9857229	360±18	311±15	282±16	318	11.10	24.8	1.28	0.57	-	NO	NO
6978	53.1064166	-28.1262429	389±24	307±19	249±27	315	15.63	44.5	1.56	1.03	-	NO	NO
185^{*1,2}	53.1121892	-28.0514201	341±18	354±22	423±20	373	10.06	21.9	1.24	1.57	24.00	NO	NO
3265*	53.1250338	-28.0383985	234±25	191±16	140±18	188	10.79	50.2	1.68	1.85	23.61	NO	NO
4501^{*1,2}	53.1367677	-27.7688610	610±20	669±19	584±18	621	10.60	13.7	1.15	0.366	20.36	NO	YES
2091	53.1518662	-27.5393472	257±31	145±21	194±30	198	9.93	56.5	1.78	0.28	-	NO	NO
2847^{*1,2}	53.1549571	-27.8767845	234±11	192±11	187±13	204	10.23	22.8	1.25	0.331	20.49	NO	NO
1925	53.1620312	-27.4562601	222±28	243±25	121±29	195	11.14	62.4	2.01	1.00	-	NO	NO
3702	53.1828042	-28.2246423	293±38	142±20	175±29	203	15.70	74.3	2.07	-	-	NO	NO
7761^{*1,2}	53.2024886	-27.8262335	227±14	208±14	151±16	195	14.12	38.9	1.50	1.117	25.08	YES	YES
4477^{*1}	53.2235604	-27.7345674	253±18	274±17	182±19	236	14.08	39.2	1.51	1.58	23.97	NO	NO
540	53.2480035	-27.5404651	139±27	114±20	235±28	162	13.26	74.3	2.06	1.72	-	NO	YES
2614^{*1,2}	53.2610999	-27.7598248	106±13	141±17	169±13	139	11.25	45.7	1.60	1.23	23.34	YES	NO
6876*	53.2681484	-28.0248935	129±23	246±20	276±26	217	21.45	67.6	2.13	0.92	22.83	NO	NO
6017*	53.2758295	-27.6029799	206±28	321±24	253±30	260	10.25	44.3	1.56	1.77	23.94	NO	NO
2409^{*1,2}	53.2795549	-27.6633534	322±27	227±20	288±32	279	9.23	34.1	1.42	0.45	21.35	NO	NO
10903*	53.2826321	-27.9443909	200±16	237±17	163±18	200	9.24	37.2	1.46	0.12	20.91	NO	NO
1209^{*1,2}	53.2846948	-27.9283298	176±13	139±15	113±14	143	11.46	44.3	1.56	0.70	21.66	NO	NO
7869^{*1,2}	53.3057210	-27.8438699	185±10	186±15	138±13	170	9.86	27.8	1.34	0.32	19.51	NO	NO
8106*	53.3173805	-27.9729970	178±13	225±17	148±16	184	11.56	42.3	1.53	0.45	22.63	NO	NO
6918^{*1,2}	53.3352837	-28.0254291	108±17	150±13	190±14	149	14.42	55.0	1.76	1.61	23.41	NO	NO
8050^{*2}	53.3430057	-27.9321166	480±19	539±16	474±15	498	10.33	13.1	1.14	1.66	23.43	NO	NO
123*	53.3747793	-27.8008735	164±10	139±12	191±11	165	10.80	31.8	1.38	1.94	-	NO	NO
3632	53.3868526	-28.1329288	303±28	189±21	249±26	247	11.93	46.5	1.61	0.62	-	NO	NO
10053	53.4529616	-27.8423718	322±13	265±14	290±12	292	9.62	19.7	1.22	-	-	NO	NO
2734	53.4539570	-27.7478151	162±16	187±24	101±19	150	9.70	57.4	1.85	0.48	-	NO	NO
1032	53.4584105	-27.7783558	168±17	191±16	126±14	162	10.35	40.0	1.51	1.05	-	NO	NO
6622	53.4639456	-27.8334061	507±18	464±21	432±17	468	9.30	15.9	1.17	-	-	NO	NO
4767	53.4656628	-27.7659261	134±14	212±17	190±16	179	14.28	44.1	1.59	0.11	-	NO	NO
1039	53.4768023	-27.7778086	168±19	244±17	132±20	181	20.08	61.8	1.85	-	-	NO	NO
6814	53.4846854	-27.9221903	180±18	144±14	217±18	180	10.95	40.6	1.51	-	-	NO	NO
5284	53.4862820	-27.9564971	225±20	144±14	195±15	188	13.10	43.0	1.56	-	-	NO	NO
7936	53.4911453	-27.8278011	363±23	269±26	368±19	333	10.89	29.5	1.37	-	-	NO	NO
12955	53.4921523	-27.8248350	212±14	175±16	281±20	222	17.93	47.8	1.61	-	-	NO	NO

$^+$ Redshifts with three decimal points are spectroscopic redshifts.

* In the E-CDFS.

[1] In COMBO-17 catalogue and only one counterpart in 2.5 arcsec in Rainbow catalogue.

[2] Only one counterpart in 2.5 arcsec in COMBO-17 catalogue.

The references for the spectroscopic redshifts are: ID 4648, 2847: Le Fèvre et al. (2004); ID 718, 7513: Balestra et al. (2010); ID 4501: Mignoli et al. (2005); ID 7761: Mainieri et al. (2008).

3.5.2 Variability Properties

In Figs. 3.14 and 3.15 we show the light curves of the long-term and the short-term variable sources. Each plot shows the name of the source, the χ^2 value and the measure of the variability Var (see below, Equation 3.2).

As a first measure of the variability, we calculated the maximum to minimum flux ratio, $R_{\rm max}$, as: $R_{\rm max} = f_{\rm max}/f_{\rm min}$. The long-term and short-term variable sources show similar values of the average and median $R_{\rm max}$ of approximately $1.5 - 1.6$ (see Table 3.5 and Fig. 3.16).

Another estimate of the variability is the ratio between the maximum and minimum values and the mean flux $\bar{f}$ measured as a %.

$$Var = \frac{f_{\rm max} - f_{\rm min}}{\bar{f}} \times 100 \tag{3.2}$$

As can be seen from Table 3.5, the typical $24\,\mu$m Var values of the long-term and short-term variable sources are $37 - 43\%$, with typical errors of $12 - 13\%$. In Fig. 3.17 we show Var against the mean $24\,\mu$m flux for each candidate (lower panel) with the typical errors (upper panel). The apparent lack of small values of Var at low $24\,\mu$m mean fluxes is because these sources have lower S/N detections and therefore higher errors in their photometry, and for the same variability they do not meet our χ^2 criterion. There is also a lack of large values of Var at high $24\,\mu$m mean fluxes. It is due to a statistical effect because the number of sources at high $24\,\mu$m mean fluxes is small, and the fraction of variable sources with low values of Var is higher than the fraction with large values of Var.

Finally, the reduced value of χ^2, which is defined as χ^2/n with n being the number of epochs, has also been used as a measure of the $10\,\mu$m variability of local quasars by Neugebauer and Matthews (1999). For the long and short-term variable sources we find median χ^2/n values of 3.2 and 3.7, respectively. These are slightly higher than the values measured for local quasars at $10\,\mu$m. We note, however that our variability criterion in both cases is more restrictive than that used for the local quasars ($\chi^2/n > 1.5$).

It is not straightforward to compare our measures of the MIPS $24\,\mu$m variability in GOODS-South with studies done in the optical. The optical studies (e.g., Sarajedini et al. 2011; Villforth et al. 2010) used the variability significance and the variability strength as a measure of the variability. These parameters are defined in a different way than our Var and it is not appropriate to calculate them for our sources because they assume equal errors for all the sources, which is not the case for our epochs as shown in Section 3.2.

We can compare the MIPS $24\,\mu$m $R_{\rm max}$ values with those measured in X-rays. Young et al. (2012) detected X-ray variable sources with maximum-to-minimum flux ratios $R_{\rm max} = 1.5 - 9.3$ with a median value of 4.1 over a period of 10.8 years. These values are noticeably higher than those measured at

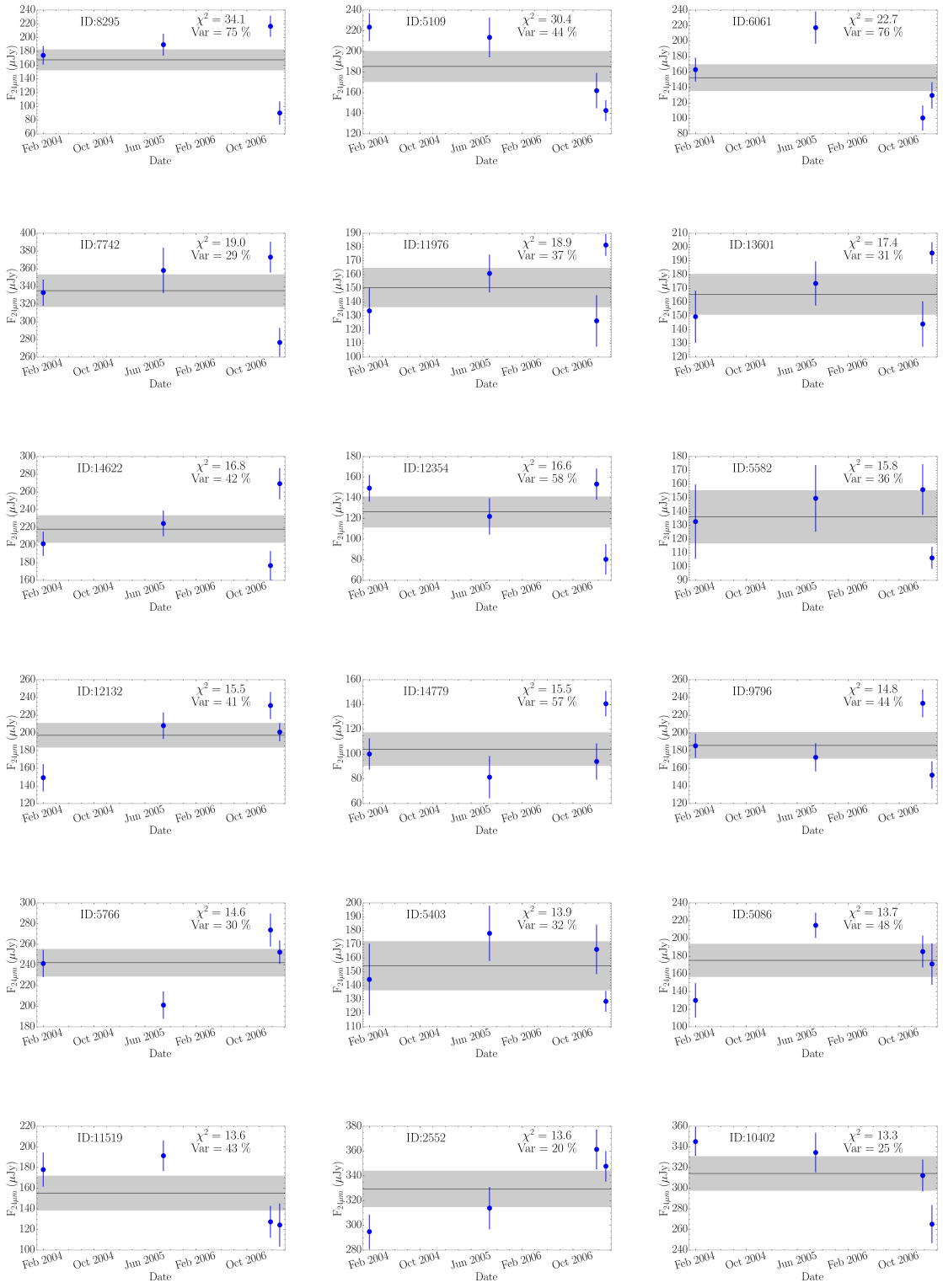

FIGURE 3.14: Light curves of MIPS 24 μm long-term variable sources (four epochs) in GOODS-South. The flux for each epoch is plotted with its corresponding photometric error. The solid line is the 24 μm mean flux of the source and the grey shaded area is the average of the errors of the source. Each plot lists the name of the source, the χ^2 value, and Var.

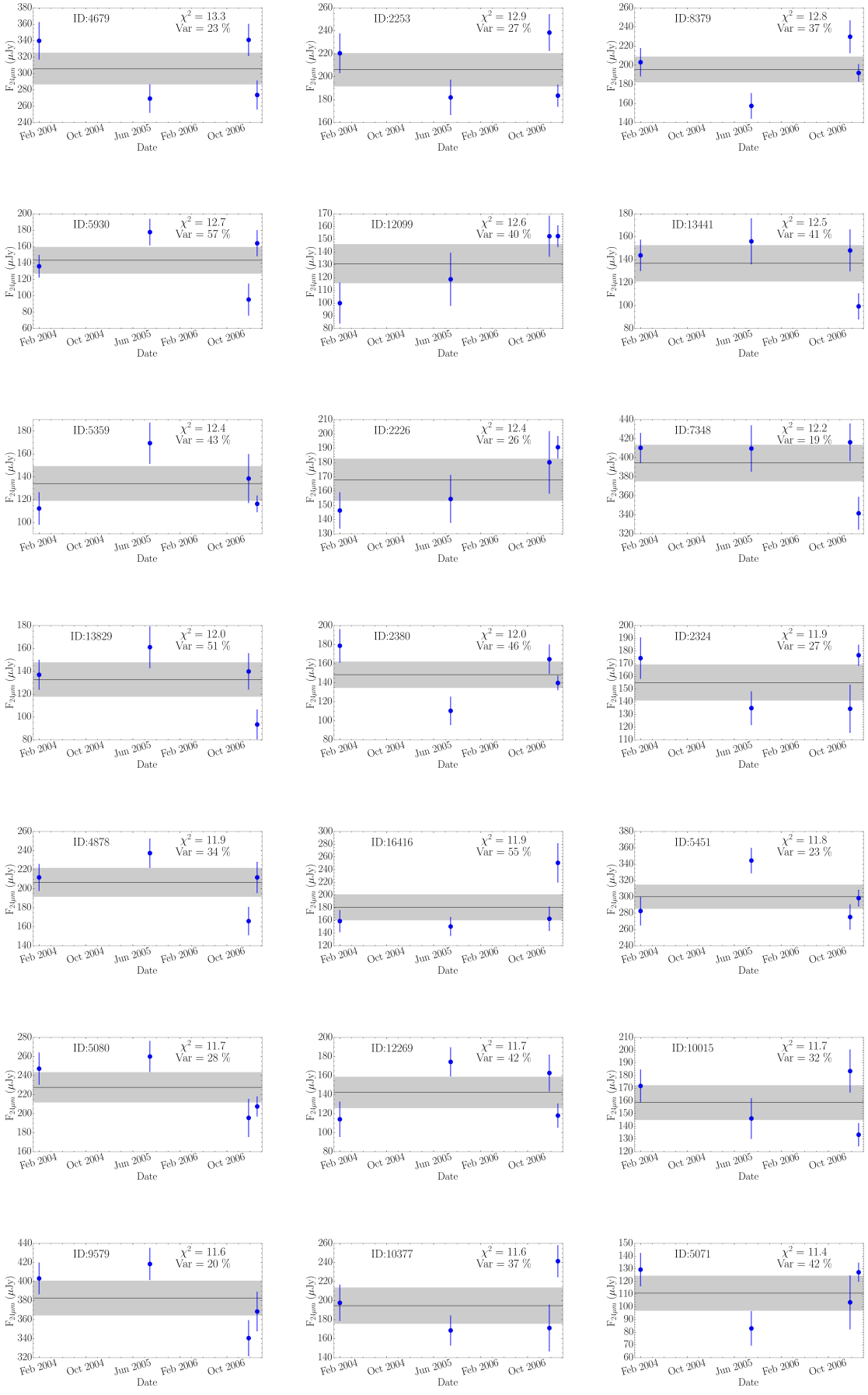
ID:4679 $\chi^2 = 13.3$ Var = 23 %
ID:2253 $\chi^2 = 12.9$ Var = 27 %
ID:8379 $\chi^2 = 12.8$ Var = 37 %
ID:5930 $\chi^2 = 12.7$ Var = 57 %
ID:12099 $\chi^2 = 12.6$ Var = 40 %
ID:13441 $\chi^2 = 12.5$ Var = 41 %
ID:5359 $\chi^2 = 12.4$ Var = 43 %
ID:2226 $\chi^2 = 12.4$ Var = 26 %
ID:7348 $\chi^2 = 12.2$ Var = 19 %
ID:13829 $\chi^2 = 12.0$ Var = 51 %
ID:2380 $\chi^2 = 12.0$ Var = 46 %
ID:2324 $\chi^2 = 11.9$ Var = 27 %
ID:4878 $\chi^2 = 11.9$ Var = 34 %
ID:16416 $\chi^2 = 11.9$ Var = 55 %
ID:5451 $\chi^2 = 11.8$ Var = 23 %
ID:5080 $\chi^2 = 11.7$ Var = 28 %
ID:12269 $\chi^2 = 11.7$ Var = 42 %
ID:10015 $\chi^2 = 11.7$ Var = 32 %
ID:9579 $\chi^2 = 11.6$ Var = 20 %
ID:10377 $\chi^2 = 11.6$ Var = 37 %
ID:5071 $\chi^2 = 11.4$ Var = 42 %
$F_{24\mu m}$ (μJy)
Feb 2004
Oct 2004
Jun 2005
Feb 2006
Oct 2006
Date

FIGURE 3.14

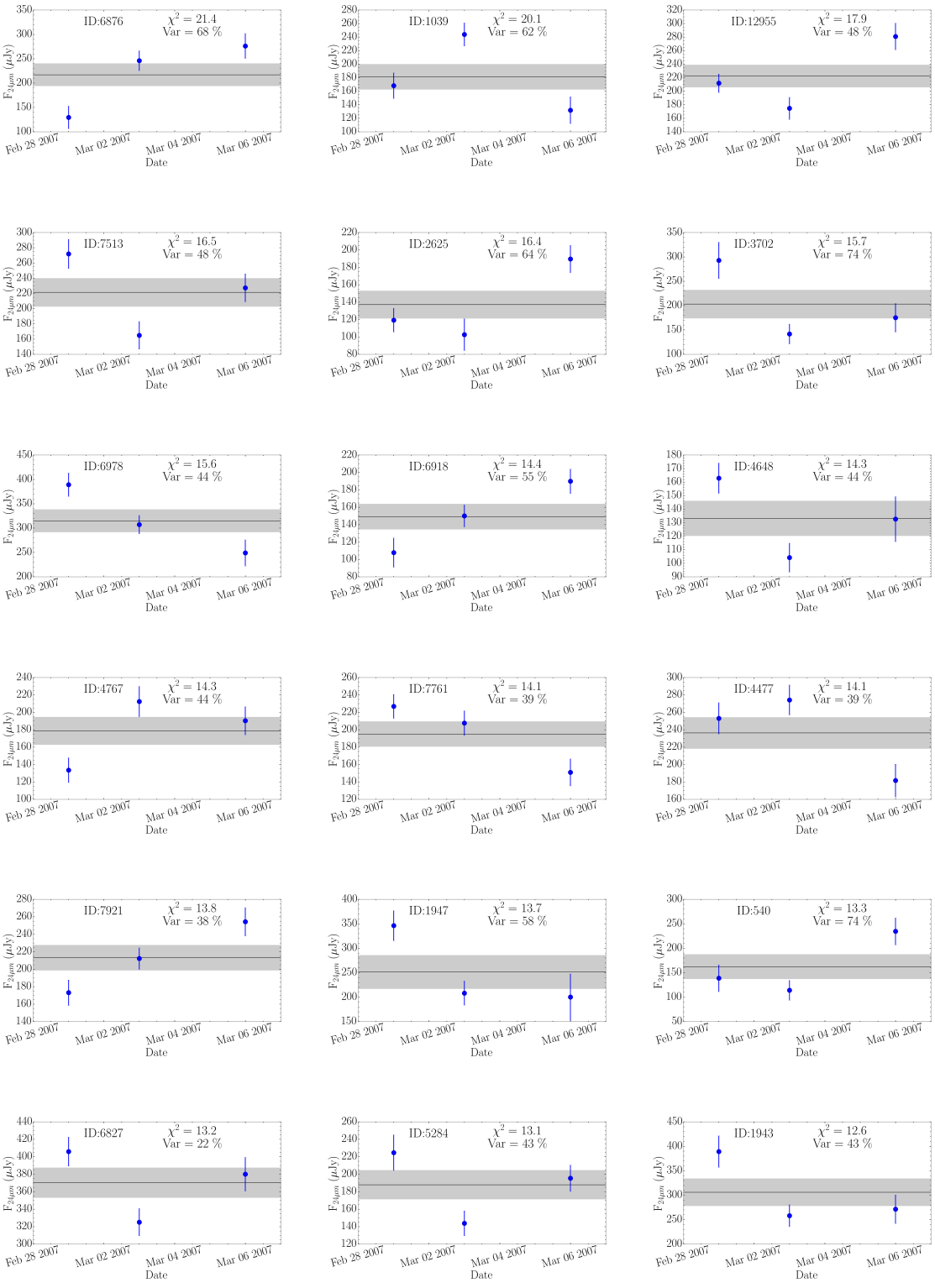

FIGURE 3.15: Light curves of MIPS 24 μm short-term variable sources (three epochs) in GOODS-South. The flux for each epoch is plotted with its corresponding photometric error. The solid line is the 24 μm mean flux of the source and the grey shaded area is the average of the errors of the source. Each plot lists the name of the source, the χ^2 value, and Var.

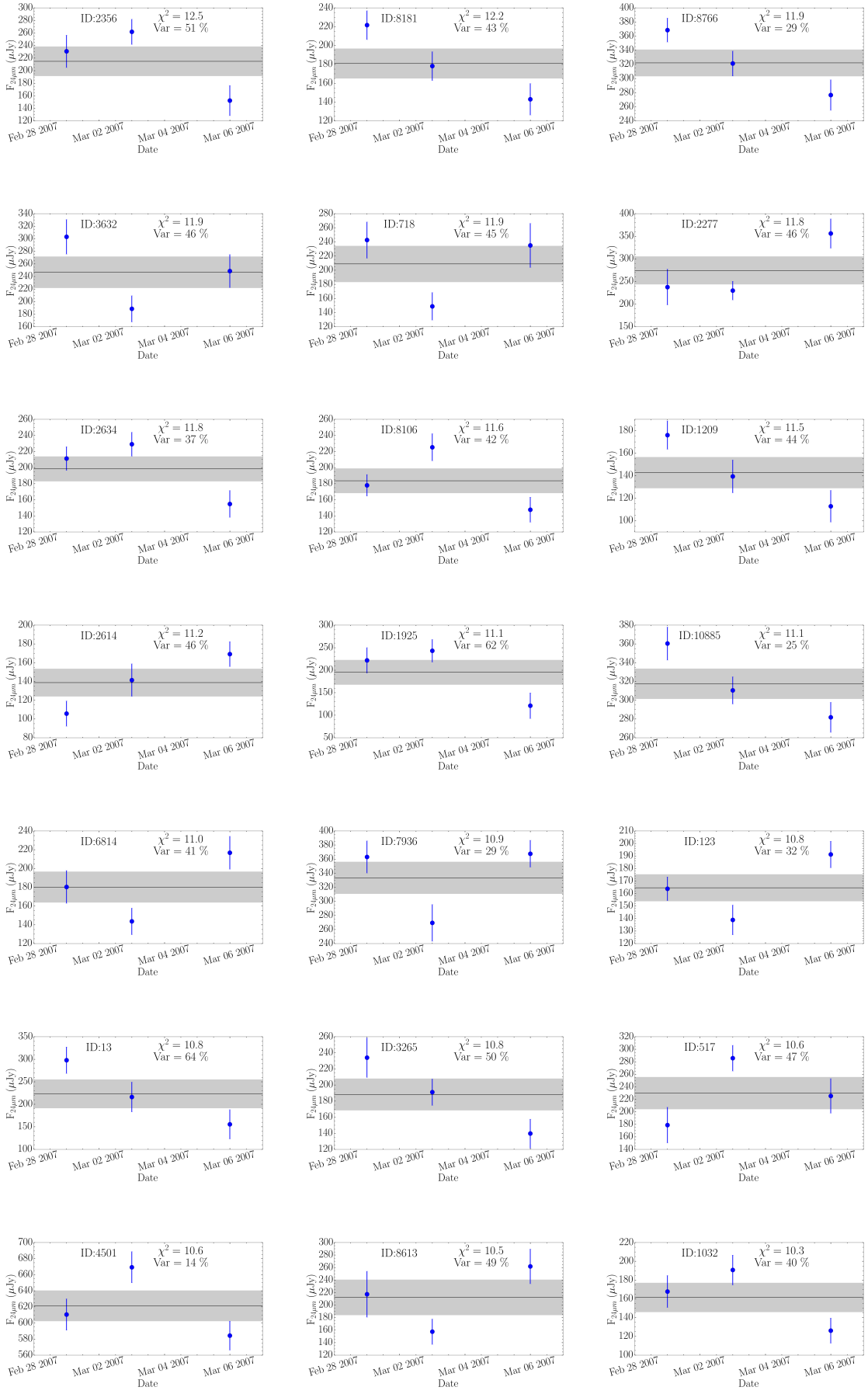
ID:2356 χ^2 = 12.5 Var = 51 %
ID:8181 χ^2 = 12.2 Var = 43 %
ID:8766 χ^2 = 11.9 Var = 29 %
ID:3632 χ^2 = 11.9 Var = 46 %
ID:718 χ^2 = 11.9 Var = 45 %
ID:2277 χ^2 = 11.8 Var = 46 %
ID:2634 χ^2 = 11.8 Var = 37 %
ID:8106 χ^2 = 11.6 Var = 42 %
ID:1209 χ^2 = 11.5 Var = 44 %
ID:2614 χ^2 = 11.2 Var = 46 %
ID:1925 χ^2 = 11.1 Var = 62 %
ID:10885 χ^2 = 11.1 Var = 25 %
ID:6814 χ^2 = 11.0 Var = 41 %
ID:7936 χ^2 = 10.9 Var = 29 %
ID:123 χ^2 = 10.8 Var = 32 %
ID:13 χ^2 = 10.8 Var = 64 %
ID:3265 χ^2 = 10.8 Var = 50 %
ID:517 χ^2 = 10.6 Var = 47 %
ID:4501 χ^2 = 10.6 Var = 14 %
ID:8613 χ^2 = 10.5 Var = 49 %
ID:1032 χ^2 = 10.3 Var = 40 %
$F_{24\mu m}$ (μJy)
Feb 28 2007
Mar 02 2007
Mar 04 2007
Mar 06 2007
Date

FIGURE 3.15

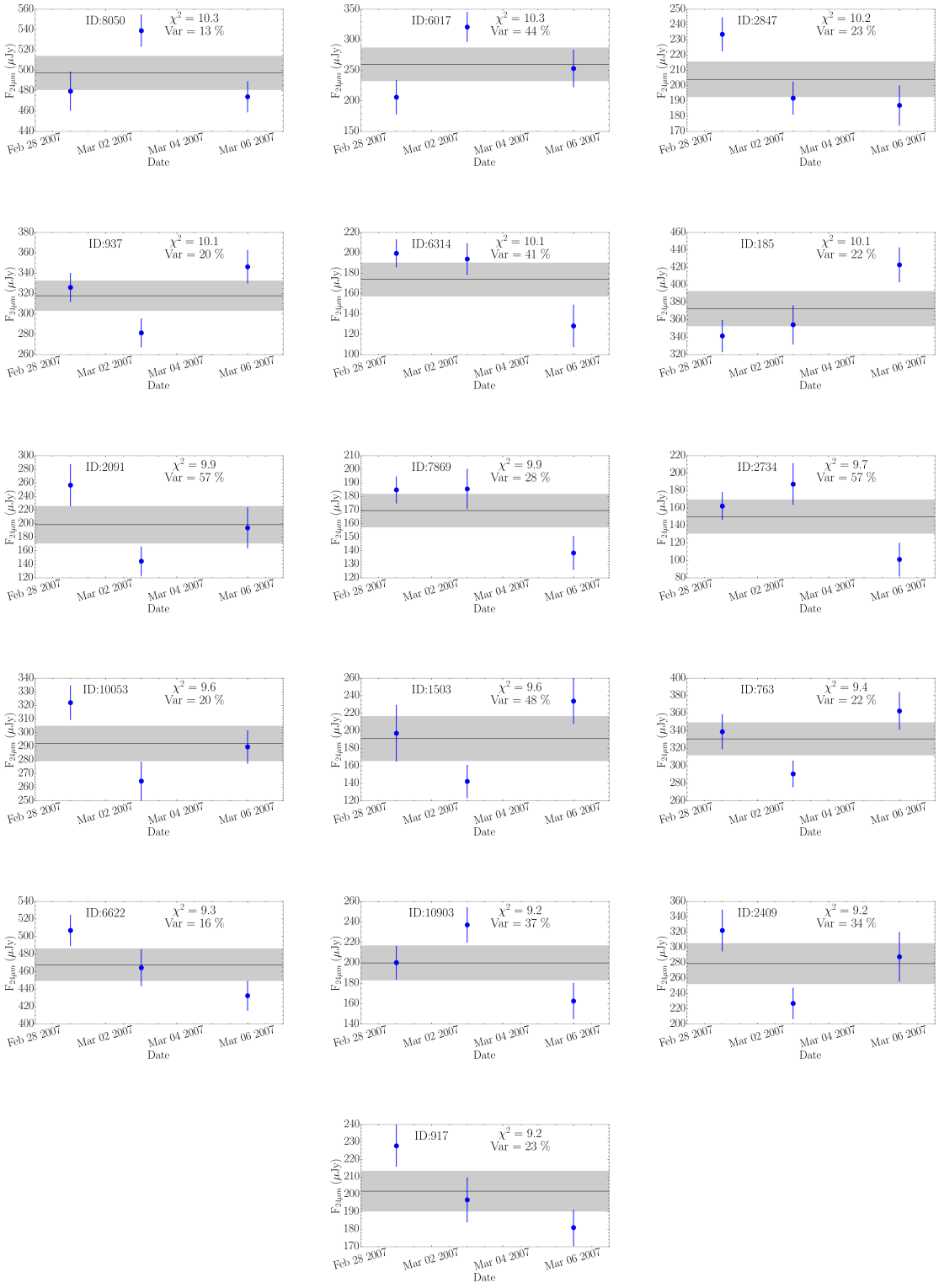
ID:8050 $\chi^2 = 10.3$ Var = 13 %
ID:6017 $\chi^2 = 10.3$ Var = 44 %
ID:2847 $\chi^2 = 10.2$ Var = 23 %
ID:937 $\chi^2 = 10.1$ Var = 20 %
ID:6314 $\chi^2 = 10.1$ Var = 41 %
ID:185 $\chi^2 = 10.1$ Var = 22 %
ID:2091 $\chi^2 = 9.9$ Var = 57 %
ID:7869 $\chi^2 = 9.9$ Var = 28 %
ID:2734 $\chi^2 = 9.7$ Var = 57 %
ID:10053 $\chi^2 = 9.6$ Var = 20 %
ID:1503 $\chi^2 = 9.6$ Var = 48 %
ID:763 $\chi^2 = 9.4$ Var = 22 %
ID:6622 $\chi^2 = 9.3$ Var = 16 %
ID:10903 $\chi^2 = 9.2$ Var = 37 %
ID:2409 $\chi^2 = 9.2$ Var = 34 %
ID:917 $\chi^2 = 9.2$ Var = 23 %
$F_{24\mu m}$ (μJy)
Feb 28 2007
Mar 02 2007
Mar 04 2007
Mar 06 2007
Date

FIGURE 3.15

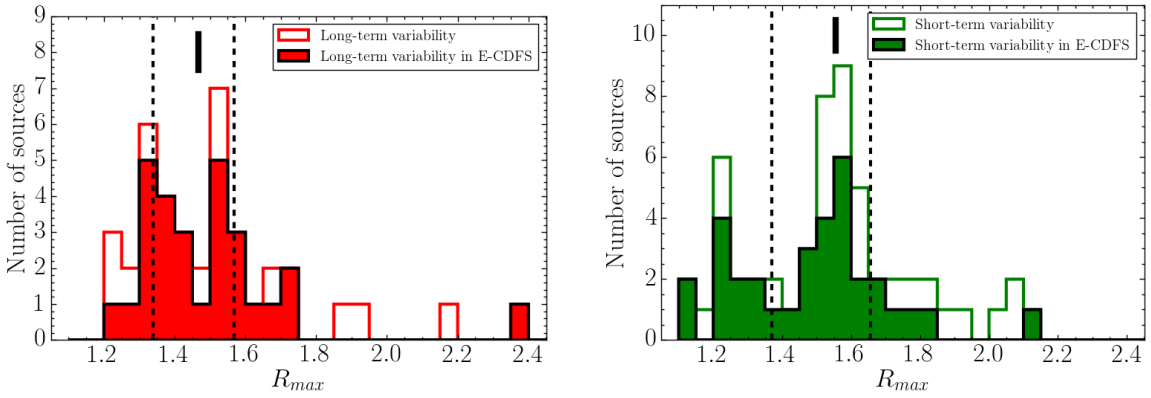

FIGURE 3.16: Distributions (open histograms) of the maximum to minimum flux ratio, $R_{\rm max}$, for the MIPS 24 μm long-term variable sources (left panel) and short-term variable sources (right panel). The black lines correspond to the median and the dashed lines to the quartiles of the distributions. In both panels the filled histograms are the distributions for variable sources in the E-CDFS

TABLE 3.5: Properties of the MIPS 24 μm variable sources.

Variability	f_ν 24 μm (μJy)		χ^2		*Var* (%)		$R_{\rm max}$	
	Average	Median[1]	Average	Median[1]	Average	Median[1]	Average	Median[1]
Long-term	196	168^{143}_{218}	14.75	$12.90^{11.94}_{15.46}$	39.0	$37.41^{28.3}_{43.7}$	1.51	$1.47^{1.33}_{1.57}$
Short-term	239	209^{181}_{279}	12.14	$11.25^{10.23}_{13.67}$	41.7	$43.4^{29.5}_{49.2}$	1.55	$1.56^{1.36}_{1.66}$

[1] Median and quartiles of the distribution.

24 μm both in short-term and long-term time scales. There are two explanations for this. First, as pointed out by Young et al. (2012), the limited photon statistics of their X-ray observations means that sources must be strongly variable to be identified as such. The second reason is due to the reprocessed nature of the AGN MIR emission. Indeed, in the context of the AGN dusty torus, the IR variability of AGN is predicted to be only a fraction of the AGN intrinsic luminosity variation, to depend of the dust distribution, to be delayed with respect to optical variations, and to depend on the IR wavelength used (see Hönig and Kishimoto 2011 and references therein). This is because the dust is further away from the central engine than the accretion disk. This has been confirmed observationally for local quasars (Neugebauer and Matthews 1999) and Seyfert galaxies (Glass 2004).

3.5.3 IRAC colours

In this subsection we investigate the Spitzer-IRAC MIR (3.6, 4.5, 5.8, and 8.0 μm) properties of the MIPS 24 μm variable sources as the IRAC emission has also been used to select AGN candidates (e.g., Lacy et al. 2004; Stern et al. 2005; Alonso-Herrero et al. 2006; Donley et al. 2012; Lacy et al. 2013).

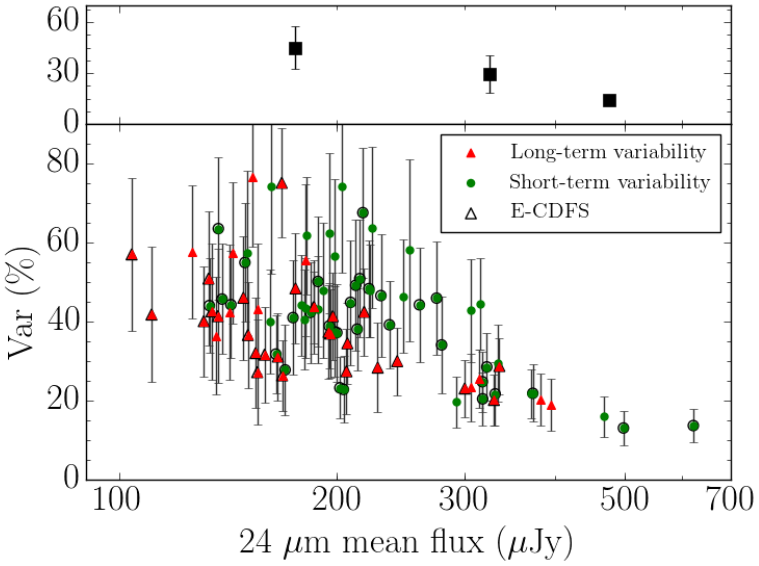

FIGURE 3.17: $Var = \frac{f_{max}-f_{min}}{\bar{f}} \times 100$ as a function of the MIPS 24 μm mean flux for long-term variable sources (red filled triangles) and short-term variable sources (green filled circles). The black marked triangles/circles correspond to the variable sources in the E-CDFS. The top panel shows the average value of Var with its error for three flux intervals (100 μJy < F < 250 μJy, 250 μJy < F < 400 μJy, F > 400 μJy).

Lacy et al. (2004) defined a wedge in an IRAC colour-colour diagram to identify AGN via their IR emission, based on the locus of the diagram occupied by quasars. Donley et al. (2012) defined a more restrictive IRAC wegde based on the IR power-law criterion of Alonso-Herrero et al. (2006) and the typical errors of the IRAC photometry. This IR power-law wedge was specifically designed to avoid contamination from high-redshift star forming galaxies. To do so, Donley et al. (2012) applied a colour cut of $\log(S_{8.0}/S_{4.5}) > 0.15$ to avoid high-redshift ($z \geq 2$) star-forming galaxies. They also applied a vertical cut of $\log(S_{5.8}/S_{3.6}) > 0.08$ to prevent contamination due to low-redshift star-forming galaxies and required that the IRAC Spectral Energy Distribution (SED) of the source rises monotonically. Donley et al. (2012) showed that this power-law wedge selects the majority of luminous X-ray identified AGN and therefore it is highly reliable at the expense of losing the least luminous AGN.

Finally, we note that recently Lacy et al. (2013) put forward a new expanded AGN selection criteria with a broader wedge when compared to that of Lacy et al. (2004) and imposed a 24 μm limit of > 600 μJy. We do not use this new wedge as only 1 short-term 24 μm variable source is above this limit (see Fig. 3.13).

To obtain the IRAC data for our sources, we used the *Rainbow* Cosmological Surveys Database, which contains multi-wavelength photometric data as well as spectroscopic information for sources in different cosmological fields, including GOODS-South (see Pérez-González et al. 2005, 2008). We cross-correlated the MIPS 24 μm catalogues with the *Rainbow* IRAC sources using a search radius

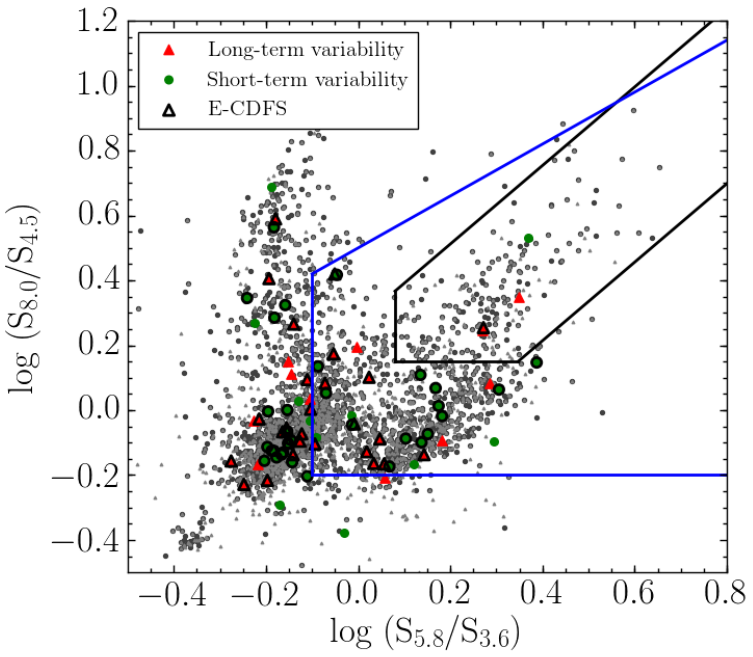

FIGURE 3.18: IRAC colour-colour plot of MIPS 24 μm sources in GOODS-South from the *Rainbow* database. The red filled triangles and green filled circles are the long-term and short-term MIPS 24 μm variable sources. The black marked triangles/circles mark the variable sources in the E-CDFS. The small grey dots are IRAC colours of the non-variable sources in the studied region. The different AGN wedges are shown as blue solid line for Lacy et al. (2004) and black solid line for Donley et al. (2012).

of 2.5 arcsec. Of the 39 long-term variable sources, 26 (67%) have a single counterpart and the remaining 13 (33%) have more than one counterpart within a radius of 2.5 arcsec. Of the 55 short-term variable candidates, 44 (80%) have a single counterpart and the remaining 11 (20%) have more than one counterpart within a radius of 2.5 arcsec. A visual inspection of the images at different wavelengths allowed us to identify the counterpart of the majority of the variable sources[4]. For the rest we used the data from the nearest source. All the long-term variable sources have fluxes in all four IRAC bands, whereas only 43 (78%) of 55 short-term variable candidates do. This is because the entire Epoch 7 region is not fully covered by the IRAC observations. The flux limits of the 24 μm variable sources are approximately 5 μJy at 3.6 μm, 4 μJy at 4.5 μm, 4 μJy at 5.8 μm, and 6 μJy at 8 μm.

Fig. 3.18 shows the IRAC colour-colour plot for all the MIPS 24 μm variable sources detected in the four IRAC bands together with the Lacy et al. (2004) and Donley et al. (2012) AGN wedges. For comparison we also plot the IRAC colours of the full (non-variable) MIPS 24 μm sample in the common area of GOODS-South as grey dots. Of the 39 long-term variable sources, only 8% fall in the Donley et al. (2012) AGN region and 44% fall in the Lacy et al. (2004) AGN region. Of the 43 short-term variable sources with IRAC fluxes, 2% fall in the Donley et al. (2012) AGN region and 44% fall in the Lacy et al. (2004) AGN region. These fractions of MIR variable sources falling inside the Lacy et al. (2004) wedge are similar to those found for variable optical sources in GOODS-South (see

[4]In the majority of the sources, inspection of the IRAC images is enough to determine which source dominates in the IR.

Villforth et al. 2012). In an IRAC variability study Kozłowski et al. (2010) found a higher fraction (approximately 75%) of NIR variable objects within an AGN wedge similar to that defined by Stern et al. (2005). This is most likely due to the relatively shallow IRAC observations of their study.

It is also worth noting that the fraction of objects in the parent MIPS 24 μm population in GOODS-South that are in the Lacy et al. (2004) wedge is 50%. However, the Lacy et al. (2004) AGN selection criteria was based on the IRAC colours of bright SDSS quasars with IRAC 8 μm fluxes greater than 1 mJy. In our general population, only about 1% of sources are above this limit. Alternatively, only 2% of the general sources in GOODS-South located inside the Lacy et al. (2004) wedge are found to be variable at 24 μm. Such a small fraction of MIR variable sources is expected, because the probability of detecting MIR variability of an AGN over the time scales probed and with three/four epochs is low. Additionally, it is likely that the AGN emission does not have a dominant contribution to the observed 24 μm emission.

3.6 Candidates in the Extended Chandra Deep Field South

In this section we investigate the multi-wavelength properties of the MIPS 24 μm variable sources located in the Extended Chandra Deep Field South (E-CDFS), which is located in the central area covered by our study (see Fig. 3.8). This field covers an area[5] $\sim$1100 arcmin^2.

The E-CDFS was observed by COMBO-17 (Classifying Objects by Medium-Band Observations, a spectrophotometric 17-filter survey) survey (Wolf et al. 2004). The COMBO-17 object catalogue contains, in addition to the 17 optical medium-band photometry, the broad-band $R_{\mathrm{COMBO-17}}$ magnitude (λ_{c} = 658 nm) and photometric redshifts for 63501 objects. We chose the E-CDFS because it has been observed with the deepest multi-wavelength data. We note that although the COMBO-17 catalogue gives a photometric redshift, for the objects without spectroscopic redshift we use the photometric redshifts provided by the *Rainbow* database because they are calculated using both optical and IR data (see Pérez-González et al. 2008). We only have spectroscopic redshifts for 8 long-term and 6 short-term variable objects.

For the cross-correlation we used again a search radius of 2.5 arcsec. All the objects within this radius are possible counterparts. Since now we are looking at the same area we find relatively similar numbers of long (28) and short term (33) variable sources, although still the number of short term variable sources is higher due to the deepest central area of Epoch 7. Of the 39 long-term variable candidates, 28 are in the E-CDFS and 27 have a detection in the COMBO-17 catalogue. Only 19 (70%) have a single counterpart, whereas the remaining 8 (30%) have more than one counterpart within a radius of 2.5 arcsec. Of the 55 short-term variable candidates, 33 are in the E-CDFS and 28 are detected

[5]The approximate location of this region compared to the region studied here can be seen from Fig. 3.8 where we marked the MIPS 24 μm variable sources in the region of the E-CDFS

TABLE 3.6: Properties of MIPS 24 μm variable candidates in the E-CDFS.

Variability	No.	f_ν 24 μm (μJy)		χ^2		*Var* (%)		$R_{\rm max}$		z		$R_{\rm mag}$	
		Average	Median[1]	Average	Median[1]	Average	Median[1]	Average	Median[1]	Average	Median[1]	Average	Median[1]
Long-term	28	186	175^{151}_{207}	14.98	$12.90^{12.01}_{15.46}$	38.1	$37.4^{30.0}_{43.6}$	1.49	$1.46^{1.36}_{1.57}$	0.94	$0.90^{0.63}_{1.27}$	22.66	$22.63^{21.38}_{23.98}$
Short-term	33	240	212^{184}_{275}	11.87	$11.10^{10.23}_{12.52}$	38.1	$39.2^{27.8}_{45.9}$	1.49	$1.51^{1.33}_{1.60}$	0.96	$1.00^{0.53}_{1.28}$	22.19	$22.29^{21.01}_{23.49}$

[1] Median and quartiles of the distribution.

in the COMBO-17 catalogue. Only 21 (75%) have a single counterpart and the other 7 (25%) have more than one counterpart in a radius of 2.5 arcsec. In the following discussion in the case of multiple counterparts we associate the MIPS 24 μm source to the nearest object in the COMBO-17 catalogue.

The COMBO-17 *R*-band magnitudes of the 24 μm variable sources are given in Tables 3.3 and 3.4. The median values are $R-$band = 22.6 mag and $R-$band = 22.3 mag for the long and short-term variable sources, respectively (see Table 3.6). These values are similar to those of X-ray selected non-broad line AGN in deep cosmological fields whose optical luminosities are dominated by the host galaxy (Bauer et al. 2004). This is probably the case as well for the MIPS 24 μm variable sources as they are not dominated by the AGN (see next section).

We also searched for counterparts in the MUSYC (Multiwavelength Survey by Yale-Chile) catalogue (Cardamone et al. 2010). See also Section 3.6.1. This catalogue covers all the E-CDFS in the optical and NIR. We used again a radius of 2.5 arcsec for the cross-correlation. We found 28 long-term variable sources detected in the MUSYC catalogue, 23 (82%) of them with a single counterpart and 33 short-term variable sources, 31 (94%) with a single counterpart.

As a sanity check, we compared the variable MIPS 24 μm sources in the E-CDFS with the full variable catalogue. We confirmed that their properties in terms of mean 24 μm fluxes (see Fig. 3.13 and Tables 3.5 and 3.6) and the variability measures $R_{\rm max}$ and *Var* (see Figs. 3.16 and 3.17) behave as the general 24 μm variable population. We therefore expect that the properties of the 24 μm variable sources in the E-CDFS might be extrapolated to the entire variable population.

3.6.1 Photometric redshifts and IRAC properties

In this section we study the distribution of the *Rainbow* redshifts for the MIPS 24 μm variable sources in the E-CDFS. For the long-term variable sources the redshifts are between 0.18 and 1.88 and for the short-term variable source between 0.12 and 1.94. This redshifts are in accordance with the redshifts of the MUSYC catalogue. The average (median) redshifts are similar for the long-term $z = 0.94\,(0.90)$ and the short term $z = 0.96\,(1.00)$ variable sources. The average (median) redshifts for the sources in the MUSYC catalogue are $z = 0.92\,(0.85)$ for the long-term and $z = 0.98\,(0.97)$ for the short-term variable candidates. We are therefore probing typically variable emission at 12 μm rest-frame. For comparison, the redshift distribution of the optical variable sources in GOODS-South has a mean value 0.94 for i-band selected sources (Villforth et al. 2012) and 1.14 for v-band selected sources (Sarajedini

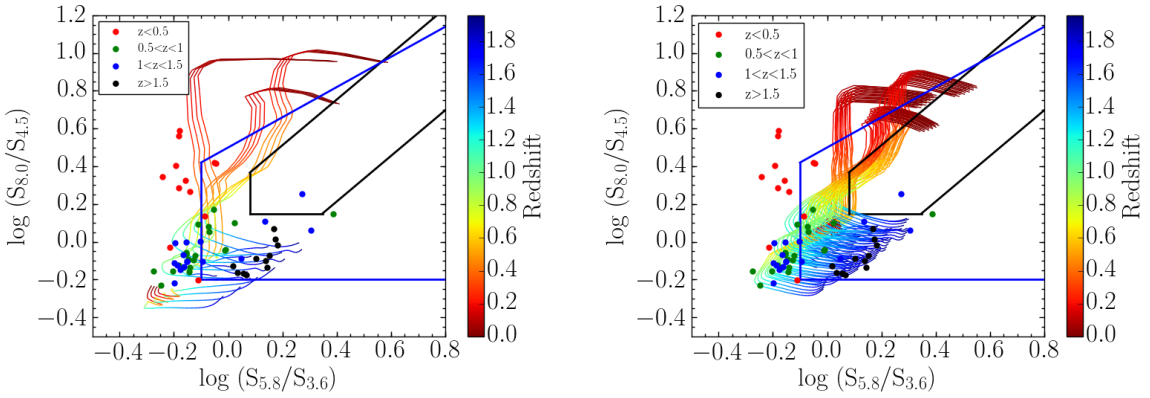

FIGURE 3.19: IRAC colour-colour plot of MIPS 24 μm variable sources in the E-CDFS, plotted according to their redshift. The multicoloured lines are the predicted IRAC colours of the star-forming templates from Donley et al. (2012) with a 20% AGN contribution (right panel) and no AGN contribution (left panel). The four sets of curves are for four different templates representing the galaxy contribution (see Donley et al. 2012 for more details). The redshift evolution from 0 (top of the curves) up to 2 (bottom of the curves) plotted (scale on the right hand side of the plots) is chosen to match the *Rainbow* z distribution of the MIPS 24 μm variable sources. The different AGN wedges are as in Fig. 3.18.

et al. 2011). For the X-ray selected AGN in our parent 24 μm catalogues the average (median) redshift is $z = 1.08\,(0.78)$.

Fig. 3.18 shows with black open symbols the IRAC colours of the MIPS 24 μm variable sources, both long and short term. As with the variability properties, the variable sources located in the E-CDFS behave as the general variable population, with approximately 50% being in the Lacy et al. (2004) wedge, and a small fraction in the Donley et al. (2012) wedge. As discussed above, the Donley et al. (2012) criteria are more restrictive to avoid contamination from star forming galaxies at different redshifts entering the AGN selection wedge but it misses a large fraction of low-luminosity AGN. In consequence, only one of the MIPS 24 μm variable sources in the E-CDFS would be classified as IR power-law galaxies according to Donley et al. (2012). Its ID is given in Table 3.7.

We can now use the redshift information in the IRAC colour-colour diagram to investigate whether variable sources in the Lacy et al. (2004) wedge can be classified as AGN, since the IRAC colours have a strong dependence with redshift. As shown in Fig. 3.19, a large fraction of the MIPS 24 μm sources falling in the Lacy et al. (2004) wedge are at $z > 1$ (62% of the objects).

In Fig. 3.19 we also plotted the tracks for an AGN/galaxy composite SED with a 20% AGN contribution (right panel) and no AGN contribution (left panel) with redshifts varying from 0 up to 2, and different degrees of extinction from Donley et al. (2012). As can be seen from these figures, the colours of approximately half of the MIPS 24 μm variable sources inside the Lacy et al. (2004) wedge agree with having a relatively small AGN fraction and are not compatible with a zero AGN fraction for their redshifts. This is similar to what is found for optical variable AGN in cosmological fields, where the AGN component is expected to be ~10% or less of the total galaxy flux in most cases (Sarajedini et al.

2011). Those outside this wedge might be compatible with just being normal galaxies (although see Section 3.6.2).

3.6.2 X-ray properties

One of the main goals of this work is to investigate whether variability at 24 μm is able to select AGN otherwise missed by deep X-ray exposures.

3.6.2.1 Fraction of 24 μm variable sources detected in X-rays

All the MIPS 24 μm variable sources, both long and short term, were matched against the deepest X-ray observations in the CDFS, that is, the 4 Ms *Chandra* catalogue presented in Xue et al. (2011), using again a search radius of 2.5 arcsec. These deep observations cover only the central part of the E-CDFS. The rest of the area is covered by shallower X-ray observations that are part of the E-CDFS observations (see references listed in Table 3.7). We also cross-matched our variable sources with these shallower X-ray catalogues with a search radius of 2.5 arcsec. We find 7 (25%) and 4 (12%) of the MIPS 24 μm long-term and short-term variable sources respectively in the E-CDFS are detected in X-rays (see Table 3.7 for the ID of the sources). The lower fraction of X-ray detections among the short-term variable sources is because a large fraction of these are located outside the deepest 4 Ms X-ray region. These fractions of 24 μm variable sources detected in X-rays are in general smaller than for AGN candidates selected by optical variability (30 − 50%) (Trevese et al. 2008; Sarajedini et al. 2011; Villforth et al. 2012).

In the central part of the E-CDFS (CDFS; ∼465 arcmin^2), which is covered by the deepest X-ray data (Xue et al. 2011 catalogue), 30% of the 24 μm variable sources are detected in X-rays. Using the catalogues of Xue et al. (2011) and Lehmer et al. (2005, 2008), and the redshifts provided by the *Rainbow* Database, we find that the 24 μm variable sources detected in X-rays have 0.5 − 8 keV luminosities ranging from $\sim 1 \times 10^{40}$ erg s^{-1} to $\sim 1 \times 10^{44}$ erg s^{-1} (See Table 3.7). Although some of our 24 μm variable sources with an X-ray counterpart are low luminosity X-ray sources and would be below the limit X-ray luminosity for the AGN definition, this does not imply that these sources are not AGN. Young et al. (2012) studied sources classified as galaxies in X-rays and found the 22% of them presented variability in X-rays, confirming that variability selects AGN that might not be selected by other methods. There are also many optical variables that are not X-ray detected or that have low X-ray to optical flux ratios (see fig. 6 in Sarajedini et al. 2011).

TABLE 3.7: MIPS 24 μm variable sources identified with other AGN criteria.

ID	Catalogs	Ref	Lacy et al. (2004)	X-ray Luminosity ($0.5-8$ keV) (erg s^{-1})
		Long-term variable sources		
2552	X-ray, compilation AGN, optical-variable, IR power law	(2), (3)*, (4), (5), (11), (13)	YES	1.20×10^{44}
13601	X-ray, Chandra 4 Ms, Radio excess	(2), (6), (9)*, (12)	NO	1.17×10^{42}
12099	X-ray	(3)*, (11)	NO	1.08×10^{43}
10015	relative IR SFR excess, X-ray	(7), (10)*	NO	8.88×10^{41}
2226	optical-variable, Chandra 4 Ms	(8), (9)*	NO	1.38×10^{40}
11976	Chandra 4 Ms	(9)*	YES	3.47×10^{42}
14779	Chandra 4 Ms	(9)*	NO	2.87×10^{40}
9796	Radio excess	(12)	YES	
9579	IR power law	(13)	YES[1]	
4679	IR power law	(13)	YES[1]	
		Short-term variable sources		
8766	IR power law, Chandra 4 Ms	(1), (9)*	YES	1.52×10^{41}
6827	X-ray, optical-variable, IR power law	(2), (3)*, (5), (11), (13)	YES[1]	1.41×10^{42}
7761	X-ray, Chandra 4 Ms, Radio excess	(2), (6), (9)*, (12)	NO	1.17×10^{42}
7513	optical-variable	(8)	YES	
917	Chandra 4 Ms	(9)*	NO	2.36×10^{40}
2614	Chandra 4 Ms	(9)*	NO	3.66×10^{42}
540	Radio excess	(12)	YES[1]	

Notes.— References for the catalogues. (1) Alonso-Herrero et al. (2006); (2) Cardamone et al. (2008); (3) Lehmer et al. (2005) (4) Véron-Cetty and Véron (2010a); (5) Trevese et al. (2008); (6) Tozzi et al. (2006); (7) Luo et al. (2011); (8) Villforth et al. (2010); (9) Xue et al. (2011); (10) Lehmer et al. (2008); (11) Silverman et al. (2010); (12) This work (radio excess); (13) This work (IR power law according to Donley et al. (2012)).
* Reference for the X-ray luminosity.
[1] Not in the E-CDFS.

3.6.2.2 Fraction of X-ray selected AGN found variable at 24 μm

As explained in Chapter 1, all AGN are expected to vary over a large range of timescales. However, the probability of detecting AGN variability in the MIR is always lower than the optical and NIR because MIR variability is predicted to be only a fraction of the AGN intrinsic luminosity variation. This is because the dust responsible for the bulk of the MIR emission is further away from the central engine than the accretion disk, and the variability signal is expected to be smoothed for large dust distribution (see Neugebauer and Matthews 1999; Glass 2004; Hönig and Kishimoto 2011).

Before we compute the fraction of X-ray selected AGN found variable at 24 μm, we need to calculate the number of X-ray sources detected in 24 μm satisfying our criteria in the parent catalogues as explained in Section 3.5.1. We found 211 X-ray sources in the central part of the E-CDFS (classified as AGN and galaxies in the Xue et al. (2011) catalogue) satisfying the properties of our parent MIPS 24 μm catalogues. Of these, only ~4% are found to be variable at 24 μm on the timescales probed by our study. This fraction is smaller than the fraction found in the optical (~25%, see Klesman and Sarajedini 2007; Sarajedini et al. 2011). This is explained by model simulations, which predict a more smothered variable signal and longer time scales in the MIR than in the optical (Hönig and Kishimoto

TABLE 3.8: Summary of fractions in the deepest X-ray region within the CDFS (~115 arcmin^2).

	No. sources parent 24 μm catalogue	parent catalogue with X-ray No. (%)	parent catalogue with variability No. (%)	X-ray sources with variability No. (%)
Long-term	189	90 (48)	8 (4)	5 (6)
Short-term	181	99 (55)	5 (3)	3 (3)

2011). In addition, for low luminosity AGN most of the MIR emission might come from the host galaxy, which would make it difficult to detect variability (see Section 3.6.1).

There are 149 sources classified as AGN in the Xue et al. (2011) catalogue in our parent 24 μm merged catalogues (see Section 3.5.1). If we assume that deep X-ray exposures provide the majority of the AGN in the field the total AGN population in this field would be 149 AGN. Assuming the 24 μm variable sources in the region covered by the Xue et al. (2011) catalogue not detected in X-ray are also AGN, they would only account for a small fraction ($\leq$ 13%) of the total AGN population in this field.

3.6.2.3 Candidates in the deepest X-ray region of the E-CDFS

As explained in Section 3.6.2.1, only the central area of the E-CDFS is covered by the deepest X-ray data (Xue et al. 2011). Since the effective exposure of the *Chandra* 4 Ms survey is not homogeneous (see fig. 2 of Xue et al. 2011), we selected a central region of ~115 arcmin^2 with the deepest and most homogeneous X-ray coverage. In this region we can compare the sources in the parent catalogue with the selected variable sources.

In this deepest X-ray region there are 189 sources in the parent 24 μm long-term catalogue and 181 in the parent 24 μm short-term catalogue. There are only 8 long-term variable sources and 5 short-term variable sources. Tables 3.8 and 3.9 summarize the results for the deepest X-ray region within the CDFS. As expected, the percentage of 24 μm variable sources with an X-ray detection (63% for long-term and 60% for short-term variable sources) is higher than the percentage in our parent 24 μm catalogue sources detected in X-ray (48% for long-term and 55% for short-term variable sources). This is expected because the fraction of X-ray detection is higher in AGN than in non AGN. Since the number of variable sources in this region is small, the percentages given at Tables 3.8 and 3.9 suffer from small number statistics.

3.6.3 Monochromatic IR luminosities

From the *Rainbow* Database we obtained the rest-frame 24 μm monochromatic luminosities for the MIPS 24 μm variable sources. As the contribution of the AGN to the total luminosity in the 24 μm variable sources is expected to be low (See Section 3.6.1), the luminosities were obtained by fitting the

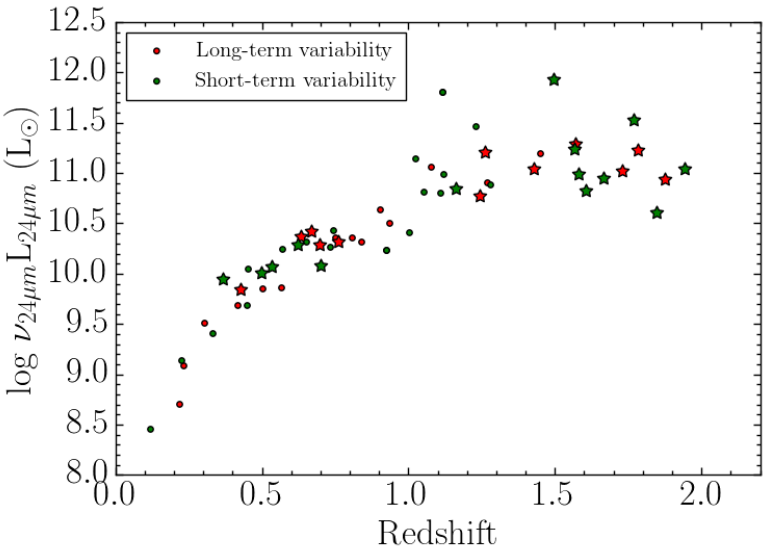

FIGURE 3.20: Rest-frame monochromatic 24 μm luminosity as a function of the redshift for the sources in the E-CDFS for long-term (red) and short-term (green) variable sources. The stars correspond to the variable sources satisfying the Lacy et al. (2004) AGN selection criteria

star forming galaxy templates from Chary and Elbaz (2001). Therefore, the fitted templates provide a reasonable approximation to the rest-frame 24 μm luminosities of the sources, which arise from star formation in the host galaxy and the putative AGN. For each source we used all the available photometric mid-to-far IR data points to fit the SEDs. Apart from the MIPS 24 μm flux, the Rainbow catalogues include photometry in the four IRAC bands, MIPS 70 μm and *Herschel*/PACS 100 and 160 μm. For our sample of 24 μm variable sources, 32% have 70 μm photometry, 23% have 100 μm photometry, and 18% have 160 μm photometry.

Fig. 3.20 shows these luminosities against the redshift for the long-term (red) and short-term (green) variable candidates in the E-CDFS. The mean value of rest-frame $\log(\nu L_{24\mu m}/L_\odot)$ is 10.5 for both, the long-term and the short-term variable sources. For those candidates satisfying the Lacy et al. (2004) AGN selection criteria the mean values are $\log(\nu L_{24\mu m}/L_\odot) = 10.7$ for both, the long-term and the short-term variable candidates. Conversely, the candidates not satisfying the Lacy et al. (2004) criteria have mean values of $\log(\nu L_{24\mu m}/L_\odot) = 10.3$ and 10.4 for the long-term and the short-term variable candidates, respectively. This is expected as galaxies in the Lacy et al. (2004) wedge tend to have a higher AGN fraction contributing to their IR emission than those outside (see previous section).

3.6.4 Radio properties

We investigate the radio properties of the MIPS 24 μm variable sources, since radio observations are in principle not biased against obscured AGN. Since star-forming galaxies also emit at radio frequencies and show a tight correlation between the IR and the radio emission (e.g. Helou et al. 1985; Condon

TABLE 3.9: Summary of fractions of MIPS 24 μm variable sources selected as AGN by other criteria.

	No. variable sources	X-ray[1] No. (%)	radio[2] excess No. (%)	other AGN[3] catalogues No. (%)	IR[4] power law No. (%)	Combined[5] No. (%)	Lacy et al. (2004)[6] criteria No. (%)	Combined[7] criteria No.(%)
Long-term variable sources								
Deepest X-ray region	8	5 (63)	1 (13)	3 (38)	0 (0)	5 (63)	3 (38)	7 (88)
In the E-CDFS	28	7 (25)	2 (7)	4 (14)	1 (4)	8 (29)	12 (43)	17 (61)
Outside the E-CDFS	11	0 (0)	0 (0)	0 (0)	2 (18)	2 (18)	5 (45)	5 (45)
In IRAC	39	7 (18)	2 (5)	4 (10)	3 (8)	10 (26)	17 (44)	22 (56)
All	39	7 (18)	2 (5)	4 (10)	3 (8)	10 (26)	17 (44)	22 (56)
Short-term variable sources								
Deepest X-ray region	5	3 (60)	1 (20)	2 (40)	0 (0)	3 (60)	2 (40)	4 (80)
In the E-CDFS	33	4 (12)	1 (3)	3 (9)	0 (0)	5 (15)	14 (42)	17 (52)
Outside the E-CDFS	22	1 (5)	1 (5)	1 (5)	1 (5)	2 (9)	5 (23)	5 (23)
In IRAC	43	5 (12)	2 (5)	4 (9)	1 (2)	7 (16)	19 (44)	22 (51)
All	55	5 (9)	2 (4)	4 (7)	1 (2)	7 (13)	19 (35)	22 (40)

[1] Variable MIPS 24 μm sources detected in X-rays.
[2] Variable MIPS 24 μm sources with radio excess.
[3] Variable MIPS 24 μm sources in other AGN catalogues. (See notes in Table 3.7).
[4] Variable MIPS 24 μm sources detected as IR power-law AGN.
[5] Combined 1^{st}, 2^{nd}, 3^{rd}, and 4^{th} criteria.
[6] Variable MIPS 24 μm sources satisfying the Lacy et al. 2004 criteria.
[7] All the criteria combined.

1992; Ivison et al. 2010), it is also possible to select AGN in cosmological fields by looking for radio excess sources (see e.g. Donley et al. 2005; Del Moro et al. 2013). We cross-correlated our 224 μm variable sources with the Miller et al. (2013) radio 1.4 GHz source catalogue and found that 2 long-term and 7 (one of which is outside the E-CDFS) short-term variable sources had a radio counterpart within a search radius of 2.5 arcsec. That is, 7% and 18% of the MIPS 24 μm long and short term variable sources.

We calculated the q ratio defined as $q = \log(f_{24\,\mu\mathrm{m}}/f_{1.4\,\mathrm{GHz}})$ (see Appleton et al. 2004) to determine if any of these sources present a radio excess. Fig. 3.21 shows q versus the redshift for the 9 MIPS 24 μm variable sources with radio detections at 1.4 GHz. Donley et al. (2005) considered radio excess sources those having $q < 0$ for non-K-corrected fluxes. On the other hand, Del Moro et al. (2013) demonstrated that this limit misses a large fraction of sources with radio excesses based on the ratio between the FIR luminosity and the radio emission. From fig. 5 of Del Moro et al. (2013), we can see that sources with $q < 0.4$ can be considered radio excess sources, and therefore AGN candidates. Among the MIPS 24 μm variable sources we find only 2 (7%) long-term and 2 (one of them out of the E-CDFS) (3%) short-term variable sources are radio excess sources, all of them at $z > 1.1$. Note that we include the short-term source just above the line (see Fig. 3.21). For reference, their IDs are given in Table 3.7. These small fractions of radio excess sources, if taken as AGN candidates among the MIPS 24 μm variable sources, are generally consistent with the little overlap between radio selected AGN and AGN selected via their X-ray and/or IR emission in cosmological fields (Donley et al. 2005; Hickox et al. 2009; Villforth et al. 2012).

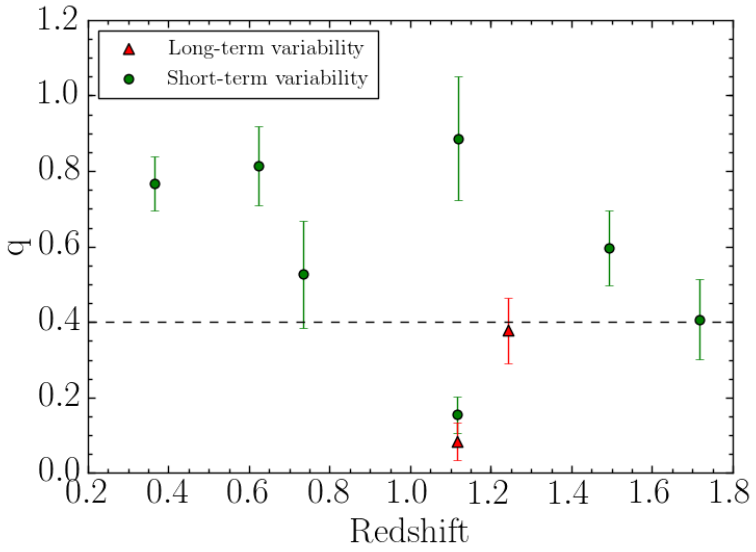

FIGURE 3.21: The $q = \log(f_{24\,\mu m}/f_{1.4\,GHz})$ ratio versus the redshift for long-term variable sources (red triangles) and short-term variable sources (green circles). Sources with $q < 0.4$ are considered to have a radio excess, as shown by Del Moro et al. (2013). Note we include a source out of the E-CDFS.

3.6.5 Comparison with other variability studies

Finally, we cross-correlated our 24 μm variable sources with sources found to be variable in other studies in the E-CDFS, using a search radius of 2.5 arcsec. We found two long term and two short term variable sources at 24 μm in common with the optical variability studies of Trevese et al. (2008) and Villforth et al. (2010), and none with those of Cohen et al. (2006), Klesman and Sarajedini (2007), and Sarajedini et al. (2011). Three of these four sources are also detected in X-rays, as can be seen from Table 3.7. The low correspondence between optical and MIR variable sources is expected given the lags and lower variation of amplitude observed and predicted in the MIR for local AGN when compared with those observed in the optical (Neugebauer and Matthews 1999; Glass 2004; Hönig and Kishimoto 2011).

3.7 Discussion and Summary

In this Chapter we have used multi-epoch deep *Spitzer*/MIPS 24 μm observations in GOODS-South to look for MIR variable sources. The goal was to identify low luminosity and possibly obscured AGN candidates not identified by other methods. To select variable sources we used a χ^2-statistics method to take into account the different photometric errors due to the different depths between epochs and varying depth within a given mosaic. By combining 24 μm data taken over three years and four epochs we studied long-term variability over time scales of months-years. Additionally we subdivided the longest duration epoch in three subepochs that allowed us to study the short-term variability in time

scales of days over a period of seven days. In each epoch and subepoch, we restricted the analysis to sources above the 5σ detection limit and without neighbours at distances of less than 10 arcsec to minimize crowding effects in the photometry. We used a 2 arcsec cross-matching radius, imposing additionally that the 2 arcsec criterion was fulfilled in each pair of epochs.

After discarding problematic sources, our sample contains 39 long-term and 55 short-term MIR variability-selected AGN candidates over the GOODS-South areas of 1360 arcmin^2 and 1960 arcmin^2, respectively, covered by the different epochs. The expected fraction of false positives in our sample of variable MIR sources is estimated to be about 40%. The MIR long and short-term variable sources comprise approximately 1.7% and 2.2% of the parent MIPS 24 μm samples, respectively. After removing the expected number of false positives the estimated percentages are 1.0% and 1.4%. These fractions of variable sources are typical of optical and near-IR variability studies in cosmological fields. The typical variability at 24 μm of the sources is 40%, both for the long and short-term variable sources.

In Section 3.6 we studied the properties of these variability selected AGN candidates restricting the region to the E-CDFS, as it contains the deepest and largest multi-wavelength coverage. We also made use of the *Rainbow* photometric redshifts that are calculated using optical and IR data for the objects without spectroscopic redshift. In the E-CDFS, we found 28 and 33 long and short term MIR variable sources, respectively, typically at $z = 1$ which implies our work is sensitive to variable emission at 12 μm rest-frame.

We cross-correlated our AGN candidates with other AGN catalogues including X-ray, radio, and variable catalogues in the E-CDFS. In the region with the best coverage by the deepest X-ray data, the *Chandra* 4 Ms catalogue of Xue et al. (2011) (CDFS; ∼465 arcmin^2), 30% of the variable sources (both short and long term) are also detected in X-rays. However, their $0.5 - 8$ keV luminosities are typically 2×10^{42} erg s^{-1}, with a few sources with X-ray luminosities of $\sim 10^{40}$ erg s^{-1}. In the *Chandra* 4 Ms catalogue of Xue et al. (2011) there are 149 sources identified as AGN due to their X-ray luminosity in our parent MIPS 24 μm catalogues (i.e., after removing close neighbours and merging individual catalogues), see Section 3.5.1. If we assume that the 24 μm variable sources in the region covered by the Xue et al. (2011) catalogue not detected in X-rays are AGN, they would only account for a small fraction ($\leq 13\%$) of the total AGN population in this field.

As expected, the fraction of 24 μm variable sources with a radio excess ($q = \log(f_{24\,\mu\mathrm{m}}/f_{1.4\,\mathrm{GHz}}) < 0.4$) is small, as is the case with variable sources identified in other wavelengths. Table 3.9 summarizes the results.

We also investigated the IRAC properties of the 24 μm variable sources. The fraction of MIR variable selected AGN candidates meeting the Donley et al. (2012) IR power-law criteria for AGN is small. This is not surprising, as this method has been proven to be a very reliable method to select luminous AGN, although it is highly incomplete for low luminosity X-ray selected AGN. Combining the AGN selected by the IR power-law criteria with the above X-ray, radio, and variability criteria, we find that

29% and 15% of the long-term and short-term MIPS 24 μm variable sources would be also identified as AGN using other methods (see Table 3.9). The lower fraction for the short-term variable candidates is because a larger fraction of them lie in the area with the shallowest X-ray coverage (that is, the E-CDFS, see Section 3.6.2).

In Table 3.9 we also included the number of MIPS 24 μm variable sources that fall in the Lacy et al. (2004) IRAC colour-colour wedge. Approximately 44% of the 24 μm variable selected AGN candidates are located in this wedge. However, using their redshifts we concluded that of these only half of them would have colours compatible with a small ($\sim$ 20%) AGN contribution (see Section 3.6.1).

If we combined all these criteria together we would obtain an upper limit of $\sim$ 56% to the fraction of MIPS 24 μm variable sources that would be identified as AGN by other methods. For reference in Table 3.9 we also listed these AGN fractions for sources outside the E-CDFS. However, as noted before the multi-wavelength coverage and depth of the observations outside this region are not as good, so these fractions should be taken as lower limits.

As explained in Section 3.6.2, only the central area of the E-CDFS is covered by the deepest X-ray data (Xue et al. 2011). We selected the region with the deepest and most homogeneous X-ray data ($\sim$115 arcmin^2), which is also covered by other AGN variability studies (Cohen et al. 2006; Klesman and Sarajedini 2007; Trevese et al. 2008; Villforth et al. 2010; Sarajedini et al. 2011). Combining all the criteria together, we obtained that $\sim$85% of the 24 μm variable sources in this region would be identified as AGN by other methods (see Table 3.9). The percentage in this region is higher than when considering the entire E-CDFS due to the deepest X-ray data and because other AGN catalogues do not cover all the E-CDFS. In this 11 arcmin^2 region we compared the parent catalogue with the variable sources (see Table 3.8). As expected, in this region the fraction of 24 μm variable sources with an X-ray detection is higher (63% for long-term and 60% for short-term variable sources) than that of sources in the parent 24 μm catalogue with X-ray detections (48% for long-term and 55% for short-term variable sources). Since the number of variable sources in this region is small, the percentages given at Tables 3.8 and 3.9 suffer from small number statistics.

In summary, we have shown that MIPS 24 μm variability provides a new method to identify AGN in cosmological fields. We find, however, that the 24 μm variable sources only account for a small fraction ($\leq$ 13 %) of the general AGN population. This is expected because model simulations predict a more smothered variable signal and longer timescales in the MIR than in the optical (Hönig and Kishimoto 2011). Moreover, we found that the AGN contribution to the MIR emission of these 24 μm variable sources is low (typically less than 20%). Since our method is only sensitive to high amplitude variability (see Section 3.4) then these 24 μm variable sources are likely to host low-luminosity AGN where the variability is expected to be stronger (Trevese et al. 1994). This study has been published in an international journal as García-González et al. (2015).

Chapter 4

The nuclear and integrated far-infrared emission of nearby Seyfert galaxies

4.1 Motivation

The integrated FIR emission of Seyfert galaxies is in general dominated by emission from the host galaxy (see Section 1.5). However, in the last years there have been several studies to quantify the AGN FIR emission using the *Herschel* telescope (see Chapter 2). Mushotzky et al. (2014) used FIR observations taken with PACS on board *Herschel* to study a sample of hard X-ray selected galaxies from the 58 month *Swift* Burst Alert Telescope (BAT) Active Galactic Nuclei catalogue. They found that $>$ 35% and 20% of the sources are point-like at 70 and 160 μm, respectively. Using the same sample, Meléndez et al. (2014) showed that the integrated FIR luminosity distributions of Seyfert 1 and Seyfert 2 galaxies are similar and their integrated $f_\nu(70\,\mu\mathrm{m})/f_\nu(160\,\mu\mathrm{m})$ ratios are indistinguishable from those of normal galaxies. Hatziminaoglou et al. (2010) studied 469 spectroscopically confirmed AGN. They used SPIRE data and showed that the FIR emission of Seyfert 1 and Seyfert 2 galaxies is identical to that of star forming galaxies. The AGN contributes very little to the integrated FIR emission and its contribution becomes important at wavelengths shorter than 70 μm, where the torus starts playing an important role.

Based on studies of individual Seyfert galaxies using *Herschel* observations, the contribution of the dust heated by the AGN to the total FIR emission varies from galaxy to galaxy. For example, Alonso-Herrero et al. (2012b) found that in NGC 1365 the AGN is the brightest source in the MIR but does not dominate in the FIR. Using the Nenkova et al. (2008b) torus models they quantified the AGN emission at 70 μm and determined that the AGN only contributes at most 1% within the central 5.4 kpc. For NGC 2992, García-Bernete et al. (2015) showed that the AGN dominates the emission between 15 and 30 μm, but its contribution decreases rapidly for wavelengths $>$ 30 μm. Ramos Almeida et al. (2011b) studied NGC 3081 and found that the FIR nuclear luminosity within a radius of $\leq$ 0.85 kpc

was well reproduced with the Nenkova et al. (2008b) clumpy torus models and concluded that the AGN dominates the FIR nuclear luminosity of this galaxy. There are however no statistical studies of the AGN contribution in the FIR, so it is important to find a method to determine if the AGN dominates in the FIR for large samples of galaxies. Mullaney et al. (2011) studied the infrared emission of a sample of local X-ray selected AGN with little evidence of host galaxy contamination in their MIR *Spitzer*/IRS spectra. They found that at least 3 of the 11 AGN in their sample are AGN dominated even at 60 μm.

In this Chapter we study the FIR (70 − 500 μm) emission of a sample of 33 nearby (median distance of 30 Mpc) Seyfert galaxies drawn from the Revised Shapley-Ames catalogue (RSA; Sandage and Tammann 1987) using *Herschel* imaging observations taken with PACS and SPIRE. The main goal is to disentangle the FIR emission of these Seyfert galaxies due to dust heated by the AGN from that due to dust heated by star formation. In particular, we take advantage of the *Herschel* angular resolution of 5.6 arcsec at 70 μm, which provides a median physical resolution of 0.8 kpc for our sample of galaxies. This allows us to study the nuclear (radii of $r = 1$ kpc and $r = 2$ kpc) and integrated FIR emission of Seyfert galaxies. The Chapter is organized as follows. In Section 4.2 we present our sample selection and the comparison with the entire RSA sample. In Section 4.3 we describe the data reduction and derive the aperture photometry. Section 4.4 presents our results, such as the unresolved 70 μm emission, the FIR colours, the grey body fitting and the nuclear and extranuclear star formation rates (SFR). In Section 4.5 we put forward a number of criteria to identify those Seyfert galaxies in our sample whose 70 μm emission is mostly due to dust heated by the AGN and discuss the *bona fide* candidates. The conclusions are presented in Section 4.6. Throughout this Chapter we use a cosmology with $H_0 = 73\,\mathrm{km\,s^{-1}\,Mpc^{-1}}$, $\Omega_m = 0.27$ and $\Omega_\Lambda = 0.73$.

4.2 The sample

We selected a sample of 33 nearby (distances $D_L < 70$ Mpc, Table 4.1) Seyfert galaxies (see Maiolino and Rieke 1995) from the RSA catalogue (Sandage and Tammann 1987) with *Herschel*/PACS imaging observations in at least two bands and SPIRE imaging observations from our own programs and from the archive[1] (see Table 4.3). We imposed the distance criterion so we could obtain at least one nuclear (radii of $r = 1$ kpc and/or $r = 2$ kpc) FIR measurement at 70 μm. We also required Seyfert galaxies with existing high angular resolution (0.3−0.4 arcsec) MIR spectroscopy (Hönig et al. 2010; González-Martín et al. 2013; Esquej et al. 2014; Alonso-Herrero et al. 2016a, and see also Chapter 5) obtained on 8 − 10 m class telescopes (T-ReCS, CanariCam and VISIR instruments). We used the spectra published in these references instead of reducing the archival data. These observations allow us to determine whether they have star formation activity on typical physical scales of 50 − 60 pc, which is necessary when trying to determine what galaxies in our sample have AGN-dominated FIR emission. 23 of these

[1] http://www.cosmos.esa.int/web/herschel/science-archive

Table 4.1: Galaxy sample.

Number	Name	D_L (Mpc)	B_T[1] (mag)	Morphological[2] type	Activity type	EW of 6.2 μm PAH (μm)	EW of 11.3 μm PAH (μm)	log $L_{bol,AGN}$[6] (erg s^{-1})	SFR (r = 1kpc)[6] ($M_\odot yr^{-1}$)	SFR (r >1kpc)[6] ($M_\odot yr^{-1}$)	Ref. Activity type
1	ESO 323-G077	60.2	13.58	(R)SAB0^0(rs)	Sy 1.2	0.049±0.005	0.126±0.005	43.9[8]			3
2	IC 5063	49.9	13.22	SA0^+(s)?	Sy 2	<0.018	0.011±0.004	44.0[8]			10
3	Mrk 1066	49.0	13.64	(R)SB0^+(s)	Sy 2	0.544±0.007	0.591±0.005				4
4	NGC 1068	14.4	9.61	(R)SA(rs)b	Sy 2			44.3[8]			5
5	NGC 1320	35.5	13.32	Sa? edge-on	Sy 2						3
6	NGC 1365	21.5	10.21	SB(s)b	Sy 1.8	0.258±0.004	0.314±0.002	44.3	4.80	8.40	3
7	NGC 1386	10.6	12.00	SB0^+(s)	Sy 2	<0.019	0.072±0.005	43.5	0.05		11
8	NGC 1808	12.3	10.76[2]	(R)SAB(s)a	Sy 2	1.078±0.006	1.013±0.003	41.2[8]			7
9	NGC 2110	32.4	14.00	SAB0^-	Sy 2	0.014±0.007	0.051±0.005	43.7[8]			12
10	NGC 2273	28.7	12.55	SB(r)a?	Sy 2	0.273±0.006	0.383±0.007	43.6	0.76		4
11	NGC 2992	34.1	12.80	Sa pec	Sy 1.9	0.295±0.008	0.328±0.017	44.7	0.77	0.54	1
12	NGC 3081	34.2	12.68	(R)SAB0/a(r)	Sy 2	0.022±0.012	0.046±0.005	44.6	0.15	0.31	13
13	NGC 3227	20.6	11.55	SAB(s)a pec	Sy 1.5	0.215±0.006	0.359±0.007	44.0	0.48	0.21	3
14	NGC 3281	44.7	12.62	SA(s)ab pec?	Sy 2	0.013±0.008	0.010±0.011	45.0	0.87		3
15	NGC 3783	36.1	12.89	(R')SB(r)ab	Sy 1.5	0.001±0.005	0.013±0.009	44.2	0.05		3
16	NGC 4051	12.9	10.93	SAB(rs)bc	Sy 1.5	0.089±0.004	0.114±0.003	43.5	0.13	0.88	1
17	NGC 4151	20.3	11.13	(R')SAB(rs)ab?	Sy 1.5	0.005±0.003	0.013±0.003	44.5	0.06		3
18	NGC 4253	61.3	13.30	(R')SB(s)a?	Sy 1.5	0.087±0.005	0.083±0.005				1
19	NGC 4258	7.98	8.95	SAB(s)bc	Sy 1.9	0.034±0.013	0.067±0.009	42.2	0.05	0.39	1
20	NGC 4388	17.0	11.83	SA(s)b? edge-on	Sy 2	0.072±0.005	0.140±0.003	44.4	0.21	0.24	14
21	NGC 4507	59.6	12.81	(R')SAB(rs)b	Sy 2	0.019±0.006	0.049±0.003	44.6	0.99		10
22	NGC 4579	17.0	10.56	SAB(rs)b	Sy 1.9			42.4[9]	0.05	0.47	1
23	NGC 4594	12.7	9.28	SA(s)a edge-on	Sy 1.9			42.5	0.03	0.66	1
24	NGC 4725	27.0	10.11[2]	SAB(r)ab pec	Sy 2			41.9	0.01	0.34	3
25	NGC 5135	57.7	12.94	SB(s)ab	Sy 2	0.742±0.009	0.777±0.007	44.9	6.10	3.60	3
26	NGC 5347	40.2	13.40	(R')SB(rs)ab	Sy 2	0.046±0.001	0.059±0.005	43.5[8]			3
27	NGC 5506	30.0	12.79	Sa pec edge-on	Sy 1.9	0.012±0.004	0.055±0.003	44.8	0.58		1
28	NGC 7130	68.7	12.98[2]	Sa pec	Sy 1.9	0.416±0.011	0.434±0.008	44.3	4.30	6.70	3
29	NGC 7172	37.6	12.85	Sa pec edge-on	Sy 2	0.052±0.006	0.205±0.009	44.2	0.79	0.68	3
30	NGC 7213	24.9	11.18	SA(s)a?	Sy 1.5	<0.025	0.059±0.006	43.1[8]	0.04	0.39	1
31	NGC 7465	28.4	13.31	(R')SB0^0?(s)	Sy 2						15
32	NGC 7479	32.4	11.70	SB(s)c	Sy 1.9		0.008±0.008	43.2	0.32	1.70	3
33	NGC 7582	22.0	11.46	(R')SB(s)ab	Sy 2	0.508±0.033	0.703±0.011	44.5	2.10	1.90	1

[1] from Maiolino and Rieke (1995); [2] NED Homogenized from de Vaucouleurs et al. (1991); [3] from Véron-Cetty and Véron (2006); [4] from Contini et al. (1998); [5] from Osterbrock and Martel (1993); [6] from Diamond-Stanic and Rieke (2012); [7] from Brightman and Nandra (2011); [8] from Esquej et al. (2014); [9] from Mason et al. (2012); [10] from Kewley et al. (2001); [11] from Reunanen et al. (2002); [12] from Bradt et al. (1978); [13] from Phillips et al. (1983); [14] from Trippe et al. (2010); [15] from Malizia et al. (2012)

galaxies also have estimates of the nuclear and integrated SFR from MIR *Spitzer*/IRS spectroscopy taken from Diamond-Stanic and Rieke (2012) (hereafter DSR2012).

In Table 4.1 we list the properties of the Seyfert galaxies in our sample including their luminosity distance, optical apparent magnitude (B_T), morphological type, and the optical activity type (15 Sy 1 galaxies and 18 Sy 2 galaxies). We consider as Sy 1 the 1.5 and 1.9 Seyfert galaxies.

We obtained the *Spitzer*/IRS SL+LL spectra from the Cornell Atlas of Spitzer/IRS Sources version 7 (CASSIS, Lebouteiller et al. 2011, 2015). The stitching of the different spectral orders has been made as described in Hernán-Caballero et al. (2016). We also provide in Table 4.1 the equivalent width (EW) of the 6.2 and 11.3 μm PAH features measured from *Spitzer*/IRS short-low (SL) spectra, except for NGC 1068 which was from a short-high (SH) spectrum (see Esquej et al. 2014). We measured the EW of the PAH features following the method described by Hernán-Caballero and Hatziminaoglou (2011). Finally, we give the AGN bolometric luminosity, and the nuclear (r = 1 kpc) and extranuclear (r > 1 kpc) SFRs taken from DSR2012. For those RSA Seyferts not in that work we take the AGN bolometric luminosities from Mason et al. (2012) and Esquej et al. (2014).

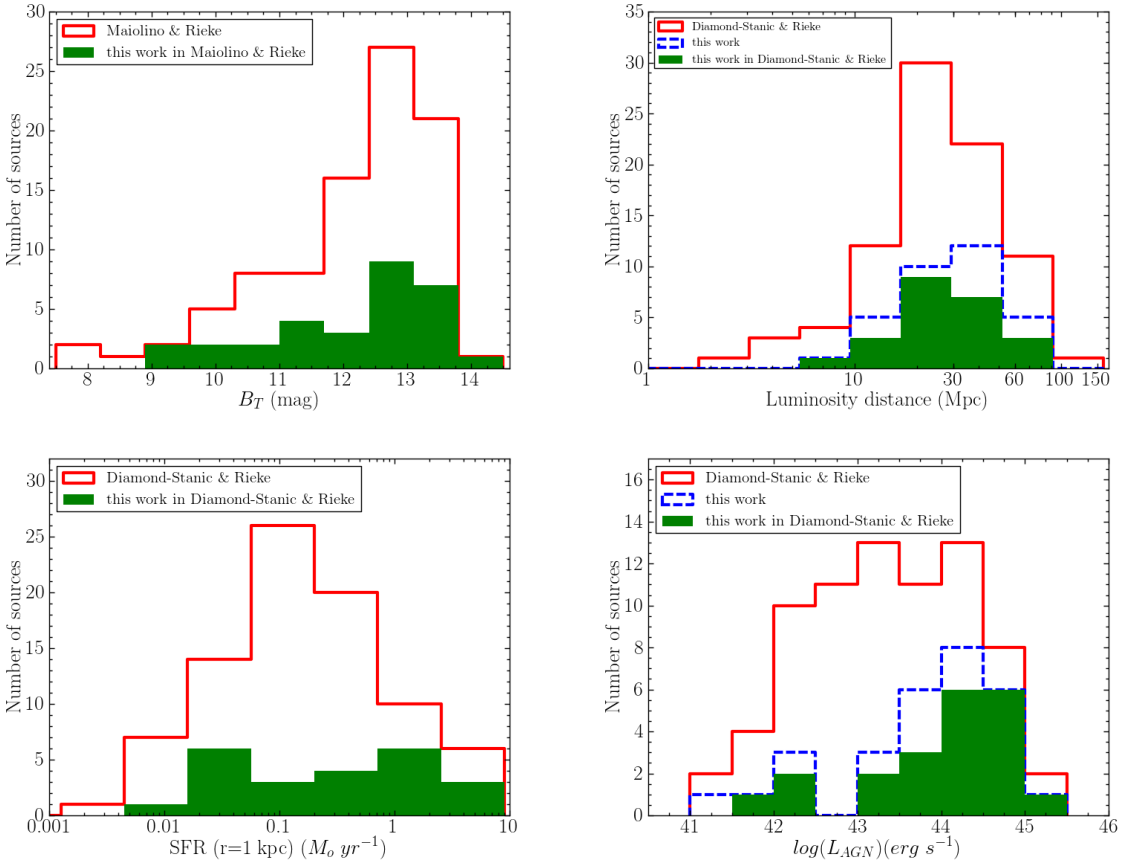

FIGURE 4.1: Sample comparison. Top left panel: Distribution of the optical apparent magnitude, B_T, for the RSA galaxies in Maiolino and Rieke (1995) (91 galaxies, in red) and our sample (30 galaxies, in green). Top right panel: Distribution of the luminosity distance for the galaxies in DSR2012 (84 galaxies, in red) and our sample (33 galaxies, in dashed blue). There are 10 galaxies in our sample not included in the DSR2012 sample. The galaxies in common between DSR2012 sample and our sample are shown in green. Bottom left panel: Distribution of the nuclear SFR (r = 1 kpc) for the galaxies in DSR2012 (84 galaxies, in red) and our sample with DSR2012 SFR values (23 galaxies, in green). Bottom right panel: Distribution of the AGN bolometric luminosity for the galaxies in DSR2012 (74 galaxies, in red), our sample (29 galaxies, in dashed blue) and our sample with DSR2012 values (21 galaxies, in blue).

4.2.1 Sample comparison

Since the RSA sample is selected based on the galaxy optical apparent magnitude, we used the B_T values from Maiolino and Rieke (1995) to determine if our galaxy selection is representative of the entire RSA sample of Seyfert galaxies. Their sample contains 91 relatively nearby Seyfert galaxies with $B_T < 13.31$ and have 30 galaxies in common with our sample. The top left panel of Fig. 4.1 shows the B_T distribution for the two samples. The 91 galaxies in Maiolino and Rieke (1995) are shown in red and the 30 of 33 galaxies in our sample are shown in blue. Inspection of Fig. 4.1 and a Kolmogorov-Smirnov test (KS-test) show that our sample is not significantly different from the RSA sample in terms of B_T (p-value = 0.92).

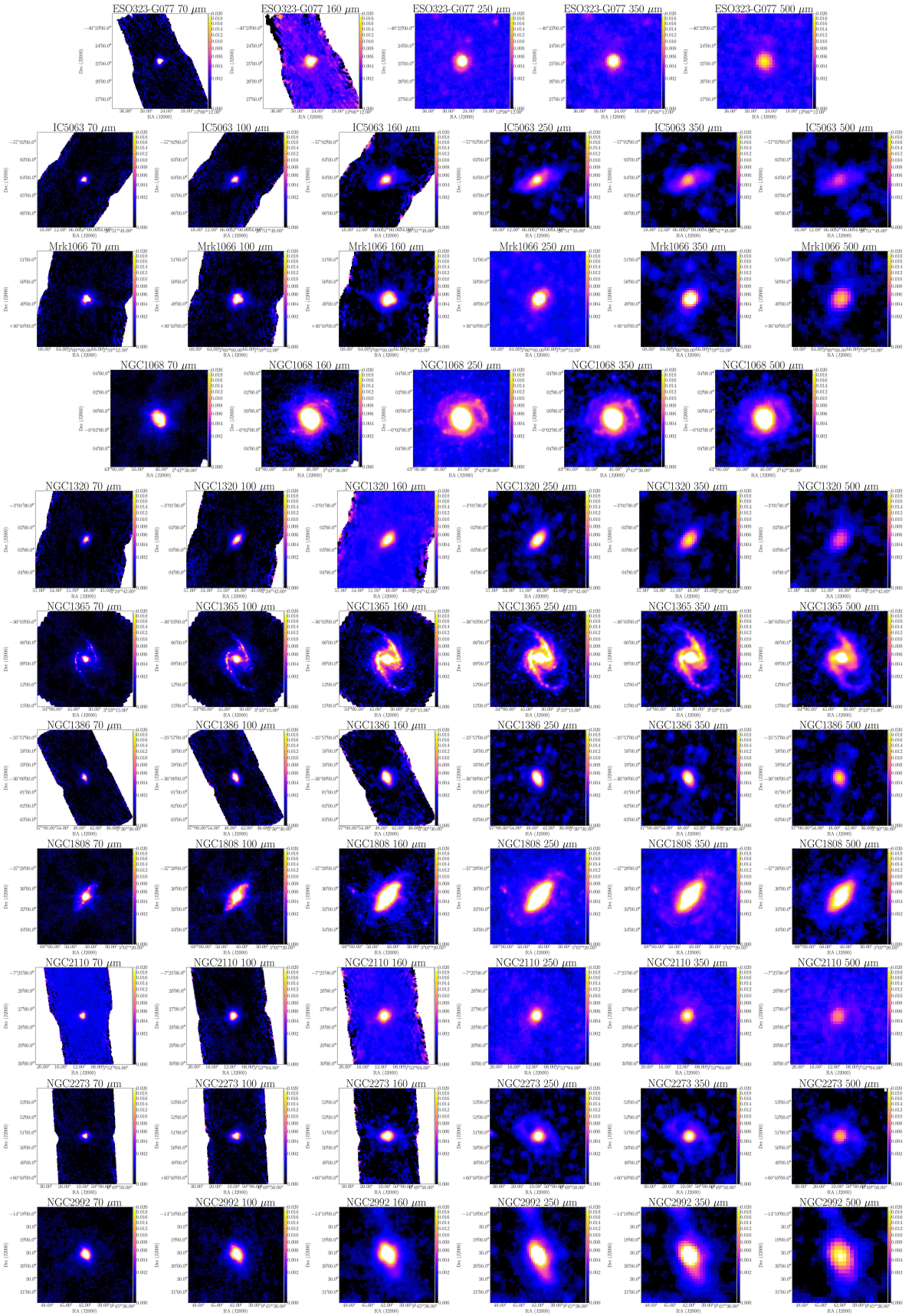

FIGURE 4.2: Mosaics of the galaxies in the PACS 70, 100, 160 μm bands (three most left panels, left to right), and in the SPIRE 250, 350, and 500 μm bands (the most right panels from left to right). The images are shown in a square root scale.

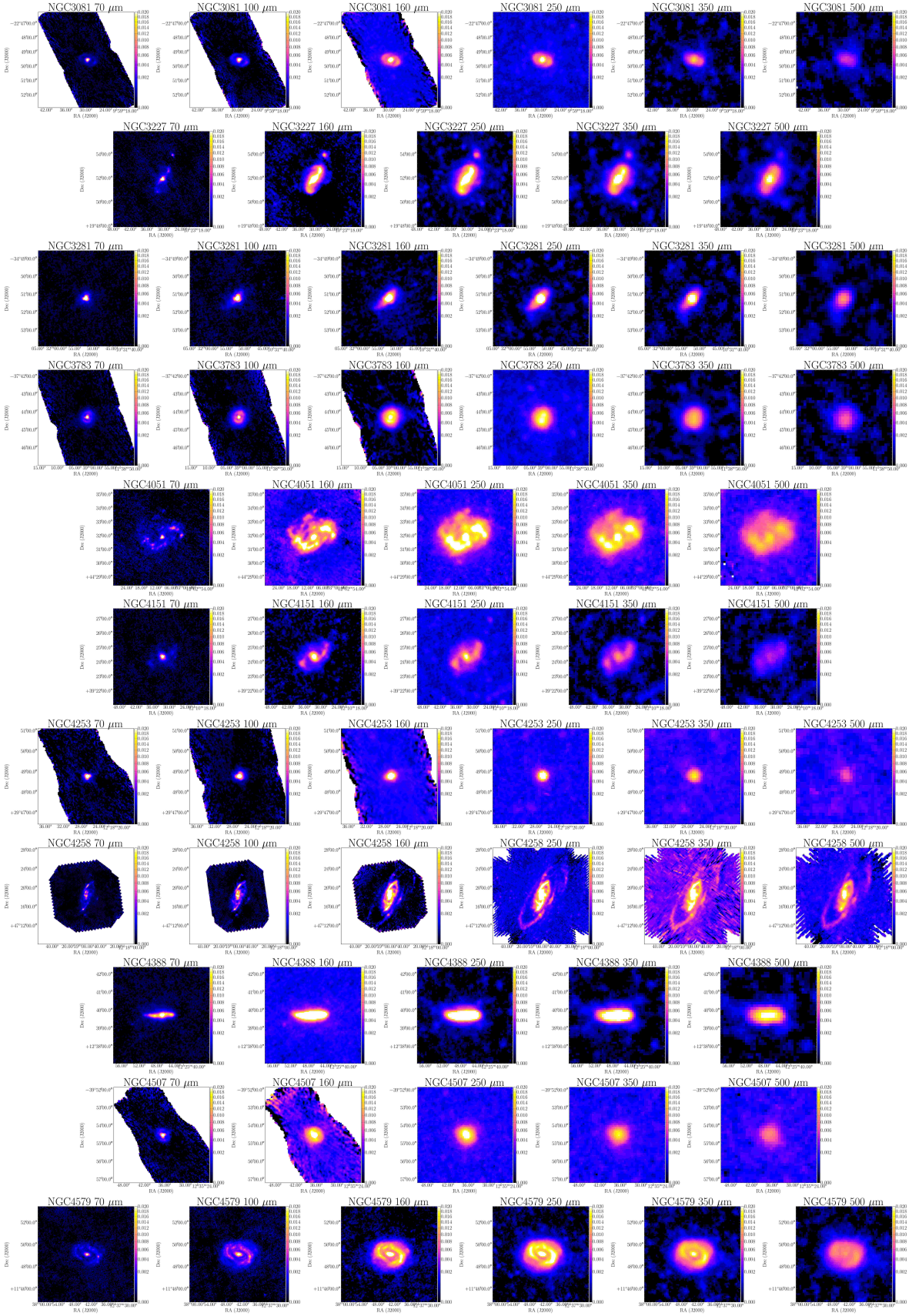
NGC3081 70 μm
NGC3081 100 μm
NGC3081 160 μm
NGC3081 250 μm
NGC3081 350 μm
NGC3081 500 μm
NGC3227 70 μm
NGC3227 160 μm
NGC3227 250 μm
NGC3227 350 μm
NGC3227 500 μm
NGC3281 70 μm
NGC3281 100 μm
NGC3281 160 μm
NGC3281 250 μm
NGC3281 350 μm
NGC3281 500 μm
NGC3783 70 μm
NGC3783 100 μm
NGC3783 160 μm
NGC3783 250 μm
NGC3783 350 μm
NGC3783 500 μm
NGC4051 70 μm
NGC4051 160 μm
NGC4051 250 μm
NGC4051 350 μm
NGC4051 500 μm
NGC4151 70 μm
NGC4151 160 μm
NGC4151 250 μm
NGC4151 350 μm
NGC4151 500 μm
NGC4253 70 μm
NGC4253 100 μm
NGC4253 160 μm
NGC4253 250 μm
NGC4253 350 μm
NGC4253 500 μm
NGC4258 70 μm
NGC4258 100 μm
NGC4258 160 μm
NGC4258 250 μm
NGC4258 350 μm
NGC4258 500 μm
NGC4388 70 μm
NGC4388 160 μm
NGC4388 250 μm
NGC4388 350 μm
NGC4388 500 μm
NGC4507 70 μm
NGC4507 160 μm
NGC4507 250 μm
NGC4507 350 μm
NGC4507 500 μm
NGC4579 70 μm
NGC4579 100 μm
NGC4579 160 μm
NGC4579 250 μm
NGC4579 350 μm
NGC4579 500 μm

FIGURE 4.2

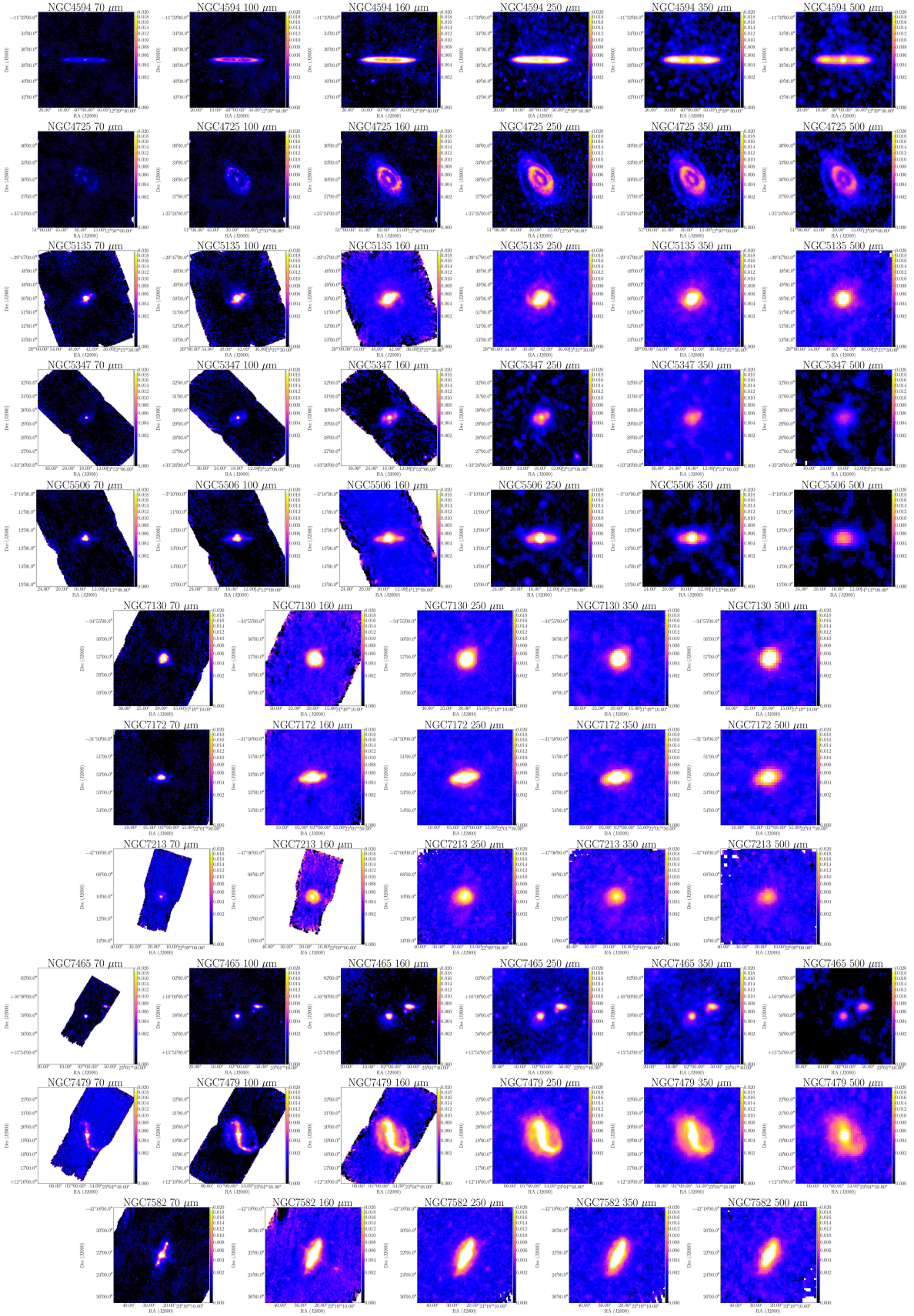
NGC4594 70 μm
NGC4594 100 μm
NGC4594 160 μm
NGC4594 250 μm
NGC4594 350 μm
NGC4594 500 μm
NGC4725 70 μm
NGC4725 100 μm
NGC4725 160 μm
NGC4725 250 μm
NGC4725 350 μm
NGC4725 500 μm
NGC5135 70 μm
NGC5135 100 μm
NGC5135 160 μm
NGC5135 250 μm
NGC5135 350 μm
NGC5135 500 μm
NGC5347 70 μm
NGC5347 100 μm
NGC5347 160 μm
NGC5347 250 μm
NGC5347 350 μm
NGC5347 500 μm
NGC5506 70 μm
NGC5506 100 μm
NGC5506 160 μm
NGC5506 250 μm
NGC5506 350 μm
NGC5506 500 μm
NGC7130 70 μm
NGC7130 160 μm
NGC7130 250 μm
NGC7130 350 μm
NGC7130 500 μm
NGC7172 70 μm
NGC7172 160 μm
NGC7172 250 μm
NGC7172 350 μm
NGC7172 500 μm
NGC7213 70 μm
NGC7213 160 μm
NGC7213 250 μm
NGC7213 350 μm
NGC7213 500 μm
NGC7465 70 μm
NGC7465 100 μm
NGC7465 160 μm
NGC7465 250 μm
NGC7465 350 μm
NGC7465 500 μm
NGC7479 70 μm
NGC7479 100 μm
NGC7479 160 μm
NGC7479 250 μm
NGC7479 350 μm
NGC7479 500 μm
NGC7582 70 μm
NGC7582 160 μm
NGC7582 250 μm
NGC7582 350 μm
NGC7582 500 μm

FIGURE 4.2

TABLE 4.2: Summary of the statistical properties of our sample and comparison samples.

	RSA sample				This work			
Quantity	Number	Mean	σ	Median	Number	Mean	σ	Median
B_T [1]	91	12.08	1.32	12.55	30	12.10	1.34	12.68
Luminosity distance (Mpc) [2]	84	30.5	21.1	24.4	33 (23)*	32.2 (29.5)*	16.4 (15.6)*	30.0 (27.0)*
SFR (r = 1 kpc) ($M_\odot$ yr^{-1}) [2]	84	0.67	1.42	0.15	23	1.03	1.66	0.32
log L_{AGN} (erg s^{-1}) [2]	74	43.4	1.0	43.4	29 (21)*	43.8 (44.0)*	1.0 (0.9)*	44.0 (44.3)*

[1] From Maiolino and Rieke (1995)
[2] From DSR2012
$*$ In parenthesis are galaxies in our sample in common with DSR2012.

We also compared the luminosity distance of our sample with those of the 84 galaxies in DSR2012. They selected Seyfert galaxies in the RSA sample with *Spitzer*/IRS observations of the 11.3 μm PAH feature. We used, as DSR2012, the luminosity distance obtained from the Nasa Extragalactic Database (NED[2]) using the corrected redshift to the reference frame defined by the Virgo cluster, the Great Attractor and the Shapley supercluster. The right top panel of Fig. 4.1 shows the luminosity distance distributions for the 84 galaxies in DSR2012 and the 33 galaxies of our sample (median luminosity distance of 30 Mpc). There are 10 Seyfert galaxies in our sample not in DSR2012 selection but in the RSA catalogue. Again, from Fig. 4.1 and a KS-test (p = 0.87) our sample is not statistically significantly different in terms of the luminosity distance.

Since the main goal of this Chapter is to select galaxies with evidence of strong contribution of the AGN at 70 μm emission, in Section 4.4.4 we will compare the nuclear SFR from MIR spectroscopy and *Herschel* 70 μm photometry. We therefore compared the nuclear SFR values obtained by DSR2012 for all their sample and the 23 galaxies in common with our sample. The bottom left panel of Fig. 4.1 shows the nuclear SFR distribution in DSR2012 and our sample with DSR2012 SFR values (median of 0.32 $M_\odot$ yr^{-1}). A KS-test shows that both samples are not statistically different in terms of the SFR (p = 0.42).

We finally compared the AGN bolometric luminosity distributions for the galaxies in DSR2012 and our galaxies with their values. This comparison is shown in the right bottom panel of Fig. 4.1. Clearly, our sample only includes the most luminous AGN $L_{bol} > 10^{43}$ erg s^{-1} when compared to the DSR2012 RSA sample. We find a p value for the KS-test of p = 0.03 when comparing with the galaxies in common and p = 0.05 when comparing with all our sample. This is because in general low-luminosity AGN are not bright in the MIR and thus few meet our requirement of having high angular resolution MIR spectroscopy obtained from the ground (see Alonso-Herrero et al. 2016a, and also Chapter 5). Even in the MIR the low-luminosity AGN do not dominate the emission at least in the 40% of the cases (González-Martín et al. 2015). Table 4.2 summarizes the statistics of the above comparisons.

[2]http://ned.ipac.caltech.edu/

4.3 *Herschel* observations

In this section we describe the process of obtaining the PACS and SPIRE images from the *Herschel* archive, the data reduction and the aperture photometry. Fore more information about the PACS and SPIRE instruments see Chapter 2.

4.3.1 Data reduction

We compiled all the PACS and SPIRE images for our 33 galaxies using the Herschel Science Data Archive (HSA)[3]. First, we processed the raw level 1 data with the Herschel interactive pipeline environment software (HIPE) version 13 (Ott 2010) to obtain the flux calibrated timelines of each bolometer. The standard HIPE pipeline corrects for instrumental effects and attaches pointing information to the timelines. Then, we combined these timelines using Scanamorphos version 24 (Roussel 2013). Scanamorphos subtracts low-frequency noise (thermal and non-thermal), masks high-frequency glitches of the data, and projects the timelines into a spatial grid. For the spatial grids, we selected a pixel size of FWHM/4 for each band. These values provide a good compromise between angular resolution and sampling (> 10 samples per pixel). We discarded mosaics at 100 μm where the galaxy reaches the edge of the image only in these band because we could not obtain reliable measurements of the background and could not obtain the integrated flux in the same aperture as the other bands. Only 22 of the 33 galaxies (67% of the sample) have observations at 100 μm after discarding these images. The list of all the observations used can be found in Table 4.3. Fig. 4.2 shows the mosaics of the galaxies in our sample observed in all PACS and SPIRE bands. The number of images used for each band is given in Table 4.4.

4.3.2 Aperture photometry

Circular aperture photometry of the galaxies was carried out using HIPE version 13. For every galaxy and every band we performed the photometry for radii of 1 kpc, and 2 kpc, as well as for the total galaxy. To determine the size in arcsec corresponding to 1 kpc and 2 kpc we took into account the luminosity distance of each galaxy. The aperture corresponding to the total galaxy was determined by visual inspection of the radial profiles in all the bands. In Table 4.7 we list the apertures used for the total photometry. We imposed that the aperture had to be the same for all the bands. In some galaxies, part of the galaxy seen in the SPIRE bands is outside the aperture used for the photometry. To avoid errors in the photometry due to the small size of the aperture, we only consider fluxes from nuclear apertures with a diameter higher than 1.5 times the angular resolution of each band. The photometric error of each image is determined by placing six apertures on the background around the source and measuring the standard deviation per pixel of the background within these apertures. The error in the

[3] http://www.cosmos.esa.int/web/herschel/science-archive

TABLE 4.3: *Herschel*/PACS and SPIRE observing programs.

Galaxy	Observation ID	Instrument	Wavelengths (μm)	PI
ESO 323-G077	1342236922	PACS	70, 160	Mushotzky R.
ESO 323-G077	1342236923	PACS	70, 160	Mushotzky R.
ESO 323-G077	1342236202	SPIRE	250, 350, 500	Mushotzky R.
IC 5063	1342216469	PACS	70, 160	Sánchez-Portal M.
IC 5063	1342216470	PACS	70, 160	Sánchez-Portal M.
IC 5063	1342216471	PACS	100, 160	Sánchez-Portal M.
IC 5063	1342216472	PACS	100, 160	Sánchez-Portal M.
IC 5063	1342206208	SPIRE	250, 350, 500	Sánchez-Portal M.
Mrk 1066	1342249288	PACS	70, 160	Alonso-Herrero A.
Mrk 1066	1342249289	PACS	70, 160	Alonso-Herrero A.
Mrk 1066	1342249286	PACS	100, 160	Alonso-Herrero A.
Mrk 1066	1342249287	PACS	100, 160	Alonso-Herrero A.
Mrk 1066	1342239823	SPIRE	250, 350, 500	Alonso-Herrero A.
NGC 1068	1342189194	PACS	70, 160	Wilson C.
NGC 1068	1342189195	PACS	70, 160	Wilson C.
NGC 1068	1342189425	SPIRE	250, 350, 500	Wilson C.
NGC 1320	1342249144	PACS	70, 160	Alonso-Herrero A.
NGC 1320	1342249145	PACS	70, 160	Alonso-Herrero A.
NGC 1320	1342249146	PACS	100, 160	Alonso-Herrero A.
NGC 1320	1342249147	PACS	100, 160	Alonso-Herrero A.
NGC 1320	1342239845	SPIRE	250, 350, 500	Alonso-Herrero A.
NGC 1365	1342183550	PACS	70, 160	Calibration
NGC 1365	1342183551	PACS	70, 160	Calibration
NGC 1365	1342183552	PACS	100, 160	Calibration
NGC 1365	1342183553	PACS	100, 160	Calibration
NGC 1365	1342201436	SPIRE	250, 350, 500	Sánchez-Portal M.
NGC 1386	1342216452	PACS	70, 160	Sánchez-Portal M.
NGC 1386	1342216453	PACS	70, 160	Sánchez-Portal M.
NGC 1386	1342216454	PACS	100, 160	Sánchez-Portal M.
NGC 1386	1342216455	PACS	100, 160	Sánchez-Portal M.
NGC 1386	1342214554	SPIRE	250, 350, 500	Sánchez-Portal M.
NGC 1808	1342204260	PACS	70, 160	Sturm E.
NGC 1808	1342204261	PACS	70, 160	Sturm E.
NGC 1808	1342204262	PACS	100, 160	Sturm E.
NGC 1808	1342204263	PACS	100, 160	Sturm E.
NGC 1808	1342203633	SPIRE	250, 350, 500	Sturm E.
NGC 2110	1342242542	PACS	70, 160	Mushotzky R.
NGC 2110	1342242543	PACS	70, 160	Mushotzky R.
NGC 2110	1342252037	PACS	100, 160	Mushotzky R.
NGC 2110	1342252038	PACS	100, 160	Mushotzky R.
NGC 2110	1342227709	SPIRE	250, 350, 500	Mushotzky R.
NGC 2273	1342243812	PACS	70, 160	Alonso-Herrero A.
NGC 2273	1342243813	PACS	70, 160	Alonso-Herrero A.
NGC 2273	1342243814	PACS	100, 160	Alonso-Herrero A.
NGC 2273	1342243815	PACS	100, 160	Alonso-Herrero A.
NGC 2273	1342240032	SPIRE	250, 350, 500	Alonso-Herrero A.
NGC 2992	1342221109	PACS	70, 160	Sánchez-Portal M.
NGC 2992	1342221110	PACS	70, 160	Sánchez-Portal M.
NGC 2992	1342221111	PACS	100, 160	Sánchez-Portal M.
NGC 2992	1342221112	PACS	100, 160	Sánchez-Portal M.
NGC 2992	1342198866	SPIRE	250, 350, 500	Sánchez-Portal M.

Notes.— The Observation ID marked with an asterisk indicates that this observation is used for the mosaic of 160 μm but not for the 100 μm.

TABLE 4.3

Galaxy	Observation ID	Instrument	Wavelengths (μm)	PI
NGC 3081	1342210628	PACS	70, 160	Sánchez-Portal M.
NGC 3081	1342210629	PACS	70, 160	Sánchez-Portal M.
NGC 3081	1342210630	PACS	100, 160	Sánchez-Portal M.
NGC 3081	1342210631	PACS	100, 160	Sánchez-Portal M.
NGC 3081	1342210523	SPIRE	250, 350, 500	Sánchez-Portal M.
NGC 3227	1342221146	PACS	70, 160	Spinoglio L.
NGC 3227	1342221147	PACS	70, 160	Spinoglio L.
NGC 3227	1342255954*	PACS	100, 160	Alonso-Herrero A.
NGC 3227	1342255955*	PACS	100, 160	Alonso-Herrero A.
NGC 3227	1342197318	SPIRE	250, 350, 500	Eales S.
NGC 3281	1342221845	PACS	70, 160	Sánchez-Portal M.
NGC 3281	1342221846	PACS	70, 160	Sánchez-Portal M.
NGC 3281	1342221847	PACS	100, 160	Sánchez-Portal M.
NGC 3281	1342221848	PACS	100, 160	Sánchez-Portal M.
NGC 3281	1342201483	SPIRE	250, 350, 500	Sánchez-Portal M.
NGC 3783	1342222503	PACS	70, 160	Sánchez-Portal M.
NGC 3783	1342222504	PACS	70, 160	Sánchez-Portal M.
NGC 3783	1342222505	PACS	100, 160	Sánchez-Portal M.
NGC 3783	1342222506	PACS	100, 160	Sánchez-Portal M.
NGC 3783	1342202198	SPIRE	250, 350, 500	Sánchez-Portal M.
NGC 4051	1342221164	PACS	70, 160	Spinoglio L.
NGC 4051	1342221165	PACS	70, 160	Spinoglio L.
NGC 4051	1342256164*	PACS	100, 160	Alonso-Herrero A.
NGC 4051	1342256165*	PACS	100, 160	Alonso-Herrero A.
NGC 4051	1342210502	SPIRE	250, 350, 500	Spinoglio L.
NGC 4151	1342188217	PACS	70, 160	Wilson C.
NGC 4151	1342188218	PACS	70, 160	Wilson C.
NGC 4151	1342255503*	PACS	100, 160	Alonso-Herrero A.
NGC 4151	1342255504*	PACS	100, 160	Alonso-Herrero A.
NGC 4151	1342188588	SPIRE	250, 350, 500	Wilson C.
NGC 4253	1342235128	PACS	70, 160	Mushotzky R.
NGC 4253	1342235129	PACS	70, 160	Mushotzky R.
NGC 4253	1342248046	PACS	100, 160	Alonso-Herrero A.
NGC 4253	1342248047	PACS	100, 160	Alonso-Herrero A.
NGC 4253	1342234910	SPIRE	250, 350, 500	Mushotzky R.
NGC 4258	1342220105	PACS	70, 160	Sánchez-Portal M.
NGC 4258	1342220106	PACS	70, 160	Sánchez-Portal M.
NGC 4258	1342220108	PACS	70, 160	Sánchez-Portal M.
NGC 4258	1342220107	PACS	100, 160	Sánchez-Portal M.
NGC 4258	1342201364	SPIRE	250, 350, 500	Sánchez-Portal M.
NGC 4258	1342222664	SPIRE	250, 350, 500	Mushotzky R.
NGC 4388	1342233038	PACS	70, 160	Davies J.
NGC 4388	1342233039	PACS	70, 160	Davies J.
NGC 4388	1342248482	SPIRE	250, 350, 500	Alonso-Herrero A.
NGC 4507	1342237736	PACS	70, 160	Mushotzky R.
NGC 4507	1342237737	PACS	70, 160	Mushotzky R.
NGC 4507	1342234818	SPIRE	250, 350, 500	Mushotzky R.
NGC 4579	1342212664	PACS	70, 160	Kennicutt R.
NGC 4579	1342212666	PACS	70, 160	Kennicutt R.
NGC 4579	1342212665	PACS	100, 160	Kennicutt R.
NGC 4579	1342212667	PACS	100, 160	Kennicutt R.
NGC 4579	1342188795	SPIRE	250, 350, 500	Eales S.

TABLE 4.3

Galaxy	Observation ID	Instrument	Wavelengths (μm)	PI
NGC 4594	1342213103	PACS	70, 160	Kennicutt R.
NGC 4594	1342213105	PACS	70, 160	Kennicutt R.
NGC 4594	1342213104	PACS	100, 160	Kennicutt R.
NGC 4594	1342213106	PACS	100, 160	Kennicutt R.
NGC 4594	1342188815	SPIRE	250, 350, 500	Kennicutt R.
NGC 4725	1342198481	PACS	70, 160	Kennicutt R.
NGC 4725	1342198483	PACS	70, 160	Kennicutt R.
NGC 4725	1342198482	PACS	100, 160	Kennicutt R.
NGC 4725	1342198484	PACS	100, 160	Kennicutt R.
NGC 4725	1342188763	SPIRE	250, 350, 500	Eales S.
NGC 5135	1342237916	PACS	70, 160	Sanders D.
NGC 5135	1342237917	PACS	70, 160	Sanders D.
NGC 5135	1342237918	PACS	100, 160	Sanders D.
NGC 5135	1342237919	PACS	100, 160	Sanders D.
NGC 5135	1342202248	SPIRE	250, 350, 500	Van der Werf P.
NGC 5347	1342246878	PACS	70, 160	Alonso-Herrero A.
NGC 5347	1342246879	PACS	70, 160	Alonso-Herrero A.
NGC 5347	1342246880	PACS	100, 160	Alonso-Herrero A.
NGC 5347	1342246881	PACS	100, 160	Alonso-Herrero A.
NGC 5347	1342259455	SPIRE	250, 350, 500	Alonso-Herrero A.
NGC 5506	1342223830	PACS	70, 160	Sánchez-Portal M.
NGC 5506	1342223831	PACS	70, 160	Sánchez-Portal M.
NGC 5506	1342223832	PACS	100, 160	Sánchez-Portal M.
NGC 5506	1342223833	PACS	100, 160	Sánchez-Portal M.
NGC 5506	1342213466	SPIRE	250, 350, 500	Sánchez-Portal M.
NGC 7130	1342218550	PACS	70, 160	Spinoglio L.
NGC 7130	1342218551	PACS	70, 160	Spinoglio L.
NGC 7130	1342210527	SPIRE	250, 350, 500	Spinoglio L.
NGC 7172	1342220760	PACS	70, 160	Spinoglio L.
NGC 7172	1342220761	PACS	70, 160	Spinoglio L.
NGC 7172	1342209301	SPIRE	250, 350, 500	Spinoglio L.
NGC 7213	1342232480	PACS	70, 160	Mushotzky R.
NGC 7213	1342232481	PACS	70, 160	Mushotzky R.
NGC 7213	1342244160	SPIRE	250, 350, 500	Mushotzky R.
NGC 7465	1342237360	PACS	70, 160	Mushotzky R.
NGC 7465	1342237361	PACS	70, 160	Mushotzky R.
NGC 7465	1342237445	PACS	100, 160	Alonso-Herrero A.
NGC 7465	1342237446	PACS	100, 160	Alonso-Herrero A.
NGC 7465	1342258533	PACS	100, 160	Crocker A.
NGC 7465	1342258534	PACS	100, 160	Crocker A.
NGC 7465	1342234763	SPIRE	250, 350, 500	Mushotzky R.
NGC 7465	1342259379	SPIRE	250, 350, 500	Crocker A.
NGC 7479	1342237358	PACS	70, 160	Mushotzky R.
NGC 7479	1342237359	PACS	70, 160	Mushotzky R.
NGC 7479	1342237443	PACS	100, 160	Alonso-Herrero A.
NGC 7479	1342237444	PACS	100, 160	Alonso-Herrero A.
NGC 7479	1342234760	SPIRE	250, 350, 500	Mushotzky R.
NGC 7582	1342221132	PACS	70, 160	Spinoglio L.
NGC 7582	1342221133	PACS	70, 160	Spinoglio L.
NGC 7582	1342245180*	PACS	100, 160	Alonso-Herrero A.
NGC 7582	1342245181*	PACS	100, 160	Alonso-Herrero A.
NGC 7582	1342210529	SPIRE	250, 350, 500	Spinoglio L.

TABLE 4.4: FWHMs measured in the six FIR bands.

	FWHM (arcsec)						Number of images			FWHM (kpc)
Galaxy	70 μm	100 μm	160 μm	250 μm	350 μm	500 μm	70 μm	100 μm	160 μm	70 μm
ESO 323-G077	6.7		12.4	19.2	25.4	36.7	2	-	2	1.9
IC 5063	6.0	7.8	13.1	22.6	33.6	51.9	2	2	4	1.4
Mrk 1066	5.9	7.2	11.8	19.5	25.9	38.4	2	2	4	1.4
NGC 1068	6.6		21.3	36.1	39.9	48.0	2	-	2	0.5
NGC 1320	6.1	8.4	14.7	22.2	28.5	41.2	2	2	4	1.0
NGC 1365	10.3	11.9	17.4	23.7	29.9	39.9	2	2	4	1.1
NGC 1386	6.1	8.0	14.5	23.8	30.4	39.8	2	2	4	0.3
NGC 1808	9.4	11.2	15.3	21.3	28.3	39.8	2	2	4	0.6
NGC 2110	6.6	8.3	13.2	20.6	27.2	46.0	2	2	4	1.0
NGC 2273	6.1	7.6	12.2	20.4	27.9	40.5	2	2	4	0.8
NGC 2992	7.9	9.5	14.2	21.1	28.6	39.9	2	2	4	1.3
NGC 3081	6.2	8.1	13.3	22.9	37.6	65.1	2	2	4	1.0
NGC 3227	6.3		12.7	22.4	31.9	46.4	2	-	4	0.6
NGC 3281	5.8	7.3	11.9	19.5	26.8	39.4	2	2	4	1.3
NGC 3783	5.7	7.4	22.0	52.7	57.8	60.8	2	2	4	1.0
NGC 4051	6.0		14.7	31.2	49.3	183.6	2	-	4	0.4
NGC 4151	5.9		13.7	31.3	44.5	141.7	2	-	4	0.6
NGC 4253	5.8	7.2	11.9	19.7	28.3	66.0	2	2	4	1.7
NGC 4258	49.9	71.4	71.3	90.8	73.3	97.7	3	1	4	1.9
NGC 4388	6.9		15.7	26.6	36.4	51.8	2	-	2	0.6
NGC 4507	5.7		12.8	28.5	44.2	58.1	2	-	2	1.6
NGC 4579	7.0	9.3	110.6	27.4	39.6	138.5	2	2	4	0.6
NGC 4594	6.9	11.8	69.7	57.9	43.8	47.0	2	2	4	0.4
NGC 4725	10.7	24.1	22.6	73.0	87.6	308.8	2	2	4	1.4
NGC 5135	6.8	8.1	12.3	19.7	26.3	40.6	2	2	4	1.9
NGC 5347	5.6	7.4	12.7	25.6	43.9	66.3	2	2	4	1.1
NGC 5506	6.0	7.4	12.0	20.2	27.4	42.8	2	2	4	0.9
NGC 7130	5.8		12.9	20.8	27.6	39.7	2	-	2	1.9
NGC 7172	7.1		13.4	20.8	27.3	41.2	2	-	2	1.3
NGC 7213	6.5		20.1	53.0	61.4	60.3	2	-	2	0.8
NGC 7465	7.3	9.2	14.1	22.1	30.0	47.2	2	4	6	1.0
NGC 7479	5.6	7.3	12.3	21.6	32.3	47.9	2	2	4	0.9
NGC 7582	6.6		12.3	19.8	26.7	42.6	2	-	4	0.7

Notes.— All the galaxies have one image at the SPIRE bands except NGC 4258 and NGC 7465, which have two images.

flux was then computed by multiplying the standard deviation per pixel by the number of pixels of the aperture.

We measured the FWHM for each galaxy at each band using Moffat with the Image Reduction and Analysis Facility (IRAF[4]). We list in Table 4.4 the measured FWHM in all six *Herschel* bands. We then applied an aperture correction using HIPE to the fluxes of those galaxies that are point sources and quasi point sources. We did not apply an aperture correction to the extended sources. We consider that a source is quasi point-like at one particular band (although it may have extended emission) when the measured FWHM (see Table 4.4) is less than the FWHM of the instrument plus the number of arcseconds in one pixel. For a typical galaxy in our sample at 30 Mpc, the aperture correction at 70 μm is 1.48 and 1.22 for photometry radio of 1 and 2 kpc, respectively. For sources that are quasi point-like

[4]IRAF is distributed by the National Optical Astronomy Observatory, which is operated by the Association of Universities for Research in Astronomy (AURA), Ibc., under cooperative agreement with the National Science Foundation.

TABLE 4.5: Aperture photometry for r = 1 kpc.

Galaxy	radius (arcsec)	Flux 70 μm (Jy)	Flux 100 μm (Jy)	Flux 160 μm (Jy)	Flux 250 μm (Jy)	Flux 350 μm (Jy)	Flux 500 μm (Jy)
ESO 323-G077	3.43						
IC 5063	4.13						
Mrk 1066	4.21	12±1					
NGC 1068	14.32	164±16		88±9	28±3		
NGC 1320	5.81	1.8±0.2	2.0±0.2				
NGC 1365	9.59	63±6	81±8	87±9			
NGC 1386	19.46	6.9±0.7	9.2±0.9	7.6±0.8	3.0±0.3	1.1±0.1	
NGC 1808	16.80	107±11	121±12	102±10	33±3		
NGC 2110	6.37	4.6±0.5	5.2±0.5				
NGC 2273	7.19	7.0±0.7	7.9±0.8				
NGC 2992	6.05	7.1±0.7	8.5±0.9				
NGC 3081	6.03	2.2±0.2	2.4±0.2				
NGC 3227	10.01	8.3±0.8		8.5±0.9			
NGC 3281	4.61	7.0±0.7	6.9±0.7				
NGC 3783	5.71	1.8±0.2	1.4±0.1				
NGC 4051	15.99	3.5±0.4		4.1±0.4	1.3±0.1		
NGC 4151	10.16	4.9±0.5		2.0±0.2			
NGC 4253	3.36						
NGC 4258	25.85	6.5±0.6	12±1	12±1	5.2±0.5	2.0±0.2	
NGC 4388	12.13	6.8±0.7		7.1±0.7			
NGC 4507	3.46						
NGC 4579	12.13	2.7±0.3	3.8±0.4	2.2±0.2			
NGC 4594	16.24	1.2±0.1	1.7±0.2	1.7±0.2	1.0±0.1		
NGC 4725	7.64	0.23±0.02	0.34±0.03				
NGC 5135	3.57						
NGC 5347	5.13	1.1±0.1	1.2±0.1				
NGC 5506	6.88	8.8±0.9	8.3±0.8				
NGC 7130	3.00						
NGC 7172	5.49	5.8±0.6					
NGC 7213	8.28	1.4±0.1					
NGC 7465	7.26	3.7±0.4	4.5±0.5				
NGC 7479	6.37	10±1	10±1				
NGC 7582	9.38	57±6		44±4			

the unresolved fluxes are probably slightly overestimated, as we shall see in Section 4.4.1. This is due to the instrumental Point Spread Function (PSF) that causes that a fraction of the external emission of the aperture to be observed in the inner region. However, although this correction cannot be calculated, it should be within the flux error and it does not modify our results.

To obtain the final error of the fluxes we added in quadrature the photometric calibration uncertainties (10%) to the error calculated above. In Tables 4.5, 4.6 and 4.7 we provide the fluxes for all galaxies and all bands for r = 1 kpc, r = 2 kpc, and the total galaxy. We also list, for every galaxy, the size in arcsec for the aperture used. As can be seen from this table, the photometric calibration uncertainty dominates in most cases.

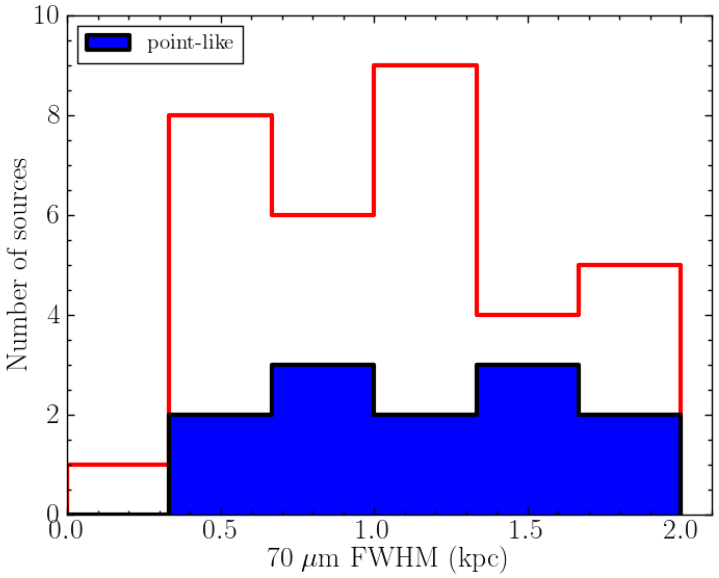

FIGURE 4.3: Distribution of the measured FWHM at 70 μm in kpc for our sample (open histogram). The filled histograms are those nuclei which appear unresolved at this wavelength, that is, with FWHM < 6 arcsec.

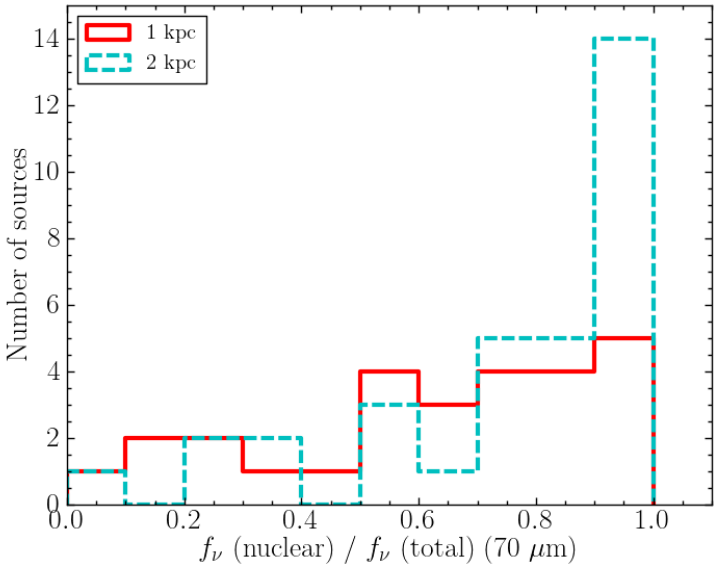

FIGURE 4.4: Distribution of the ratio between nuclear and total flux at 70 μm for $r = 1$ kpc for (27 galaxies, in red) and $r = 2$ kpc (33 galaxies, in dashed cyan).

TABLE 4.6: Aperture photometry for $r = 2$ kpc.

Galaxy	radius (arcsec)	Flux 70 μm (Jy)	Flux 100 μm (Jy)	Flux 160 μm (Jy)	Flux 250 μm (Jy)	Flux 350 μm (Jy)	Flux 500 μm (Jy)
ESO 323-G077	6.85	6.9±0.7					
IC 5063	8.27	4.5±0.5	3.6±0.4				
Mrk 1066	8.42	12±1	12±1				
NGC 1068	28.65	253±25		186±19	65±7	23±2	8.0±0.8
NGC 1320	11.62	2.2±0.2	2.8±0.3	2.3±0.2			
NGC 1365	19.19	96±10	131±13	128±13	49±5	19±2	
NGC 1386	38.92	7.1±0.7	10±1	8.8±0.9	3.7±0.4	1.5±0.1	0.50±0.05
NGC 1808	33.54	119±12	142±14	118±12	42±4	16±2	3.4±0.3
NGC 2110	12.73	5.1±0.5	6.2±0.6	4.5±0.5			
NGC 2273	14.37	7.3±0.7	8.8±0.9	6.4±0.6	2.3±0.2		
NGC 2992	12.10	8.8±0.9	11±1	8.9±0.9			
NGC 3081	12.06	2.5±0.3	2.9±0.3	2.3±0.2			
NGC 3227	20.03	9.1±0.9		11±1	4.4±0.4	1.7±0.2	
NGC 3281	9.23	7.3±0.7	7.5±0.8	5.0±0.5			
NGC 3783	11.43	2.0±0.2	1.9±0.2	1.0±0.1			
NGC 4051	31.98	4.4±0.5		6.6±0.7	3.0±0.3	1.2±0.1	0.41±0.04
NGC 4151	20.32	5.7±0.6		3.2±0.3	0.80±0.08	0.26±0.03	
NGC 4253	6.73	4.2±0.4	4.2±0.4				
NGC 4258	51.70	14±1	27±3	29±3	13±1	5.3±0.5	1.8±0.2
NGC 4388	24.27	9±1		12±1	13.8±0.4	1.4±0.1	
NGC 4507	6.92	3.7±0.4					
NGC 4579	24.27	3.4±0.4	5.7±0.6	4.4±0.4	1.8±0.2	0.69±0.07	
NGC 4594	32.48	2.3±0.3	4.4±0.4	5.2±0.5	2.9±0.3	1.5±0.2	0.74±0.07
NGC 4725	15.28	0.59±0.06	1.0±0.1	1.0±0.1	0.43±0.04		
NGC 5135	7.15	20±2	27±3				
NGC 5347	10.26	1.2±0.1	1.4±0.1	1.2±0.1			
NGC 5506	13.75	9.0±0.9	8.8±0.9	5.7±0.6	1.9±0.2		
NGC 7130	6.00	16±2					
NGC 7172	10.97	7.3±0.7		10±1			
NGC 7213	16.57	2.1±0.2		1.0±0.1	0.92±0.09		
NGC 7465	14.53	4.4±0.4	5.7±0.6	4.4±0.4	1.5±0.2		
NGC 7479	12.73	10±1	11±1	8.5±0.9			
NGC 7582	18.75	60±6		51±5	18±2		

4.4 Results

In this Section we analyse the FIR properties of our sample, such as, the unresolved 70 μm emission, the FIR colour distributions, the results from fitting the data to a grey body and the SFR nuclear and extranuclear obtained from the 70 μm data.

4.4.1 Unresolved 70 μm emission

Of the 33 galaxies in our sample, 12 nuclei (31%) appear point-like at 70 μm, i.e., have FWHM < 6 arcsec (see Table 4.4). As can be seen from Fig. 4.3, the 70 μm emission for those nuclei seen as

TABLE 4.7: Integrated photometry

Galaxy	radius (arcsec)	Flux 70 μm (Jy)	Flux 100 μm (Jy)	Flux 160 μm (Jy)	Flux 250 μm (Jy)	Flux 350 μm (Jy)	Flux 500 μm (Jy)
ESO 323-G077	50	6.8±0.8		7.1±0.8	3.2±0.3	1.3±0.1	0.43±0.04
IC 5063	60	4.7±0.5	4.6±0.5	3.7±0.4	2.1±0.2	0.9±0.1	0.30±0.04
Mrk 1066	50	12±1	13±1	8.5±0.9	3.0±0.3	1.1±0.1	0.33±0.04
NGC 1068	230	292±30		299±30	117±12	45±5	15±2
NGC 1320	50	2.4±0.3	3.4±0.4	3.0±0.4	1.5±0.2	0.58±0.07	0.20± 0.03
NGC 1365	365	143±16	216±23	220±23	102±10	44±5	16±2
NGC 1386	60	7.0±0.7	10±1	8.9±0.9	3.9±0.4	1.6±0.2	0.57±0.06
NGC 1808	250	134±14	173±18	153±16	62±7	24±3	8±1
NGC 2110	50	5.2±0.6	6.8±0.7	5.2±0.6	2.0±0.2	0.79±0.09	0.25±0.03
NGC 2273	50	7.4±0.8	10±1	7.5±0.8	3.3±0.3	1.3±0.1	0.48±0.05
NGC 2992	80	10±1	13±1	11±1	4.8±0.5	2.0±0.2	0.76±0.09
NGC 3081	60	3.0±0.4	4.1±0.6	4.6±0.5	2.3±0.2	0.90±0.09	0.31±0.04
NGC 3227	110	12±1		21±2	12±1	5.2±0.6	1.8±0.2
NGC 3281	120	7.4±0.9	8±1	7.1±0.8	2.8±0.4	1.1±0.2	0.30±0.09
NGC 3783	50	3.5±0.4	5.2±0.6	5.1±0.6	2.5±0.3	1.0±0.1	0.36±0.04
NGC 4051	170	15±4		31±4	22±2	10±1	3.9±0.4
NGC 4151	150	8±1		9±1	4.3±0.6	1.9±0.3	0.6±0.2
NGC 4253	40	4.2±0.5	4.5±0.5	3.0±0.3	1.2±0.1	0.45±0.05	0.10±0.01
NGC 4258	290	39±5	72±10	101±11	58±7	27±5	10±1
NGC 4388	130	13±2		20±2	8.1±0.8	3.3±0.4	1.2±0.2
NGC 4507	50	5.0±0.6		5.8±0.7	2.5±0.3	1.0±0.1	0.32±0.04
NGC 4579	200	11±3	26±5	35±4	20±2	9±1	3.1±0.5
NGC 4594	280	9±2	27±7	38±5	24±3	11±1	4.3±0.7
NGC 4725	450	10±4	28±7	45±5	33±4	17±2	7±1
NGC 5135	80	22±2	33±3	29±3	13±1	5.3±0.5	1.7±0.2
NGC 5347	60	1.7±0.3	2.6±0.3	3.2±0.4	1.8±0.2	0.84±0.09	0.30±0.04
NGC 5506	70	8.9±0.9	9±1	7.4±0.8	3.0±0.3	1.2±0.1	0.39±0.04
NGC 7130	60	20±2		22±2	9.2±0.9	3.6±0.4	1.1±0.1
NGC 7172	60	7.6±0.9		14±1	6.7±0.7	2.7±0.3	0.90±0.09
NGC 7213	55	4.0±0.5		7.4±0.8	4.7±0.5	1.9±0.2	0.64±0.07
NGC 7465	50	4.4±0.4	6.3±0.6	5.5±0.6	2.5±0.3	1.0±0.1	0.35±0.05
NGC 7479	80	17±2	28±3	29±3	15±2	6±0.6	2.1±0.2
NGC 7582	130	70±7		73±8	32±3	13±1	4.0±0.4

point sources originates in regions with sizes (diameters) of less than $\sim 0.5-2$ kpc, with a median size of 1.3 kpc. These values are, however, comparable to those nuclei in our sample that appear clearly extended at 70 μm (median size of 1.0 kpc). The fraction of RSA Seyfert galaxies with unresolved emission is similar to that of the *Swift*/BAT hard X-ray selected AGN sample of Mushotzky et al. (2014). They found that >35% of their sources are point-like at 70 μm with typical sizes at 70 μm of 2 kpc. However, the *Swift*/BAT AGN sample is on average at $z \sim 0.025$, compared to the average $z = 0.007$ of our sample. Therefore, it is likely that the difference in redshifts between our sample and the *Swift*/BAT sample explains the different physical sizes for the 70 μm emitting nuclear region.

To study further the unresolved 70 μm emission we estimated the contribution of the nuclear region to the total flux at 70 μm, as is shown in Fig. 4.4. The median values of the nuclear contributions to the

TABLE 4.8: Contribution of the nuclear regions of r = 1 kpc and 2 kpc to the total flux at 70 μm in RSA Seyferts

Quantity	Number	Mean	σ	Median
f_ν(r=1kpc)/f_ν(total)	27	0.63	0.28	0.68
f_ν(r=2kpc)/f_ν(total)	33	0.76	0.26	0.86

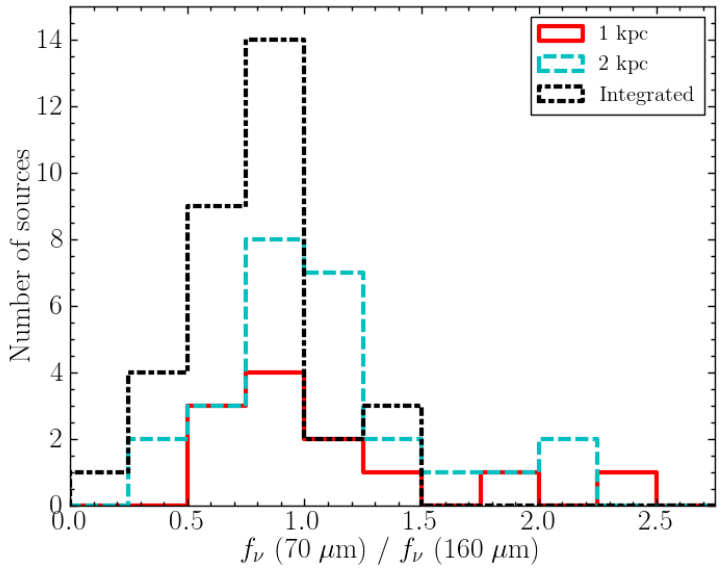

FIGURE 4.5: Distribution of the $f_\nu(70\ \mu m)/f_\nu(160\ \mu m)$ flux ratios within $r = 1$ kpc (12 galaxies, solid red line), within $r = 2$ kpc (26 galaxies, dashed cyan line), and for the integrated galaxy (33 galaxies, dash-dot black line) for the RSA Seyferts.

total flux are 0.68 and 0.86 for $r = 1$ kpc and $r = 2$ kpc, respectively (see Table 4.8).

Of the 27 galaxies with measurements of the nuclear flux in $r = 1$ kpc at 70 μm, 20 (74%) have a nuclear 1 kpc contribution to the total flux greater than 50%. Of the 33 galaxies with nuclear fluxes within $r = 2$ kpc at 70 μm, 28 (85%) have a nuclear $r = 2$ kpc contribution greater than 50%. The values obtained for 1 kpc and 2 kpc are similar because 88% of the galaxies required an aperture correction for the fluxes. Our results are in agreement with Mushotzky et al. (2014). They found that 92.5% (274 out of 296 galaxies) of their sample had a point source contribution greater than 50% of the total flux at 70 μm. They found a slightly higher percentage because they performed the photometry with an aperture of 6 arcsec for the PACS 70 μm images for all the galaxies, independently of their distance. As their galaxies are more distant than our sample, then the regions for their nuclear photometry are larger than our $r = 1$ kpc and $r = 2$ kpc nuclear regions. We note that Mushotzky et al. (2014) also performed an aperture correction to the fluxes.

TABLE 4.9: Comparison of the observed $f_\nu(70\,\mu\mathrm{m})/f_\nu(160\,\mu\mathrm{m})$ flux ratios for different samples

Region	Number	Mean	σ	Median
RSA Seyferts				
$r = 1$ kpc	12	1.13	0.52	0.98
$r = 2$ kpc	26	1.08	0.44	1.01
Integrated	33	0.78	0.30	0.80
Swift/BAT AGN				
Integrated	258	0.79	0.44	0.68
PG quasars				
Integrated	68	1.41	0.87	1.25
KINGFISH galaxies				
Integrated normal	29	0.75	0.45	0.66
Integrated AGN	31	0.51	0.27	0.43
Integrated all	60	0.63	0.39	0.50

4.4.2 FIR colours

We first start by discussing the $f_\nu(70\,\mu\mathrm{m})/f_\nu(160\,\mu\mathrm{m})$ flux ratio since we can still obtain nuclear values for a significant fraction of galaxies in our sample. It provides information about the peak of the galaxy spectral energy distribution (SED) and is a proxy for the dust temperature (Skibba et al. 2011; Meléndez et al. 2014). Fig. 4.5 shows the distributions of this ratio for $r = 1$ kpc and $r = 2$ kpc, and for the entire galaxy. As can be seen from this figure (see Table 4.9 for the statistical information), the flux ratios for the nuclear regions tend to be higher than those measured for the entire galaxies. This is in good agreement with the decreasing $f_\nu(70\,\mu\mathrm{m})/f_\nu(160\,\mu\mathrm{m})$ flux ratios with galactocentric radius found for M81 and M83 (Bendo et al. 2012). These authors suggested that this ratio tends to be more strongly influenced by star forming regions than other FIR ratios involving longer wavelengths. Therefore, the higher nuclear ratios in our sample could be due to higher star formation activity but also to higher dust temperature due to AGN heating (see further discussion in Section 4.5).

For the *Swift*/BAT AGN sample, Meléndez et al. (2014) measured a mean integrated $f_\nu(70\,\mu\mathrm{m})/f_\nu(160\,\mu\mathrm{m})$ flux ratio of 0.81 ± 0.43 for Seyfert 1s and 0.77 ± 0.47 for Seyfert 2s. These are fundamentally the same as for our sample of optically selected AGN. Meléndez et al. (2014) also compared their observed colours with predictions from three different torus models and found that the torus models cannot produce $f_\nu(70\,\mu\mathrm{m})/f_\nu(160\,\mu\mathrm{m})$ ratios of less than unity. This suggests that the 70 μm and 160 μm integrated emission is dominated by the host galaxy.

Meléndez et al. (2014) also compared the *Swift*/BAT AGN FIR colour distribution with the Key Insights on Nearby Galaxies: a Far-Infrared Survey with *Herschel* (KINGFISH) sample of nearby galaxies (Dale et al. 2012). For this comparison, they only selected the normal galaxies in the KINGFISH sample using the spectral classification of Moustakas et al. (2010), and demonstrated that the BAT AGN FIR colours are statistically indistinguishable from those of normal galaxies. As our colour

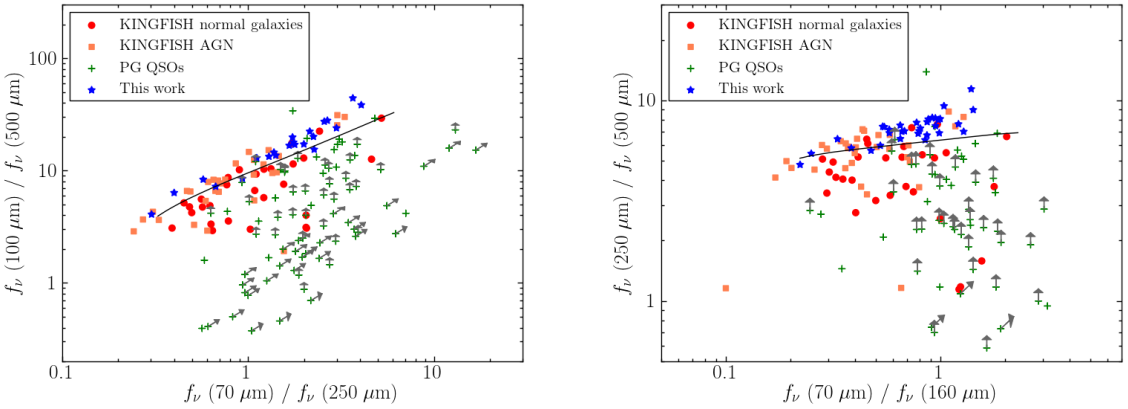

FIGURE 4.6: Colour-colour diagrams for our RSA Seyfert galaxies (blue stars), the normal galaxies from the KINGFISH sample (red circles) of Dale et al. (2012), the AGN galaxies from the KINGFISH sample (coral squares) and the PG quasar sample (green crosses) of Petric et al. (2015). The grey arrows are quasars with an upper limit to the flux. The solid lines indicate the models from Dale and Helou (2002). These models of SEDs are derived from the average global trends for a sample of normal star-forming galaxies.

distribution for the total galaxies is compatible with the BAT AGN colour distribution, the colours of our galaxies are not statistically different from those of normal galaxies ($p = 0.20$) comparing our galaxies with normal galaxies in the KINGFISH sample (see also Table 4.9).

Shimizu et al. (2016) also studied the BAT sample and found anomalous colours for 6 BAT AGN with $f_\nu(250\,\mu\text{m})/f_\nu(350\,\mu\text{m}) < 1.5$ and $f_\nu(350\,\mu\text{m})/f_\nu(500\,\mu\text{m}) < 1.5$. They suggested that this might be an excess based on the synchrotron emission from the jet or the corona from the accretion disks. We do not find these anomalous colours for our galaxies.

We also compare the other integrated FIR colours of our galaxies with the KINGFISH sample of Dale et al. (2012) (including normal galaxies and AGN) and with the 85 nearby ($z \leqslant 0.5$) quasars from the Palomar-Green (PG) sample of Petric et al. (2015). In Fig. 4.6 we show the $f_\nu(100\,\mu\text{m})/f_\nu(500\,\mu\text{m})$ vs. $f_\nu(70\,\mu\text{m})/f_\nu(250\,\mu\text{m})$ colour-color diagram (left) and $f_\nu(250\,\mu\text{m})/f_\nu(500\,\mu\text{m})$ vs. $f_\nu(70\,\mu\text{m})/f_\nu(160\,\mu\text{m})$ colour-colour diagram (right) for our galaxies, the KINGFISH sample and the PG quasar sample. Most of the PG quasars only have upper limits of the fluxes for some bands. There are 65 quasars with upper limits at 500 μm, 29 at 250 μm, 16 at 160 μm, 4 at 100 μm and 2 at 70 μm. We do not display quasars with upper limits in the two fluxes involved in a ratio. In the left panel of Fig. 4.6 we show 81 quasars of the PG sample and in the right panel we show 54 quasars. We indicate with grey arrows the quasars with upper limits.

From Fig. 4.6, we observe that the $f_\nu(250\,\mu\text{m})/f_\nu(500\,\mu\text{m})$ and $f_\nu(70\,\mu\text{m})/f_\nu(160\,\mu\text{m})$ ratios of the RSA Seyfert galaxies (7.26 ± 1.21 and 0.78 ± 0.30, respectively) are, on average, higher than those of the KINGFISH sample (4.96 ± 1.73 and 0.63 ± 0.39, respectively). A KS-test indicates that the distributions of the two flux ratios are statistically different for our sample and the KINGFISH sample. We obtain p-values of $p = 0.002$ and $p = 10^{-7}$ for the $f_\nu(70\,\mu\text{m})/f_\nu(160\,\mu\text{m})$ and $f_\nu(250\,\mu\text{m})/f_\nu(500\,\mu\text{m})$ ratios,

which indicates that they are statistically drawn from different parent samples. This may be due to the large range of morphologies and metallicities of the KINGFISH galaxies, whereas the RSA Seyfert galaxies are mostly early type (see Table 4.1). The differences in the integrated $f_\nu(70\,\mu\text{m})/f_\nu(160\,\mu\text{m})$ flux ratios are not in conflict with the comparison between the BAT AGN sample and the KINGFISH sample. Meléndez et al. (2014) compared their galaxies with the normal galaxies in the KINGFISH sample. A KS-test indicates that $f_\nu(70\,\mu\text{m})/f_\nu(160\,\mu\text{m})$ ratios of Meléndez et al. (2014) and all the KINGFISH sample are statistically different ($p = 0.003$).

4.4.3 Grey-body fitting

In this section we estimate the dust temperature by fitting the *Herschel* SED to a grey body. We use SHERPA (Doe et al. 2007), that is, the Chandra Interactive Analysis of Observations (*CIAO's*) *modelling and fitting package* (Freeman et al. 2001) module for PYTHON. We fit νF_ν versus the rest-frame wavelength, using the following expression:

$$\nu F_{\nu_{model}} = \frac{A}{\lambda^{3+\beta}(e^{\frac{hc}{\lambda kT}} - 1)} \frac{c}{\lambda} \tag{4.1}$$

where λ is the rest-frame wavelength, and the free parameters of the fitting are the amplitude (A), the dust temperature (T), and the dust emissivity index (β). To estimate the best fit to the data we first minimized the usual χ^2 statistics leaving all the parameters to vary freely:

$$\chi^2 = \sum_i^N \frac{(\nu F_{\nu_i} - \nu F_{\nu_{i,model}})^2}{\sigma_i^2} \tag{4.2}$$

where N is the number of data points, F_{ν_i} is the flux at the ith wavelength, σ_i is the uncertainty of the observed flux at the ith wavelength, and $F_{\nu_{i,model}}$ is the predicted F_ν for the ith wavelength. We perform the fits for the integrated SEDs as well as for the nuclear $r = 1$ kpc and $r = 2$ kpc SEDs. We require four or more data points for the fittings.

Fig. 4.7 shows the best-fits to the SEDs for $r = 1$ kpc, $r = 2$ kpc, and the total galaxy. The values of the best-fit β and T parameters are listed in Table 4.10. Fig. 4.8 shows the β distribution for each galaxy for $r = 1$ kpc, $r = 2$ kpc, and the total galaxy. In Fig. 4.9 we show, for each galaxy, the dust temperature obtained in the fitting of the different regions (1 kpc, 2 kpc, the total galaxy). In Table 4.11 we provide the statistical information corresponding to Figs. 4.8 and 4.9. We show in parenthesis the total values for those 14 galaxies in our sample with SED fits within $r = 2$ kpc so we can compare the results for these galaxies in 2 kpc and the total galaxy.

For galaxies with SED fits in the three physical regions, we find that the nuclear regions with $r = 1$ kpc have the highest temperatures in agreement with the spatially resolved maps of the dust temperatures of Sánchez-Portal et al. (2013) for a few nearby Seyfert galaxies. The values obtained for the dust

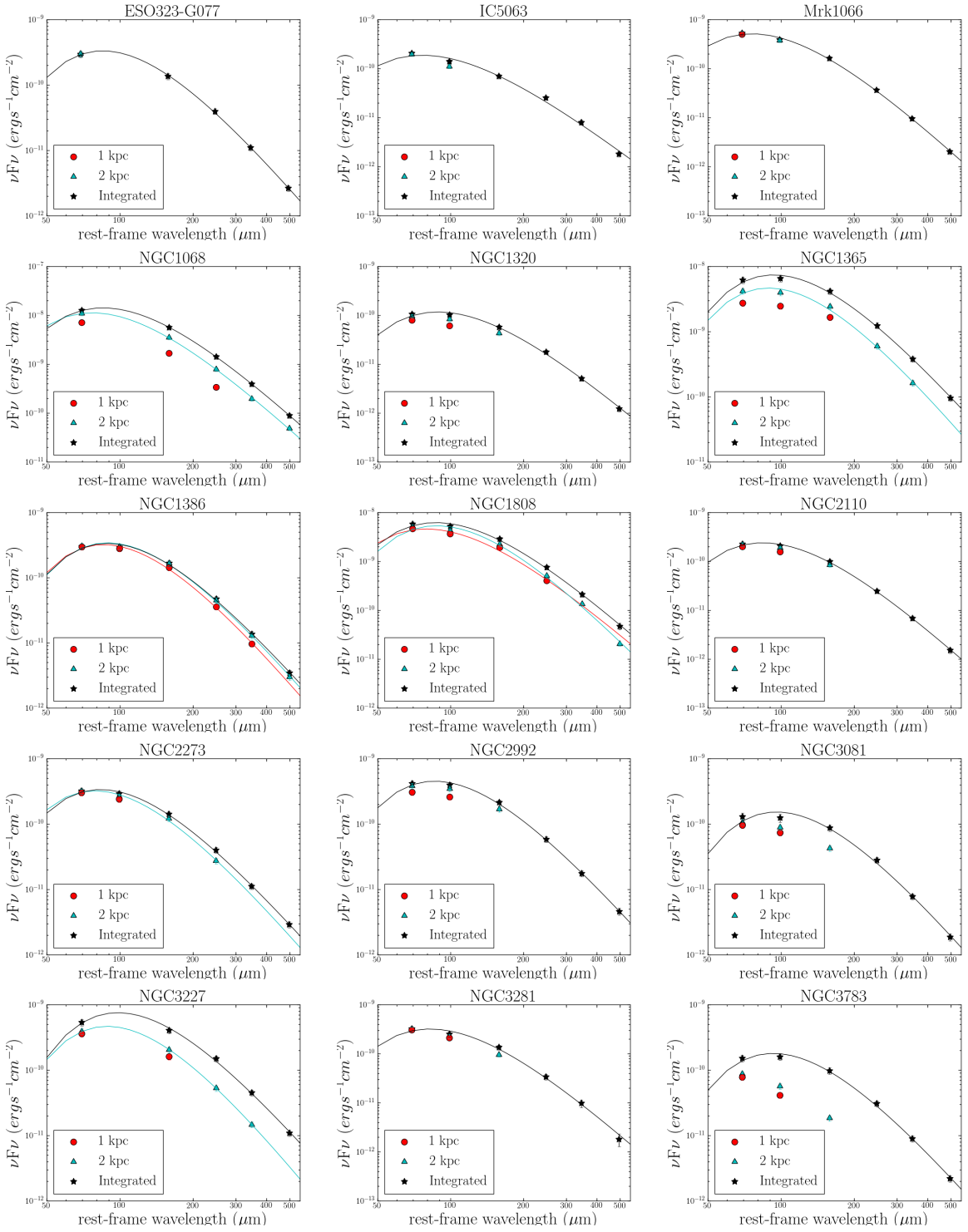

FIGURE 4.7: Best fits to the FIR SEDs of the galaxies with all the parameters left free to vary. The red circles are the fluxes for r = 1 kpc, the cyan triangles for r = 2 kpc and black stars for the total galaxy. The lines indicate the best fit in each region (only if there are 4 or more data points), with the colours as for the data points.

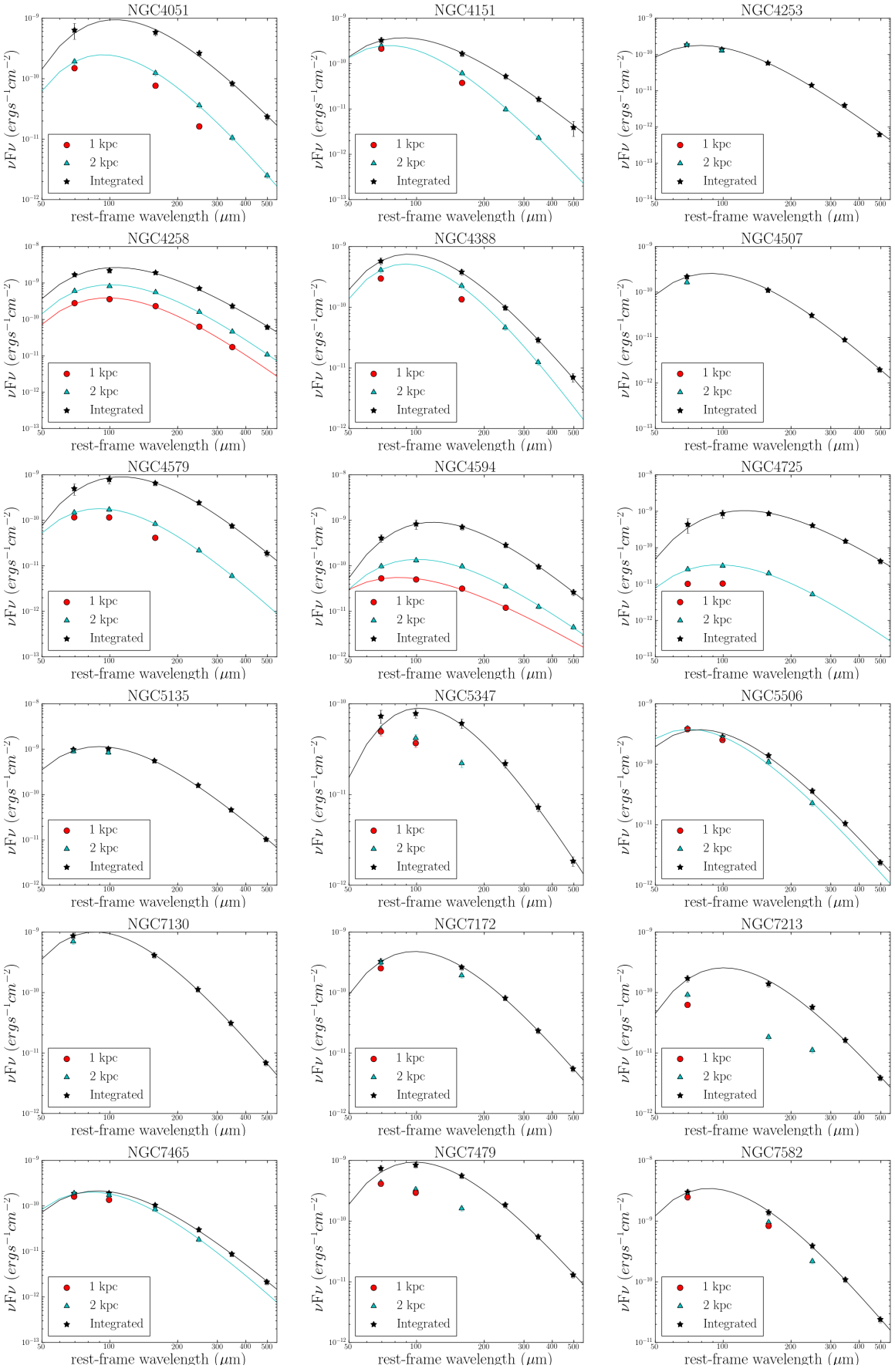
NGC4051
NGC4151
NGC4253
NGC4258
NGC4388
NGC4507
NGC4579
NGC4594
NGC4725
NGC5135
NGC5347
NGC5506
NGC7130
NGC7172
NGC7213
NGC7465
NGC7479
NGC7582
1 kpc
2 kpc
Integrated
rest-frame wavelength (μm)
$\nu F\nu$ ($ergs^{-1}cm^{-2}$)

FIGURE 4.7:

TABLE 4.10: Results from grey body fits.

	emission in 1 kpc			emission in 2 kpc			Integrated emission			Integrated emission $\beta = 2$		70 μm
Galaxy	T	β	χ^2	T	β	χ^2	T	β	χ^2	T	χ^2	excess (%)
ESO323-G077							30±2	1.7±0.2	0.21	27.1±0.6	0.90	6
IC5063							38±4	1.0±0.2	2.82	25.9±0.8	6.99	59
Mrk1066							33±3	1.8±0.2	0.56	30.8±0.7	0.56	9
NGC1068				32±3	1.9±0.2	0.39	29±2	1.9±0.2	0.01	27.8±0.6	0.11	1
NGC1320							30±3	1.5±0.2	0.88	25.3±0.6	1.75	22
NGC1365				28±3	1.7±0.3	2.04	28±2	1.5±0.2	0.77	24.2±0.5	1.84	24
NGC1386	29±3	1.8±0.3	0.79	29±2	1.7±0.2	0.71	30±2	1.5±0.2	0.65	25.4±0.5	1.59	19
NGC1808	33±5	1.5±0.5	3.79	26±2	2.4±0.2	3.04	29±3	1.7±0.2	0.95	26.6±0.6	1.05	15
NGC2110							30±3	1.8±0.2	0.29	27.8±0.7	0.40	10
NGC2273				33±5	1.6±0.5	1.10	32±3	1.5±0.2	0.38	26.6±0.6	1.72	18
NGC2992							31±3	1.4±0.2	0.44	25.9±0.6	1.81	19
NGC3081							27±2	1.7±0.3	1.65	24.0±0.6	1.69	32
NGC3227				28±3	1.9±0.4	0.03	27±2	1.6±0.2	0.85	23.5±0.5	1.83	9
NGC3281							31±4	1.7±0.3	1.26	27.9±0.9	1.21	17
NGC3783							28±2	1.5±0.2	0.88	24.4±0.5	1.60	24
NGC4051				27±2	1.8±0.2	0.06	26±3	1.3±0.3	1.15	19.4±1.1	2.16	170
NGC4151				29±3	2.7±0.4	0.57	31±4	1.3±0.4	0.13	25.8±1.0	0.96	10
NGC4253							30±2	2.0±0.2	2.12	30.6±0.8	1.60	9
NGC4258	25±2	1.9±0.3	0.75	24±2	1.9±0.2	0.52	25±2	1.4±0.3	1.07	21.5±0.5	2.18	28
NGC4388				25±2	2.5±0.4	0.52	27±2	1.9±0.3	0.07	25.8±0.7	0.11	1
NGC4507							29±2	1.8±0.2	0.18	26.8±0.7	0.36	4
NGC4579				27±2	1.9±0.3	0.06	22±2	1.8±0.3	0.28	21.0±0.7	0.31	32
NGC4594	43±9	0.1±0.5	0.57	30±2	0.9±0.2	0.40	22±2	1.6±0.3	0.06	20.2±0.6	0.47	14
NGC4725				27±3	1.7±0.5	0.93	22±3	1.4±0.4	0.22	17.9±0.8	0.72	114
NGC5135							28±2	1.7±0.2	0.65	25.8±0.5	0.92	14
NGC5347							26±3	1.4±0.3	1.55	21.5±0.5	2.36	78
NGC5506				37±6	1.5±0.5	1.53	33±3	1.5±0.2	1.12	27.9±0.7	2.11	24
NGC7130							29±2	1.9±0.2	0.16	27.5±0.6	0.24	2
NGC7172							25±2	1.9±0.2	0.12	24.3±0.5	0.21	3
NGC7213							26±2	1.6±0.2	1.80	23.0±0.5	2.12	11
NGC7465				30±4	1.8±0.5	1.52	30±2	1.5±0.2	0.45	25.6±0.6	1.28	16
NGC7479							26±2	1.6±0.2	1.17	23.3±0.5	1.52	32
NGC7582							29±2	1.8±0.2	0.26	27.2±0.6	0.37	3

emissivity indices and temperatures for the integrated values are $1.0 < \beta < 2.0$ and $21 < T < 38$ K. These values of temperatures are in agreement with those obtained by Dale et al. (2012) ($18 < T < 40$ K) from fits to the $100 - 500\,\mu$m SEDs of KINGFISH galaxies. Our β values are also in agreement with the ones of Dale et al. (2012) ($1.2 < \beta < 1.9$). Perez Garcia et al. (1998) studied 10 Seyfert galaxies observed with *ISO* and obtained that the MIR to FIR SEDs can be reproduced with three different components: warm, cold and very cold dust. Our temperature range is between the very cold component (T$\sim 10 - 20$ K) and the cold component (T$\sim 40 - 50$ K), so it may be due to dust heated by stars in the disc (cold component) and by the general interstellar radiation field of the galaxy (very cold component).

For some galaxies (e.g., NGC 3081, NGC 3783, and NGC 5347) the fit to the integrated SED does not reproduce well the $70\,\mu$m data point. We also tried fits to the integrated SEDs without this data point and found that for the majority of galaxies the reduced χ^2 values are higher with 70 μm data than without it. This suggests that in some galaxies this excess of $70\,\mu$m emission requires another component with a higher dust temperature, which could be associated with dust heated by the AGN. We will come back to this issue in Section 4.5.

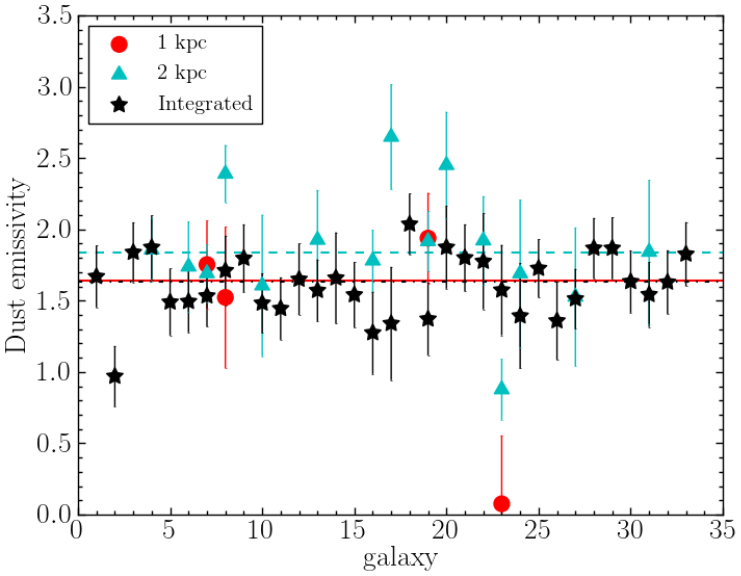

FIGURE 4.8: Distribution of the fitted dust emissivity indices β. For each galaxy, which is labelled on the horizontal axis with the number given in Table 4.1, we show β for $r = 1$ kpc (4 galaxies, red circles), $r = 2$ kpc (15 galaxies, cyan triangles), and the total galaxy (33 galaxies, black stars). The horizontal lines indicate the median values, red for $r = 1$ kpc, dashed cyan line for $r = 2$ kpc and the dash-dot black line for the total galaxy.

TABLE 4.11: Statistical information for the modified black body fits.

Quantity	Region	Number	Mean	σ	Median
Dust emissivity β	1 kpc	4	1.3	0.7	1.6
Dust emissivity β	2 kpc	15	1.9	0.4	1.8
Dust emissivity β	integrated	33 (15)	1.6 (1.6)	0.2 (0.2)	1.6 (1.5)
Reduced χ^2	1 kpc	4	1.47	1.34	0.77
Reduced χ^2	2 kpc	15	0.90	0.81	0.57
Reduced χ^2	integrated	33 (15)	0.76 (0.55)	0.66 (0.40)	0.65 (0.45)
Reduced χ^2, $\beta = 2$	integrated	33 (15)	1.37 (1.23)	1.21 (0.73)	1.28 (1.28)
Dust temperature T(K)	1 kpc	4	33	7	31
Dust temperature T(K)	2 kpc	15	29	39	28
Dust temperature T(K)	integrated	33 (15)	28 (28)	3 (3)	29 (28)
Dust temperature T(K), $\beta = 2$	integrated	33 (15)	25 (24)	3 (3)	26 (25)

Notes.— We show in parenthesis the total values for the 15 galaxies that also have SED fits within $r = 2$ kpc.

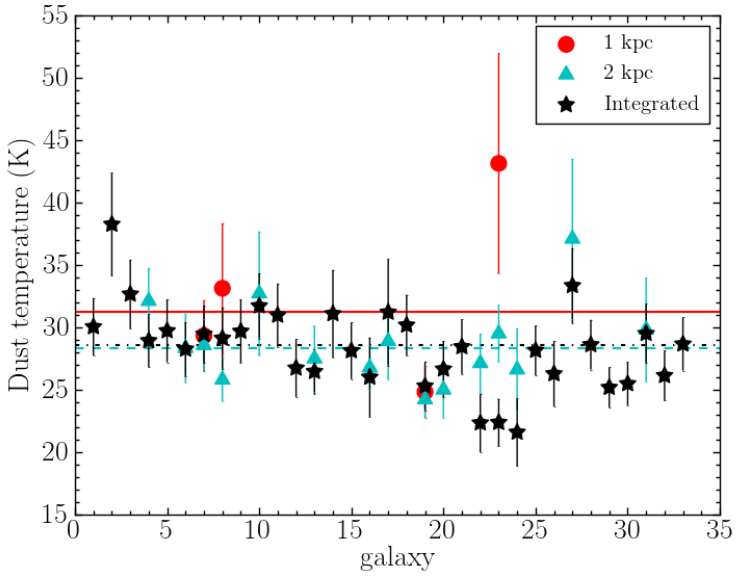

FIGURE 4.9: Dust temperature obtained through the grey body fitting for each galaxy labelled according to Table 4.1. We give the fitted temperature if available for $r = 1$ kpc (4 galaxies, red circles), $r = 2$ kpc (15 galaxies, cyan triangles), and the total galaxy (33 galaxies, black stars). The horizontal lines indicate the median values for $r = 1$ kpc (solid red line), $r = 2$ kpc (dashed cyan line) and total galaxy (dash-dot black line).

To quantify the 70 μm excess in the integrated SED from the single temperature fits, we performed new grey body fits imposing $\beta = 2$, which is the typical value for star forming galaxies (Li and Draine 2001). The statistical information about the fitted values of the dust temperature for $\beta = 2$ are listed in Table 4.11. The range of dust temperatures obtained with the fit imposing $\beta = 2$ is $18 - 31$ K, which are the normal temperatures for star forming galaxies. As expected, since β and T are anticorrelated (see e.g. Galametz et al. 2012, and also Figs. 4.8 and 4.9), for a given galaxy the fits with fixed dust emissivity $\beta = 2$ produce lower dust temperatures.

In Fig. 4.10 we show the 33 Seyfert galaxies with integrated SED fits with fixed dust emissivity $\beta = 2$. The data are shown in black, and the best fit with $\beta = 2$ is shown in blue. The red lines indicate the best fit $\pm 1\sigma$ of the free parameters. IC 5063, NGC 4051, NGC 4725, and NGC 5347 show the highest excesses at 70 μm over the single temperature fits, which puts them clearly above the 1σ uncertainty of their fits.

We quantify the excess over the fit at 70 μm as, $\frac{f_\nu(\text{obs}) - f_\nu(\text{model})}{f_\nu(\text{model})}$, where f_ν(model) is the grey body fitted with $\beta = 2$ and free dust temperature and f_ν(obs) is the observed integrated value at 70 μm. In Table 4.10 we list in the last column the 70 μm excess. The average and median 70 μm excess of the sample are 26% and 16%, respectively, although some galaxies have high excesses, such as NGC 4051 (170% excess) and NGC 4725 (114% excess). In Fig. 4.11 we show the 70 μm excess distribution. We note that all the sources have a positive excess. These 70 μm excesses might be due to a hotter dust

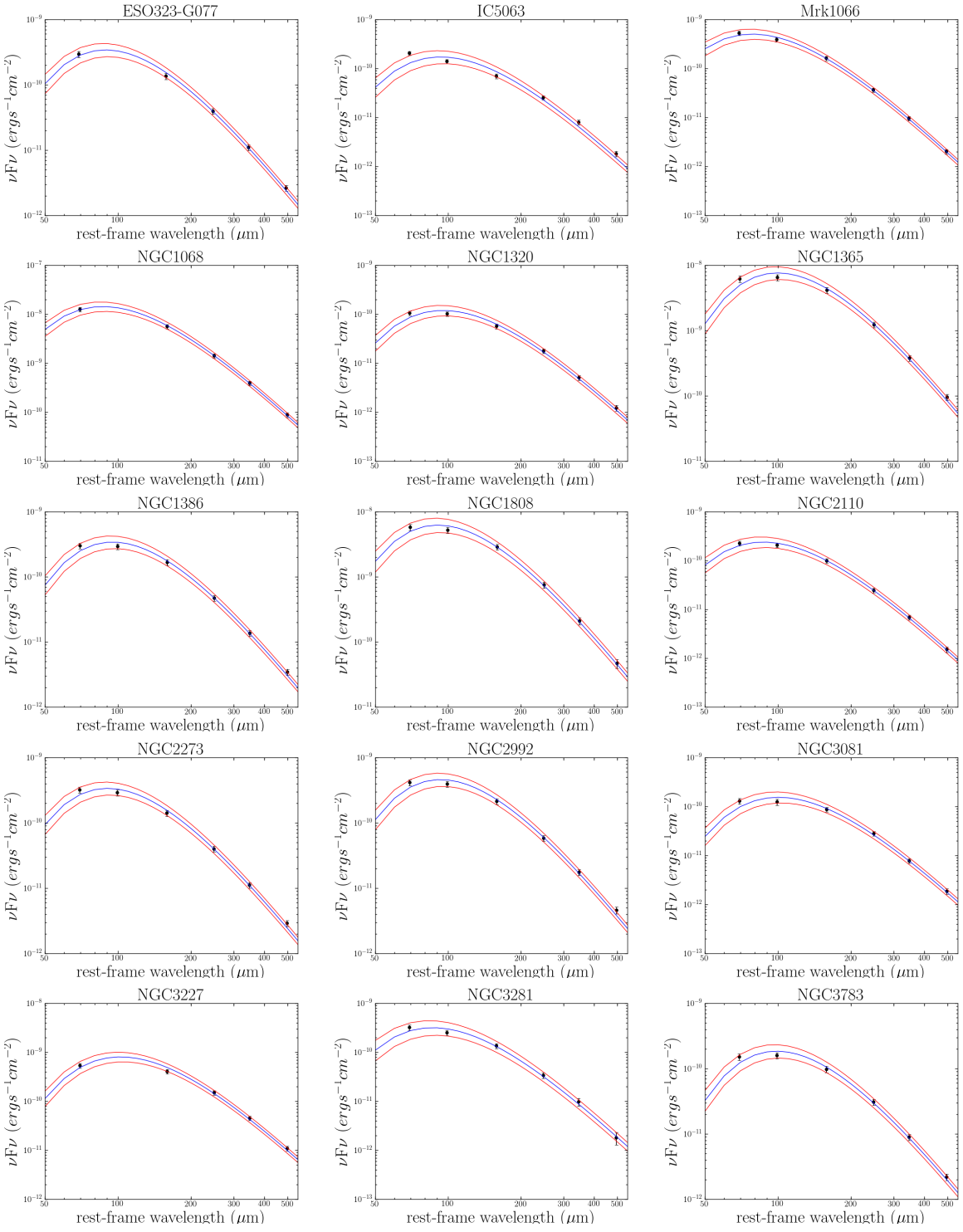

FIGURE 4.10: Fits to the integrated galaxies SEDs with $\beta = 2$. The blue line indicates the best fit whereas the red lines delineate the $\pm 1\sigma$ uncertainty of the best fit.

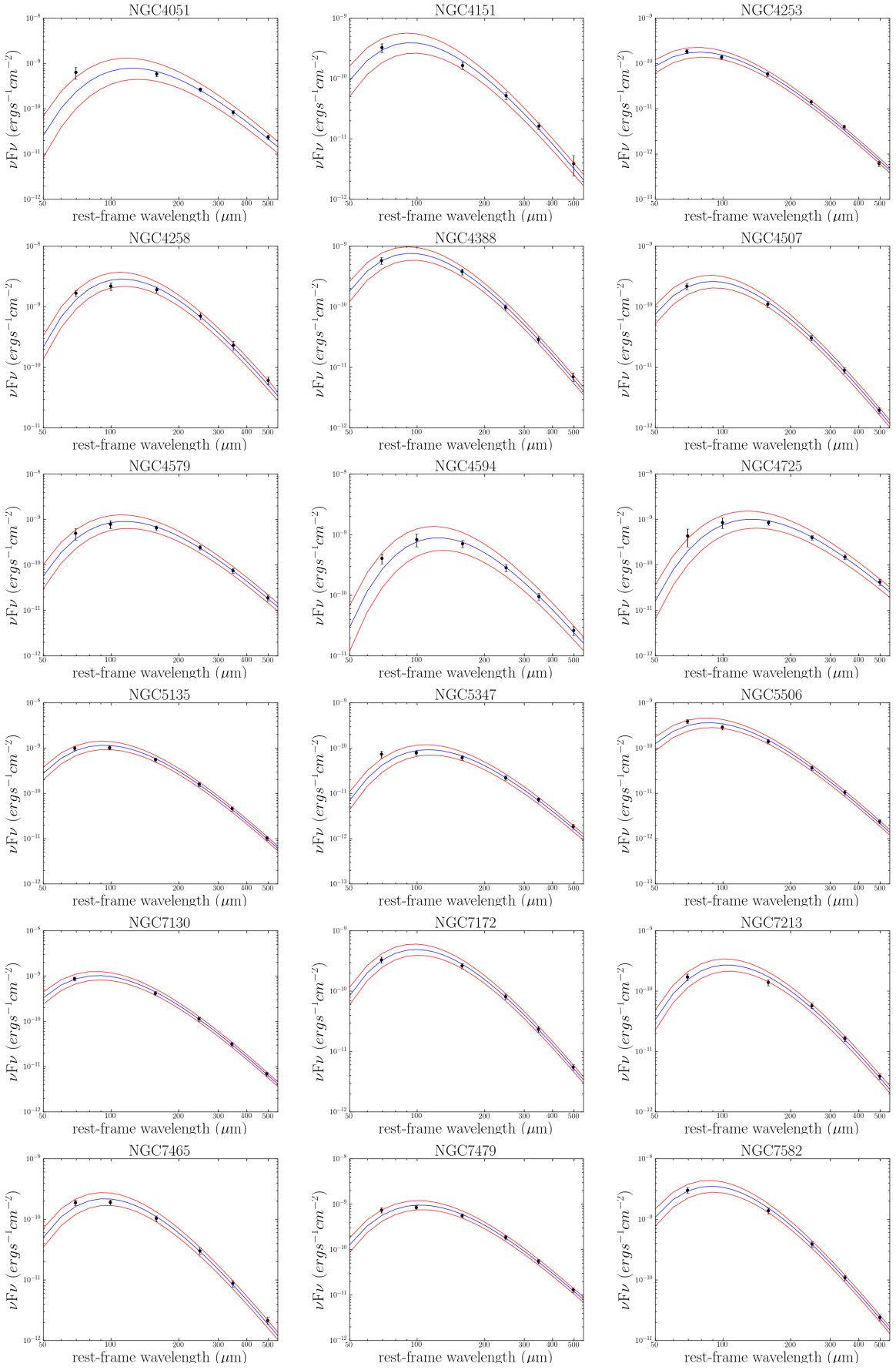
NGC4051
NGC4151
NGC4253
NGC4258
NGC4388
NGC4507
NGC4579
NGC4594
NGC4725
NGC5135
NGC5347
NGC5506
NGC7130
NGC7172
NGC7213
NGC7465
NGC7479
NGC7582
νFν (ergs⁻¹cm⁻²)
rest-frame wavelength (μm)

FIGURE 4.10

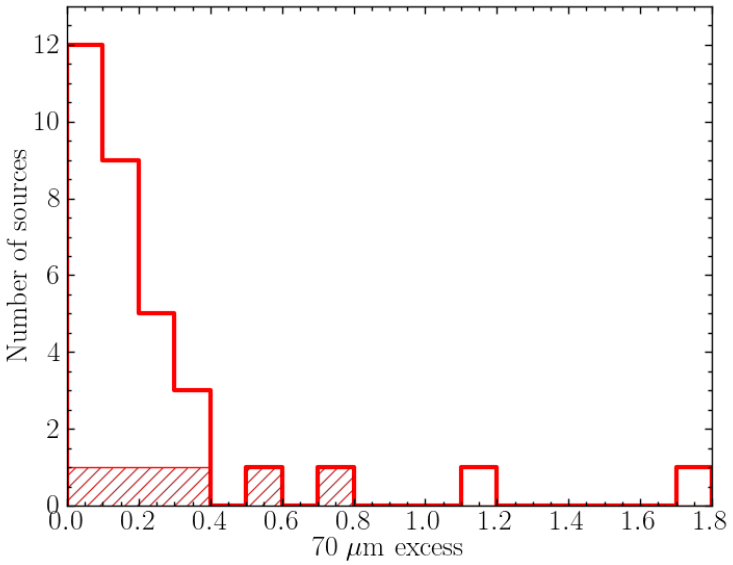

FIGURE 4.11: Distribution of the 70 μm integrated flux excesses calculated as $\frac{f_\nu(\text{obs})-f_\nu(\text{model})}{f_\nu(\text{model})}$ (see Section 4.4.3). The hatched histogram shows the final sample of Seyferts with significant nuclear 70 μm AGN emission (see Section 4.5.6).

component not necessarily related to dust heated by an AGN (Galametz et al. 2012; Alonso-Herrero et al. 2012b). We will discuss this further in Section 4.5.

4.4.4 Star Formation Rates

In this subsection we calculate the nuclear and extranuclear SFR using the 70 μm luminosity and compare them with the SFR obtained with other indicators. The goal is to identify galaxies where there is excess emission at 70 μm due to the AGN. We use the recipe from Li et al. (2013), which assumes a Kroupa (2001) IMF:

$$SFR(70\,\mu m)(M_\odot\,yr^{-1}) = C_{70\,\mu\text{m,region}} \times 10^{-43} \times L(70\,\mu m)(erg\,s^{-1})$$

The calibration coefficient $C_{70\,\mu\text{m,region}}$ is different depending on the region of the galaxy. To calculate the SFR we used the coefficients from Calzetti et al. (2010) and Li et al. (2010), which are $C_{70\,\mu\text{m,galaxy}} = 0.58$ and $C_{70\,\mu\text{m,0.5–2 kpc}} = 0.94$, respectively. The Calzetti et al. (2010) coefficient was derived from the integrated emission of galaxies and includes contributions from the diffuse component at 70 μm whereas the Li et al. (2010) measurements are local (star forming regions on scales of 0.5 – 2 kpc) and minimize the contribution of any diffuse component.

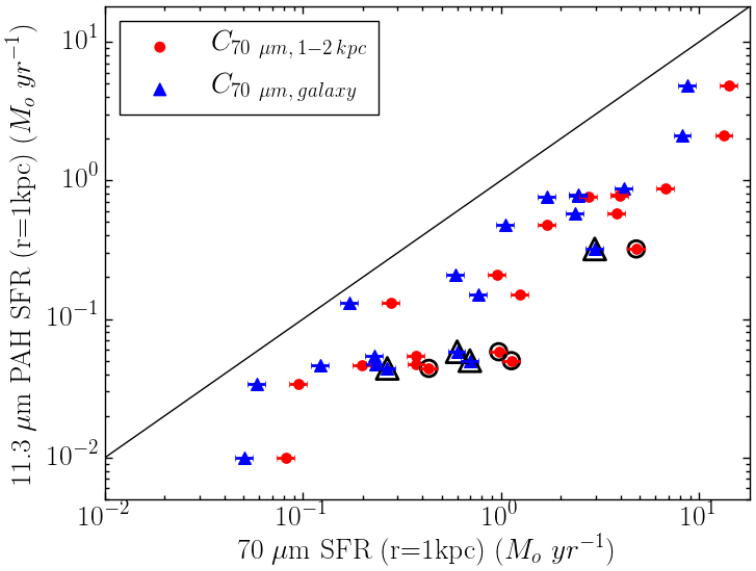

FIGURE 4.12: Nuclear SFR (r = 1 kpc) from the 70 μm luminosity versus the 11.3 μm PAH SFR (r = 1 kpc) from DSR2012. Red circles are the 70 μm-based SFR calculated with $C_{70\mu m,0.5-2\,kpc}$ = 0.94 (regions 0.5 − 2 kpc in size), whereas the blue triangles are SFR obtained with $C_{70\,\mu m,galaxy}$ = 0.58 (entire galaxy). The black line indicates the 1:1 relation. The 70 μm nuclear SFR uncertainties are derived by propagation of errors in the SFR formula, using the flux errors given in Tables 4.5, 4.6 and 4.7. The black symbols show the final selected Seyferts with significant nuclear 70 μm AGN emission (see Section 4.5.6). We note that there are two symbols for each galaxy, one for each coefficient.

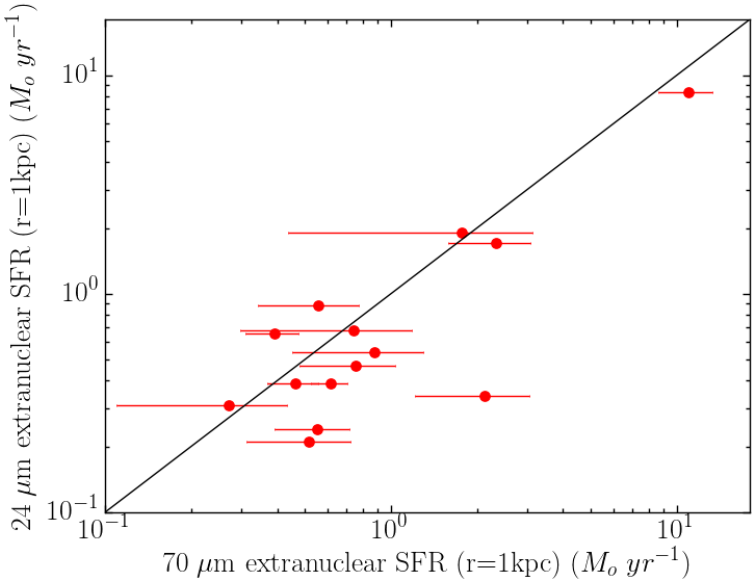

FIGURE 4.13: Extranuclear SFR (r > 1 kpc) estimated with the 70 μm-based SFR versus extranuclear (r > 1 kpc) 24 μm SFR from DSR2012. The black line indicates the 1:1 relation. The 70 μm extranuclear SFR uncertainties are calculated by propagation of errors in the SFR formula, using the flux errors given in Tables 4.5, 4.6 and 4.7.

Figs. 4.12 and 4.13 compare the values for the SFR obtained by DSR2012 with our 70 μm-based SFRs for the nuclear (r = 1 kpc) and extranuclear (r > 1 kpc) regions, respectively. We have 20 galaxies in common with DSR2012 with nuclear SFR values and 14 galaxies in common with the DSR2012 extranuclear SFR values. They obtained their nuclear SFR values from the luminosity of the 11.3 μm PAH feature and the extranuclear SFR from the luminosity of the extended 24 μm continuum emission after subtracting the contribution from the nuclear source. For the nuclear SFRs our values derived with the $C_{70\,\mu\mathrm{m,galaxy}}$ coefficient for the whole galaxy are on average four times higher than those of DSR2012, and even a factor of 7 if we used the coefficient for 0.5 – 2 kpc regions. These differences are larger than the quoted scatter of 0.14 dex of the Li et al. (2010) calibration with some galaxies showing large discrepancies. For instance, NGC 3783 has a nuclear 70 μm based SFR 13.6 times higher than the nuclear 11.3 μm PAH based SFR. For the extranuclear SFRs, the majority of the galaxies in our sample have higher SFRs using the 70 μm emission than the DSR2012 value, although the galaxies appear to be closer to the 1:1 line.

The discrepancies in SFRs found for the RSA Seyferts are similar to those for the *Swift*/BAT AGN of Mushotzky et al. (2014). They calculated the total SFR using the Calzetti et al. (2010) 70 μm calibration, that is for the entire galaxy, and compared them with the SFR obtained from the 11.3 μm PAH feature using the calibration from DSR2012. They obtained a discrepancy of a factor of 3 between the two SFR. Petric et al. (2015) also found that the integrated galaxy SFRs of a sample of PG quasars obtained from the 11.3 μm PAH feature were on average 3 times lower than the SFR estimated from the 40 – 500 μm emission.

All the differences in SFR described above could be explained if the carriers of the 11.3 μm PAH feature were being destroyed by the AGN radiation field, if there were aperture correction issues and/or if there were systematics in the calibrations. DSR2012 argued that SFR estimates using the 11.3 μm PAH feature appear to be robust to the effects of AGN and shock processing based on the good correlation with the [Ne II]12.8 μm line on kpc scales. Additionally Esquej et al. (2014) showed that even on smaller physical nuclear scales of nearby Seyferts there is no strong evidence for destruction of the 11.3 μm PAH carriers. The SFR differences do not seem to be due to the aperture corrections applied because all three works (DSR2012, Mushotzky et al. 2014 and Petric et al. 2015) also applied aperture corrections to their fluxes.

4.5 Identifying galaxies with significant 70 μm emission due to AGN heated dust

As the goal of this work is to select galaxies whose 70 μm emission is mostly due to dust heated by the AGN, in this section we put forward four different criteria to identify this type of galaxies. We also

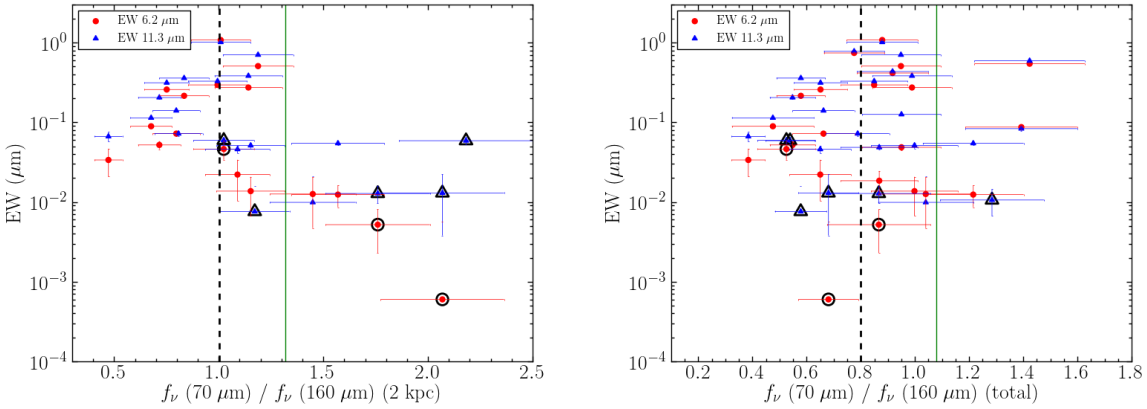

FIGURE 4.14: Relation between the $f_\nu(70\,\mu\text{m})/f_\nu(160\,\mu\text{m})$ flux ratio and the EW of the 6.2 μm (red circles) and 11.3 μm (blue triangles) PAH features as measured from *Spitzer*/IRS spectra. The left panel shows the relation for $r = 2$ kpc and the right panel for the total galaxy. The dashed black line indicates the median of each sample and the green line the median plus 1.4826 × M.A.D. The black symbols show the final selected Seyferts with significant nuclear 70 μm AGN emission (see Section 4.5.6).

compare them with other results in the literature and propose candidate RSA galaxies with significant nuclear 70 μm AGN emission.

4.5.1 Elevated $f_\nu(70\,\mu\text{m})/f_\nu(160\,\mu\text{m})$ flux ratios

If the $f_\nu(70\,\mu\text{m})/f_\nu(160\,\mu\text{m})$ flux ratios are higher than the typical values for star forming galaxies, this might indicate that part of the nuclear 70 μm emission is due to the dust heated by the AGN instead of star formation. To select the galaxies with an elevated $f_\nu(70\,\mu\text{m})/f_\nu(160\,\mu\text{m})$ flux ratio we choose all the galaxies with a value higher than the median plus 1.4826 × M.A.D, where the M.A.D (absolute median deviation) is calculated as the median of the absolute deviations from the data median, M.A.D. = median($|x_i - \text{median}_{\text{data}}|$). We do this for the $r = 1$ kpc, $r = 2$ kpc, and integrated flux ratios using the statistics in Table 4.9, each one with its own value.

We select 9 galaxies with this criterion (see Table 4.12). We note that the 2 galaxies with high $f_\nu(70\,\mu\text{m})/f_\nu(160\,\mu\text{m})$ flux ratios within $r = 1$ kpc also show it within $r = 2$ kpc. All the galaxies with a high flux ratio within $r = 2$ kpc have high flux ratio at $r = 1$ kpc or have no measurements within 1 kpc. The same happens with the total flux ratio, galaxies with high total flux ratio have also high 2 kpc flux ratio or have no measurement at 2 kpc. However, not all galaxies with a high nuclear flux ratio have also high total flux ratio. Only NGC 5506 is selected from the flux ratios within $r = 2$ kpc and with the total galaxy flux. The rest have extended diffuse emission at 160 μm and therefore their measured integrated flux is higher at 160 μm than at 70 μm (see Fig. 4.2 and Table 4.7).

Fig. 4.14 shows the relation between the $f_\nu(70\,\mu\text{m})/f_\nu(160\,\mu\text{m})$ flux ratio and the EW of the 6.2 and 11.3 μm PAH features measured from *Spitzer*/IRS spectra. The emission from these features is an

indicator of the presence of on-going/recent star formation activity (Peeters et al. 2004) but can be diluted by the AGN continuum, resulting in lower EW (Spoon et al. 2007; Díaz-Santos et al. 2010; Hernán-Caballero and Hatziminaoglou 2011; Esquej et al. 2014). Note that not all the galaxies in our sample have a value of the EW (see Table 4.1). There is one galaxy that satisfies the criterion for $r = 2$ kpc without EW data.

As expected, those galaxies with a high value of the $f_\nu(70\,\mu\mathrm{m})/f_\nu(160\,\mu\mathrm{m})$ have a small value of the EW of the PAH features, indicating that it is a good criterion to select galaxies with the dust heated by the AGN. We note that the size of the IRS SL slit is similar to the FWHM at 70 μm. The only discrepant galaxy is the Seyfert 2 galaxy Mrk 1066, which has a high total $f_\nu(70\,\mu\mathrm{m})/f_\nu(160\,\mu\mathrm{m})$ flux ratio, but also a high value of the EW of the PAHs. Alonso-Herrero et al. (2014) and Ramos Almeida et al. (2014a) have shown, based on high angular resolution (0.3arcsec) MIR spectroscopy, that this galaxy has a strong nuclear starburst including the central $\sim$ 60 pc region. This would explain the elevated FIR colours of this galaxy. However, as can be seen from Fig. 4.14, not all galaxies with low PAH EWs features satisfy this criterion. Since the PAH features probe mostly the emission from O and B stars (Peeters et al. 2004), it is possible that some galaxies in our sample have most of their FIR emission mainly due to heating from older stars (see e.g. Li et al. 2010) explaining why they do not have bright PAH emission but still have normal FIR colours. Alternatively for these galaxies the torus emission might dominate in the MIR but it decays rapidly in the FIR (see Mullaney et al. 2011).

4.5.2 Dust temperature gradient higher than typical star forming galaxies

If the nuclear dust temperature is higher than those typical of star forming galaxies, this may indicate that the nuclear dust is not only heated by star forming but also by the AGN. However, because star-forming galaxies show a range of dust temperatures (Dale et al. 2012), for a given galaxy we compare the nuclear ($r = 1$ kpc and $r = 2$ kpc) temperatures to the dust temperature fitted for entire galaxy.

To select the galaxies with an elevated dust temperature gradient we use as criterion the ratio between the nuclear temperature and the total temperature for each galaxy. We select all the galaxies with a value higher than the median plus 1.4826 $\times$ M.A.D for our sample of galaxies. For this criterion we can use 15 galaxies, which are the galaxies with at least four data points to fit the $r = 2$ kpc SEDs. These 15 galaxies have similar mean integrated dust temperatures to those of the other RSA Seyfers (see Table 4.11). With this criterion we select 3 galaxies with higher dust temperature gradient than the typical in our sample. These are NGC 4579, NGC 4594, and NGC 4725.

4.5.3 Excess 70 μm emission with respect to the fit of the FIR SEDs with a grey body

The 70 μm excess with respect to the fit of the FIR SEDs with a grey body with $\beta = 2$ could in principle indicate that this emission is not only due to star formation but that there is some contribution from the

TABLE 4.12: Summary of criteria to select galaxies with a significant AGN contribution at 70 μm.

Galaxy	#1			#2		#3	#4	
	$f_\nu(70\,\mu\text{m})/f_\nu(160\,\mu\text{m})$			$T_{\text{region}}/T_{\text{Integrated}}$		70 μm	$\text{SFR}_{70\mu\text{m}}/\text{SFR}_{\text{D-S}}$	criteria
	$r = 1$ kpc	$r = 2$ kpc	Integrated	$r = 1$ kpc	$r = 2$ kpc	excess	$r = 1$ kpc	
ESO 323-G077	-	-	x	-	-	x	-	0/2
IC 5063	-	-	✓	-	-	✓	-	2/2
Mrk 1066	-	-	✓	-	-	x	-	1/2
NGC 1068	✓	✓	x	-	x	x	-	1/3
NGC 1320	-	x	x	-	-	x	-	0/2
NGC 1365	x	x	x	-	x	x	x	0/4
NGC 1386	x	x	x	x	x	x	x	0/4
NGC 1808	x	x	x	x	x	x	-	0/3
NGC 2110	-	x	x	-	-	x	-	0/2
NGC 2273	-	x	x	-	x	x	x	0/4
NGC 2992	-	x	x	-	-	x	x	0/3
NGC 3081	-	x	x	-	-	✓	x	1/3
NGC 3227	x	x	x	-	x	x	x	0/4
NGC 3281	-	✓	x	-	-	x	x	1/3
NGC 3783	-	✓	x	-	-	x	✓	2/3
NGC 4051	x	x	x	-	x	✓	x	1/4
NGC 4151	✓	✓	x	-	x	x	✓	2/4
NGC 4253	-	-	✓	-	-	x	-	1/2
NGC 4258	x	x	x	x	x	x	x	0/4
NGC 4388	-	x	x	-	x	x	x	0/4
NGC 4507	-	-	x	-	-	x	-	0/2
NGC 4579	x	x	x	-	✓	✓	x	2/4
NGC 4594	x	x	x	✓	✓	x	x	1/4
NGC 4725	-	x	x	-	✓	✓	x	2/4
NGC 5135	-	-	x	-	-	x	-	0/2
NGC 5347	-	x	x	-	-	✓	-	1/2
NGC 5506	-	✓	✓	-	x	x	x	1/4
NGC 7130	-	-	x	-	-	x	-	0/2
NGC 7172	-	x	x	-	-	x	x	0/3
NGC 7213	-	✓	x	-	-	x	✓	2/3
NGC 7465	-	x	x	-	x	x	-	0/3
NGC 7479	-	x	x	-	-	✓	✓	2/3
NGC 7582	x	x	x	-	-	x	x	0/3

Notes.— In bold are marked galaxies satisfying at least half of the conditions.

AGN. We select those galaxies whose excess at 70 μm is higher than the median plus 1.4826 $\times$ M.A.D for our sample of galaxies (28%).

Figure 4.15 plots the 70 μm excess against the EW of the 6.2 and 11.3 μm PAH features as measured from the *Spitzer*/IRS spectra. Since those galaxies with a considerable excess also have small values of EW for both features, it is likely that this criterion selects galaxies with a contribution to the 70 μm from dust heated by the AGN. Again, as found for the FIR colours, not all galaxies with low EW of the PAH features have a 70 μm excess.

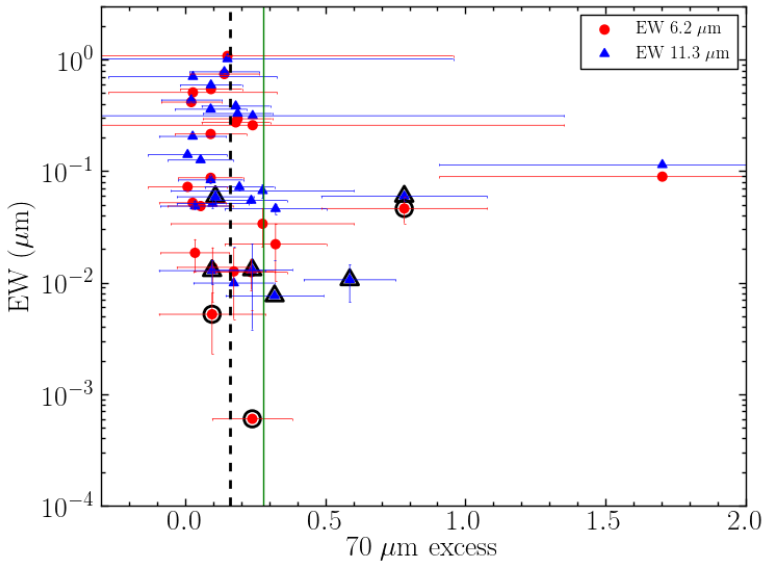

FIGURE 4.15: Relation between the 70 μm excess and the EW of the 6.2 μm (red circles) and 11.3 μm (blue triangles) PAH features as measured from *Spitzer*/IRS spectra. The dashed black line indicates the median of each sample and the green line the median plus 1.4826 × M.A.D. The black symbols show the final selected Seyferts with significant nuclear 70 μm AGN emission (see Section 4.5.6).

4.5.4 Excess of nuclear SFR obtained from 70 μm over SFR from mid-infrared indicators

As showed in Section 4.4.4, all the nuclear 70 μm-based SFR are systematically higher than those obtained by DSR2012 using the 11.3 μm PAH feature luminosity. We explained this as due to systematics in the calibrations. For this reason, we select those galaxies with the most discrepant values of SFR, i.e. all the galaxies with a value of SFR_{1kpc}/SFR_{D-S} higher than the median plus 1.4826 × M.A.D.. This could indicate that part of the nuclear 70 μm emission of these galaxies is due to the dust heated by the AGN. For this criterion we can use 20 galaxies that are the ones in common with DSR2012 and with measurements at 70 μm for r = 1 kpc. We select 4 galaxies with 70 μm-based nuclear SFR higher than expected taking into account the systematics in the calibrations, namely, NGC 3783, NGC 4151, NGC 7213, and NGC 7479. These four galaxies also satisfy some of the other criteria above.

4.5.5 Comparison with other works

The results about the nuclear 70 μm emission obtained with the above criteria are in good agreement with the detailed *Herschel* imaging studies of the infrared emission of three Seyfert galaxies, NGC 1365, NGC 2992, and NGC 3081 mentioned in Section 4.1. Alonso-Herrero et al. (2012b) and García-Bernete et al. (2015) found that the AGN emission does not dominate the 70 μm emission of NGC 1365 and NGC 2992, respectively. These two galaxies do not satisfy any of our selection criteria. On the other hand, Ramos Almeida et al. (2011b) assumed that the nuclear 70μm flux of NGC 3081 is

due to dust heated in the torus surrounding the AGN. They modelled the unresolved infrared emission of this galaxy with the Nenkova et al. (2008b) clumpy torus models and were able to reproduce the AGN bolometric luminosity. This galaxy satisfies the 70 μm excess emission with respect to the fit of the FIR SEDs with a grey body with $\beta = 2$ criterion. The reason why this galaxy does not meet the other criteria may be due to the nuclear ring of 2 kpc in diameter. Because of its distance we were not able to derive nuclear $r = 1$ kpc dust temperature and $f_\nu(70\,\mu m)/f_\nu(160\,\mu m)$ flux ratio. Therefore we were restricted to measurements within $r = 2$ kpc and the total galaxy.

We have 4 galaxies in common with the work of Mullaney et al. (2011), namely, NGC 2110, NGC 4507, NGC 5506, and IC 5063. Among these they found that the only galaxy dominated by the AGN emission at 60 μm is IC 5063 in good agreement with our results.

4.5.6 Inspection of the candidates to significant nuclear 70 μm AGN emission

Table 4.12 summarizes the selection criteria fulfilled by each galaxy. In the last column we indicate the number of criteria satisfied by each galaxy. 16 galaxies (48% of the sample) satisfy at least one of these requirements, while 10 of them fit at least half of the criteria. We found no differences between Seyfert 1 and 2 in terms of the selection requirements ($p = 0.30$ with the Fisher's test). Of the 16 galaxies that satisfy at least one criterion, 9 are Seyfert 1 and 7 Seyfert 2. We also found no differences between the galaxies that satisfy at least one criterion and the galaxies that do not satisfy any of them in terms of AGN luminosity or 70 μm luminosity.

In what follows we take a conservative approach by only considering the 10 RSA Seyferts in our sample that satisfy half or more of the criteria defined in the previous sections to select candidates with a significant AGN contribution to the nuclear 70 μm emission.

We start by discarding two galaxies, NGC 4253 and Mrk 1066, as both show 11.3 μm PAH emission in the inner 0.5 arcseconds, equivalent to physical sizes of 120 and 145 pc, respectively (Alonso-Herrero et al. 2014, 2016a) as well as high SFR within $r = 1$ kpc scales. This probably suggests that the elevated $f_\nu(70\,\mu m)/f_\nu(160\,\mu m)$ flux ratios are due to strong star formation rather than AGN dominated fluxes at 70 μm (see Ramos Almeida et al. 2014a, for a detailed discussion of Mrk 1066).

We next discuss NGC 4579 and NGC 4725, which are among the least luminous AGN in our sample of RSA Seyferts. Both are close to the low-luminosity AGN (LLAGN) limit of 10^{42} erg s^{-1} below which the dusty torus is predicted to disappear (Elitzur and Shlosman 2006). As can be seen from Table 4.10, both galaxies show a significant excess at 70 μm with respect to the $\beta = 2$ grey body fit to the integrated SED. However, if we assumed that the excess is entirely due to dust heated by the AGN, then the AGN flux at 70 μm would be similar to the measured nuclear $r = 1$ kpc flux for NGC 4579 which is resolved (FWHM = 600 pc) at this wavelength. For NGC 4725 the predicted AGN flux would be more than twenty times brighter than that arising from the nuclear (resolved) region with a 1.4 kpc size (FWHM).

We therefore conclude that the 70 μm nuclear emission of NGC 4579 and NGC 4725 at the *Herschel* resolution is not dominated by dust heated from the AGN.

We are left with six (18% of the sample) *bona fide* candidates, namely, IC 5063, NGC 3783, NGC 4151, NGC 5347, NGC 7213, and NGC 7479.

4.5.7 MIR and FIR emission of the candidates to significant nuclear 70 μm AGN emission

None of the six candidates shows 11.3 μm PAH emission in high angular resolution (0.5 − 0.7 arcsec scales) MIR spectroscopy (Alonso-Herrero et al. 2011; González-Martín et al. 2013; Esquej et al. 2014; Alonso-Herrero et al. 2016a) and all of them show low values of the nuclear SFRs (see Table 4.1). Hernán-Caballero et al. (2015) performed a spectral decomposition of 118 *Spitzer* IRS spectra of local AGN. The 6 candidates have a high AGN contribution (within the IRS slit) at $\lambda < 15\,\mu$m and an AGN 12 μm luminosity in agreement with the estimates from nuclear high angular resolution spectra (Alonso-Herrero et al. 2011; González-Martín et al. 2013). We show the selected galaxies as the hatched histogram in Fig. 4.11 and with black symbols in Figs. 4.12, 4.14, and 4.15.

We used the different criteria to estimate the range of the AGN flux at 70 μm. For each galaxy we only used the criteria satisfied (see Table 4.12). For the galaxies that have a 70 μm excess with respect to the fit of the FIR SEDs with a $\beta = 2$ grey body (see Section 4.5.3), we can estimate directly the AGN flux. For the galaxies that satisfied the elevated $f_\nu(70\,\mu\text{m})/f_\nu(160\,\mu\text{m})$ flux ratios (see Section 4.5.1), or the excess of nuclear SFR obtained from 70 μm over SFR from MIR indicators (see Section 4.5.4) we make the observed values compatible with the typical values of the sample, and the excess is assumed to be the AGN emission. For IC 5063 we obtain an AGN flux at 70 μm of 1.8 Jy (40% of the nuclear $r = 2$ kpc flux) using the two criteria. For NGC 5347 we can only calculate the contribution with the excess with respect to the $\beta = 2$ grey body fit. The AGN contribution is approximately 0.7 Jy (61% of the nuclear $r = 1$ kpc flux). For the rest of the galaxies we obtain different fluxes depending on the criterion used to estimate the 70 μm AGN flux. The ranges are 1.0 − 1.3 Jy for NGC 3783 (56 − 73% of the nuclear $r = 1$ kpc flux); 2.4 − 3.0 Jy for NGC 4151 (49 − 62% of the nuclear $r = 1$ kpc flux); 0.5 − 1.1 Jy for NGC 7213 (35 − 76% of the nuclear $r = 1$ kpc flux); and 4.1 − 5.4 Jy for NGC 7479 (43 − 57% of the nuclear $r = 1$ kpc flux). We finally note that the estimated AGN 70 μm fluxes for IC 5063 and NGC 4151 are in good agreement with the predicted torus FIR emission from the extrapolation of the fits to the unresolved NIR and MIR emission (Alonso-Herrero et al. 2011; Ichikawa et al. 2015) using clumpy torus models.

Figure 4.16 shows the *Spitzer*/IRS SL+LL spectra for these six galaxies, normalized at 30 μm. We also plot the estimated AGN 70 μm flux ranges and the average SEDs of the low luminosity ($\log(\frac{L_{2-10keV}}{\text{erg s}^{-1}}) < 42.9$) and high luminosity ($\log(\frac{L_{2-10keV}}{\text{erg s}^{-1}}) > 42.9$) AGN of Mullaney et al. (2011), all of them normalized at

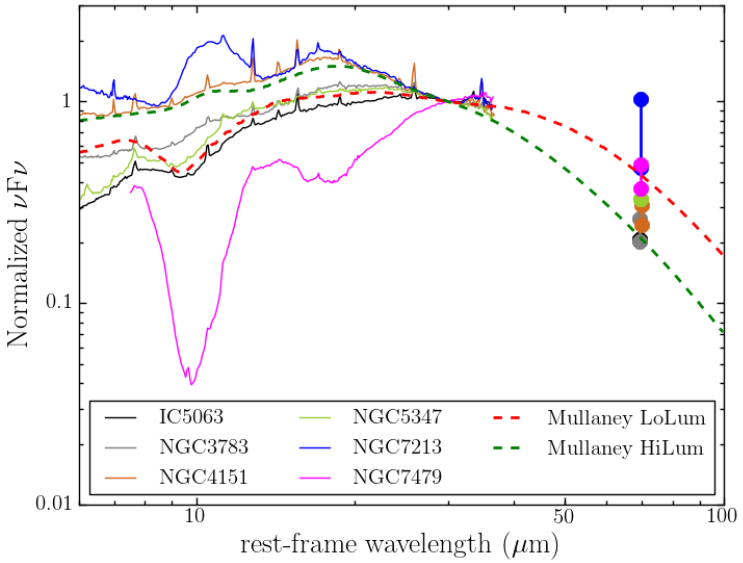

FIGURE 4.16: *Spitzer*/IRS SL+LL spectra normalized at 30 μm of the six candidates to significant nuclear 70 μm AGN emission. The estimated AGN 70 μm flux ranges (see Section 4.5.6) are shown with filled circles, normalized to the IRS flux at 30 μm for each galaxy. The red and green dashed lines indicate, respectively, the average SED of the empirically determined low luminosity ($\log(\frac{L_{2-10keV}}{\mathrm{erg\,s^{-1}}}) < 42.9$) and high luminosity ($\log(\frac{L_{2-10keV}}{\mathrm{erg\,s^{-1}}}) > 42.9$) AGN of Mullaney et al. (2011), also normalized at 30 μm.

30 μm. All our candidates have MIR and 70 μm AGN emission entirely consistent with the empirically determined low and high luminosity AGN templates of Mullaney et al. (2011), except around the 9.7 μm silicate feature range for the two most extreme features (NGC 7213 and NGC 7479).

In summary, for our sample of 33 RSA Seyferts we found a small fraction of galaxies (6/33, 18%) with a significant contribution from AGN heated dust to the nuclear 70 μm emission. This fraction is similar to the findings of Mullaney et al. (2011) for a sample of X-ray selected sample with no evidence of host emission in their MIR *Spitzer*/IRS spectra. They only identified 4 galaxies out of the 25 AGN with FIR emission dominated by the AGN. This demonstrates that our FIR method to select galaxies with significant nuclear 70 μm AGN emission for optically selected Seyferts produces similar results to their MIR based method for X-ray selected AGN.

4.6 Summary and conclusions

In this Chapter we studied the nuclear and integrated FIR (70 – 500 μm) emission of 33 nearby (median distance of 30 Mpc) Seyfert galaxies from the RSA catalogue using *Herschel*/PACS and SPIRE imaging observations. We selected these galaxies because they are nearby and have estimates of their nuclear and integrated SFR. The goal was to identify galaxies with a significant fraction of their 70 μm emission produced by dust heated by the AGN by taking advantage of the broad FIR spectral coverage and the good angular resolution at 70 μm (median 0.8 kpc FWHM for our sample). We analysed the

FIR properties of our sample, such as the unresolved 70 μm emission and the nuclear ($r = 1$ kpc and $r = 2$ kpc) and integrated FIR colours. We fitted grey-bodies to their SEDs and derived nuclear and integrated SFR. We finally put forward four criteria to select galaxies whose nuclear 70 μm emission has a significant AGN contribution. These were: (1) elevated $f_\nu(70\,\mu\mathrm{m})/f_\nu(160\,\mu\mathrm{m})$ flux ratios to the typical colours of star forming galaxies, (2) dust temperature gradient higher than typical values of star forming galaxies, (3) 70 μm excess emission with respect to the fit of the integrated FIR SEDs with a grey body with a fixed dust emissivity $\beta = 2$, and (4) excess of nuclear SFR obtained from 70 μm over SFR from MIR indicators. The main results are as follows,

- At 70 μm most RSA Seyfert galaxies (85%) in our sample have a nuclear $r = 2$ kpc contribution to the total flux greater than 50%. This is in good agreement with results for the *Swift*/BAT AGN sample of Mushotzky et al. (2014). The derived 70 μm sizes (FWHM) indicate that a significant fraction of this emission arises from regions $0.3 - 2$ kpc in size.

- The nuclear $f_\nu(70\,\mu m)/f_\nu(160\,\mu m)$ flux ratio is higher in the nuclear regions than for the entire galaxy. The integrated $f_\nu(70\,\mu m)/f_\nu(160\,\mu m)$ flux ratio distribution is statistically indistinguishable from the distribution of the *Swift*/BAT AGN sample of Meléndez et al. (2014) and from the normal galaxies of the KINGFISH sample Dale et al. (2012). This confirms previous results that the integrated FIR emission of Seyfert galaxies is in general dominated by the emission from their host galaxies rather than from the AGN.

- The grey body fits to the nuclear regions and the total galaxy SEDs show that for a given galaxy the nuclear regions ($r = 1$ kpc) have the highest temperatures, in agreement with the spatially resolved maps of the dust temperatures of nearby Seyfert and normal galaxies (see e.g. Bendo et al. 2012; Sánchez-Portal et al. 2013). The fitted dust temperatures ($21 < T < 38$ K) and dust emissivities ($1.0 < \beta < 2.0$) from the integrated SEDs are similar to those of normal galaxies.

- When fitting the integrated SEDs using $\beta = 2$, which is the typical value for star forming galaxies (Li and Draine 2001), we found that 7 Seyfert galaxies in our sample have a 70 μm excess over the fit greater than 28%. This suggests the presence of a hotter dust component, which could be associated to the presence of a nuclear starburst and/or dust heated by the AGN.

- The 70 μm nuclear SFRs derived with the $C_{70\mu\mathrm{m,galaxy}}$ coefficient are on average 4 times higher than those obtained by DSR2012 using the 11.3 μm PAH feature. Mushotzky et al. (2014) and Petric et al. (2015) also found a discrepancy of 3 between the SFR calculated through 70 μm and through 11.3 μm PAH feature.

- Taking into account the four criteria defined to select galaxies whose nuclear 70 μm emission has a significant AGN contribution, we found that 16 galaxies (48% of the sample) satisfy at least one of these criteria, whereas 10 satisfy half or more of the criteria.

- By careful examination of the 10 candidates satisfying at least half of the criteria, we selected six RSA Seyfert galaxies (18% of the initial sample) whose nuclear ($r = 1 - 2$ kpc) 70 μm emission has a significant ($\sim 40 - 70\%$) contribution from dust heated by the AGN. These galaxies are IC 5063, NGC 3783, NGC 4151, NGC 5347, NGC 7213, and NGC 7479. Four of them are Sy1 and 2 of them are Sy2. None of them show 11.3 μm PAH emission on scales of tens of parsecs from high angular resolution MIR spectroscopy or high nuclear SFR.

- Our FIR method to select galaxies whose nuclear 70 μm emission has a significant AGN contribution for optically selected Seyferts produces similar results to the Mullaney et al. (2011) MIR based method for X-ray selected AGN, in terms of the fraction of galaxies dominated by the AGN at 70 μm and the spectral shapes between 5 and 70 μm.

The criteria defined in this work provide a good way to select statistically Seyferts with significant contribution of the AGN at 70 μm using Herschel data. This study has been published in an international journal as García-González et al. (2016).

Chapter 5

A statistical investigation of clumpy torus model predictions in the MIR

5.1 Motivation

The dusty torus is the key ingredient of the unified model of AGN (see Introduction). As explained in Section 1.6, there are different kinds of torus models, and in the last years there has been a transition from smooth models to more complicated clumpy models. The dust of the torus reprocesses the optical and UV radiation from the accretion disk and re-emits it in the IR range. Therefore, if we wish to constrain the torus model parameters we have to compare predictions of clumpy torus models with high angular resolution IR observations of AGN.

Even on the physical scales probed by high angular resolution (sub-arcsecond scales) MIR spectroscopy of the nuclear region of our Seyfert galaxies, there can be emission from the host galaxy (see Hönig et al. 2010; González-Martín et al. 2013; Esquej et al. 2014; Alonso-Herrero et al. 2014, 2016a), not related to that due to dust heated by the AGN. To compare the observations with the predictions of the models it is important to disentangle the AGN MIR emission from that arising in the host galaxy. There are several methods to separate the MIR emission into the AGN component and the host galaxy component (e.g., Laurent et al. 2000; Tran et al. 2001; Lutz et al. 2004; Sajina et al. 2007; Hernán-Caballero et al. 2009; Alonso-Herrero et al. 2012a; Hernán-Caballero et al. 2015) most of them fitting the spectrum with a superposition of two or three different components.

In the last decade there have been different works comparing the MIR observations with the torus models predictions in order to constrain the torus models parameters. Hönig et al. (2010) studied 9 type 1 and 10 type 2 AGN with MIR imaging and $8 - 13\,\mu$m spectroscopy. They compared the MIR spectral index and the strength of the silicates obtained from the spectra with the predictions of their CAT3D clumpy torus models (Hönig and Kishimoto 2010). They found that the MIR spectral index

depends on the radial dust distribution power-law index of the models, while the strength of the silicates depends on the number of clouds along the equatorial line of sight and the torus inclination. They also found that the type 2 AGN are better reproduced with models with larger number of clouds than the type 1 AGN. This result is in agreement with Ramos Almeida et al. (2011a). They studied 21 AGN, using the Nenkova et al. (2008a,b) clumpy models and found that the torus of Seyfert 1 are different from those of Seyfert 2. The type 2 tori were broader, with more clouds along the equatorial line of sight and the clouds with lower optical depth than those of type 1 tori. Therefore, the covering factors for Seyfert 1 are lower than those of Seyfert 2. Alonso-Herrero et al. (2011) studied 13 nearby Seyfert galaxies and fitted the SEDs using the clumpy models of Nenkova et al. (2008a,b). They found that inclination is not the only parameter that determines the separation between type 1 and type 2 AGN, in concordance with the results of Ramos Almeida et al. (2011a) and Mateos et al. (2016). Alonso-Herrero et al. (2011) also studied the dependence of the covering factor with the AGN luminosity and noticed the importance of the extinction produced by the host galaxy. Ichikawa et al. (2015) studied 21 AGN also using the Nenkova et al. (2008a,b) clumpy models. They found that Seyfert 2 galaxies without hidden broad line region have smaller torus opening angles and larger covering factors than Seyfert 2 galaxies with hidden broad line region. They also found that the tori of Seyfert 1 galaxies have smaller opening angles, number of clouds along the equatorial line of sigh, and covering factors than those of Seyfert 2.

The main goal of the study presented in this Chapter is to make a statistical comparison of the MIR properties of Seyfert nuclei and predictions from the CAT3D clumpy torus models of Hönig and Kishimoto (2010) and new models with improved physics. We study 52 nearby Seyfert galaxies (median distance of 36 Mpc) with high angular ground-based MIR spectroscopy. We use the DEBLENDIRS tool (Hernán-Caballero et al. 2015) to disentangle the AGN component and compare it with the predictions of the models to constrain the parameters. The Chapter is organized as follows. In Section 5.2 we present our sample selection and the MIR spectroscopic observations. In Section 5.3 we describe the method used to disentangle the AGN component and the comparison with direct measurements of the spectra. Section 5.4 presents the MIR properties of AGN obtained using DEBLENDIRS, as the AGN MIR spectral index, the strength of the silicate feature, the AGN fractional contribution, and the AGN rest-frame 12 μm luminosities. In Section 5.5 we present the CAT3D clumpy torus models and compare the MIR properties of the AGN, namely, the strength of the silicate feature and the MIR spectral index with predictions of the CAT3D clumpy torus models. The conclusions are presented in Section 5.6. Throughout this Chapter we use a cosmology with $H_0 = 73\,\mathrm{km\,s^{-1}\,Mpc^{-1}}$, $\Omega_m = 0.27$ and $\Omega_\Lambda = 0.73$.

5.2 Sample and MIR ground based observations

We compiled a sample of 52 Seyfert galaxies (see Table 5.1) with existing high angular resolution MIR spectroscopy (Table 5.2) obtained on 8 − 10 m class telescopes. We chose instruments on such large

telescopes to take advantage of the angular resolutions typically achieved in the MIR, 0.3 – 0.4 arcsec. This allows us to probe the nuclear regions of Seyfert galaxies with angular resolutions almost a factor of ten better than with Spitzer/IRS. We used observations taken with four different instruments covering the N-band atmospheric window, approximately between 7.5 and 13.5 μm. The instruments are: T-ReCS, VISIR, CanariCam, and Michelle (see Chapter 2)

Ground-based MIR spectroscopic observations of galaxies are by necessity flux-limited so one can obtain sufficiently high signal-to-noise ratios (S/N) with reasonable integration times. Typically these MIR fluxes within small apertures are above 20 mJy and the acquisition of the target also requires relatively compact morphologies (see for instance Alonso-Herrero et al. 2016a for a more detailed discussion). Although not a complete sample, it is likely to be representative, at least to the median distance of the sample. For instance, it contains 80% the Seyferts in the complete volume-limited sample (distances between 10 and 40 Mpc) selected from the nine-month Swift-BAT catalogue at 14 – 195 keV (Tueller et al. 2008) analysed by García-Bernete et al. (2016). We obtained MIR spectra published in several works (mostly from Hönig et al. 2010; González-Martín et al. 2013; Esquej et al. 2014; Alonso-Herrero et al. 2016a, but see the last column of Table 5.2 for a complete list of references). The large majority of the Seyfert galaxies belongs to the Revised Shapley-Ames catalogue (RSA; Sandage and Tammann 1987) compiled by Maiolino and Rieke (1995) or the 12 Micron Active Galaxy Sample (Spinoglio et al. 1995), or both. The extended RSA catalogue (Maiolino and Rieke 1995) contains 91 relatively nearby Seyfert galaxies selected based on their integrated optical magnitude with $B_T < 13.4$. The 12 Micron Galaxy Sample contains 893 galaxies, of which 120 are classified as Seyfert. They were selected to an *IRAS* 12 μm flux limit of 0.22 Jy.

In Table 5.1 we summarize the properties of the Seyfert galaxies in our sample including their redshift, luminosity distance, morphological type, the axis ratio (b/a), and the optical activity type (see below). We also indicate in this table whether they are in the RSA catalogue or in the 12 Micron Active Galaxy Sample or both. We used the luminosity distance obtained from the NASA Extragalactic Database (NED[1]) using the corrected redshift to the reference frame defined by the Virgo cluster, the Great Attractor and the Shapley supercluster. We obtained the spectral classification of our galaxies from the literature (see last column of Table 5.1 for the references). Of the 52 galaxies, 30 are Seyfert 2, 15 are Seyfert 1-1.5 and 7 are Seyfert 1.8/1.9. Out of the full sample, 34 galaxies belong to the RSA sample and 33 to the 12 μm sample. 31 of the galaxies, all of them belonging to the RSA sample, were studied in Chapter 4.

In Fig. 5.1 we show the luminosity distance distributions for all the galaxies and the galaxies in the RSA and 12 μm samples (left panel) and for the Seyfert 2, Seyfert 1-1.5, and Seyfert 1.8/1.9 (right panel). In Table 5.3 we show the statistics for this figure. Inspection of Fig. 5.1 and a Kolmogorov-Smirnov test (KS-test) show that there are no statistically significant differences between the galaxies in the RSA sample and in the 12 μm sample. The distances of the different type Seyfert galaxies are similar,

[1] http://ned.ipac.caltech.edu/

TABLE 5.1: Summary of sample properties

Name	z	D_L (Mpc)	Morphological type	b/a	Activity type	RSA sample	12 μm sample	Ref. Activity type
Circinus	0.001448	4.2	SA(s)b?	0.4	Sy 2	YES	NO	f
ESO 103-G35	0.013286	59.1	S0?	0.4	Sy 2	NO	NO	j, k, l
ESO 323-G077	0.015014	60.2	(R)SAB0^0(rs)	0.7	Sy 1.2	YES	NO	k, l
ESO 428-G14	0.005664	23.3	SAB0^0(r) pec	0.6	Sy 2	NO	NO	l
IC 4329A	0.016054	79.8	SA0^ edge-on	0.3	Sy 1.2	NO	YES	j, k, l
IC 4518W	0.016261	79.2	Sc pec	0.5	Sy 2	NO	NO	k, l
IC 5063	0.011348	49.9	SA0^+(s)?	0.7	Sy 2	YES	YES	j, k
MGC-3-34-64	0.016541	78.8	S0/a	0.8	Sy 1.8	NO	NO	j, k
MGC-5-23-16	0.008486	35.8	S0?	0.5	Sy 2	NO	NO	j, k
MCG-6-30-15	0.007749	26.8	S?	0.6	Sy 1.2	NO	YES	j, k
Mrk 3	0.013509	58.5	S0?	0.9	Sy 2	NO	NO	j, k
Mrk 1066	0.012025	49.0	(R)SB0^+(s)	0.6	Sy 2	YES	NO	l
Mrk 1210	0.013496	58.9	S?	1.0	Sy 2	NO	NO	l
Mrk 1239	0.019927	88.9	E-S0	1.0	Sy 1.5	NO	YES	h
NGC 931	0.016652	67.5	SAbc	0.2	Sy 1.5	NO	YES	j, k
NGC 1068	0.003793	15.2	(R)SA(rs)b	0.9	Sy 2	YES	YES	k
NGC 1194	0.013596	54.5	SA0^+?	0.6	Sy 1.9	NO	YES	l
NGC 1320	0.008883	35.5	Sa? edge-on	0.3	Sy 2	YES	YES	l
NGC 1365	0.005457	21.5	SB(s)b	0.6	Sy 1.5	YES	YES	i
NGC 1386	0.002895	10.6	SB0^+(s)	0.4	Sy 2	YES	YES	f
NGC 1808	0.003319	12.3	(R)SAB(s)a	0.6	Sy 2	NO	YES	b
NGC 2110	0.007789	32.4	SAB0^-	0.8	Sy 2	YES	NO	j, k
NGC 2273	0.006138	28.7	SB(r)a?	0.8	Sy 2	YES	NO	c
NGC 2992	0.007710	34.4	Sa pec	0.3	Sy 1.9	YES	YES	l
NGC 3081	0.007976	34.5	(R)SAB0/a(r)	0.8	Sy 2	YES	NO	j, k
NGC 3094	0.008019	38.3	SB(s)a	0.7	Sy 2	NO	YES	a
NGC 3227	0.003859	20.4	SAB(s)a pec	0.7	Sy 1.5	YES	YES	j, k, l
NGC 3281	0.010674	45.0	SA(s)ab pec?	0.5	Sy 2	YES	NO	j, k, l
NGC 3783	0.009730	36.4	(R')SB(r)ab	0.9	Sy 1	YES	NO	j, k
NGC 4051	0.002336	12.9	SAB(rs)bc	0.7	Sy 1.5	YES	YES	j, k
NGC 4151	0.003319	20.0	(R')SAB(rs)ab?	0.7	Sy 1.5	YES	YES	j, k, l
NGC 4253	0.012929	61.3	(R')SB(s)a?	0.8	Sy 1.5	YES	YES	j
NGC 4258	0.001494	7.98	SAB(s)bc	0.4	Sy 1.9	YES	NO	d
NGC 4388	0.008419	17.0	SA(s)b? edge-on	0.2	Sy 2	YES	YES	j, k
NGC 4418	0.007268	34.9	(R')SAB(s)a	0.5	Sy 2	NO	YES	l
NGC 4507	0.011801	60.2	(R')SAB(rs)b	0.8	Sy 2	YES	NO	j, k
NGC 4579	0.00506	17.0	SAB(rs)bc	0.8	Sy 1.9	YES	YES	d
NGC 4593	0.009000	41.6	(R)SB(rs)b	0.7	Sy 1	YES	YES	j, k, l
NGC 5135	0.013693	58.3	SB(s)ab	0.7	Sy 2	YES	YES	l
NGC 5347	0.007789	40.2	(R')SB(rs)ab	0.8	Sy 2	YES	YES	l
NGC 5506	0.006181	30.1	Sa pec edge-on	0.2	Sy 1.9	YES	YES	j, k
NGC 5548	0.017175	80.3	(R')SA0/a(s)	0.9	Sy 1.5	YES	YES	j, k, l
NGC 5643	0.003999	14.4	SAB(rs)c	0.9	Sy 2	YES	NO	l
NGC 5995	0.025194	115	S(B)c	0.9	Sy 2	NO	YES	k
NGC 7130	0.016151	69.6	Sa pec	0.9	Sy 2	NO	YES	f
NGC 7172	0.008683	37.9	Sa pec edge-on	0.6	Sy 2	YES	YES	j, k, l
NGC 7213	0.005839	25.1	SA(s)a?	0.9	Sy 1.5	YES	YES	j, k
NGC 7465	0.006538	28.4	(R')SB0^0?(s)	0.7	Sy 2	YES	NO	e
NGC 7469	0.016317	67.9	(R')SAB(rs)ab?	0.7	Sy 1.2	YES	YES	j, k
NGC 7479	0.007942	33.9	SB(s)c	0.8	Sy 1.9	YES	YES	l
NGC 7582	0.005254	22.1	(R')SB(s)ab	0.4	Sy 2	YES	YES	j, k
NGC 7674	0.028924	120	SA(r)bc pec	0.9	Sy 2	NO	YES	g

Notes.— [a] from Asmus et al. (2014); [b] from Brightman and Nandra (2011); [c] from Contini et al. (1998); [d] from Maiolino and Rieke (1995);[e] from Malizia et al. (2012);[f] from Marinucci et al. (2012); [g] from Osterbrock and Martel (1993);[h] from Polletta et al. (1996);[i] from Schulz et al. (1999); [j] from Tueller et al. (2008); [k] from Tueller et al. (2010);[l] from Véron-Cetty and Véron (2010b)

TABLE 5.2: Summary of MIR spectroscopic observations

Name	Instrument	slit width (arcsec)	slit width (pc)	Ref
Circinus	**VISIR**	0.75	15	d
	T-ReCS	0.35	7	e, h
ESO 103-G35	T-ReCS	0.35	100	e
ESO 323-G077	VISIR	0.75	219	d
ESO 428-G14	VISIR	0.75	85	d
IC 4329A	VISIR	0.75	290	d
IC 4518W	T-ReCS	0.70	269	e, f
IC 5063	**VISIR**	0.75	181	d
	T-ReCS	0.65	157	e, j
MGC-3-34-64	VISIR	0.75	287	d
MGC-5-23-16	VISIR	0.75	130	d
MCG-6-30-15	VISIR	0.75	97	d
Mrk 3	CanariCam	0.52	147	b
Mrk 1066	CanariCam	0.52	124	b
Mrk 1210	CanariCam	0.52	148	b
Mrk 1239	VISIR	0.75	323	c
NGC 931	CanariCam	0.52	170	b
NGC 1068	VISIR	0.4	29	d
NGC 1194	CanariCam	0.52	137	b
NGC 1320	CanariCam	0.52	89	b
NGC 1365	VISIR	0.75	78	c
	T-ReCS	0.35	36	e, g
NGC 1386	T-ReCS	0.31	16	e
NGC 1808	T-ReCS	0.35	21	e, k
NGC 2110	VISIR	0.75	118	d
NGC 2273	CanariCam	0.52	75	b
NGC 2992	CanariCam	0.52	87	b
NGC 3081	T-ReCS	0.65	109	e
NGC 3094	T-ReCS	0.35	65	e, i
NGC 3227	VISIR	0.75	74	d
	CanariCam	0.52	51	b
NGC 3281	**VISIR**	0.75	164	c
	T-ReCS	0.35	76	e, l
NGC 3783	VISIR	0.75	132	d
NGC 4051	CanariCam	0.52	33	b
NGC 4151	Michelle	0.36	35	a
NGC 4253	CanariCam	0.52	155	b
NGC 4258	CanariCam	0.52	20	b
NGC 4388	CanariCam	0.52	43	b
NGC 4418	T-ReCS	0.35	59	e
NGC 4507	VISIR	0.75	219	d
NGC 4579	CanariCam	0.52	43	b
NGC 4593	VISIR	0.75	151	d
NGC 5135	T-ReCS	0.70	198	e, f
NGC 5347	CanariCam	0.52	101	b
NGC 5506	T-ReCS	0.35	51	e, i
NGC 5548	CanariCam	0.52	202	b
NGC 5643	**VISIR**	0.75	52	d
	T-ReCS	0.35	24	e
NGC 5995	VISIR	0.75	418	d
NGC 7130	T-ReCS	0.70	236	e, f
NGC 7172	T-ReCS	0.35	64	e, i
NGC 7213	VISIR	0.75	91	d
NGC 7465	CanariCam	0.52	72	b
NGC 7469	VISIR	0.75	247	d
NGC 7479	T-ReCS	0.35	58	e
NGC 7582	**VISIR**	0.75	80	d
	T-ReCS	0.70	75	e
NGC 7674	VISIR	0.75	436	d

Notes.— For galaxies with spectra in two different instruments we show in bold the best one, that is used in the results of Section 5.4 (see Section 5.3.1 for details) [a] from Alonso-Herrero et al. (2011);[b] from Alonso-Herrero et al. (2016a); [c] from Burtscher et al. (2013); [d] from Hönig et al. (2010); [e] from González-Martín et al. (2013); [f] from Díaz-Santos et al. (2010); [g] from Alonso-Herrero et al. (2012b); [h] from Roche et al. (2007); [i] from Roche et al. (2006); [j] from Young et al. (2007); [k] from Sales et al. (2013); [l] from Sales et al. (2011).

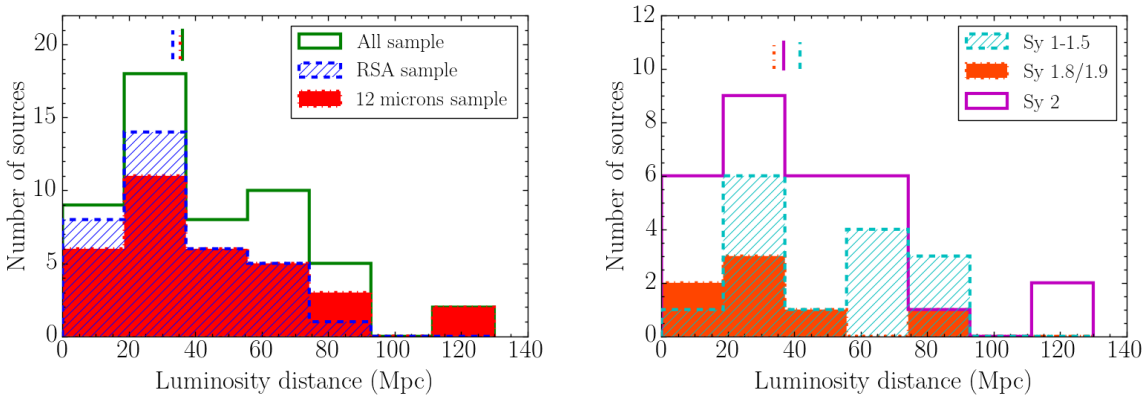

FIGURE 5.1: Left panel: distribution of the luminosity distance for all the sample (52 galaxies, in green), the galaxies in the RSA sample (34 galaxies, blue hatched histogram), and the galaxies in the 12 μm sample (33 galaxies, in filled red). The vertical lines indicate the median of the distributions. Right panel: The same for Seyfert 2 galaxies (30, in magenta), Seyfert 1-1.5 galaxies (15, cyan hatched histogram), and Seyfert 1.8/1.9 (7, filled orange).

TABLE 5.3: Statistics for Figs. 5.1 and 5.2.

	Number of galaxies	Luminosity distance (Mpc)	Slit width (pc)
All the sample	52	36.1 [17.5, 67.8]	101 [43, 219]
RSA sample	34	33.1 [15.7, 55.9]	84 [35, 176]
12 μm sample	33	35.5 [17.4, 69.4]	89 [37, 232]
Seyfert 1-1.5	15	41.6 [20.6, 76.9]	151 [40, 240]
Seyfert 1.8/1.9	7	33.9 [16.6, 55.5]	58 [42, 143]
Seyfert 2	30	36.8 [16.4, 59.5]	101 [49, 205]

Notes.— We give the median value and in parenthesis the 16% and 84% percentiles.

although the Seyfert 1-1.5 galaxies are slightly further away (median of 42 Mpc) than the Seyfert 2 galaxies (median of 37 Mpc) in our sample.

In Table 5.2 for each galaxy in the sample we summarize some of the observational details of the MIR spectroscopy, namely, the instrument, the slit width in arcsec and pc, and the reference to the published spectra. As can be seen from this table, the slit widths for the different instruments vary between 0.35 arcsec and 0.75 arcsec, which are appropriate for the the typical image quality values (FWHM) of the observations in the MIR (see e.g., Hönig et al. 2010 and Alonso-Herrero et al. 2016a). For the distances of our Seyfert galaxies, the slits probe nuclear regions between 7 and 436 pc, with a median value of 101 pc for the entire sample. As can also be seen from this table, 7 galaxies in our sample were observed with two different instruments. For those cases, in Section 5.3.1 we will discuss in detail which one is used for the analysis. Finally, we used for this work the fully reduced 1-dimensional spectra of the galaxies. We refer the reader to the original articles (see Table 5.2) for details of the observations and data reduction.

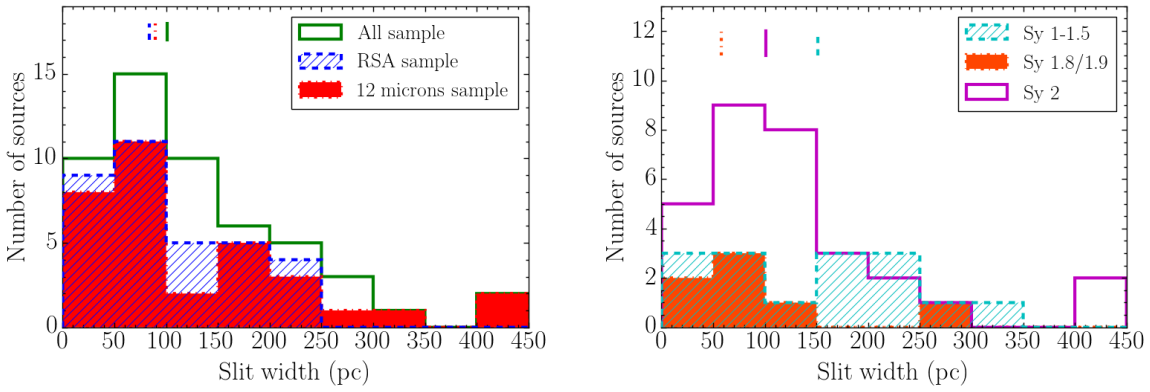

FIGURE 5.2: Left panel: distribution of the slit width (pc) for all the sample (52 galaxies, in green), the galaxies in the RSA sample (34 galaxies, in blue hatched histogram), and the galaxies in the 12 μm sample (33 galaxies, in filled red). The vertical lines indicate the median of the distributions. Right panel: The same for Seyfert 2 galaxies (30, in magenta), Seyfert 1-1.5 galaxies (15, cyan hatched histogram), and Seyfert 1.8/1.9 (7, filled orange).

In Fig. 5.2 we show the slit width (in pc) distributions for all the galaxies and the galaxies in the RSA and 12 μm samples (left panel) and for the Seyfert 2, Seyfert 1-1.5, and Seyfert 1.8/1.9 (right panel). In Table 5.3 we list the statistics for this figure. Inspection of Fig. 5.2 and a KS-test show that there are not statistically significant differences between the galaxies in the RSA sample and in the 12 μm sample. The same occurs for the Seyfert 2 and Seyfert 1-1.5. The median of the slit width is larger for the Seyfert 1-1.5 galaxies (median physical sizes of 151 pc) than the Seyfert 2 (101 pc), as expected because the former are more distant on average. However, a KS-test shows that these differences are not significant (p = 0.48). This is also the case for the comparison between the Seyfert 1-1.5 and the Seyfert 1.8/1.9 (p = 0.29). Nonetheless, we must take into account the differences in the slit width between individual objects for our analysis. A slit width covering a larger nuclear region would in principle have more contribution from emission from the host galaxy (see Section 5.4.2).

In Fig. 5.3 we show the ground-based MIR spectra, normalized at 12 μm rest-frame, for all the galaxies, divided in Seyfert 1-1.5 (top panel), Seyfert 1.8/1.9 (middle panel) and Seyfert 2 (bottom panel).

5.3 DeblendIRS decomposition

5.3.1 The method

The host galaxy may contribute a significant fraction of the MIR emission in Seyfert nuclei even at sub-arcsecond spatial resolution (see Hönig et al. 2010; González-Martín et al. 2013; Esquej et al. 2014; Alonso-Herrero et al. 2014; Asmus et al. 2014; Alonso-Herrero et al. 2016a; García-Bernete et al. 2016). Since the MIR emission from dust heated by the AGN is considered unresolved even for

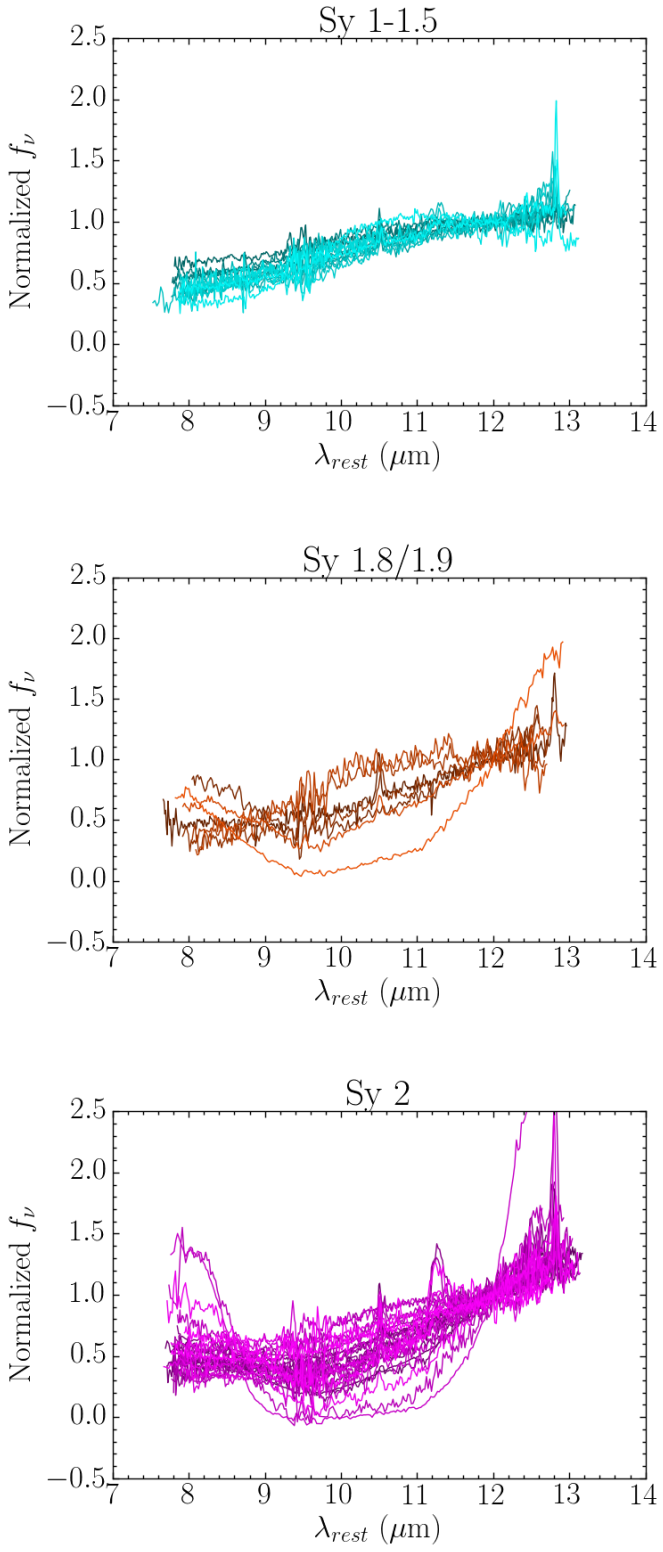

FIGURE 5.3: Spectra of the Seyfert 1-1.5 (top panel), Seyfert 1.8/1.9 (middle panel) and Seyfert 2 (bottom panel), normalized at 12 μm rest-frame.

the nearest galaxies in our sample, eliminating the host contribution allows a direct comparison of the nuclear spectra obtained with different physical apertures.

We use the DEBLENDIRS tool[2] (Hernán-Caballero et al. 2015) to do the decomposition of the spectra. DEBLENDIRS is an IDL/GDL routine that decomposes with a χ^2 minimization technique the MIR spectra in three components: AGN, stellar emission (STR), and interstellar emission (PAH), using a large library of *Spitzer*/IRS spectra as templates for these components. In addition to the best-fit combination, DEBLENDIRS calculates the probability distribution functions (PDF) of 8 parameters using the "max" method (Noll et al. 2009): the fractional contribution to the MIR ($5-15\,\mu$m) luminosity within the slit for the AGN (rAGN), the interstellar emission (rPAH) and the stellar (rSTR) components; the spectral index of the AGN spectrum (AGN $\alpha_{\rm MIR}$) measured in the $8.1-12.5\,\mu$m spectral range; the strength of the $9.7\,\mu$m silicate emission/absorption feature in the AGN spectrum (silicate strength, $S_{\rm Sil}$); the fractional contribution within the slit of the AGN to the rest-frame $6\,\mu$m luminosity ($L6_{\rm AGN}$), to the rest-frame $12\,\mu$m luminosity ($L12_{\rm AGN}$), and of the host galaxy to the rest-frame $12\,\mu$m luminosity ($L12_{\rm SB}$). To obtain PDFs for $\alpha_{\rm MIR}$ and $S_{\rm Sil}$ DEBLENDIRS has already incorporated this properties for each AGN template. For the templates the spectral index is defined assuming a power-law continuum, $f_\nu \propto \nu^\alpha$, and the silicate strength is defined as $S_{\rm Sil} = ln(f_{\nu,\,silicate}/f_{\nu,\,continuum})$, where positive numbers indicate that the feature is in emission and negative numbers in absorption. To estimate the continuum Hernán-Caballero et al. (2015) used anchor points at both sides of the silicate feature and interpolated with a power law and the peak was identified by visual inspection.

We note that DEBLENDIRS uses Spitzer/IRS spectra as templates to represent the AGN, stellar and PAH emission spectra, which probe in principle physical scales larger than those of our ground-based nuclear spectra. When we perform the spectral decomposition of the nuclear spectra of our Seyfert galaxies, we are implicitly assuming that the PAH and stellar emission in the MIR probed on kpc scales by the IRS spectra are also representative of those on tens of parsecs. As shown by Alonso-Herrero et al. (2016b), the IRS templates work well for the majority of nuclear regions hosting an AGN in local (U)LIRGs and quasars. This probably indicates that the MIR emission associated with stars and the ISM is not fundamentally affected by the presence of the radiation field of the AGN (at least at the typical physical scales probed by the slits, $100-150\,$pc). The only exception was for nuclei with deep silicate features. As explained in Hernán-Caballero et al. (2015), this is because the small number of AGN templates with deep silicate absorption ("obscured" templates). This is a consequence of the relative scarcity of IRS spectra for AGN that feature both deep silicate absorption and no PAH emission.

In Table 5.4 we list the results for the DEBLENDIRS spectral decomposition for the galaxies of our sample. For each galaxy we provide the reduced χ^2 value (χ^2_ν) of the best-fit model, the rest-frame $12\,\mu$m monochromatic AGN luminosity, calculated using the best-fit AGN component at that wavelength, the best fit value of the AGN, PAH and STR contributions, the median value of the AGN fractional

[2]http://www.denebola.org/ahc/deblendIRS/

contribution within the slit at rest-frame 12 μm, the median value of the strength of the silicate feature (positive values are for the feature in emission and negative for the feature in absorption), and the median value of the AGN MIR spectral index. For the last three we also provide the 1σ confidence interval (i.e., the 16% and 84% percentiles of the PDF).

In Fig. 5.4 we show three examples of the output of DEBLENDIRS, one for a Seyfert 1.5 (Mrk 1239), one for a Seyfert 1.9 (NGC 1194), and one for a Seyfert 2 galaxy (NGC 7130). All DEBLENDIRS outputs can be seen in Appendix A. Mrk 1239 is a Seyfert 1.5 galaxy with silicates in emission ($S_{\rm Sil} = 0.2$). It has an AGN MIR contribution of 83% with very little contribution of PAH (1%), and an AGN MIR spectral index of $\alpha_{\rm MIR} = -1.7$. The quality of the fit is good, $\chi^2_\nu = 0.25$. We note that generally a value of $\chi^2_\nu < 1$ usually indicates the errors are overestimated or that the errors include a correlated component, which is the absolute flux calibration. NGC 1194 is a Seyfert 1.9 galaxy. It also has a AGN MIR contribution of 83% with no PAH contribution. The AGN component shows a moderate silicate absorption ($S_{\rm Sil} = -1.2$), and an AGN MIR spectral index of $\alpha_{\rm MIR} = -1.2$. The quality of the fit is good, with $\chi^2_\nu = 1.59$. NGC 7130 is a Seyfert 2 galaxy whose nuclear MIR spectrum shows a dominant AGN contribution (84%) but also a clear PAH contribution of 14%, as already noted by several works (Díaz-Santos et al. 2010; Esquej et al. 2014). It shows the silicate feature in absorption ($S_{\rm Sil} = -0.6$) and has a steeper SED (AGN $\alpha_{\rm MIR} = -2.7$). It also has a good fit ($\chi^2_\nu = 1.49$).

Looking at the χ^2_ν values we see that in the majority of the cases the reliability of the fits is good. Most of the galaxies with reduced $\chi^2 < 1$ correspond to VISIR spectra. The errors of the VISIR spectra include an additional correlated source of uncertainty which comes from the averaging (and deviation) of the chop-nod beams in each spectral setting. This is a significant component in the error budget which some times can even dominate the computed total error of the spectra. NGC 3094 and NGC 4418, have very large values of χ^2 due to their deep silicate absorption. As explained in Alonso-Herrero et al. (2016b), for the deepest silicate feature the χ^2_ν values worsen. Roche et al. (2015) compared the IRS and T-ReCS spectra of NGC 4418 and found that the T-ReCS spectrum only shows the deep silicate absorption whereas the larger IRS aperture spectrum shows other spectral features that may be due to the diffuse emission of the host galaxy. This causes differences in the spectral shape, explaining the high value of χ^2_ν. The same happens with NGC 3094, which was studied by Roche et al. (2007). They found evidence of a spectral structure at 11 μm that may explain the differences in shape between the T-ReCS spectrum and the IRS larger aperture spectrum. The shortage of templates with strong silicate absorption compared to the others also increases the value of χ^2_ν.

For the galaxies observed with two instruments, we performed the DEBLENDIRS decomposition for each spectra. In order to select the best one, we compared the values obtained for the AGN spectral index and the AGN silicate strength. For each galaxy we selected the spectrum for which the estimated $\alpha_{\rm MIR}$ and $S_{\rm Sil}$ had the smallest 1σ confidence interval (16% and 84% percentiles), i.e, the one with smaller error bars in Fig. 5.5. The best spectrum for each galaxy is marked in bold in Table 5.2. From Fig. 5.5 we can see that for each galaxy the silicate strengths obtained from the different instrument spectra

TABLE 5.4: DEBLENDIRS results for the galaxy sample.

Name	χ^2_ν	AGN νL_ν (12 μm) (erg s^{-1})	MIR Contribution AGN	PAH	STR	AGN Frac. at 12 μm	AGN $S_{\rm Sil}$	AGN $\alpha_{\rm MIR}$
Seyfert 1-1.5 galaxies								
ESO 323-G77	0.50	3.2×10^{43}	0.66	0.01	0.33	0.71 [0.53, 0.90]	-0.2 [-0.6, 0.2]	-1.9 [-2.7, -1.1]
IC 4329A	0.30	1.7×10^{44}	0.75	0.00	0.25	0.83 [0.72, 0.93]	-0.1 [-0.3, 0.1]	-2.0 [-2.5, -1.5]
MCG-6-30-15	0.49	5.8×10^{42}	0.80	0.03	0.17	0.82 [0.67, 0.94]	0.0 [-0.3, 0.3]	-1.8 [-2.6, -1.4]
Mrk 1239	0.25	7.3×10^{43}	0.78	0.01	0.21	0.86 [0.71, 0.94]	0.2 [0.0, 0.3]	-1.7 [-2.6, -1.3]
NGC 931	1.69	6.0×10^{43}	0.93	0.01	0.06	0.90 [0.78, 0.97]	-0.1 [-0.3, 0.2]	-2.0 [-2.5, -1.7]
NGC 1365 (T)	3.94	4.5×10^{42}	0.97	0.03	0.00	0.86 [0.81, 0.98]	0.1 [0.0, 0.3]	-2.3 [-2.9, -2.0]
NGC 3227 (C)	2.15	5.0×10^{42}	0.71	0.06	0.23	0.88 [0.81, 0.96]	-0.1 [-0.3, 0.2]	-2.4 [-2.8, -2.0]
NGC 3783	1.89	2.0×10^{43}	1.00	0.00	0.00	0.86 [0.81, 0.98]	0.0 [-0.2, 0.2]	-2.2 [-2.8, -1.9]
NGC 4051	3.17	1.8×10^{42}	0.90	0.10	0.00	0.85 [0.74, 0.94]	0.1 [-0.2, 0.3]	-2.1 [-2.8, -1.8]
NGC 4151	1.73	1.5×10^{43}	0.83	0.00	0.17	0.90 [0.84, 0.97]	0.0 [-0.2, 0.2]	-2.3 [-2.8, -1.9]
NGC 4253	1.94	3.7×10^{43}	0.91	0.03	0.06	0.92 [0.83, 0.97]	-0.2 [-0.3, 0.1]	-2.4 [-2.7, -2.1]
NGC 4593	1.30	1.3×10^{43}	0.65	0.00	0.35	0.83 [0.68, 0.94]	0.3 [0.1, 0.5]	-1.9 [-2.8, -1.3]
NGC 5548	4.22	3.8×10^{43}	0.86	0.04	0.10	0.83 [0.69, 0.94]	0.1 [-0.2, 0.4]	-1.7 [-2.5, -1.3]
NGC 7213*	3.89	4.4×10^{42}	1.00	0.00	0.00	0.99 [0.98, 1.00]	0.5 [0.3, 0.6]	-2.2 [-2.3, -2.0]
NGC 7469	1.54	7.5×10^{43}	0.99	0.00	0.01	0.85 [0.79, 0.97]	0.1 [-0.2, 0.3]	-2.2 [-2.8, -1.8]
Seyfert 1.8/1.9 galaxies								
Name	χ^2_ν	AGN νL_ν (12 μm) (erg s^{-1})	MIR Contribution AGN	PAH	STR	AGN Frac. at 12 μm	AGN $S_{\rm Sil}$	AGN $\alpha_{\rm MIR}$
MCG-3-34-64	2.37	1.4×10^{44}	0.79	0.04	0.17	0.88 [0.79, 0.95]	-0.2 [-0.5, 0.0]	-2.3 [-2.7, -2.0]
NGC 1194	1.59	1.5×10^{43}	0.78	0.00	0.22	0.87 [0.79, 0.91]	-1.2 [-1.4, -0.9]	-1.2 [-1.7, -1.0]
NGC 2992	5.12	8.8×10^{42}	0.99	0.00	0.01	0.98 [0.96, 1.00]	-0.3 [-0.5, -0.3]	-2.7 [-2.9, -2.6]
NGC 4258	3.11	2.6×10^{41}	0.72	0.00	0.28	0.89 [0.86, 0.93]	0.3 [0.1, 0.4]	-2.7 [-2.9, -1.8]
NGC 4579	5.13	7.3×10^{41}	0.87	0.00	0.13	0.96 [0.93, 0.98]	0.4 [0.3, 0.6]	-2.1 [-2.4, -1.7]
NGC 5506	0.30	2.7×10^{43}	0.80	0.05	0.15	0.68 [0.32, 0.90]	-1.1 [-2.6, -0.2]	-1.8 [-2.7, -0.9]
NGC 7479	11.2	1.4×10^{43}	0.86	0.06	0.08	0.89 [0.83, 0.93]	-3.4 [-3.6, -2.7]	-1.6 [-1.8, -1.2]
Seyfert 2 galaxies								
Name	χ^2_ν	AGN νL_ν (12 μm) (erg s^{-1})	MIR Contribution AGN	PAH	STR	AGN Frac. at 12 μm	AGN $S_{\rm Sil}$	AGN $\alpha_{\rm MIR}$
Circinus (V)	7.51	6.5×10^{42}	0.99	0.00	0.01	0.99 [0.97, 1.00]	-1.4 [-1.5, -1.2]	-1.9 [-2.0, -1.7]
ESO 103-G35*	1.54	5.7×10^{43}	0.97	0.03	0.00	0.97 [0.88, 0.99]	-0.8 [-1.0, -0.6]	-2.2 [-2.6, -1.9]
ESO 428-G14	3.37	3.8×10^{42}	0.87	0.13	0.00	0.90 [0.84, 0.96]	-0.6 [-0.8, -0.4]	-2.6 [-2.9, -2.3]
IC 4518W	2.19	2.9×10^{43}	0.99	0.01	0.00	0.94 [0.83, 0.98]	-1.5 [-1.9, -1.2]	-2.0 [-2.4, -1.5]
IC 5063 (V)	2.18	7.5×10^{43}	0.82	0.00	0.18	0.93 [0.91, 0.97]	-0.3 [-0.5, -0.2]	-2.6 [-2.8 -2.2]
MCG-5-23-16	1.39	2.5×10^{43}	0.93	0.02	0.05	0.89 [0.83, 0.96]	-0.4 [-0.5, -0.2]	-2.5 [-2.8, -2.1]
Mrk 3	4.11	4.0×10^{43}	0.85	0.00	0.15	0.96 [0.93, 0.99]	-0.5 [-0.7, -0.3]	-2.8 [-3.0, -2.6]
Mrk 1066	6.22	9.7×10^{42}	0.69	0.31	0.00	0.73 [0.62, 0.82]	-0.8 [-1.1, -0.6]	-2.6 [-3.0, -2.2]
Mrk 1210	5.39	5.5×10^{43}	0.94	0.00	0.06	0.98 [0.96, 0.99]	-0.3 [-0.5, -0.2]	-2.7 [-2.9, -2.5]
NGC 1068	1.00	8.0×10^{43}	0.80	0.00	0.20	0.87 [0.79, 0.92]	-0.4 [-0.6, -0.2]	-2.1 [-2.7, -1.9]
NGC 1320	2.14	1.3×10^{43}	0.90	0.00	0.10	0.93 [0.85, 0.98]	-0.2 [-0.4, 0.0]	-2.4 [-2.7, -2.0]
NGC 1386	1.33	7.9×10^{41}	0.82	0.07	0.11	0.85 [0.73, 0.93]	-0.8 [-1.2, -0.5]	-2.2 [-2.7, -1.7]
NGC 1808	24.6	1.3×10^{42}	0.87	0.13	0.00	0.91 [0.87, 0.94]	-0.6 [-0.7, -0.4]	-2.9 [-3.0, -2.7]
NGC 2110	2.11	8.4×10^{42}	0.81	0.06	0.13	0.88 [0.77, 0.95]	0.2 [0.0, 0.4]	-1.8 [-2.7, -1.5]
NGC 2273	1.76	7.7×10^{42}	0.93	0.00	0.07	0.97 [0.96, 0.99]	-0.4 [-0.5, -0.2]	-2.7 [-2.9, -2.6]
NGC 3081	0.93	5.9×10^{42}	1.00	0.00	0.00	0.91 [0.85, 0.97]	-0.1 [-0.3, 0.2]	-2.4 [-2.8, -2.0]
NGC 3094	209	2.8×10^{43}	1.00	0.00	0.00	0.99 [0.98, 1.00]	-4.0 [-4.0, -3.8]	-0.5 [-0.6, -0.3]
NGC 3281* (V)	3.39	1.9×10^{43}	0.94	0.02	0.04	0.97 [0.93, 0.99]	-1.2 [-1.4, -1.1]	-1.4 [-1.6, -1.1]
NGC 4388	11.5	2.6×10^{42}	0.69	0.20	0.11	0.85 [0.80, 0.95]	-1.1 [-1.4, -0.8]	-3.5 [-3.8, -2.5]
NGC 4418*	267	2.1×10^{43}	1.00	0.00	0.00	0.99 [0.98, 1.00]	-4.1 [-4.2, -3.9]	-1.8 [-2.0, -1.7]
NGC 4507	0.81	5.5×10^{43}	0.80	0.00	0.20	0.84 [0.72, 0.95]	0.0 [-0.3, 0.2]	-2.0 [-2.6, -1.5]
NGC 5135	4.10	1.1×10^{43}	0.81	0.03	0.16	0.88 [0.80, 0.94]	-0.7 [-0.9, -0.5]	-2.4 [-2.7, -2.0]
NGC 5347	6.83	1.5×10^{43}	1.00	0.00	0.00	0.96 [0.93, 0.99]	-0.3 [-0.4, -0.1]	-2.5 [-2.8, -2.3]
NGC 5643 (V)	6.65	1.7×10^{42}	0.95	0.05	0.00	0.97 [0.95, 0.99]	-0.5 [-0.7, -0.3]	-2.7 [-2.9, -2.6]
NGC 5995	0.92	1.0×10^{44}	0.56	0.03	0.41	0.77 [0.64, 0.90]	-0.3 [-0.6, 0.0]	-2.1 [-2.7, -1.4]
NGC 7130	1.49	1.9×10^{43}	0.83	0.17	0.00	0.89 [0.83, 0.95]	-0.6 [-0.8, -0.4]	-2.7 [-3.0, -2.4]
NGC 7172	6.70	6.1×10^{42}	0.94	0.06	0.00	0.94 [0.80, 0.98]	-2.4 [-2.7, -1.8]	-1.0 [-1.9, -0.8]
NGC 7465	2.33	1.4×10^{42}	0.67	0.11	0.22	0.77 [0.66, 0.89]	-0.1 [-0.4, 0.3]	-2.2 [-2.8, -1.7]
NGC 7582 (V)	3.29	6.6×10^{42}	0.89	0.11	0.00	0.86 [0.78, 0.94]	-1.1 [-1.4, -0.9]	-1.7 [-2.0, -1.3]
NGC 7674	1.61	1.6×10^{44}	0.71	0.04	0.25	0.84 [0.76, 0.92]	-0.2 [-0.4, 0.1]	-2.2 [-2.7, -1.8]

Notes.— The MIR contributions of the AGN, PAH and STR components are estimated in the 5–15 μm range. The spectral index is estimated in the 8.1–12.5 μm range. We give the median value and in parenthesis the 16% and 84% percentiles of the distributions for the AGN fractional contribution at 12 μm (within the slit), the strength of the silicates and the spectral index. The galaxies fitted with themselves are marked with an asterisk.

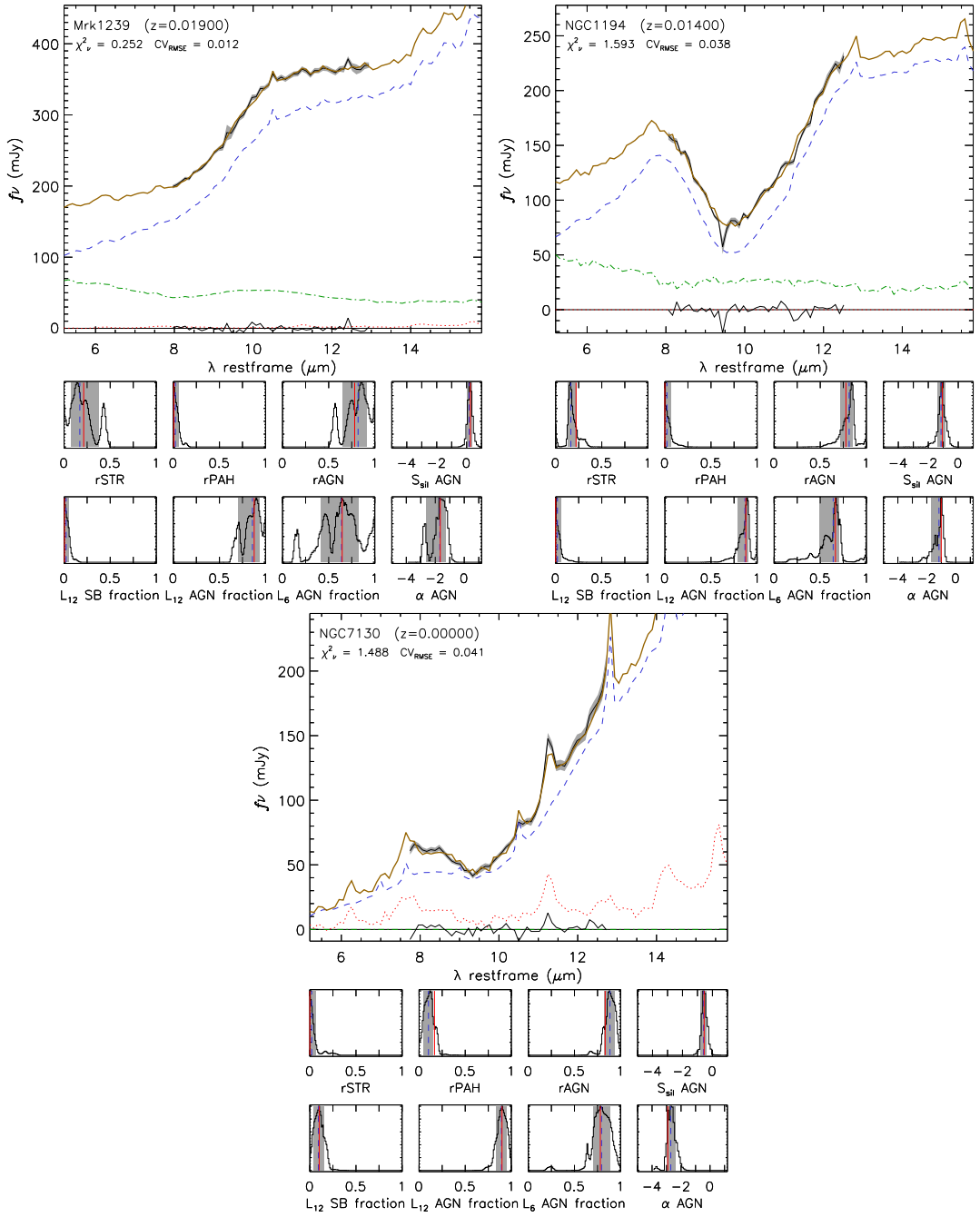

FIGURE 5.4: Examples of the output of DEBLENDIRS for Mrk 1239 (Seyfert 1-1.5, top left panel), NGC 1194 (Seyfert 1.8/1.9, top right panel) and NGC 7130 (Seyfert 2, bottom panel). For each example, the top panels show the rest-frame spectrum with the best fitting model (orange), and the three components: stellar (dash-dotted green), PAH (dotted red) and AGN (dashed blue). The bottom panels show the PDF for the STR, PAH and AGN emission fraction within the slit ($5-15\,\mu$m), namely rSTR, rPAH, and rAGN, respectively; the strength of the $9.7\,\mu$m silicate feature ($S_{\rm Sil}$) and the spectral index ($\alpha_{\rm AGN}$) in the AGN spectrum (8.1-12.5 μm); the fractional contribution within the slit of the AGN to the rest-frame $6\,\mu$m ($L6_{\rm AGN}$) and $12\,\mu$m ($L12_{\rm AGN}$) luminosity; and the fractional contribution of the host galaxy to the rest-frame $12\,\mu$m luminosity ($L12_{\rm SB}$). For the PDFs the solid red line indicates the value for the best fitting decomposition model whereas the dashed blue line indicates the expected value. The shaded area represents the 16% and 84% percentiles, i.e, the 1σ confidence interval. The outputs for all galaxies are shown in Appendix A.

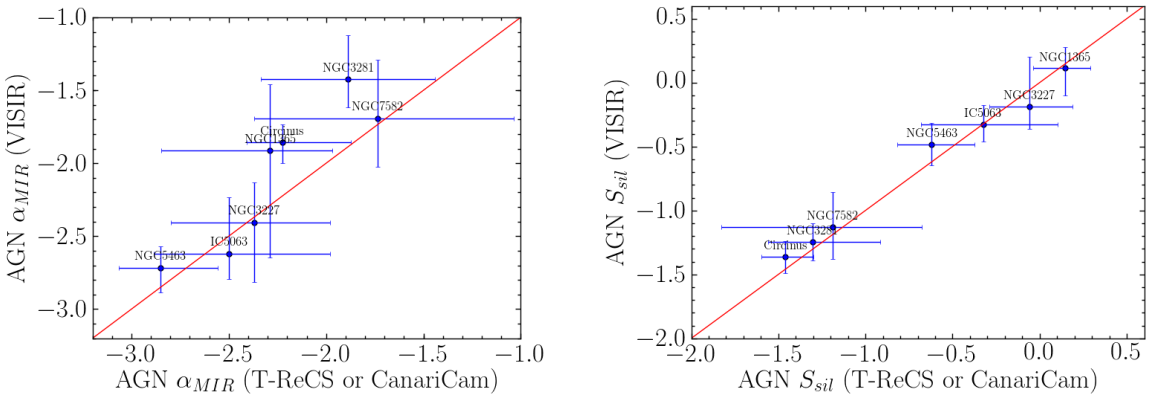

FIGURE 5.5: Comparison of the values obtained with DEBLENDIRS for the AGN MIR spectral index (AGN $\alpha_{\rm MIR}$, left panel) and the silicate strength (AGN $S_{\rm Sil}$, right panel) for the galaxies observed with two different instruments. The error bars represent the 1σ confidence interval (16% and 84% percentiles). The solid red line is not a fit but it represents the 1:1 relation.

are similar. In the case of the AGN spectral index, for each galaxy the values from the two spectra are compatible within the 1σ confidence interval. Except for NGC 1365 and NGC 3227, the VISIR spectrum provides values with smallest 1σ confidence interval.

5.3.2 Comparison with direct measurements on the spectra

In order to assess the possible differences in the measurement of the MIR spectral index and the strength of the silicate feature, in this section we compare these values as derived with DEBLENDIRS and measured directly from the spectra.

We computed the MIR spectral index as $f_\nu \propto \nu^{\alpha_{8.1-12.5\mu m}}$, using the flux ratios at rest-frame 8.1 and 12.5 μm. We used the expression $S_{\rm Sil,8.1-12.5\mu m} = ln(f_{\nu,peak}/f_{\nu,continuum})$ for the strength of the silicate feature, were $f_{\nu,peak}$ is the flux density of the peak of the silicate feature and the $f_{\nu,continuum}$ is the continuum flux density at the rest-frame wavelength of the peak. We used 9.7 μm for the galaxies with the silicate feature in absorption and 10.2 μm for the galaxies with the silicate feature in emission. Hatziminaoglou et al. (2015) found that the peak of the silicates has a bimodal distribution, with the absorption at 9.7 μm and the emission at longer wavelengths (65% with $\lambda_{peak} > 10.2\mu$m). We did not identify visually the peak due to the low S/N of the spectra. We fitted the continuum as a straight line between rest-frame 8.1 and 12.5 μm.

To estimate the uncertainties we performed 1000 Montecarlo simulations allowing the flux densities at 8.1, 9.7, 10.2, and 12.5 μm to vary within their estimated errors. Then we calculated the average and the standard deviation of the 1000 values of the MIR spectral index and the silicate strength feature obtained with the simulations. The results are shown in Table 5.5.

TABLE 5.5: Direct measurements on the spectra.

Name	$S_{\mathrm{Sil},8.1-12.5\mu m}$	$\alpha_{8.1-12.5\mu m}$
Circinus	-1.40±0.04	-1.51±0.10
ESO 103-G35	-1.02±0.14	-2.29±0.21
ESO 323-G77	0.09±0.09	-0.89±0.27
ESO 428-G14	-0.78±0.22	-2.43±0.17
IC 4329A	-0.01±0.04	-1.48±0.09
IC 4518W	-1.62±0.39	-1.88±0.59
IC 5063	-0.40±0.10	-2.07±0.20
MCG-3-34-64	-0.17±0.13	-2.06±0.37
MCG-5-23-16	-0.39±0.05	-2.10±0.12
MCG-6-30-15	-0.01±0.09	-1.18±0.23
Mrk 3	-0.61±0.16	-2.46±0.26
Mrk 1066	-1.22±0.15	-2.41±0.13
Mrk 1210	-0.35±0.05	-2.76±0.10
Mrk 1239	0.11±0.08	-1.43±0.18
NGC 931	-0.03±0.06	-2.04±0.15
NGC 1068	-0.37±0.04	-1.75±0.11
NGC 1194	-0.88±0.08	-0.86±0.12
NGC 1320	-0.35±0.16	-1.96±0.30
NGC 1365	0.00±0.04	-2.00±0.09
NGC 1386	-0.81±0.14	-1.97±0.37
NGC 1808	-0.52±0.04	-2.87±0.09
NGC 2110	-0.05±0.10	-1.65±0.28
NGC 2273	-0.47±0.05	-2.78±0.17
NGC 2992	-0.32±0.12	-3.07±0.35
NGC 3081	-0.03±0.12	-2.18±0.25
NGC 3094	-3.90±0.11	-0.47±0.11
NGC 3227	-0.08±0.06	-2.43±0.18
NGC 3281	-1.54±0.27	-1.24±0.16
NGC 3783	-0.02±0.06	-1.87±0.13
NGC 4051	0.32±0.13	-2.54±0.34
NGC 4151	-0.02±0.06	-1.98±0.08
NGC 4253	-0.29±0.05	-2.13±0.17
NGC 4258	0.09±0.12	-2.52±0.37
NGC 4388	-1.02±0.19	-3.55±0.43
NGC 4418	-8.34±1.22	-1.73±0.39
NGC 4507	-0.06±0.17	-1.64±0.36
NGC 4579	0.15±0.17	-3.90±0.60
NGC 4593	-0.14±0.20	-1.28±0.48
NGC 5135	-0.81±0.10	-1.98±0.10
NGC 5347	-0.31±0.09	-3.39±0.37
NGC 5506	-1.10±0.65	-1.51±0.92
NGC 5548	0.18±0.15	-1.55±0.19
NGC 5643	-0.72±0.14	-2.87±0.28
NGC 5995	-0.19±0.09	-1.17±0.20
NGC 7130	-0.62±0.12	-2.46±0.25
NGC 7172	-3.52±0.99	-0.65±0.33
NGC 7213	0.24±0.09	-2.45±0.28
NGC 7465	-0.03±0.25	-1.77±0.57
NGC 7469	0.08±0.10	-1.90±0.29
NGC 7479	-2.82±0.47	-2.02±0.38
NGC 7582	-1.22±0.33	-1.58±0.25
NGC 7674	-0.26±0.09	-1.86±0.21

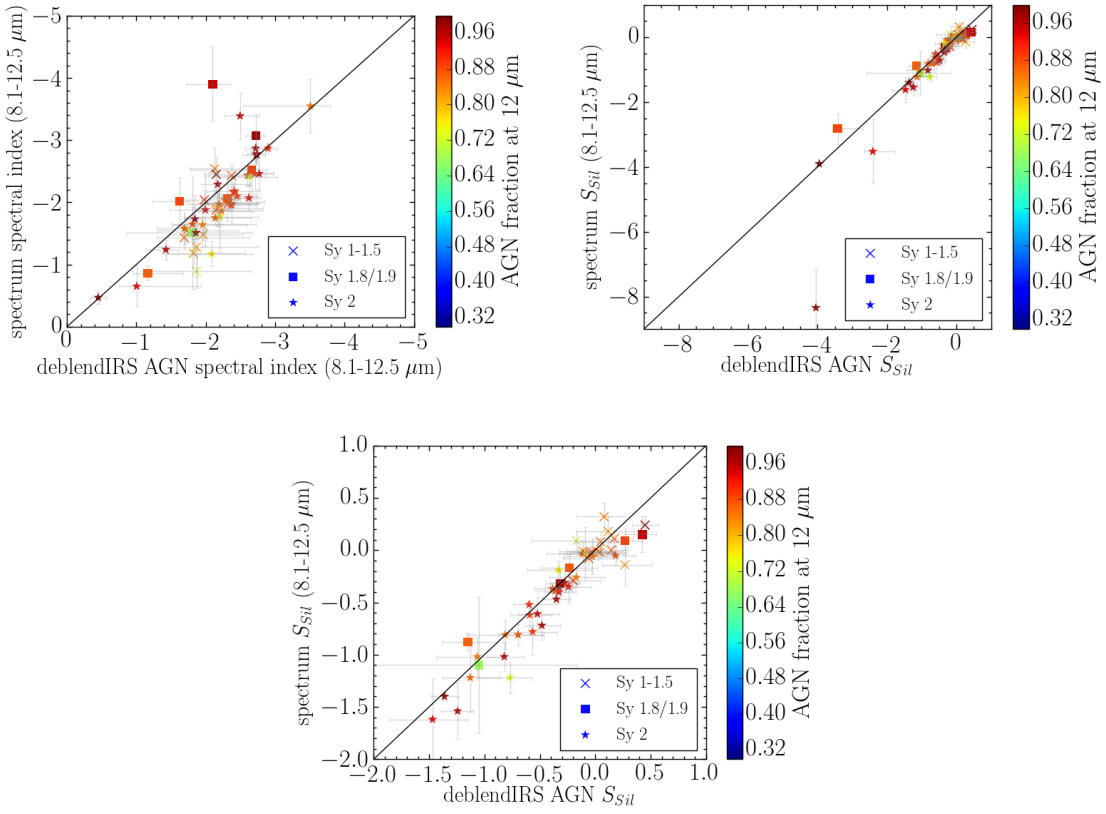

FIGURE 5.6: Top left panel: DEBLENDIRS AGN spectral index (8.1 − 12.5 μm) versus the spectrum spectral index (8.1 − 12.5 μm). Top right panel: DEBLENDIRS AGN $S_{\rm Sil}$ versus the spectrum $S_{\rm Sil}$ (8.1 − 12.5 μm). Bottom panel: Zoom of the DEBLENDIRS AGN $S_{\rm Sil}$ versus the spectrum $S_{\rm Sil}$ (8.1 − 12.5 μm). The Seyfert 1-1.5 galaxies are marked with crosses, the Seyfert 1.8/1.9 with squares and the Seyfert 2 with star symbols. The colour indicates the AGN fractional contribution at 12 μm within the slit for each galaxy. The solid black line indicates the 1:1 relation.

In Fig. 5.6 we compare the spectral index and the strength of the silicate feature as obtained with DEBLENDIRS and as measured directly from the spectra. The differences are expected as DEBLENDIRS provides the spectral index for the AGN component whereas when measuring directly from the spectrum there might be contamination from the host galaxy. In general, the spectral indices obtained with DEBLENDIRS are more negative than the ones from the spectrum, due to the host contamination.

In the case of the strength of the silicate feature, the agreement is good except for the cases with the deepest silicate feature. In the case of NGC 4418 and NGC 7172 the difference between both methods is because the flux density at the wavelength used to evaluate the strength of the silicate is nearly zero. This is the reason why the strength of the silicate feature is so negative when measuring directly from the spectra. In other cases, as NGC 7479, the strength of the silicate feature is more negative when calculated through DEBLENDIRS. The silicates are so deep that the 8.1 μm is still affected by the absorption, so measuring directly from the spectra we are sub-estimating the continuum flux density. This results in a less negative value of the strength of the silicate. Therefore for the deepest silicate

features there are significant differences between doing a decomposition and the values obtain directly from spectra. In what follows we will use only the results from DEBLENDIRS.

5.4 MIR properties of AGN

In this section we analyse the results obtained using DEBLENDIRS, for the AGN MIR spectral index, the strength of the silicate feature, the AGN fractional contribution, and the AGN rest-frame 12 μm luminosities.

5.4.1 AGN MIR spectral index and strength of the silicate feature

For each galaxy in the sample, we list in Table 5.4 the median values and the 16 and 84 percentiles of the AGN MIR spectral index and the strength of the silicate feature. We also list in Table 5.6 the median values and the 16 and 84 percentiles of the AGN MIR spectral index and the strength of the silicate feature for each type of Seyfert galaxy. As can be seen from these tables, the Seyfert 1-1.5 galaxies in our sample show a narrower range of strengths of the silicate feature than the Seyfert 2 galaxies. In terms of the AGN MIR spectral index, all samples show similar ranges. We performed KS-tests to confirm if these differences are statistically significant. We found that the AGN MIR spectral indices of Seyfert 1-1.5 and Seyfert 2 are similar. However, there are statistically significant differences in terms of the strength of the silicate feature. According to the KS-test the MIR properties are not statistically different for the entire sample and for Seyferts in the RSA sample and the galaxies in the 12 μm sample. However, there are statistically significant differences in the derived strengths of the silicate features of Seyfert 2 galaxies and Seyfert 1-1.5 galaxies ($p = 0.000002$) and between Seyfert 1-1.5 and Seyfert 1.8/1.9 ($p = 0.02$). Conversely, there are no statistically significant differences between Seyfert 2 and Seyfert 1.8/1.9 ($p = 0.54$). This indicates that the behaviour of the Seyfert 1.8/1.9 is closer to the Seyfert 2 than to the Seyfert 1-1.5 in terms of the strength of the silicate feature. However, this is not necessarily reflecting the properties of the torus because the MIR nuclear emission of some Seyfert galaxies may be due to extended dust components in the host galaxy (Hönig et al. 2010; Alonso-Herrero et al. 2011; González-Martín et al. 2013; Esquej et al. 2014; Alonso-Herrero et al. 2014, 2016a). We will come back to this issue in Section 5.4.3 and also when we compare the observations with torus model predictions in Section 5.5.3.

We now compare the AGN MIR properties of our Seyfert galaxies with those of IR-weak PG quasars (type 1) derived by Alonso-Herrero et al. (2016b). They obtained ground-based MIR spectroscopy of 10 optically selected local quasars that are IR-weak based on their IR to optical B-band luminosity ratios (L_{IR}/L_B between 1 and 3), and with a median luminosity distance of 319 Mpc. Alonso-Herrero et al. (2016b) also used DEBLENDIRS to do a decomposition of the spectra of these 10 quasars and obtained a median value for the AGN MIR spectral index $\alpha_{MIR} = -1.7$ (1σ confidence interval of

TABLE 5.6: Statistics of the DEBLENDIRS results.

	Number of galaxies	AGN $\alpha_{\rm MIR}$	AGN $S_{\rm Sil}$	AGN Frac. at 12 μm	log AGN νL_ν (12 μm; erg s^{-1})
All the sample	52	-2.2 [-2.7, -1.8]	-0.3 [-1.1, 0.1]	0.87 [0.72, 0.98]	43.2 [42.6, 43.8]
Seyfert 1-1.5	15	-2.1 [-2.3, -1.8]	0.0 [-0.1, 0.2]	0.86 [0.71, 0.98]	43.3 [42.7, 43.8]
Seyfert 1.8/1.9	7	-2.1 [-2.7, -1.6]	-0.3 [-1.2, 0.3]	0.80 [0.77, 0.88]	43.1 [41.8, 43.5]
Seyfert 2	30	-2.3 [-2.7, -1.8]	-0.5 [-1.3, -0.2]	0.88 [0.76, 0.98]	43.2 [42.5, 43.7]

Notes.– The AGN MIR spectral index is estimated in the 8.1 − 12.5 μm range. The AGN fractional contribution refers to the 5 − 15 μm luminosity. We give the median value and in parenthesis the 16% and 84% percentiles.

[−2.4, −1.0]) and for the strength of the silicate feature of $S_{\rm Sil} = 0.1$ (1σ confidence interval of [−0.2, 0.3]). The PG quasars have flatter MIR spectral indices than the Seyfert 1-1.5s ($\alpha_{\rm MIR} = -2.1$) but similar strengths of the silicate feature. A KS-test shows that the Seyfert 1-1.5 galaxies and the IR-weak quasars are not statistically different in terms of the strength of the silicate feature ($p = 0.29$) but are statistically different in terms of the spectral index ($p = 0.03$). In Section 5.5.3 we will use clumpy torus model predictions to see whether these differences also imply differences in the torus properties of different types of AGN.

5.4.2 MIR AGN fractional contribution within the slit

In Table 5.4 we also list the AGN fractional contribution within the slit to the 5 − 15 μm emission from the AGN template in the best-fit model for each galaxy. We list in Table 5.6 the median values and the 16 and 84 percentiles for each type of Seyfert galaxy. As can be seen from the latter table, the median AGN fractional contributions within the slit are similar for the Seyfert 2 and the Seyfert 1-1.5 in our sample. The AGN dominates (median value of 87%) the nuclear (100 − 150 pc) MIR emission in Seyfert galaxies.

The AGN contributions to the MIR fluxes within the slit are not statistically different for all the types of Seyfert galaxies according to a KS-test. We note, however, that the physical sizes covered by the slits of the Seyfert 1 nuclei are larger than those of the Seyfert 2 nuclei, on average. This means that if the slits were similar the AGN fractional contribution in the MIR in Seyfert 1 nuclei would be slightly higher. This is in agreement with the the prediction of a nearly isotropic emission at 12 μm of the clumpy torus models of Nenkova et al. (2008b). This result is also in agreement with other observational results that find no differences between the MIR emission of type 1 and type 2 AGN when compared with their hard X-ray luminosity, which is a proxy for the AGN bolometric luminosity (see e.g. Alonso-Herrero et al. 2001; Krabbe et al. 2001; Lutz et al. 2004; Gandhi et al. 2009; Levenson et al. 2009; Asmus et al. 2015; Mateos et al. 2015).

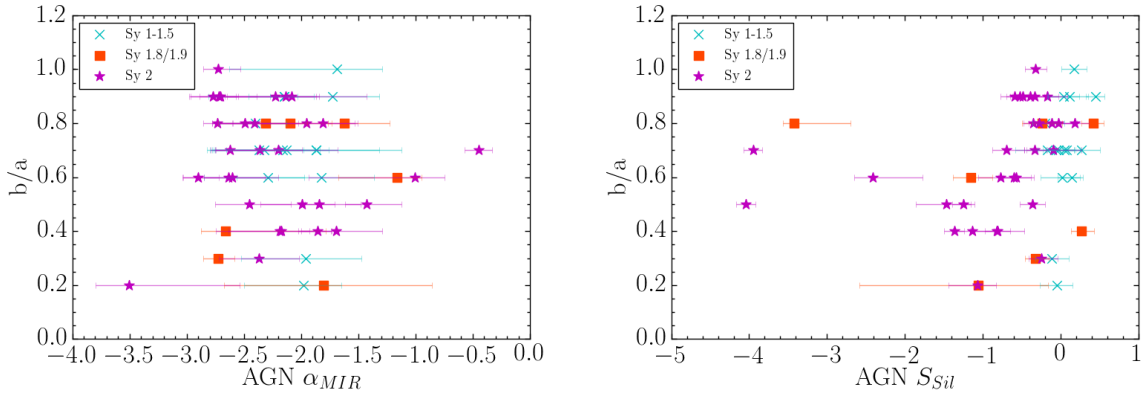

FIGURE 5.7: Left panel: AGN MIR (8.1 – 12.5 μm) spectral index derived with DEBLENDIRS versus b/a. Right panel: the strength of the silicate feature derived with DEBLENDIRS versus b/a. The different types of Seyfert are shown with different colours and symbols: Seyfert 1-1.5 (cyan crosses), Seyfert 1.8/1.9 (orange squares) and Seyfert 2 (magenta star symbols). The error bars represent the 1σ confidence interval (16% and 84% percentiles).

5.4.3 Relation with host galaxy properties

In Fig. 5.7 we also compare the DEBLENDIRS AGN spectral index and strength of the silicate feature with the inclination of the galaxies to see if there is contamination by extended dust components (e.g. dust lanes). In this figure we show the different types of Seyfert with different colours and symbols: Seyfert 1-1.5 (cyan crosses), Seyfert 1.8/1.9 (orange squares) and Seyfert 2 (magenta star symbols). We did not find any clear dependency of the spectral index or the strength of the silicates with the inclination of the galaxies. For the strength of the silicate feature, the face-on galaxies (b/a $\sim$ 1) present a narrow range, in agreement with Goulding et al. (2012). They also found that the deepest silicate absorption appears in galaxies with visible dust-lanes, disturbed morphologies (e.g, due for instance to interactions/mergers) and/or galaxies which are highly-inclined along the line-of-sight. Our four galaxies with $S_{\rm Sil} < -2$ are NGC 3094, NGC 4418, NGC 7172 and NGC 7674. NGC 7172 and NGC 7674 are classified as peculiar galaxies and NGC 7172 is also an edge-on galaxy (see Table 5.1). Moreover, NGC 4418, the galaxy in our sample with deepest $S_{\rm Sil}$, is known to be the galaxy with the deepest silicate absorption feature (Roche et al. 2015). This galaxy is seen nearly edge-on and it also likely interacting with a distorted companion a few kpc away (see Evans et al. 2003).

5.4.4 AGN rest-frame 12 μm luminosities

Using the results of DEBLENDIRS, we derived the AGN rest-frame 12 μm luminosity for each galaxy on the sample (see Table 5.4). Fig. 5.8 shows the corresponding distributions for the Seyfert 1-1.5, Seyfert 1.8/1.9 and Seyfert 2 galaxies and the statistics are given in Table 5.6. As can be seen from the figure and the statistics, the typical AGN luminosities at rest-frame 12 μm of Seyfert 1-1.5 galaxies ($\log(\nu L_{12\mu{\rm m}}/{\rm erg\,s^{-1}}) = 43.3$) are only slightly higher than those of Seyfert 2 galaxies

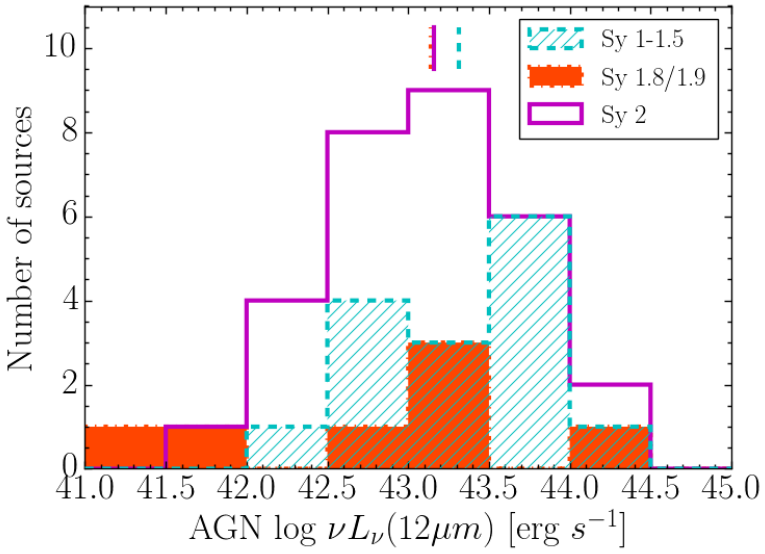

FIGURE 5.8: Derived AGN rest-frame 12 μm luminosities distribution for Seyfert 1-1.5 galaxies (dashed cyan), Seyfert 1.8/1.9 (filled orange) and Seyfert 2 galaxies (magenta). The vertical lines indicate the median of the distributions.

($\log(\nu L_{12\mu m}/\mathrm{erg\,s^{-1}}) = 43.2$). This result is similar to the finding in other works (e.g. Asmus et al. 2014). However, a KS-test indicates there are no statistically significant differences between Seyfert 1-1.5 and Seyfert 2 ($p = 0.82$) nor Seyfert 1.5 and Seyfert 1.8/1.9 ($p = 0.70$). The Seyfert 1-1.5 galaxies are further away (median of 42 Mpc) than the Seyfert 2 galaxies (median of 37 Mpc), which perfectly explains the slight observed differences in MIR AGN luminosity. As expected, the AGN MIR luminosities of our sample of Seyferts are about one order of magnitude less luminous than the IR-weak quasars (median of $\log(\nu L_{12\mu m}/\mathrm{erg\,s^{-1}}) = 44.5$, see Alonso-Herrero et al. 2016b).

We compared our derived AGN rest-frame 12 μm luminosities with those derived by Asmus et al. (2014) using imaging data. They calculated the nuclear sub-arcsecond-scale continuum flux densities at rest-frame 12 μm for 253 objects from publicly available images taken with the COMICS, Michelle, T-ReCS, and VISIR instruments. They calculated the 12 μm flux densities for all images with two different methods for compact and extended sources. Then, they unified the fluxes to obtain one flux for each object using a recipe consisting in four methods with decreasing priority. They also corrected the fluxes of 40 sources with strong silicate features using IR spectra.

Of our 52 Seyfert galaxies, 45 are in common with Asmus et al. (2014) sample. With their 12 μm rest-frame wavelength fluxes, we calculated the luminosity of the galaxies using our cosmology in order to compare it to our derived luminosity. Fig. 5.9 shows this comparison. Our derived AGN rest-frame 12 μm luminosities are very similar to those of Asmus et al. (2014). The main differences in the luminosities are due to the correction applied by Asmus et al. (2014) to the sources with strong silicate features. This can be seen in Fig. 5.10. Excluding the Seyfert nuclei with deep silicate features, the

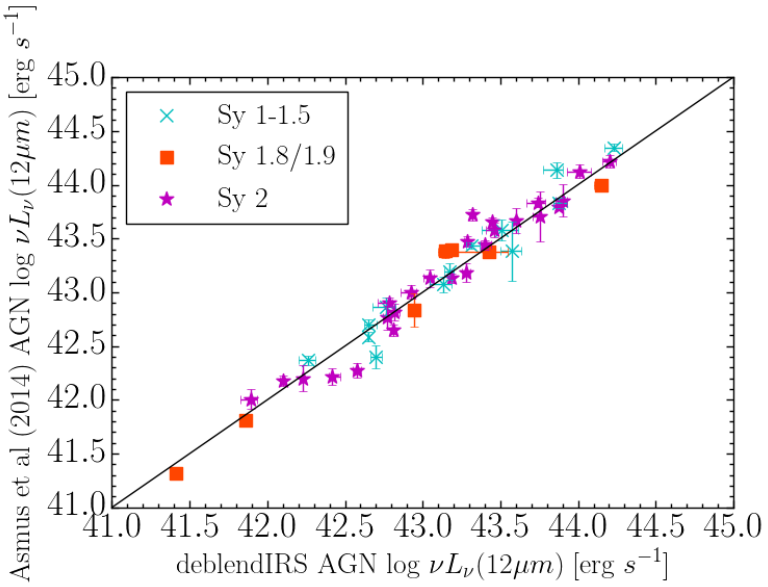

FIGURE 5.9: Comparison of our DEBLENDIRS derived AGN rest-frame 12 μm luminosities versus the 12 μm rest-frame luminosities from Asmus et al. (2014). The different types of Seyfert are shown with different colours and symbols: Seyfert 1-1.5 (cyan crosses), Seyfert 1.8/1.9 (orange squares) and Seyfert 2 (magenta star symbols). The solid black line indicates the 1:1 relation.

differences in the luminosities have a median of 4% (median of 5% for all the sources). If we consider only the galaxies with strong silicate features in absorption, the differences in the luminosities have a median of 20%. That is expected as Asmus et al. (2014) corrected these luminosities, so their fluxes are overall higher than ours. For the galaxies with strong silicate features in emission, the median value of the differences is -13%. That is also expected because as the silicate feature is in emission, the corrected fluxes are lower than the fluxes measured directly from the spectra. Furthermore, we cannot discard differences in the IR luminosity due to variability (García-González et al. 2015 and Chapter 3).

5.4.5 Statistical comparison for different Seyfert types and other AGN

To make a statistical comparison of the MIR properties of Seyfert 2 and Seyfert 1-1.5 we obtained the combined PDF of each of the subsamples as a simple average of the PDF of the individual galaxies for the AGN MIR spectral index, the strength of the silicate feature and the AGN fractional contribution within the slit to the 5 − 15 μm luminosity. We show the results for the AGN MIR spectral index in Fig. 5.11, the results of the strength of the silicate feature in Fig. 5.12 and the results of the AGN fractional contribution to 5 − 15 μm luminosity in Fig. 5.13. The statistics for these figures are in Table 5.7.

Figures 5.11 and 5.12 show that the combined PDF of the MIR spectral index and the AGN contribution within the slit, respectively are similar for all the Seyfert types (see also the statistics in Table 5.7). However, the combined PDF of the silicate strength of the Seyfert 1.8/1.9 and Seyfert 2 show a broad

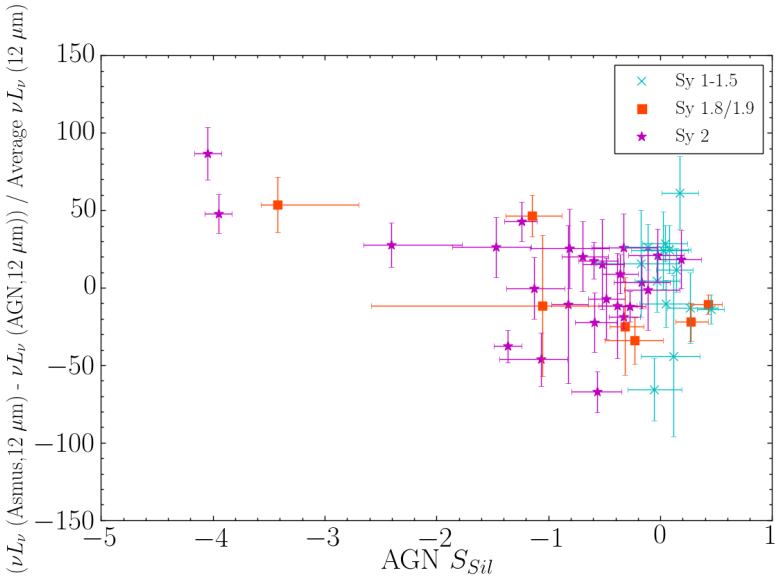

FIGURE 5.10: Differences in the 12 μm rest-frame luminosities versus the strength of the silicates. The different types of Seyfert are shown with different colours and symbols: Seyfert 1-1.5 (cyan crosses), Seyfert 1.8/1.9 (orange squares) and Seyfert 2 (magenta star symbols).

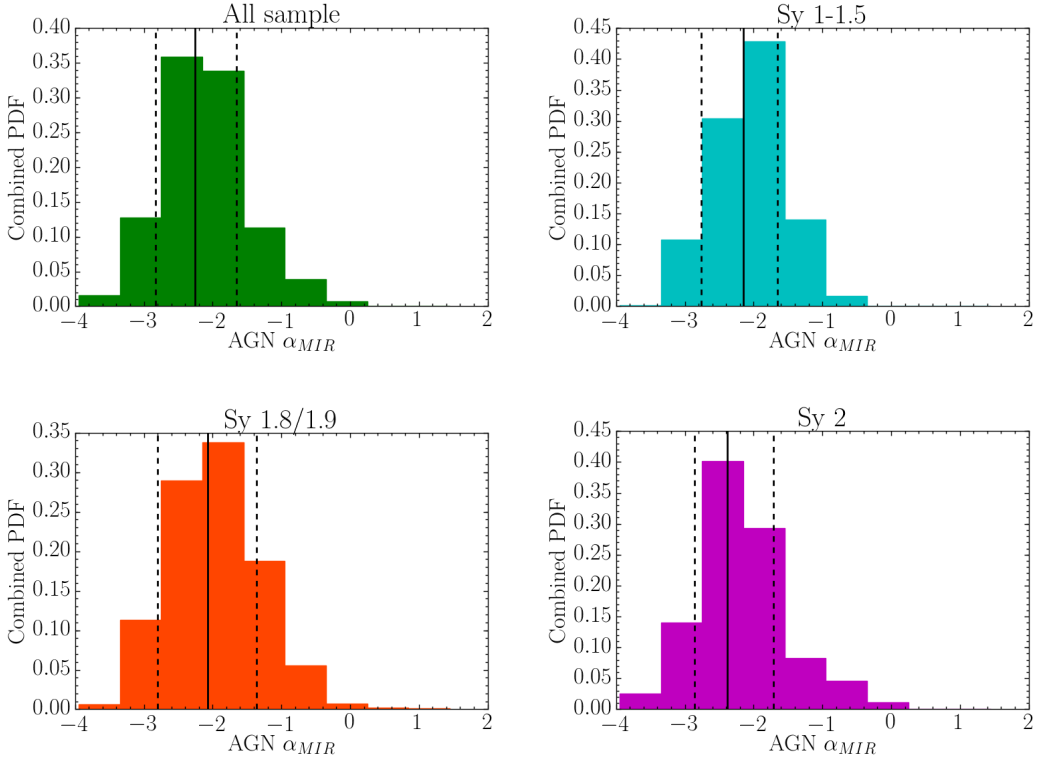

FIGURE 5.11: Combined probability distribution functions of the AGN MIR (8.1 – 12.5 μm) spectral index derived with DEBLENDIRS. In all panels the solid lines indicate the median of the distributions and the dashed lines the 16% and 84% percentiles. The top left panel is for the entire sample (green), the top right panel for Seyfert 1-1.5 galaxies (cyan), the bottom left panel for Seyfert 1.8/1.9 (orange), and the bottom right panel for Seyfert 2 galaxies (magenta).

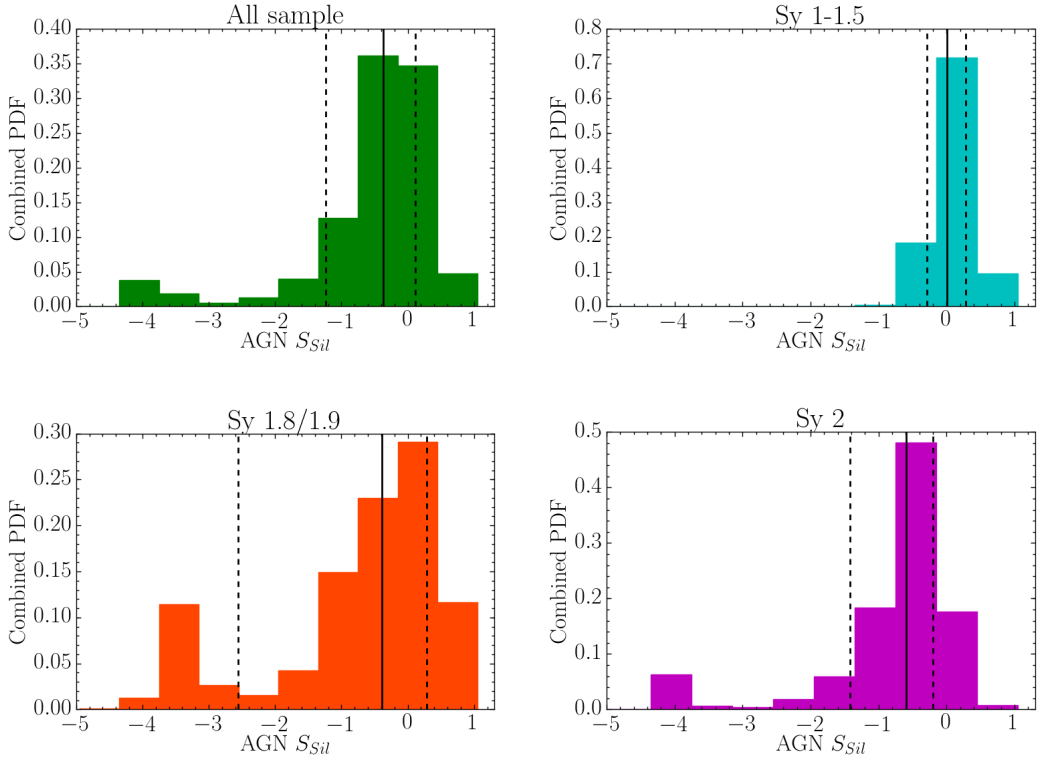

FIGURE 5.12: Combined probability distribution functions of the strength of the silicate feature derived with DEBLENDIRS. In all panels the solid lines indicate the median of the distributions and the dashed lines the 16% and 84% percentiles. The top left panel is for the entire sample (green), the top right panel for Seyfert 1-1.5 galaxies (cyan), the bottom left panel for Seyfert 1.8/1.9 (orange), and the bottom right panel for Seyfert 2 galaxies (magenta).

TABLE 5.7: Statistics of the combined probability distributions

	Number of galaxies	AGN $\alpha_{\rm MIR}$	AGN $S_{\rm Sil}$	AGN Frac. at 12 μm
All the sample	52	-2.3 [-2.8, -1.7]	-0.4 [-1.2, 0.1]	0.88 [0.73, 0.97]
Seyfert 1-1.5	15	-2.2 [-2.8, -1.7]	0.0 [-0.3, 0.3]	0.82 [0.68, 0.96]
Seyfert 1.8/1.9	7	-2.1 [-2.8, -1.4]	-0.4 [-2.6, 0.3]	0.86 [0.75, 0.97]
Seyfert 2	30	-2.4 [-2.9, -1.7]	-0.6 [-1.4, -0.2]	0.90 [0.76, 0.98]

Notes.– We give the median value and in parenthesis the 16% and 84% percentiles.

tail towards the feature in absorption whereas the Seyfert 1-1.5 show a narrow distribution peaking at $S_{\rm Sil} = 0$. This is the same result as obtained with the KS-test for the values of the individual galaxies (see Sections 5.4.1 and 5.4.2).

Although there are no statistically differences between the different types of Seyfert galaxies, the median combined AGN fractional contribution to $5 - 15\,\mu$m luminosity is slightly lower for Seyfert 1-1.5 than for Seyfert 2. This is in apparent contradiction with the isotropic emission at $12\,\mu$m explained in Section 5.4.2. The apparent contradiction of our results is easily explained with the differences in the slit width, that cover larger physical sizes in the Seyfert 1-1.5s than Seyfert 2s in our sample (see

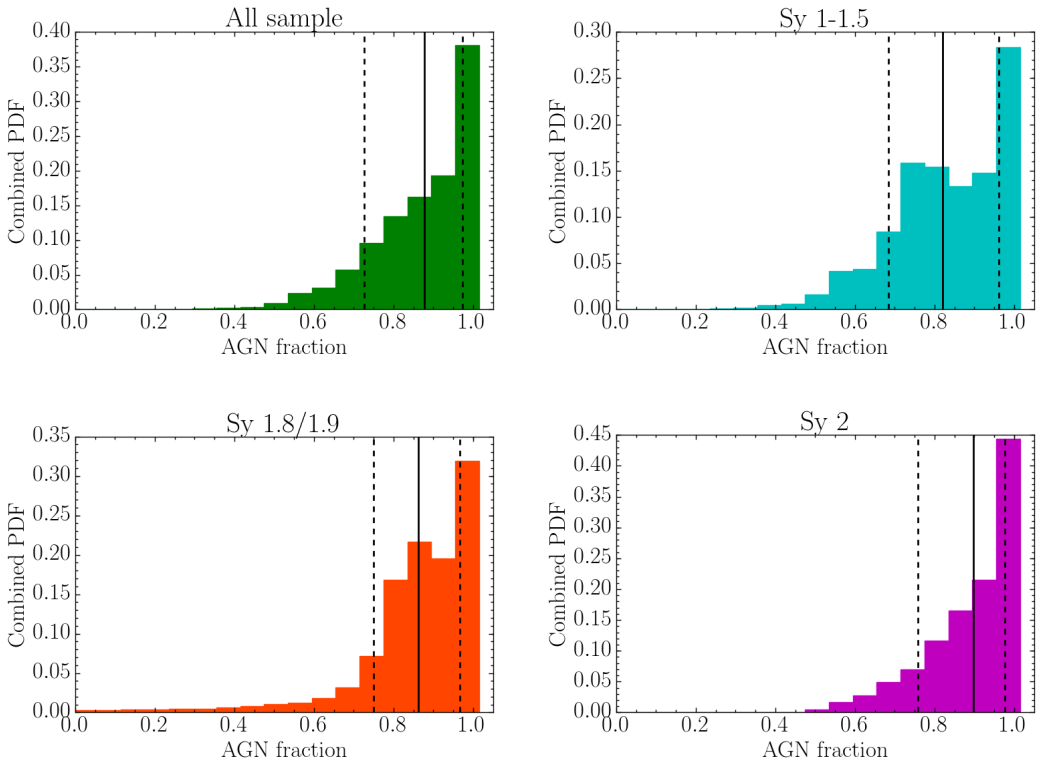

FIGURE 5.13: Combined probability distribution functions of the AGN fractional contribution to 5 – 15 μm luminosity from AGN template in the best fitting model. The solid lines indicate the median of the distributions and the dashed lines the 16 and 84 percentiles. The top left panel is for the entire sample (red), the top right panel for Seyfert 1-1.5 galaxies (cyan), the bottom left panel for Seyfert 1.8/1.9 (orange), and the bottom right panel for Seyfert 2 galaxies (magenta).

Section 5.2). A larger physical size would in principle imply more contribution from emission from the host galaxy in the MIR spectrum, so the AGN contribution to the total flux is lower for these galaxies.

5.5 Statistical comparison with the CAT3D clumpy torus models

As explained in Chapter 1, many observational properties of AGN are explained if there is a clumpy dusty torus surrounding the central engine of an active galaxy. In this Section we compare the MIR properties of AGN, namely, the strength of the silicate feature and the MIR spectral index with predictions of the CAT3D clumpy torus models of Hönig and Kishimoto (2010) including new models with improved physics.

5.5.1 Brief description of the models

In this work we used the Hönig and Kishimoto (2010) CAT3D clumpy torus models that provide the model SED for clumpy dust emission in a torus around the AGN accretion disk. These models are

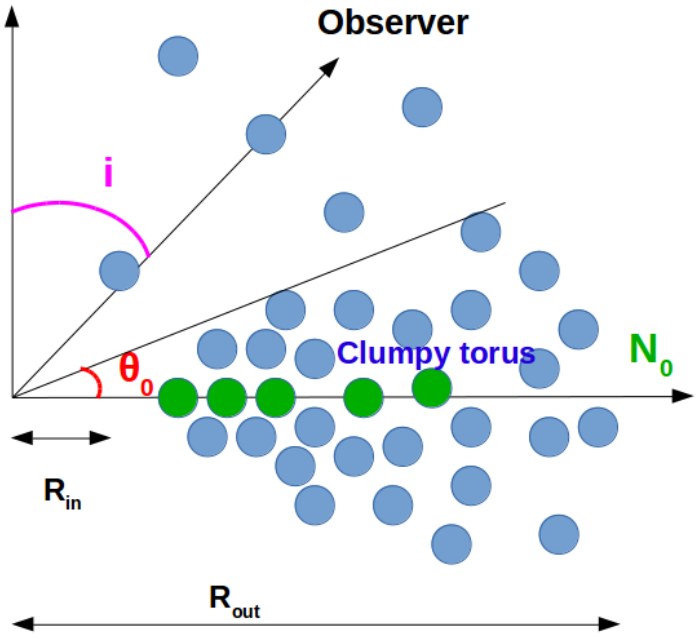

FIGURE 5.14: Representation of the CAT3D clumpy torus showing some of the parameters that characterize the models, namely the half-covering angle, in red; the inclination, in magenta, the number of clouds along an equatorial line-of-sight, in green; and the outer torus radius, in black.

characterized by six parameters that have direct influence on the IR SEDs of AGN. These are: (1) the power-law index of the radial dust-cloud distribution a, that is $\propto r^a$; (2) the half-covering angle of the torus θ_0; (3) the number of clouds along an equatorial line-of-sight N_0; (4) the torus outer radius $R_{\rm out}$; (5) the optical depth of the individual clouds $\tau_{\rm V}$; and (6) the inclination (i.e., the viewing angle) i. In Fig. 5.14 we show a sketch of some of the CAT3D torus model parameters. The AGN is assumed to be radiating in an isotropic manner.

In Fig. 5.15 we show the false colour images of dusty clumpy torus for two examples representative of a type 1 and type 2 AGN. The dusty clouds are coloured in terms of their emission. The blue, green, and red colours represent the near-IR, MIR, and FIR emission, respectively. As can be seen from these figures, most of the NIR and MIR emission arises from the inner part of the torus where the dust is hot and warm, respectively. Most of the FIR emission comes from the outer part of the torus where the dust is cooler. Clearly, in a type 1 view (left panel) we can see more NIR and MIR emission than in a more edge-on view (similar to a type 2 in first approximation).

The Hönig and Kishimoto (2010) CAT3D clumpy torus models (hereafter old models) assume a standard interstellar medium (ISM) composition for the dust, containing 47% of graphite and 53% of silicates. The new version of the models (hereafter referred to as new models) includes additional more realistic physics in an attempt to model the differential dust grain sublimation. According to Phinney (1989), it is expected that graphite grains can sustain higher temperatures than silicate grains,

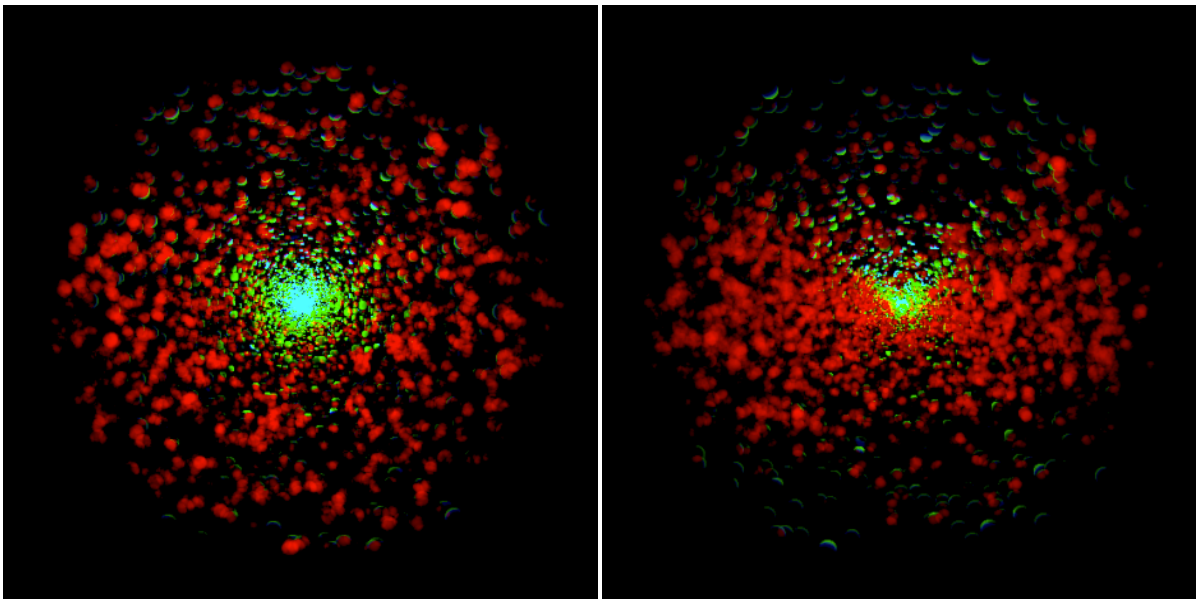

FIGURE 5.15: Representation of the dusty clumpy torus for type 1 (left) and type 2 (right). The blue, green, and red colours represent the near-IR, MIR, and FIR emission respectively.

with the former being able to heat up to $\sim 1900 - 2000$ K and the latter sublimating at $\sim 800 - 1200$ K, depending on density. The sublimation model assumes that silicates are sublimated away once their temperature goes above 1250 K. This means that all those clouds as close to the AGN as to heat up to temperatures above 1250 K will not contain any silicates. Therefore, in the new models the absorption and scattering efficiencies are adjusted accordingly. In addition, the hottest dust at T $\sim$ 1900 K will only contain larger graphite grains, i.e. the minimum grain size for the ISM dust size distribution is increased from 0.025 μm to 0.075 μm. This accounts for the fact that small grains are cooling less efficiently and will reach the sublimation temperature at larger distances than larger grains. As we shall see, since graphites have higher emissivity, this will result in bluer NIR to MIR SEDs for a given set of torus model parameters than in the old models, which had plain and standard ISM dust composition without a sublimation model. We note that the new physics included in the new models is unique to these models and is not taken into account in other available clumpy torus models. Additionally, it may solve the problem of the excess of nuclear NIR emission with respect to the current clumpy torus predictions found mostly for type 1 AGN (Mor et al. 2009; Alonso-Herrero et al. 2011; Ichikawa et al. 2015) but also type 2 AGN (Lira et al. 2013)

The old and the new models cover different ranges of the torus parameters. In Table 5.8 we list the values used in the old and new models. The index of the radial distribution of clouds a covers different ranges, namely [0.00, -2.00] for the old models and [0.50, -1.75] for the new ones, and different steps of 0.50 and 0.25, respectively. We note that for the new models we are adding inverted radial cloud distributions (positive values of a). Although, probably not very common, inverted radial distributions resemble a disk-like accretion flow that thins out towards the inner radius. This may be the kind of geometry needed to explain the population of hot dust poor quasars (Hao et al. 2010). In the case of

Table 5.8: Parameters of the CAT3D clumpy torus models.

	Old models	New models
a	0.00, -0.50, -1.00, -1.50, -2.00	0.50, 0.25, 0.00, -0.25, -0.50, -0.75, -1.00,-1.25, -1.50, -1.75
θ_0	30°, 45°, 60°, 85°	30°, 45°, 60°
N_0	2.5, 5.0, 7.5, 10.0	2.5, 5.0, 7.5, (10.0, 12.5)*
τ_V	30, 50, 80	50
R_{out}	150	450
i	0°, 15°, 30°, 45°, 60°, 75°, 90°	0°, 15°, 30°, 45°, 60°, 75°, 90°

Notes.— *The values of $N_0 = 12.5$ are only for models with $a < 0$ and the values of $N_0 = 10.0$ only for models with $a \leqslant 0$ for computational reasons.

the half-covering angle of the torus θ_0, the old models provided more values ($\theta_0 = 30°, 45°, 60°, 85°$) than the new ones ($\theta_0 = 30°, 45°, 60°$). For the number of clouds N_0 the ranges are also different, [2.5, 10.0] for the old models and [2.5, 12.5] for the new models, both in steps of 2.5.

The new and old CAT3D models have different values of the torus outer radius R_{out} (measured in units of the sublimation radius) due to the smaller dust sublimation radius of the graphite/large dust grains than the silicate grains[3]. Also, the value of the outer radius of the torus needs to be sufficiently large so that it encompasses the physical sizes of the torus measured at all wavelengths. This way and from the perspective of the dust and temperature distributions, the new models are the same as the old models just with a smaller inner radius. In the old models we have three values of cloud optical depth τ_V, 30, 50, and 80, whereas the new models only have one value $\tau_V = 50$. The range of the inclination i is the same for both, the old and the new models, from 0° to 90° in steps of 15°.

To calculate the IR SEDs of these models several steps are carried out. The first step is to simulate each cloud by Monte Carlo radiative transfer simulations. Then, dust clouds are randomly distributed around the AGN, according to the physical and geometrical parameters, each one associated with a model cloud from the first step. The final torus SED is calculated via raytracing along the line-of-sight from each cloud to the observer. This method allows to take into account the three dimensional distribution of clouds and the statistical variations of randomly distributed clouds. We refer the reader to Hönig and Kishimoto (2010) for a complete description of the calculations.

As explained above, the old and new models cover different ranges of torus parameters. We have a total of 1680 configurations for old models and 966 configurations for new models, with 336 configurations sharing the same values of the parameters. For each configuration of parameters, we have one SED obtained from a random arrangement of clouds for the old models and ten for the new ones, obtained from ten random distributions of the clouds satisfying the same configuration of parameters.

In Fig. 5.16 we show some examples of SEDs for the old and the new models in dashed and solid lines respectively, for a random cloud distribution. Each column represents a different inclination ($i = 0°$,

[3] According to Hönig and Kishimoto (2010), 0.305 pc is the sublimation radius for large grains and 0.955 pc for the typical ISM dust composition and an AGN bolometric luminosity of 10^{46} erg s^{-1}, see their table 2.

45°, and 90°) and each row different values of the number of clouds in the equatorial line-of-sight (N_0 = 2.5, 5.0, 7.5, and 10.0). They all have fixed values of τ_V = 50 and θ_0 = 45°. Each panel shows four different values of the power-law index of the radial dust-cloud distribution, a, indicated with different colours. For both the old and new models the total SEDs becomes redder when the radial cloud distribution becomes flatter (more positive values of a). As explained in Hönig and Kishimoto (2010), this is because the flat power-law distributions have more cool dust at larger distances. There are differences in the continuum shape depending of the value of a. For the flat and nearly flat distributions (a = 0.0 and -0.50), the continuum peaks at longer wavelengths than for the steeper distributions ($a = -1.0$ and -1.50). This is because in the steeper distributions there is more dust at small distances from the AGN so the average dust temperature is higher (Hönig and Kishimoto 2010). This trend does not depend on the inclination.

The a values also have an effect in the strength of the silicate feature. For the steepest value of a (a = -1.5), the silicate feature is always in emission, whereas for the rest of the a values the strength of the feature depends on the values of N_0 and the inclination. While the SEDs have a substantial dependence on a, the dependence on N_0 is small. This dependence on N_0 is more important for the strength of the silicate feature than for the shape of the SED (related to α_{MIR}). The silicate feature in emission is the strongest for N_0 = 2.5, whereas the feature becomes less prominent when there are more clouds along the equatorial direction (larger values of N_0). In the case of the silicate in absorption, for higher N_0 and higher inclination the absorption is deeper. As expected, the new models have bluer SEDs for a given set of torus parameters than the old models. The differences in the shape are larger for the steepest distributions ($a = -1.5$), as there is more dust at small distances from the AGN, containing only graphite for the new models while the old models have silicates and graphites at the same distance. The differences also increase when there are more clouds along the equatorial direction (larger values of N_0) and for more inclined views.

In Fig. 5.17 we show the SEDs for the new models, as in Fig. 5.16, but representing ten random distributions of clouds for each configuration of parameters. The differences between the random distributions for the same parameters are larger for more inclined views and for the flattest radial distributions (a = 0.0 and -0.50). This figure shows the importance of doing several random distributions instead of using only one.

5.5.2 CAT3D predictions for the MIR emission

In this section we present the CAT3D torus model predictions for the MIR emission of AGN and in particular for the properties we analysed in Section 5.4, namely the MIR spectral index and the strength of the silicate feature. As explained by Hönig and Kishimoto (2010), although the angular size of the torus, θ_0, could be an additional source of degeneracy, there is a strong relation between the index of the dust radial distribution, a and the MIR spectral index. There is also a strong relation between the

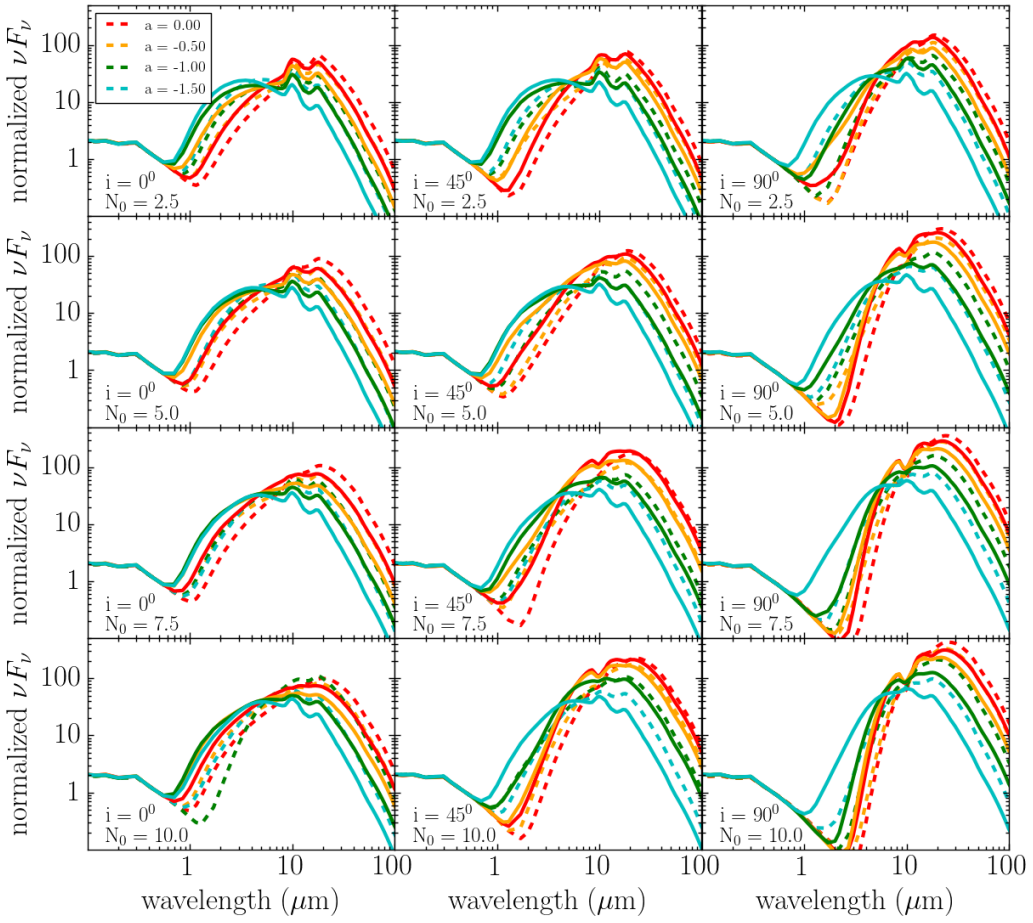

FIGURE 5.16: Old models SEDs (dashed lines) and new models SEDs (solid lines) normalized at 0.5 μm. From top to bottom, the rows show an increasing number of N_0, N_0 =2.5, 5.0, 7.5, and 10.0, respectively. The left column shows models for an inclination of 0°, the middle column is for i = 45° and the right column is for i = 90°. In each panel we show the SEDs for one random cloud distribution for a = 0.00 (red), -0.50 (orange), -1.00 (green), -1.50 (cyan). They all have fixed values of τ_V = 50 and θ_0 = 45°.

number of clouds along the equatorial direction, N_0, and the strength of the silicate feature, even though the strength of the silicate feature also depends on a and τ_V. Using the clumpy torus models of Nenkova et al. (2008a,b), Ramos Almeida et al. (2014b) investigated the sensitivity of different observations in the near and MIR to these torus model parameters. Specifically, they found that a detailed modelling of the 8 − 13 μm spectroscopy (not only the spectral index and strength of the silicate feature) of Seyfert galaxies can constrain reliably the number of clouds and their optical depth.

We measured for each SED the spectral index and the strength of the silicate feature in the same way as in Section 5.3.2, i.e., with the same method we used to measure directly from spectra. We use the 8.1 and 12.5 μm values to estimate the flux ratios, 8 and 14 μm to fit the continuum and 10 μm for the peak of the silicates, as the CAT3D models have both, the emission and the absorption features centred

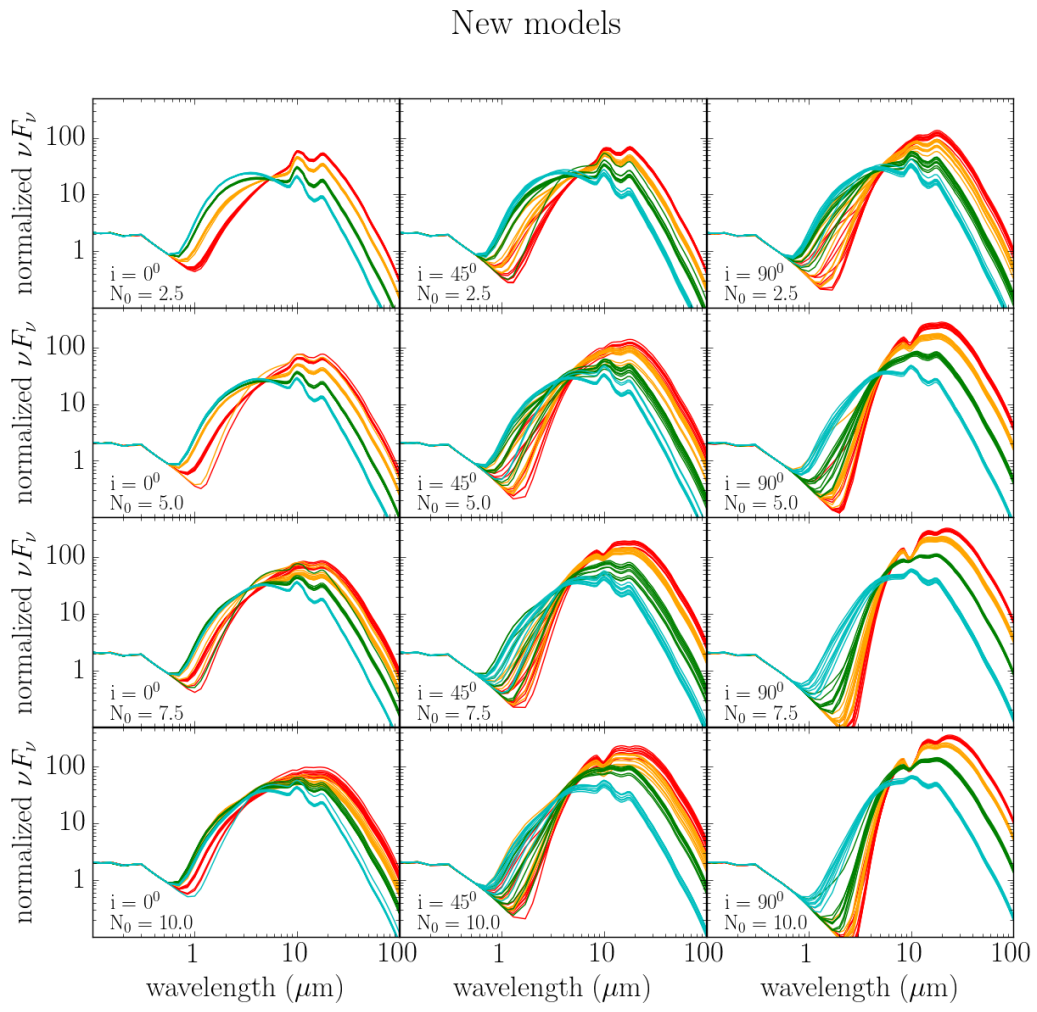

FIGURE 5.17: Same as Fig. 5.16 but only for the new models and showing ten random distributions of clouds for each configuration of parameters.

at 10 μm (Hönig et al. 2010). For the old models, for each of the 336 configurations we obtained one value of the spectral index and the strength of the silicate feature. For the new models we measured ten values for each configuration, which allows us to estimate the average and the standard deviation for the ten values of the spectral index and the strength of the silicate feature for each configuration of parameters. The typical scatters in the measured $\alpha_{\rm MIR}$ are 0.02 – 0.06, although in the case of a radial distribution index $a = 0.5$ the scatter can be as high as 0.2. The typical scatter in the measured $S_{\rm Sil}$ is 0.01 – 0.04.

In Fig. 5.18 we show the MIR spectral index against the strength of the silicate feature for the old and new models. Each panel displays the values for the entire range in a (dotted lines) and N_0 (dashed lines) for a fixed inclination and torus half-covering angle, θ_0. As can be seen from these figures, for a given configuration of set θ_0 and i, fewer clouds along the equatorial direction tend to produce weaker silicate features than configurations with more clouds with a slight dependence with the optical depth of the clouds $\tau_{\rm V}$. Interestingly, for both the old and the new models for thin tori, $\theta_0 = 30°$ and values

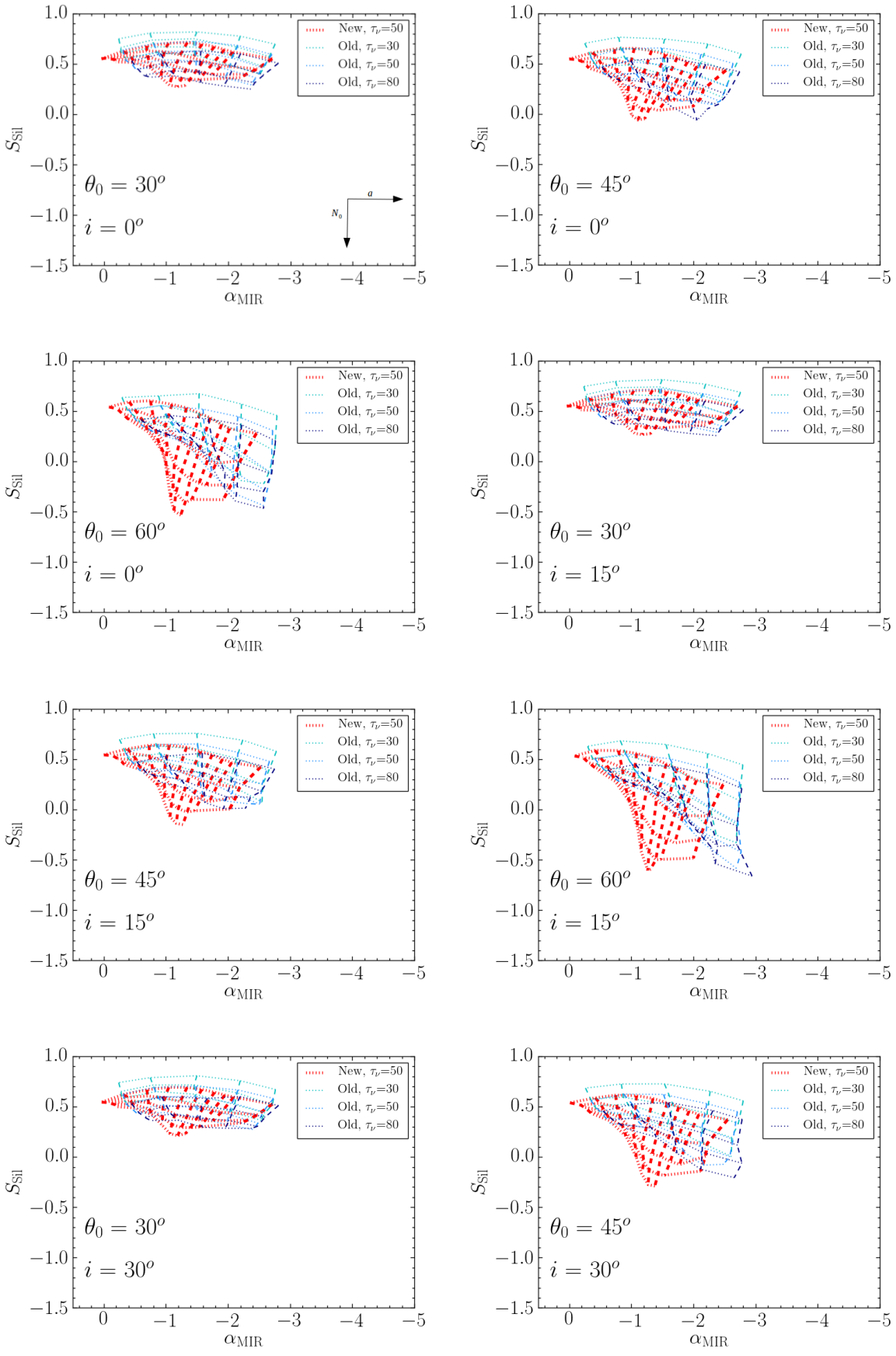

FIGURE 5.18: Strength of the silicate feature against the MIR spectral index for the old models (in light blue $\tau_V = 30$, medium blue $\tau_V = 50$, and dark blue $\tau_V = 80$), and the new models (in red, $\tau_V = 50$). Each panel shows the estimated values for all range of a (dotted lines, values of a becoming more negative to the left) and N_0 (dashed lines, larger values moving down) for a fixed inclination and torus half-covering angle.

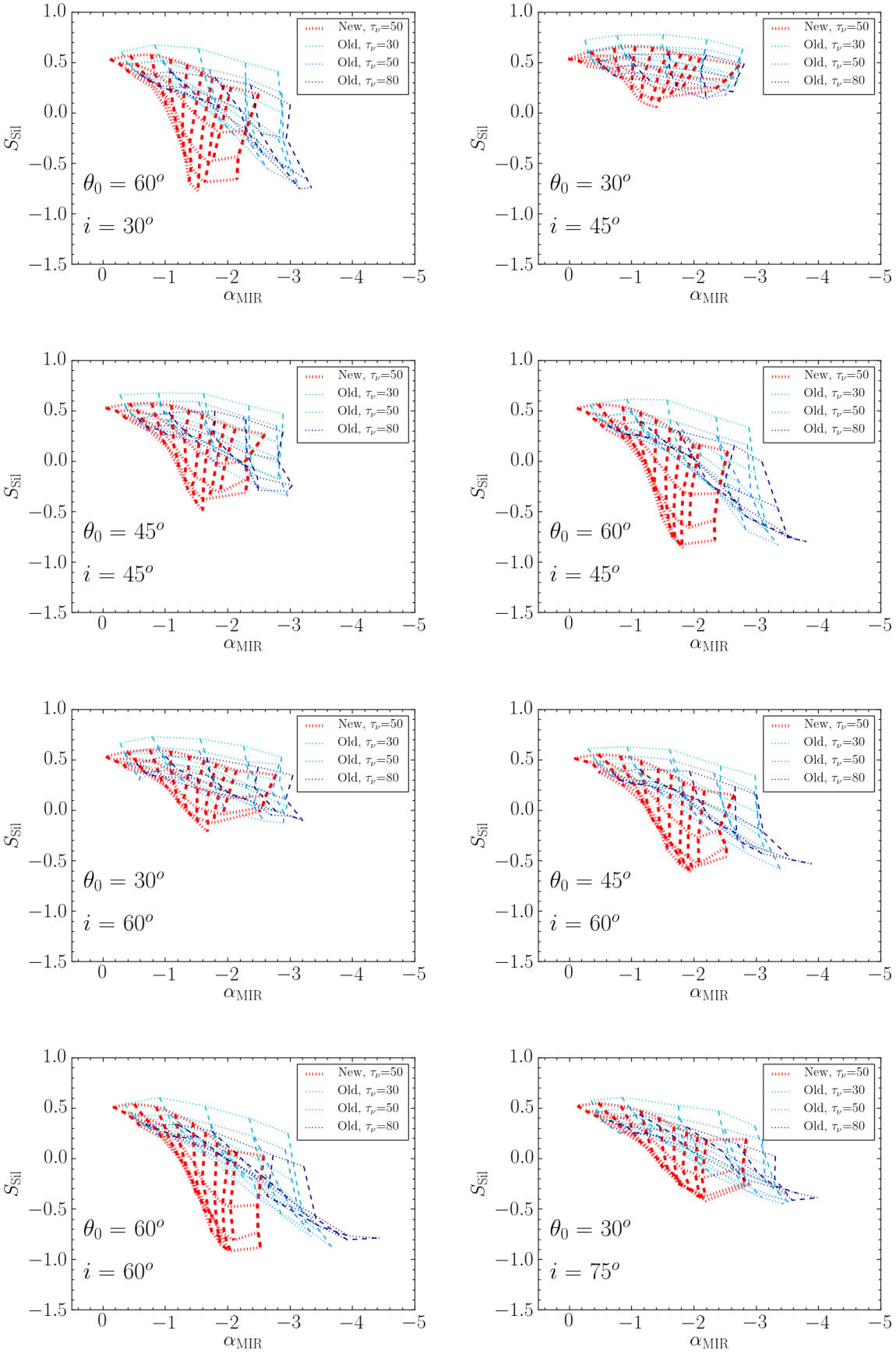
New, τ_ν=50
Old, τ_ν=30
Old, τ_ν=50
Old, τ_ν=80
$\theta_0 = 60^o$
$i = 30^o$
$\theta_0 = 30^o$
$i = 45^o$
$\theta_0 = 45^o$
$i = 45^o$
$\theta_0 = 60^o$
$i = 45^o$
$\theta_0 = 30^o$
$i = 60^o$
$\theta_0 = 45^o$
$i = 60^o$
$\theta_0 = 60^o$
$i = 60^o$
$\theta_0 = 30^o$
$i = 75^o$
$S_{\rm Sil}$
$\alpha_{\rm MIR}$

FIGURE 5.18

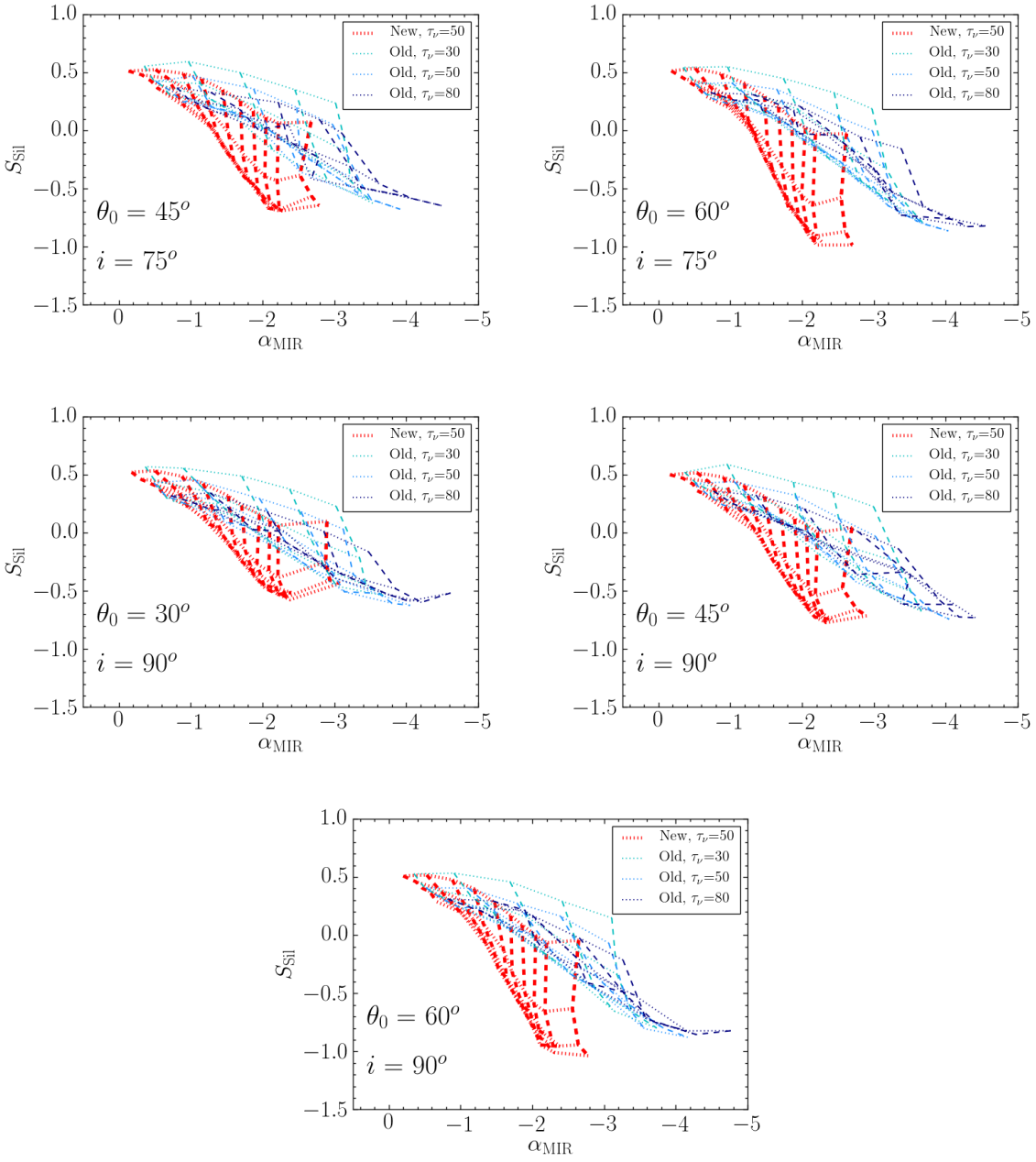
New, τ_ν=50
Old, τ_ν=30
Old, τ_ν=50
Old, τ_ν=80
$\theta_0 = 45^o$
$i = 75^o$
$\theta_0 = 60^o$
$i = 75^o$
$\theta_0 = 30^o$
$i = 90^o$
$\theta_0 = 45^o$
$i = 90^o$
$\theta_0 = 60^o$
$i = 90^o$
$S_{\rm Sil}$
$\alpha_{\rm MIR}$

FIGURE 5.18

of the inclination of $i < 45°$, the silicate feature is always produced in emission. We can also see from these figures that thicker tori tend to decrease the strength of the silicate feature when seen in emission or make it deeper when the silicate is in absorption.

For the predicted MIR ($8.1 - 12.5\,\mu$m) spectral index there is a clear dependence with the index of the radial distribution and the thickness of the torus in the sense that thicker tori and steeper dust radial distributions (more negative values of a) produce more negative spectral indices. However, this strictly applies only to geometries and viewing angles where self-obscuration is not strong (that is, few clouds and low-intermediate values of i). On the other hand, for a given value of θ_0 and a range of values of a and τ_V, the spectral index has only a small dependence in terms of the viewing angle, the spectral index becoming steeper for more inclined views.

Hönig and Kishimoto (2010) stated that there is very little dependence of model output SED on the assumed optical depth of the clouds and that $\tau_V = 50$ for a standard ISM composition gives a good representation of observations. In Fig. 5.18 we can see indeed that the dependence of the MIR spectral index and strength of the silicate feature on τ_V is small for the old models. The only noticeable trend when the silicate feature is in emission is that the $\tau_V = 30$ models always produce a stronger feature than the $\tau_V = 80$ models. For inclinations $i < 45°$ when the feature is observed in absorption also the $\tau_V = 30$ models always produce a stronger feature than the $\tau_V = 80$ models.

In order to make a better comparison between the old and the new models we repeat in Fig. 5.19 the comparison of the strength of the silicate feature and the MIR spectral index for the old and new models but only for the parameters in common. That is, $\tau_V = 50$; a = 0.00, -0.50, -1.00, -1.50; and N_0 = 2.5, 5.0, 7.5, 10.0. Looking at the figure we can see that for the same configuration (same i, θ_0, a and N_0) the new models reach a less negative value of the MIR spectral index. This is expected due to the sublimation model introduced in the new models, as explained at the beginning of this section. Due to self-obscuration effects becoming important further in, the silicate-bearing clouds are on average cooler, thereby contributing more to silicate absorption via obscuration/extinction than to emission. For this reason, it is necessary to include positive values of a for the new models, in order to reach more negative values of the MIR spectral index. In the case of the strength of the silicate feature, the new models appear to produce always slightly deeper silicate features with the differences becoming larger for the thickest tori and more inclined views.

5.5.3 Comparison between old and new model predictions and observations

In this section we compare the predictions for the MIR emission of the old and new CAT3D models with our observations of Seyfert galaxies to see if the improved physical model for the dust sublimation produces a better description of the observations.

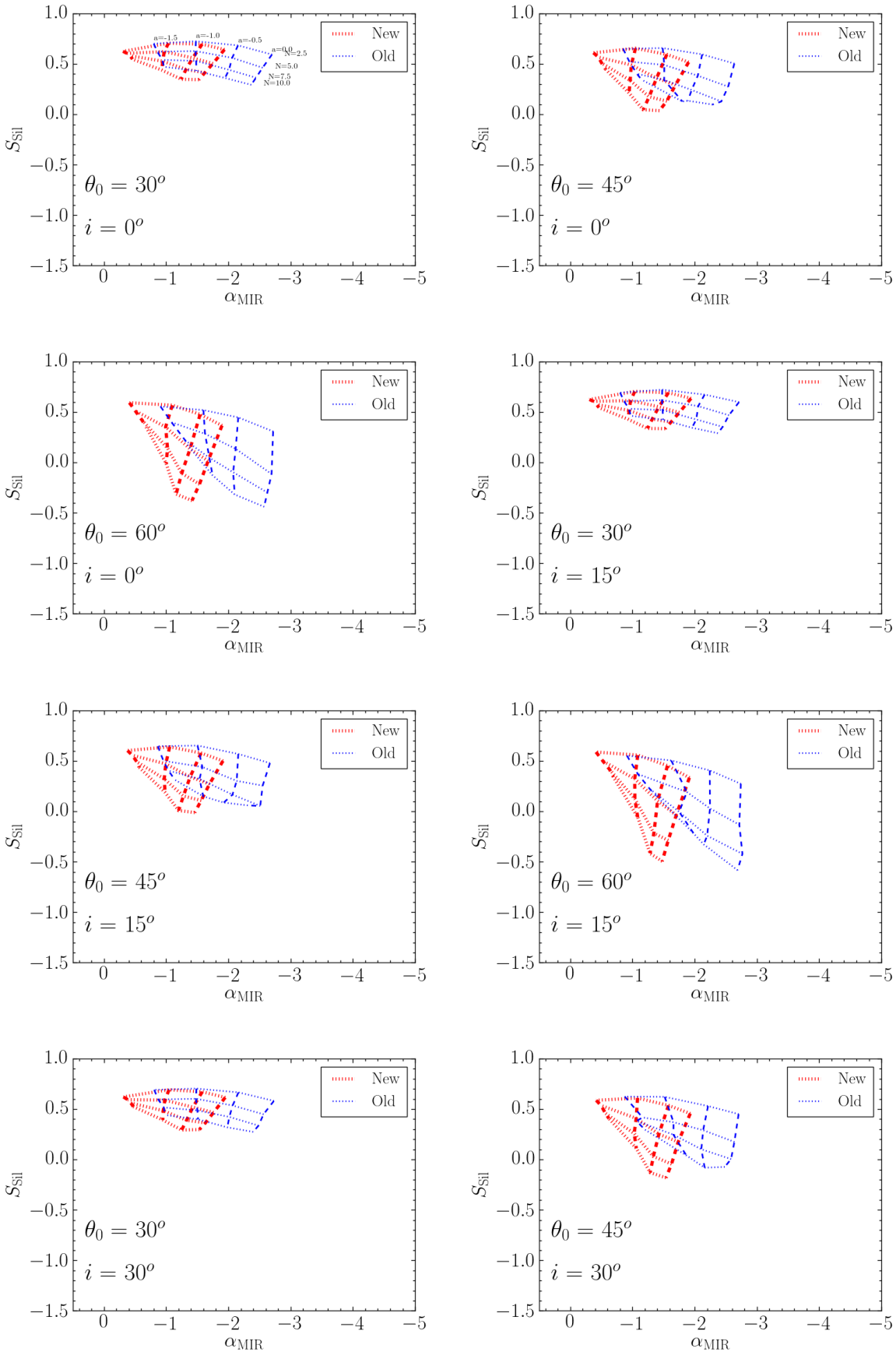

FIGURE 5.19: Comparison of the strength of the silicate feature and the MIR spectral index for the old models (in blue), and the new models (in red) only for the common parameters (see Table 5.8). Each panel shows the estimated values for different values (see top left panel) of a (dotted lines) and N_0 (dashed lines) for a fixed inclination and torus half-covering angle.

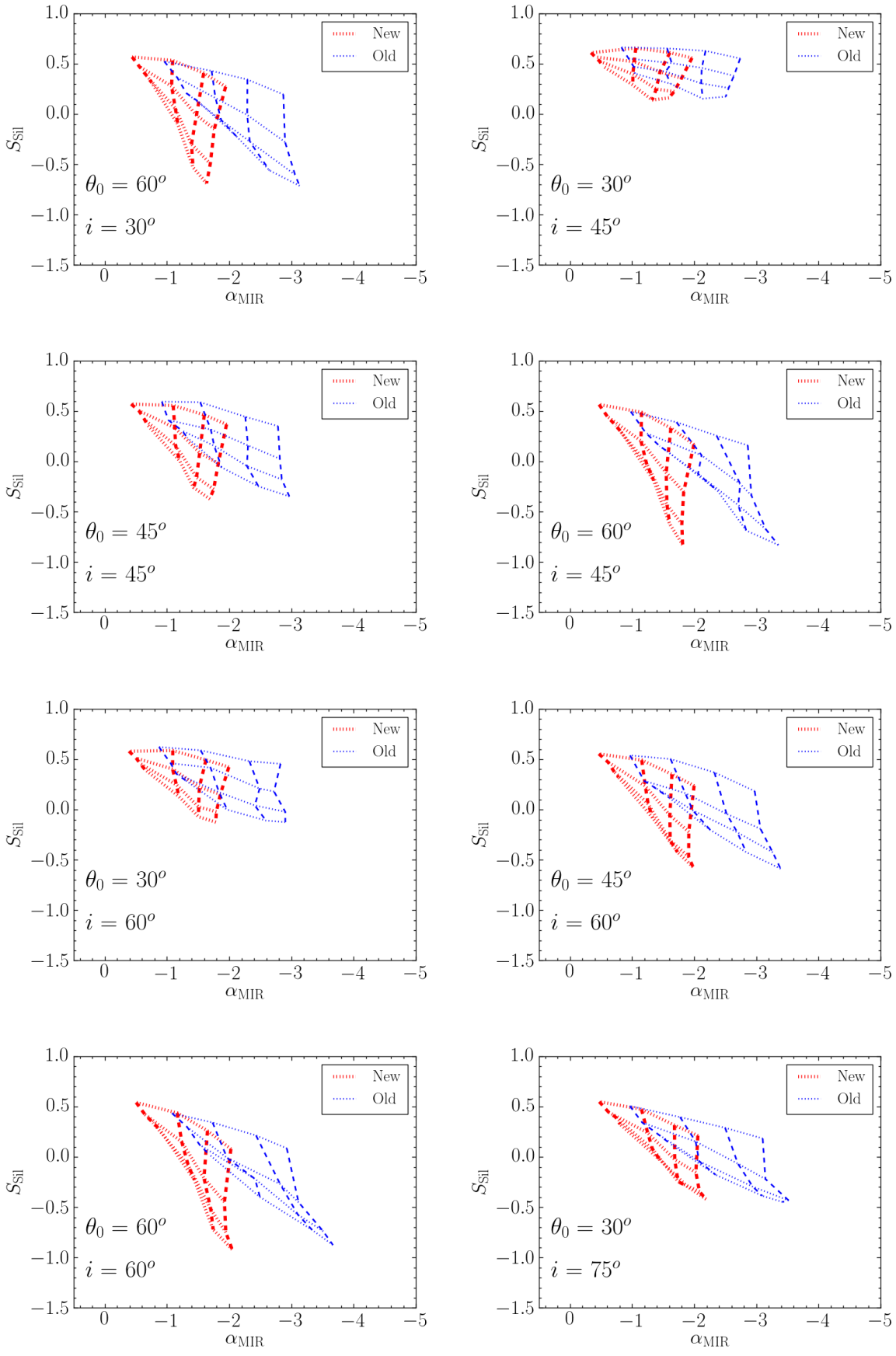
New
Old
$\theta_0 = 60^o$
$i = 30^o$
$\theta_0 = 30^o$
$i = 45^o$
$\theta_0 = 45^o$
$i = 45^o$
$\theta_0 = 60^o$
$i = 45^o$
$\theta_0 = 30^o$
$i = 60^o$
$\theta_0 = 45^o$
$i = 60^o$
$\theta_0 = 60^o$
$i = 60^o$
$\theta_0 = 30^o$
$i = 75^o$
$S_{\rm Sil}$
$\alpha_{\rm MIR}$

FIGURE 5.19

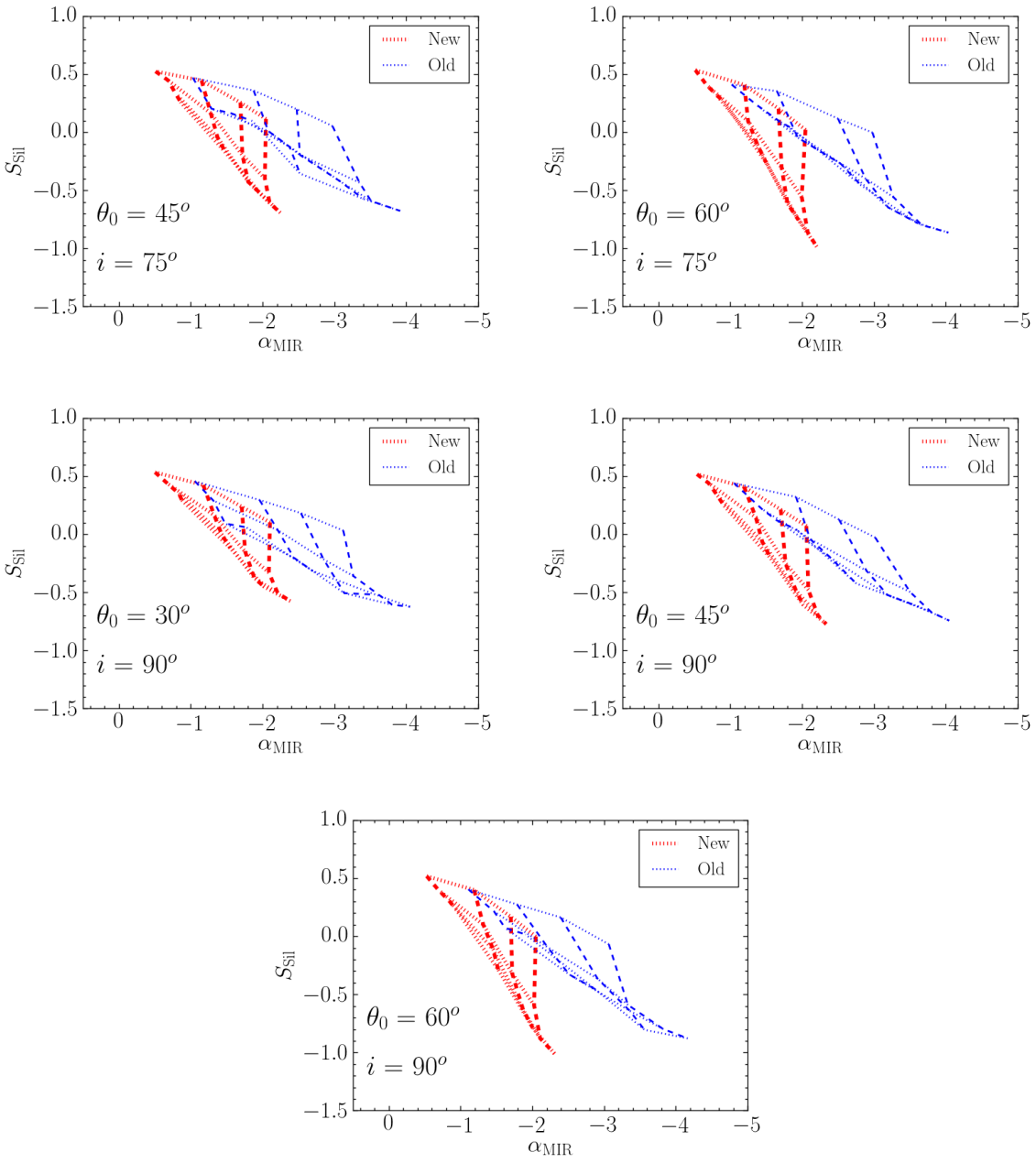
New
Old
$\theta_0 = 45^o$
$i = 75^o$
$\theta_0 = 60^o$
$i = 75^o$
$\theta_0 = 30^o$
$i = 90^o$
$\theta_0 = 45^o$
$i = 90^o$
$\theta_0 = 60^o$
$i = 90^o$
$S_{\rm Sil}$
$\alpha_{\rm MIR}$
1.0
0.5
0.0
−0.5
−1.0
−1.5
0
−1
−2
−3
−4
−5

FIGURE 5.19

In Fig. 5.20 we compare the spectral index and the strength of the silicate feature for the Seyfert galaxies obtained with DEBLENDIRS and the 10 IR-weak quasars from Alonso-Herrero et al. (2016b) with the values obtained for the old models (left panel) and new models (right panel). The model symbols are colour coded in terms of the AGN produced photon escape probability. As the classification in Seyfert 1 or 2 is a probabilistic effect in torus models where the dust in distributed in clumps, to compare the models with the Seyfert galaxies, we calculate for each model the probability that an AGN produced photon escapes unabsorbed, using the following expression:

$$P_{\rm esc} = exp\left(-N_0 \times exp\left(\frac{-(90-i)^2}{{\theta_0}^2}\right)\right) \tag{5.1}$$

If the escape probability is high the models correspond to a Seyfert 1 galaxy, and if the probability is low to a Seyfert 2 galaxy (Elitzur 2012). The idea is to have a gradual transition between Seyfert 1 and Seyfert 2 instead of using an arbitrary value of the probability to separate the models between type 1 and type 2. We note that Hönig et al. (2010) used an inclination criterion to separate Seyfert 1 (inclination of $i = 30°$) and Seyfert 2 (inclination of $i = 75°$) models. However, Ramos Almeida et al. (2011a) and Alonso-Herrero et al. (2011) demonstrated that the viewing angle is not the determinant torus parameter to separate out Seyfert 1 and Seyfert 2, and therefore the escape probability of an AGN-produced photon is a better way to separate the Seyfert 1 models from the Seyfert 2 models (see also Elitzur 2012). Indeed, as can be seen from Fig. 5.20, most Seyfert 2 nuclei are close to models with low escape probabilities, although the Seyfert 1 nuclei in this diagram are in a region populated by models with both low and relatively high escape probabilities (see next section too). However, for the new CAT3D models the majority of silicate features in emission are observed for parameter configurations resulting in relatively high escape probabilities as also found by Nikutta et al. (2009) for the clumpy models.

In general, Fig. 5.20 shows that the new models represent better the distributions of the MIR spectral indices and strengths of the silicate features of the IR-weak quasars, the Seyfert 2 and Seyfert 1.8/1.9 galaxies than the old ones. The Seyfert 1-1.5 are well represented with both the old and the new models. Finally, the old models for certain parameter configurations produce very steep MIR spectra indices (up to $\alpha_{\rm MIR} = -4$) that are not observed in Seyfert nuclei or local type 1 quasars. We therefore conclude that the new models with the improved dust physics reproduce better the MIR properties of the local type 1 (IR-weak) quasars, the Seyfert 2 and Seyfert 1.8/1.9 galaxies.

From Fig. 5.20 we can see that neither the new nor the old models explain those galaxies with nuclear deep silicate absorption, i.e. values of the strength of the silicate feature approximately $S_{\rm Sil} < -1$. This is similar to findings by other works (Levenson et al. 2007; Sirocky et al. 2008; Alonso-Herrero et al. 2011; González-Martín et al. 2013) using the clumpy torus models of Nenkova et al. (2008a,b). There are 11 galaxies in our sample whose values are not represented by the new models and we study the possibility that they are objects with host obscuration. Eight of them are classified as Seyfert 2, namely,

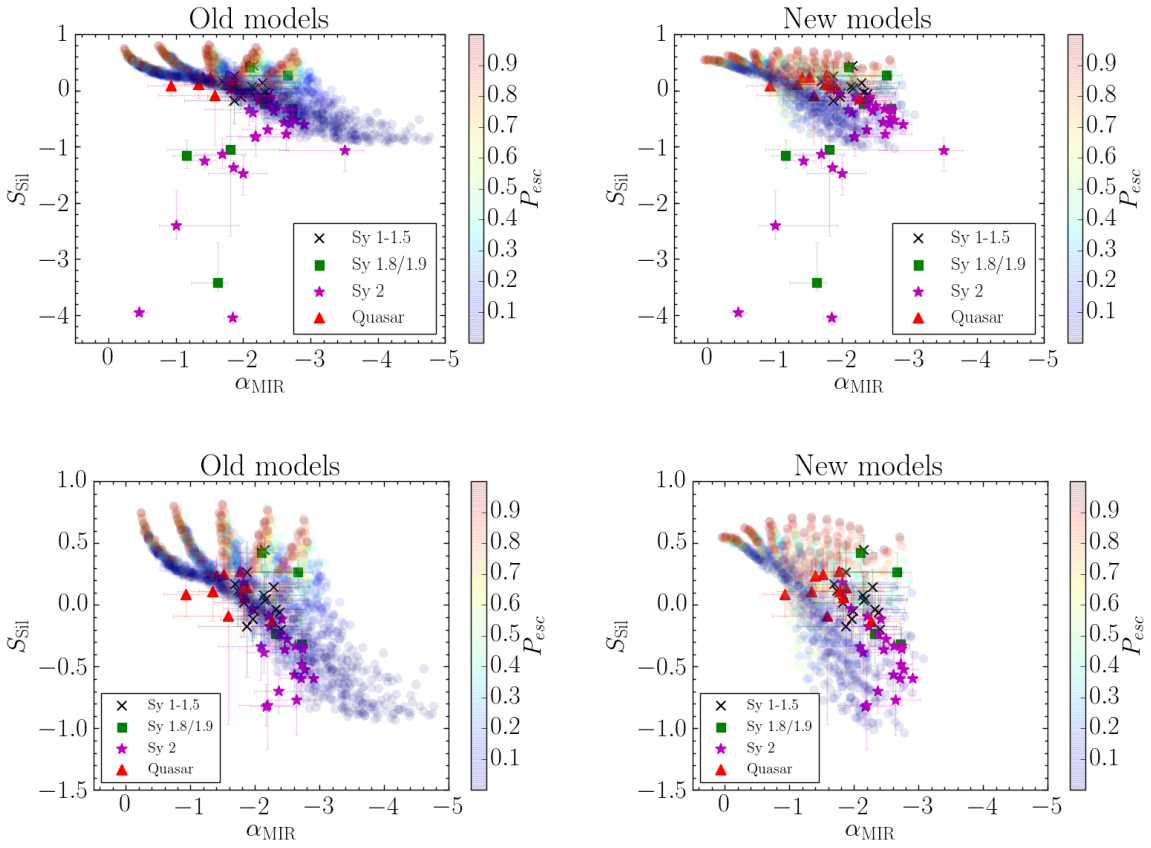

FIGURE 5.20: Top: Comparison between the MIR spectral index and the strength of the silicate feature for the Seyfert galaxies in our sample and the IR-weak quasars from (Alonso-Herrero et al. 2016b) with the values for all parameters (see Table 5.8) of the CAT3D old torus models (left) and the new torus models (right) The model symbols are colour coded in terms of the escape probability (see equation 5.1) of an AGN-produced photon. The different types of Seyfert are shown with different colours and symbols: Seyfert 1-1.5 (black crosses), Seyfert 1.8/1.9 (green squares), Seyfert 2 (magenta star symbols), and IR-weak quasars (red triangles). Bottom: Same as upper panels but excluding those galaxies not represented by the models and thus zooming in the Y axis for $S_{Sil} > -1.5$.

Circinus, IC 4518W, NGC 3094, NGC 3281,NGC 4388, NGC 4418, NGC 7172, and NGC 7582 and 3 of them Seyfert 1.8/1.9 galaxies, namely, NGC 1194, NGC 5506 and NGC 7479. In Fig. 5.21 we show the distribution of the inclination of the host galaxy (b/a) for all Seyfert 2 and 1.8/1.9 galaxies and the galaxies that are not represented by the new models. We can see that the galaxies not represented by the CAT3D torus models tend to be in more edge-on galaxies (lower values of b/a) when compared with all Seyfert 2 and 1.8/1.9. This result is in agreement with Goulding et al. (2012) and the other works discussed in Section 5.4.1. However, a KS-test shows that both distributions are not statistically significantly different ($p = 0.08$).

It is possible that the presence of host galaxy obscuration in highly inclined galaxies produces MIR spectral indices and silicate features that cannot be explained even with the new CAT3D models. Also, as previously noted by González-Martín et al. (2013), some of these are in interacting systems or systems with disturbed morphologies (i.e., IC 4518W and NGC 7479). Finally, Alonso-Herrero et al.

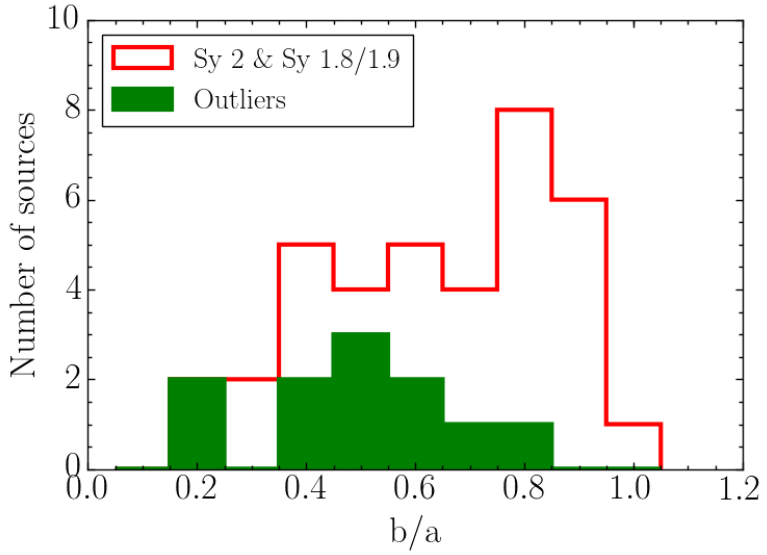

FIGURE 5.21: Distribution of the inclination of the host galaxy (b/a) for all Seyfert 2 and 1.8/1.9 galaxies (red histogram) and for the outliers, i.e., those Seyfert nuclei whose MIR properties are not represented by the models (green filled histogram).

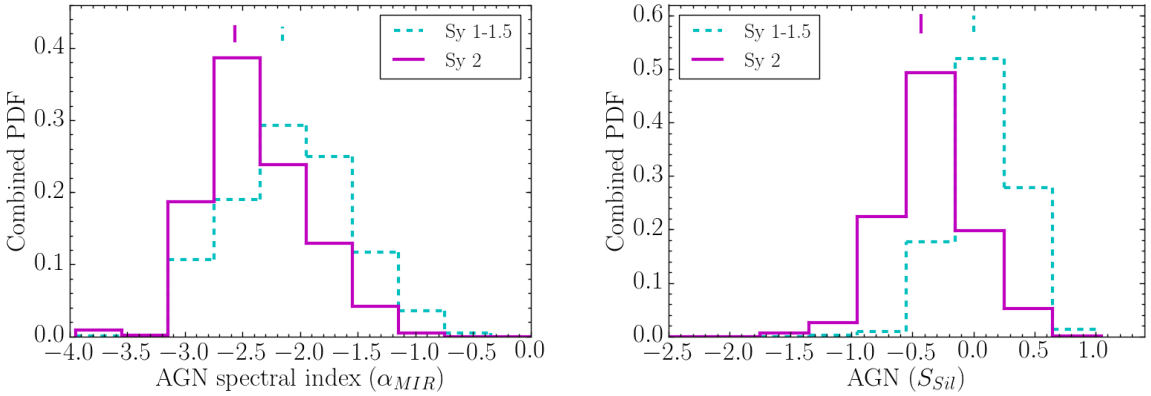

FIGURE 5.22: Combined probability distributions of the AGN MIR (8.1 – 12.5 μm) spectral index derived with DEBLENDIRS (left) and the combined probability distributions of the strength of the silicate feature derived with DEBLENDIRS (right) for the Seyfert 1-1.5 (cyan) and the Seyfert 2 galaxies (magenta) excluding those not represented by the models.

(2011) fitted the near-IR SEDs and MIR spectroscopy of a sample of Seyfert galaxies including four not reproduced by the CAT3D models using the Nenkova et al. (2008a,b) clumpy torus models. They found that the nuclear IR SED of Circinus could be reproduced with the clumpy torus models plus foreground dust, whereas NGC 5506, NGC 7172 and NGC 7582 could not be modelled using the foreground dust. This may be due to an important contamination from extended dust structures, not related to the dusty torus.

Once we excluded those Seyfert nuclei not reproduced by the CAT3D new models, we performed a

KS-test, as in Section 5.4.1, to see whether there are significant differences between the Seyfert 1-1.5 and the Seyfert 2. We did not include the Seyfert 1.8/1.9 galaxies here because there are only four Seyfert 1.8/1.9 galaxies well reproduced by the models. The KS-test shows that the Seyfert 1-1.5 and the Seyfert 2 galaxies are statistically different both in terms of the MIR spectral index ($p = 0.005$) and the strength of the silicate feature ($p = 0.00005$). The difference in the strength of the silicate feature is a well known property as Seyfert 1-1.5 generally show the silicate feature in emission and the Seyfert 2 galaxies in absorption (Shi et al. 2006, Thompson et al. 2009, Alonso-Herrero et al. 2014, but also see Hatziminaoglou et al. 2015).

The difference in the MIR spectral index has also been noted by, among many works, Ramos Almeida et al. (2011a) who found that Seyfert 2 show steeper $1 - 18\,\mu$m SEDs than Seyfert 1. However, they found that the difference in the $8-13\,\mu$m spectral range was small (see also Alonso-Herrero et al. 2014). This is consistent with our results with the Seyfert 1-1.5 nuclei having a median of $\alpha_{\rm MIR} = -2.15$ and the Seyfert 2 excluding those galaxies not represented by the models having a median of $\alpha_{\rm MIR} = -2.56$. These differences can also be seen in Fig. 5.22, where we show the combined probability distribution functions for $\alpha_{\rm MIR}$ and $S_{\rm Sil}$.

5.5.4 Constraining the CAT3D torus model parameters

In the previous sections we compared the CAT3D old and the new torus models with all the Seyfert galaxies and the IR-weak quasars. In this section we focus on the old and new models and the Seyfert galaxies whose MIR properties are explained by the models. The goal is to determine if we can constrain some of the CAT3D clumpy torus model parameters from a statistical point of view using the MIR observations.

To do so, we plot in Fig. 5.23 the median values and 1σ uncertainties of the combined PDF of the Seyfert 1-1.5, Seyfert 2 (only those reproduced by the models) and PG quasars (Alonso-Herrero et al. 2016b). The model symbols are colour coded in terms of the escape probability of an AGN produced photon. From this figure we can see that, as expected, the Seyfert 2 galaxies are explained by models with low photon escape probability for both the old and the new models. However, the Seyfert 1-1.5 galaxies and the PG quasars lie in a region of this diagram occupied by models with relatively high and low AGN photon escape probabilities. This is due to the the degeneracy inherent to clumpy torus models, with models with different set of parameters producing the same values of the strength of the silicates and the MIR spectral index. On the other hand, detailed fits to the individual IR SEDs of Seyfert 1s with the clumpy torus models of Nenkova et al. (2008a,b) show that the derived escape probabilities are never high (typically $P_{\rm esc} = 0.2 - 0.3$, see Ramos Almeida et al. 2011a; Alonso-Herrero et al. 2011). This is also in good agreement with our statistical result that the models (both the old and the new ones) with high photon escape probabilities tend to lie in a region of the diagram not populated by the observations (i.e., approximately $\alpha_{\rm MIR} > -1$ and $S_{\rm Sil} > 0.25$).

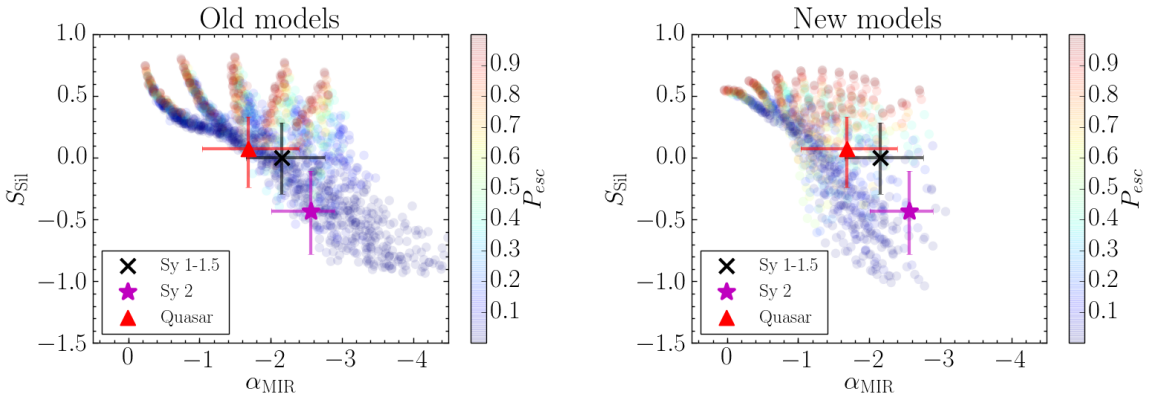

FIGURE 5.23: Comparison between median values and 1σ uncertainties of the combined PDF of the MIR spectral index and the strength of the silicate feature for the Seyfert 1-1.5 and Seyfert 2 galaxies (only those reproduced by the models, see text) and the IR-weak quasars from Alonso-Herrero et al. (2016b) with the values for all parameters (see Table 5.8) of the CAT3D old torus models (left) and the new torus models (right). The model symbols are colour coded in terms of the AGN produced photon escape probability. The different types of Seyfert are shown with different colours and symbols: Seyfert 1-1.5 (black crosses), Seyfert 2 (magenta star symbols), and IR-weak quasars (red triangles).

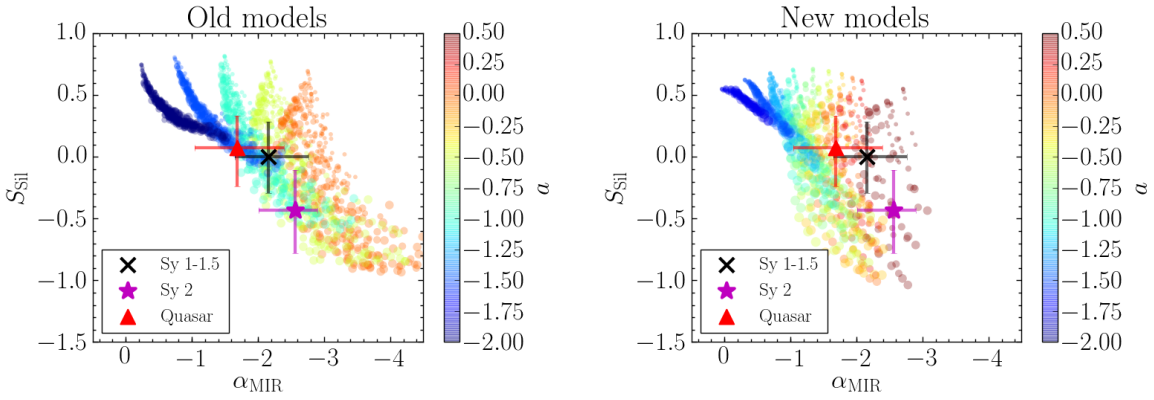

FIGURE 5.24: As Fig. 5.23 but the model symbols are colour coded in terms of the value the power-law index of radial dust-cloud distribution, a, and the size of the model symbols is proportional to the number of clouds along an equatorial line-of-sight, N_0 (smallest symbols correspond to $N_0 = 2.5$ and largest symbols to $N_0 = 12.5$ (see Table 5.8.)

In Fig. 5.24 we show the same comparison, but now we colour code the model symbols in terms of the value of the power-law index of the radial dust-cloud distribution, a. The size of the model symbols is proportional to the number of clouds along an equatorial line-of-sight, N_0. From this figure we can observe that from a statistical point of view Seyfert 2 galaxies are reproduced with models with more clouds in the equatorial direction than type 1 AGN. For the new models, those Seyfert 1-1.5 galaxies in our sample with a nearly flat silicate feature ($S_{\rm Sil} \sim 0$) are also reproduced with models with more clouds, whereas the Seyfert 1-1.5 galaxies with silicate emission are only reproduced with a few clouds in the equatorial direction (see also Fig. 5.20 where we plotted the values of the individual objects). This is in good agreement with the conclusions of Hönig and Kishimoto (2010), who showed

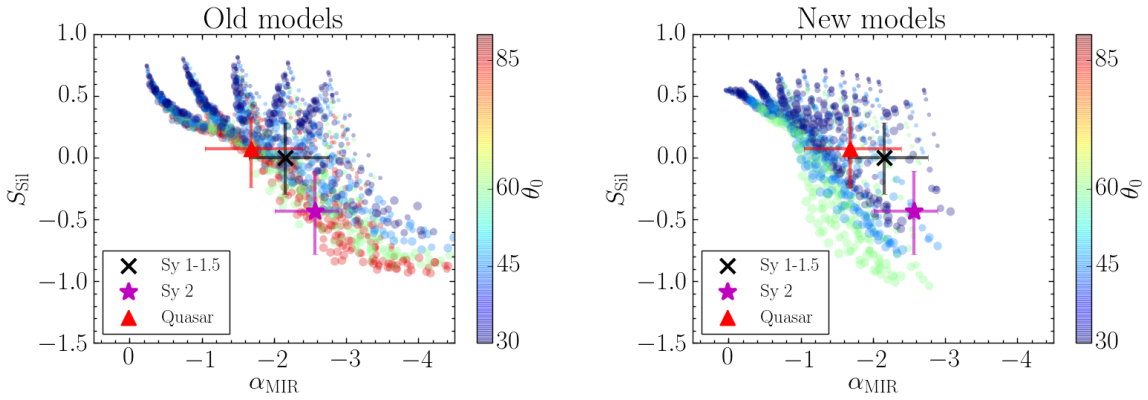

FIGURE 5.25: As Fig. 5.23 but the model symbols are colour coded in terms of the value the torus half-covering angle, θ_0, and the size of the model symbols is proportional to the number of clouds along an equatorial line-of-sight, N_0.

that more clouds along an equatorial direction (larger values of N_0) produce weaker emission at 10 μm in Seyfert 1. For Seyfert 2, the silicate feature is deeper for the higher values of N_0. We note they calculated the MIR spectral index and the strength of the silicate feature at rest-frame wavelengths from 8.5 and 12.5 μm whereas we have calculated it between 8.1 and 12.5 μm and they separated their models into type 1 and type 2 only using the inclination angle. The same result was obtained by Ramos Almeida et al. (2014b) using the clumpy torus of Nenkova et al. (2008a,b). They found that for Seyfert 1, flat silicate features can also be reproduced with high values of N_0 ($\sim 10-15$), whereas strong silicates in emission are produced by configurations with a few optically thin clouds along the equatorial direction. For Seyfert 2, the silicate feature in absorption is also reproduced with high N_0 ($\sim 8-15$). Ichikawa et al. (2015) also used the Nenkova et al. (2008a,b) clumpy models and found that there were statistically significant differences between the distributions of N_0 for the Seyfert 1 and the Seyfert 2 with hidden broad line region. For the old models there is more degeneracy in terms of the number of clouds for the Seyfert 1-1.5 galaxies and they can be explained with models with low and high number of clouds. From this figure we can also set a limit on the values of a that can reproduce our Seyfert galaxies using the CAT3D models. Very negative values of a, i.e. $a \leq -2.0$ for the old models and $a \leq -1.5$ for the new models, cannot reproduce the values observed in Seyfert galaxies or even the PG quasars. To represent the Seyfert 2 values it is necessary to have positive values of a ($a = 0.25, 0.50$). We also found steeper radial distributions of clouds in the old models than in the new ones. We can also conclude that there is a tendency for quasars, Seyfert 1s and Seyfert 2s to be reproduced with increasingly flatter indices of radial distributions of the torus clouds (more positive values of a). This is in good agreement with the result of Martínez-Paredes et al. (2017) using a detailed modeling of the nuclear SEDs with the clumpy torus models of (Nenkova et al. 2008b).

We finally compare the data and the models in Fig. 5.25 colour coding the model symbols in terms of the torus half-covering angle, θ_0. We can observe a tendency for the Seyfert 1-1.5 and the IR-weak PG quasars to be represented with relatively thinner tori ($\theta_0 \leq 45°$) than the Seyfert 2 galaxies

(old models), but there is a degeneracy produced by the clumpy torus models. This is consistent with the finding of thinner tori in Seyfert 1-1.5 than Seyfert 2s byRamos Almeida et al. (2011a) and Ichikawa et al. (2015) using detailed fits of the IR SEDs of Seyfert nuclei. For the new models, this tendency is not observed and all galaxies are better represented with relatively thinner tori. To break this degeneracy, it is required to have information about the nuclear near-IR emission (Ramos Almeida et al. 2014b).

In conclusion, we are able to constrain some of parameter ranges of the old and new CAT3D torus models. In particular, we set a lower limit to the index of the power-law radial distribution of clouds ($a \geq -1.5$ for the old models and $a \geq -1.25$ for the new models). We derive statistical tendencies for Seyfert 1 nuclei, which are represented better with steeper dust radial distributions and thinner tori than Seyfert 2 nuclei for the old models, whereas there is more degeneracy for the new models. We also find that the MIR properties of Seyfert 2 nuclei are well reproduced with CAT3D models with combination of parameters that result in small escape probabilities of AGN-produced photons.

5.6 Summary and conclusions

In this work we analysed the ground-based ($\sim 7.5-13.5\,\mu$m) MIR spectroscopy of 52 Seyfert galaxies, using published observations taken with 8 – 10 m class telescopes with the instruments T-ReCS, VISIR, CanariCam, and Michelle. Using data from the literature we classified the galaxies into Seyfert 1-1.5 (15 galaxies), Seyfert 1.8-1.9 (7 galaxies) and Seyfert 2 (30 galaxies). The galaxies are at a median distance of 36 Mpc and the ground-based slits cover typical nuclear regions of 101 pc in size. We decomposed the spectra using DEBLENDIRS to disentangle the AGN MIR emission from the stellar and the PAH emission arising from the host galaxy. We derived the AGN MIR $8.1 - 12.5\,\mu$m spectral index, the strength of the silicate feature, the MIR AGN contribution within the slit, and the AGN rest-frame $12\,\mu$m luminosities. We also compared the DEBLENDIRS values with direct measurements on the spectra. We showed that both methods produce consistent results except in cases with very deep silicate features.

We did not find statistically significant differences between Seyfert 1-1.5, Seyfert 2 and Seyfert 1.8./1.9 in terms of the DEBLENDIRS derived MIR spectral index. However the MIR spectral indices of Seyfert 1-1.5 galaxies are significantly steeper than those of the IR-weak quasars analysed by Alonso-Herrero et al. (2016b). In terms of the strength of the silicate feature there are statistically significant differences between Seyfert 1-1.5 and Seyfert 2 galaxies and between Seyfert 1-1.5 and Seyfert 1.8/1.9 galaxies. This indicates that the behaviour of the Seyfert 1.8/1.9 is closer to the silicate features observed in absorption of Seyfert 2 than to the flatter or slightly in emission silicate features observed in Seyfert 1-1.5. There are not significant differences between Seyfert 1-1.5 and the IR-weak quasars.

The main goal of this work is to make a statistical comparison of the MIR properties of Seyfert nuclei and predictions from the CAT3D clumpy torus models of Hönig and Kishimoto (2010). We used the published version of the models (old models) with a standard ISM dust composition. We also presented new calculations of the models including an improved physical representation of the dust sublimation properties (new models). Prior to comparing the MIR properties of Seyfert galaxies with the CAT3D clumpy torus models we analysed the differences between the old and the new version of the models. We found that for the same parameter configuration the new models reach a less negative value of the MIR ($8.1 - 12.5\,\mu$m) spectral index, as expected by the introduction of the differential dust grain sublimation model. In the case of the strength of the silicate feature, the new models appear to produce always slightly deeper silicate features than the old models. When comparing the models with the MIR properties of Seyfert galaxies we found that both, the old and the new models, do not reproduce the Seyfert galaxies with deep silicate absorption ($S_{\rm Sil} < -1$) in our sample (11 out of the 52 galaxies). These galaxies tend to have low values of b/a (highly inclined galaxies) and some of them are in mergers. These are likely objects with contamination from obscuration in the host galaxy (Goulding et al. 2012). Excluding these 11 galaxies, we found that the new models improve the representation of the quasars, Seyfert 1.8/1.9 and y 2 galaxies whereas the Seyfert 1-1.5 are well represented with both, the old and the new models. However, the old models, for certain configurations, produce very steep MIR spectral indices not observed in Seyfert nuclei. We conclude that the inclusion of a more realistic dust sublimation physics reproduces better the overall MIR properties of local AGN.

We finally attempted to constrain the new CAT3D torus model parameters from a statistical point of view using the MIR observations. To do so, we focused on the old and new models with all the parameters available and only used the observations of those Seyfert nuclei explained by the models. We obtained that the Seyfert 2 galaxies well reproduced with models with low photon escape probability, as expected. The Seyfert 1-1.5 galaxies and the IR-weak quasars are explained by models with relatively high and low AGN photon escape probabilities, due to the degeneracy produced by the CAT3D models in the MIR, as with other clumpy torus models. The moderate silicate features in absorption of Seyfert 2 galaxies are reproduced with models with more clouds along an equatorial direction (N_0) for both the old and new models, whereas the Seyfert 1-1.5 galaxies and the IR-weak quasars with silicate emission are explained with a few clouds (new models). This is in good agreement with previous works (Hönig and Kishimoto 2010; Ramos Almeida et al. 2011a; Ichikawa et al. 2015). We also investigated the dependency of the MIR emission on other CAT3D torus model parameters, such as the power-law index of the radial dust distribution a and the torus half-covering angle θ_0. Very negative values of a, i.e. $a \leq -2.0$ for the old models and $a \leq -1.5$ for the new models (that is, most of the clouds are concentrated towards the inner regions of the torus) tend to produce flatter MIR spectral indices and stronger silicate features than observed in Seyfert galaxies or even the PG quasars. There is also a tendency for quasars and Seyfert 1 nuclei to show steeper radial distributions than Seyfert 2 nuclei (old and new models). For the Seyfert 2 galaxies, the values are better represented with positive values of a, which implies that there is more clouds in the outer regions of the torus. For the torus

half-covering angle θ_0 we observed a tendency for the Seyfert 1-1.5 and the IR-weak PG quasars to be represented with relatively thinner tori ($\theta_0 \leq 45°$) than the Seyfert 2 galaxies (old models), but with high degeneracy produced by the clumpy torus models.

In conclusion, we cannot break fully the degeneracy in all parameters of the CAT3D models (or any other clumpy torus models) by using MIR spectroscopy alone (see also Ramos Almeida et al. 2014b) even after isolating the AGN component. However, by using a large sample of Seyfert galaxies we were able to uncover some different trends between type 1s and type 2s in terms of the index of the radial distribution of the clouds a, the number of clouds along the equatorial direction N_0, and the half-covering angle of the torus θ_0. This study has been submitted to an international journal.

Chapter 6

Conclusions and future work

One of the most important discoveries in the modern extragalactic astronomy is that SMBH are believed to exist in the centre of all galaxies containing a significant bulge component. According to the simplest version of the unified model, all the observational differences observed between different types of AGN are explained by orientation effects, being the dusty torus the key ingredient to explain this orientation dependence. Since the torus reprocesses the optical/UV radiation from the accretion disk and re-emits in the IR range, it is important to study this IR emission to understand the dusty torus of the AGN. It is also important to disentangle the emission from the host galaxy from that of the AGN.

During this thesis we studied the IR emission for both, AGN in cosmological fields and AGN in nearby galaxies. It is, therefore, divided into two different parts. The first part (Chapter 3) focused on a novel technique to select AGN by using MIR variability in a cosmological field while the second part (Chapters 4 and 5) centred on the study of the dust heated by the AGN in nearby Seyfert galaxies.

6.1 AGN candidates selected by 24 μm variability

Since there is no single technique to identify the entire AGN population, it is important to use different methods and wavelengths in the same region of the sky to detect sources other methods may miss. There are a number of studies that have identified AGN in the GOODS fields, some of them using variability as a method to detect AGN (Sarajedini et al. 2003; Cohen et al. 2006; Klesman and Sarajedini 2007; Trevese et al. 2008; Villforth et al. 2010; Sarajedini et al. 2011; Paolillo et al. 2004; Young et al. 2012; Mooley et al. 2013). Variability is a unique method to select AGN because practically all AGN vary on different time-scales, from hours to million of years. In Chapter 3 we presented a new way to select low-luminosity and obscured AGN using MIPS 24 μm (observed wavelength) variability and a χ^2-statistics method.

Among the 2277 sources detected in Epochs 1, 3, 6, and 7 and 2452 sources in Epochs 7a, 7b, and 7c, we found 39 long-term (months) and 55 short-term (days) MIPS 24 μm variability selected AGN candidates in GOODS-South with a probability $\leqslant$ 1% that the observed variability is due to statistical errors alone. They showed a typical variability at 24 μm of 40% and their photometric redshifts indicate they are located typically at z = 1. We compared our candidates with AGN selected in the X-ray and radio bands as well as AGN candidates selected by their IR emission. We found that $\sim$ 50% of the MIPS 24 μm variable sources are identified as AGN by these other methods. Therefore, MIPS 24 μm variability allows to identify AGN candidates that might be missed by other methods. However, the contribution of the MIPS 24 μm variable identified AGN to the general AGN population is small ($\leqslant$13%) in GOODS-South. Moreover, we estimated that the AGN contribution to the MIR emission of these 24 μm variable sources is low (typically less than 20%). Since our method is only sensitive to high amplitude variability then these 24 μm variable sources are likely to host low-luminosity AGN where the variability is expected to be stronger (Trevese et al. 1994).

The results obtained in this work can be extended using this variability method in other cosmological fields to select low-luminosity AGN missed by other methods. To strengthen the conclusions that the selected variable sources are AGN, the candidates that are not selected with other methods should be studied spectroscopically, with instruments such as x-shooter (Vernet et al. 2011) at VLT. This instrument allows to take multi-wavelength (300 − 2500 nm) medium resolution spectra, what would allow to prove the AGN nature of the variable sources.

6.2 The nuclear and integrated FIR emission of Seyfert galaxies

The FIR emission in Seyfert galaxies is in general dominated by emission from the host galaxy, even in the central regions (kpc to a hundred pc scales) of the galaxies. However, studies of individual Seyfert galaxies show that the contribution of the dust heated by the AGN to the total FIR emission varies from galaxy to galaxy (e.g. Alonso-Herrero et al. 2012b; García-Bernete et al. 2015; Ramos Almeida et al. 2011b; Mullaney et al. 2011). Up until now there have been no statistical studies of the AGN contribution in the FIR using data obtained with the *Herschel* telescope, so it is important to find a method to determine if the AGN dominates in the FIR for large samples of galaxies. In Chapter 4 we presented a method based in four criteria to select galaxies whose nuclear 70 μm emission has a significant AGN contribution.

We studied 33 nearby (median distance of 30 Mpc) Seyfert galaxies from the RSA catalogue with PACS (70, 100, and 160 μm) and SPIRE (250, 350, and 500 μm) images. We took advantage of the Herschel angular resolution of 5.6 arcsec at 70 μm and obtained the FIR nuclear (r = 1 kpc and r = 2 kpc) and integrated spectral SEDs. We estimated the unresolved nuclear emission at 70 μm and we fit the nuclear and integrated FIR SEDs with a grey body model. We found that, as expected, the integrated FIR emission of the RSA Seyferts in our sample is dominated by emission from the host galaxy, with

dust properties similar to those of normal galaxies (non-AGN). We used four criteria to select galaxies whose nuclear 70 μm emission has a significant AGN contribution: (1) elevated 70/160 μm flux ratios, (2) spatially resolved, high dust temperature gradient, (3) 70 μm excess emission with respect to the fit of the FIR SEDs with a grey body, and (4) excess of nuclear SFR obtained from 70 μm over SFR from MIR indicators. Taking into account these four criteria, we found that 16 galaxies (48% of the initial sample) satisfy at least one of these conditions, whereas 10 satisfy half or more. After careful examination of these, we selected six *bona fide* candidates (18% of the initial sample) and estimate that $\sim 40-70\%$ of their nuclear ($r = 1-2$ kpc) 70 μm emission is contributed by dust heated by the AGN. These galaxies are IC 5063, NGC 3783, NGC 4151, NGC 5347, NGC 7213, and NGC 7479. None of them show 11.3 μm PAH emission on scales of tens of parsecs from high angular resolution MIR spectroscopy or high nuclear SFR. The estimated AGN 70 μm fluxes for IC 5063 and NGC 4151 are in good agreement with the predicted torus FIR emission from the extrapolation of the fits to the unresolved NIR and MIR emission (Alonso-Herrero et al. 2011; Ichikawa et al. 2015) using clumpy torus models.

The criteria defined in Chapter 4 provide a good way to select statistically Seyfert galaxies with significant contribution of the AGN at 70 μm using Herschel data.

The results obtained in this work can be strengthen by estimating the AGN 70 μm fluxes using clumpy torus model predictions for all the selected galaxies whose nuclear 70 μm emission has a significant AGN contribution, as done for IC 5063 and NGC 4151 (Alonso-Herrero et al. 2011; Ichikawa et al. 2015). Additionally, interferometry with ALMA can be used to resolve the torus in the FIR ($\sim$450 μm) in other AGN besides NGC 1068 (see García-Burillo et al. 2016).

6.3 A statistical investigation of clumpy torus model predictions in the MIR

Since the dusty torus is the key ingredient of the unified model of AGN, a number of different clumpy torus models have been developed in the last few years (Hönig et al. 2006; Nenkova et al. 2008a,b; Schartmann et al. 2008; Hönig and Kishimoto 2010). The dust in the torus reprocesses the optical and UV radiation from the accretion disk and re-emits in the IR range. Therefore, to constrain the torus model parameters we have to compare predictions of clumpy torus models with high angular resolution IR observations of AGN. To compare the observations with the predictions of the models it is important to disentangle the AGN MIR emission from that arising in the host galaxy. In Chapter 5 we presented a statistical comparison of the MIR properties of Seyfert nuclei and predictions from the CAT3D clumpy torus models of Hönig and Kishimoto (2010) and new models with improved physics.

We analysed ground-based MIR spectroscopy of 53 nearby Seyfert galaxies (median distance of 36 Mpc). We decomposed their spectra using DEBLENDIRS to disentangle the AGN MIR emission from that of the

host galaxy. We studied the derived AGN MIR properties, such as the AGN MIR $8.1-12.5\,\mu$m spectral index, the strength of the $9.7\,\mu$m silicate feature, the MIR AGN contribution within the slit, and the AGN rest-frame $12\,\mu$m luminosities. We focused on the AGN MIR spectral index and the strength of the silicate feature to compare the observations with the clumpy torus models.

We used the published version of the CAT3D models (old models) of Hönig and Kishimoto (2010) with a standard ISM dust composition and new calculations of the models including an improved physical representation of the dust sublimation properties (new models). We analysed the differences between the old and new models and found that for the same parameter configuration the old models reach a more negative value of the MIR ($8.1-12.5\,\mu$m) spectral index whereas the new models appear to produce always slightly deeper silicate features than the old models.

When comparing the observations with the old and new clumpy torus models we found that they do not reproduce the Seyfert galaxies with deep silicate absorption ($S_{\rm Sil} < -1$). Excluding those, we conclude that the new CAT3D models reproduce better the observed $\alpha_{\rm MIR}$ and $S_{\rm Sil}$ of Seyfert galaxies as well as those of IR-weak quasars. Therefore, the inclusion of a more realistic dust sublimation physics reproduces better the overall MIR properties of local AGN.

We finally attempted to constrain the new CAT3D torus model parameters from a statistical point of view using the MIR observations. We find that Seyfert 2 galaxies are reproduced with models with low photon escape probabilities, while the IR-weak quasars and the Seyfert 1-1.5 galaxies are reproduced by models with both, low and high photon escape probabilities. IR-weak quasars and Seyfert 1-1.5 tend to show steeper radial cloud distributions and fewer clouds along an equatorial line-of-sight than Seyfert 2 galaxies. The MIR properties of Seyfert 1-1.5 and the IR-weak quasars are generally reproduced better with thinner tori than the Seyfert 2 galaxies. However, using MIR observations alone we cannot break the high degeneracy in the CAT3D torus model parameters, which is inherent to all clumpy torus models.

The results obtained in this work can be extended in the future by exploring the effects on the MIR properties of introducing AGN anisotropic emission in the new CAT3D models to take into account the expected angular dependence of an AGN UV emission. The dependence can be introduced as $cos(i)$ in the AGN illumination of the torus clouds as an approximation of the more general angular dependence of the UV radiation of an accretion disk $\propto 1/3cos(i) * (1 + 2cos(i))$ (Netzer 1987), also adopted by other works (e.g. Hönig et al. 2006; Schartmann et al. 2005, 2008).

Appendix A

Outputs of DEBLENDIRS

In this appendix we show all the outputs of DEBLENDIRS for the galaxies analysed in Chapter 5.

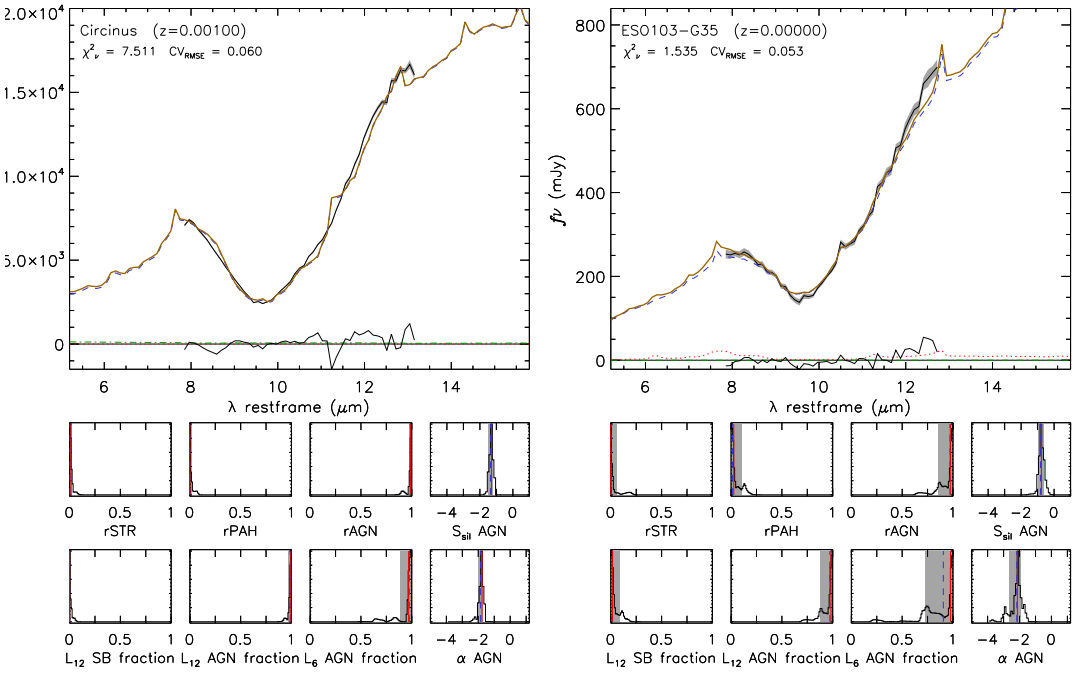

FIGURE A.1: For each galaxy, the top panels show the rest-frame spectrum with the best fitting model (orange), and the three components: stellar (dash-dotted green), PAH (dotted red) and AGN (dashed blue). In the bottom panels DEBLENDIRS shows the PDF for the STR, PAH and AGN emission fraction within the slit (5-15 μm), namely rSTR, rPAH, and rAGN, respectively; the strength of the 9.7 μm silicate feature (S_{sil}) and the spectral index (α_{AGN}) in the AGN spectrum (5-15 μm); the fractional contribution within the slit of the AGN to the rest-frame 6 μm ($L6_{AGN}$) and 12 μm ($L12_{AGN}$) luminosity; and the fractional contribution of the host galaxy to the rest-frame 12 μm luminosity ($L12_{SB}$). For the PDFs the solid red line indicates the value for the best fitting decomposition model whereas the dashed blue line indicates the expectation value. The shaded area represents the 16% and 84% percentiles, i.e, the 1 σ confidence interval.

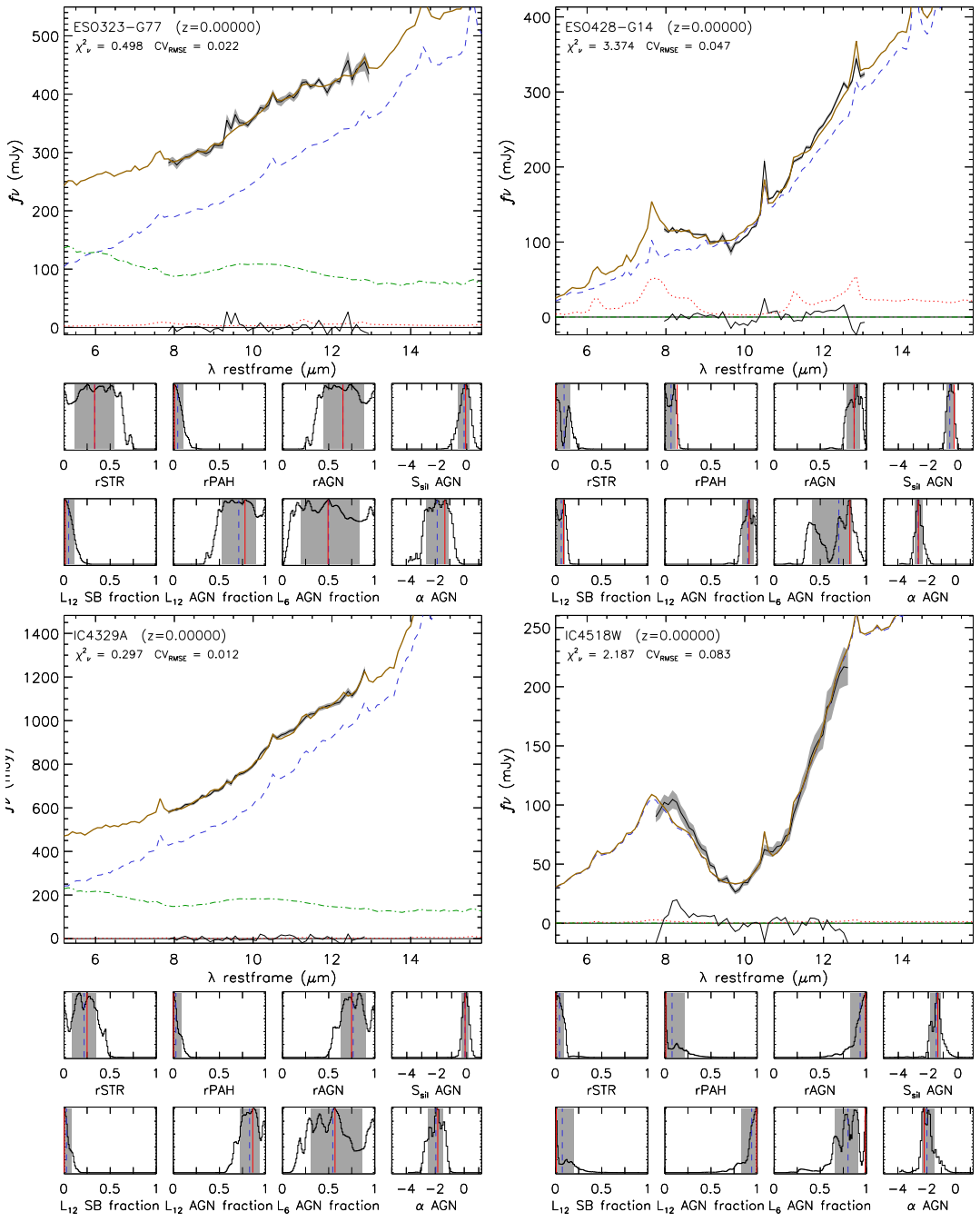
ESO323−G77 (z=0.00000)
χ^2_ν = 0.498 CV_{RMSE} = 0.022
ESO428−G14 (z=0.00000)
χ^2_ν = 3.374 CV_{RMSE} = 0.047
IC4329A (z=0.00000)
χ^2_ν = 0.297 CV_{RMSE} = 0.012
IC4518W (z=0.00000)
χ^2_ν = 2.187 CV_{RMSE} = 0.083
fν (mJy)
λ restframe (μm)
rSTR
rPAH
rAGN
S_{sil} AGN
L_{12} SB fraction
L_{12} AGN fraction
L_6 AGN fraction
α AGN

FIGURE A.1

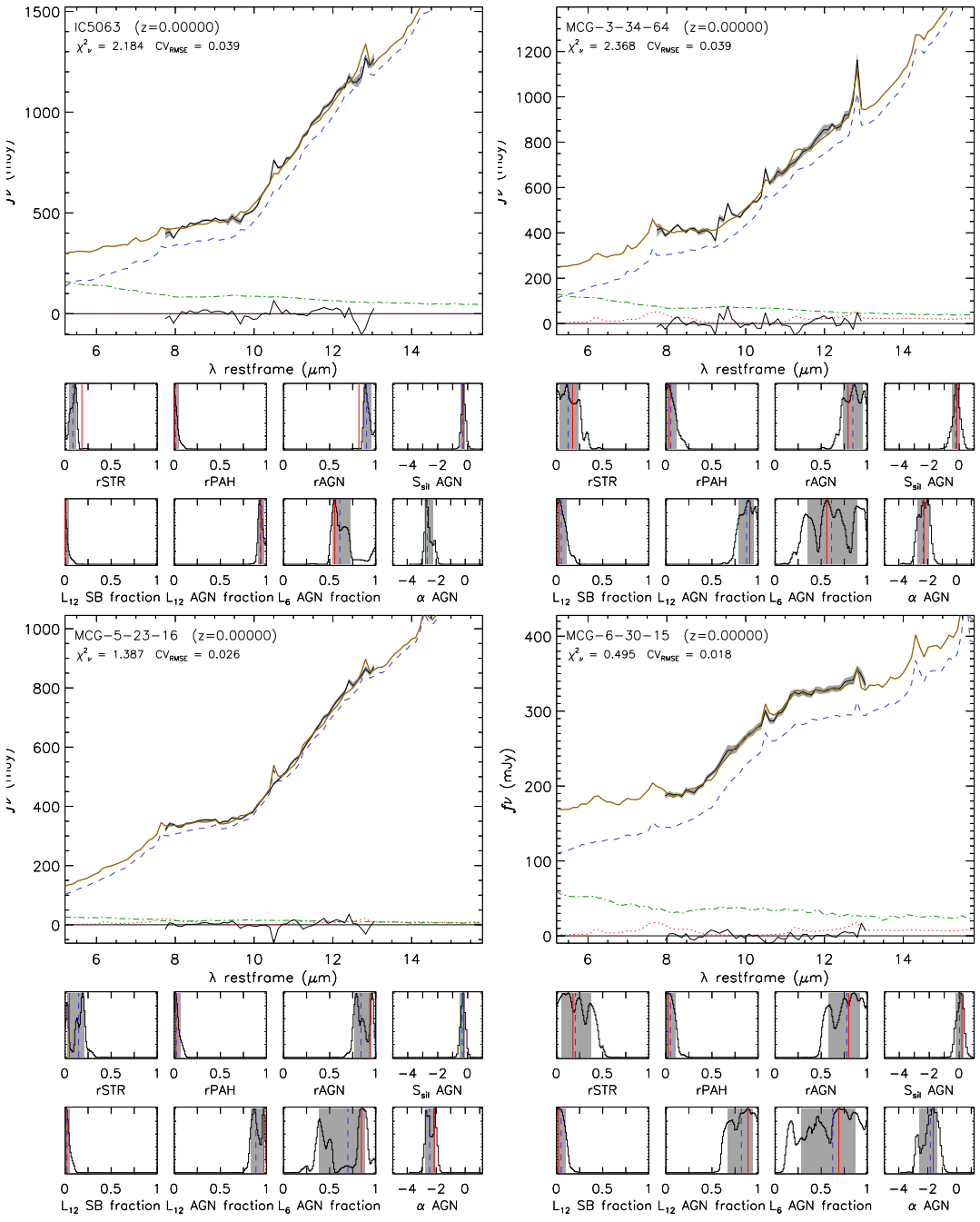
IC5063 (z=0.00000)
χ^2_ν = 2.184 CV_{RMSE} = 0.039
MCG−3−34−64 (z=0.00000)
χ^2_ν = 2.368 CV_{RMSE} = 0.039
MCG−5−23−16 (z=0.00000)
χ^2_ν = 1.387 CV_{RMSE} = 0.026
MCG−6−30−15 (z=0.00000)
χ^2_ν = 0.495 CV_{RMSE} = 0.018
fν (mJy)
λ restframe (μm)
rSTR
rPAH
rAGN
S_{sil} AGN
L_{12} SB fraction
L_{12} AGN fraction
L_6 AGN fraction
α AGN

FIGURE A.1

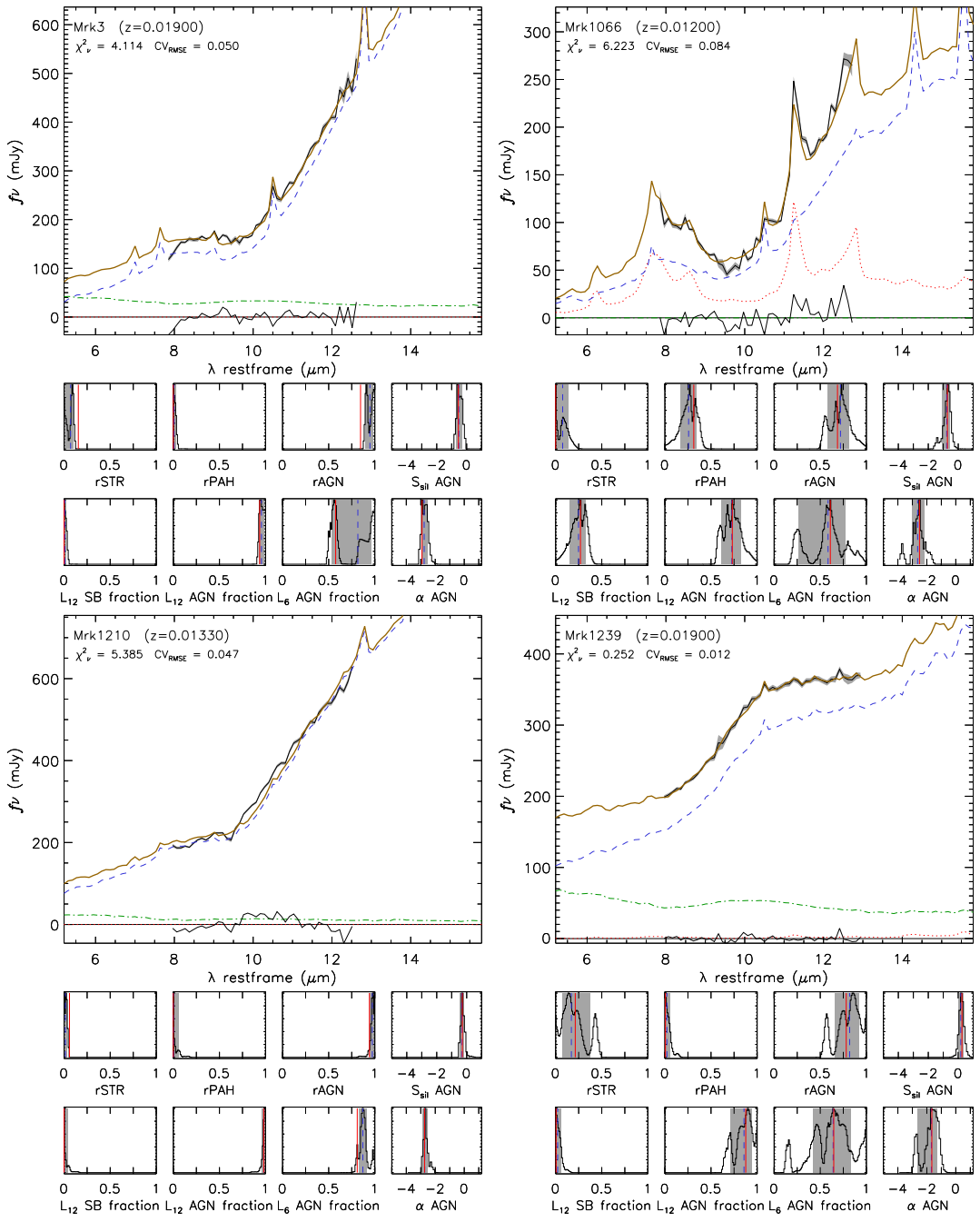
Mrk3 (z=0.01900)
χ^2_ν = 4.114 CV_{RMSE} = 0.050
Mrk1066 (z=0.01200)
χ^2_ν = 6.223 CV_{RMSE} = 0.084
Mrk1210 (z=0.01330)
χ^2_ν = 5.385 CV_{RMSE} = 0.047
Mrk1239 (z=0.01900)
χ^2_ν = 0.252 CV_{RMSE} = 0.012
fν (mJy)
λ restframe (μm)
rSTR
rPAH
rAGN
S_{sil} AGN
L_{12} SB fraction
L_{12} AGN fraction
L_6 AGN fraction
α AGN

FIGURE A.1

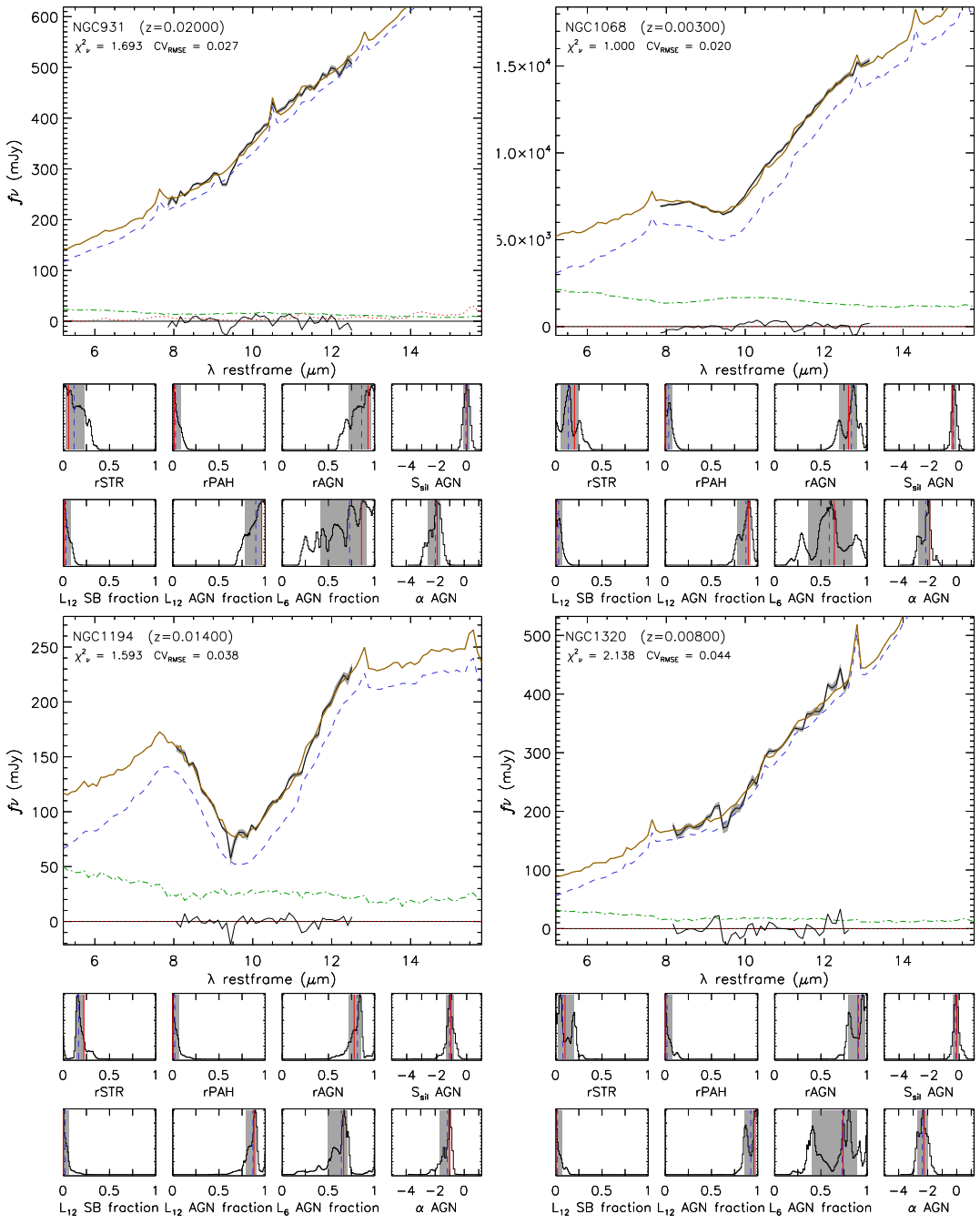
NGC931 (z=0.02000)
χ^2_ν = 1.693 CV$_{RMSE}$ = 0.027
NGC1068 (z=0.00300)
χ^2_ν = 1.000 CV$_{RMSE}$ = 0.020
NGC1194 (z=0.01400)
χ^2_ν = 1.593 CV$_{RMSE}$ = 0.038
NGC1320 (z=0.00800)
χ^2_ν = 2.138 CV$_{RMSE}$ = 0.044
fν (mJy)
λ restframe (μm)
rSTR
rPAH
rAGN
S$_{sil}$ AGN
L$_{12}$ SB fraction
L$_{12}$ AGN fraction
L$_6$ AGN fraction
α AGN

FIGURE A.1

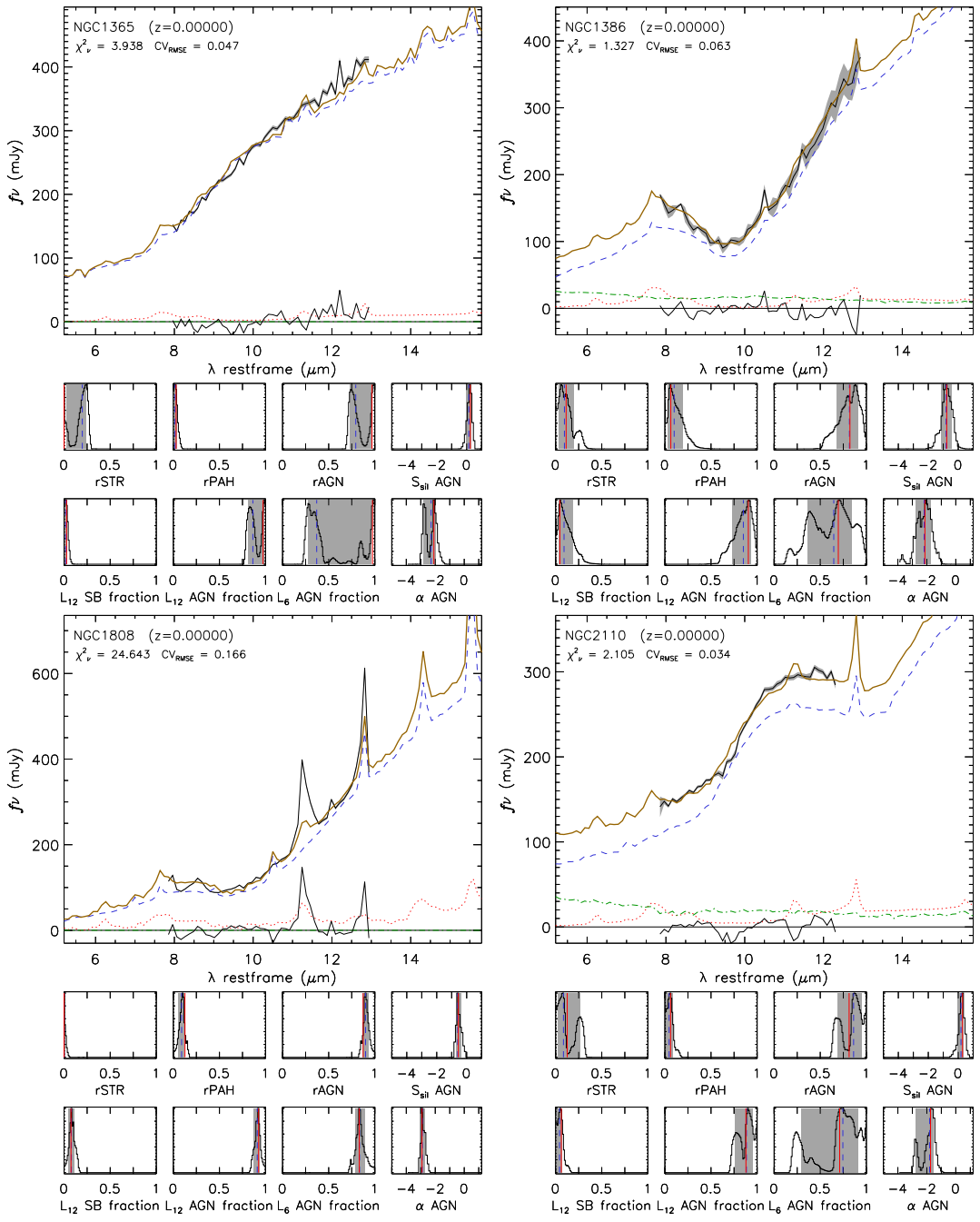
NGC1365 (z=0.00000)
χ^2_ν = 3.938 CV_{RMSE} = 0.047
NGC1386 (z=0.00000)
χ^2_ν = 1.327 CV_{RMSE} = 0.063
NGC1808 (z=0.00000)
χ^2_ν = 24.643 CV_{RMSE} = 0.166
NGC2110 (z=0.00000)
χ^2_ν = 2.105 CV_{RMSE} = 0.034
fν (mJy)
λ restframe (μm)
rSTR
rPAH
rAGN
S_{sil} AGN
L_{12} SB fraction
L_{12} AGN fraction
L_6 AGN fraction
α AGN

FIGURE A.1

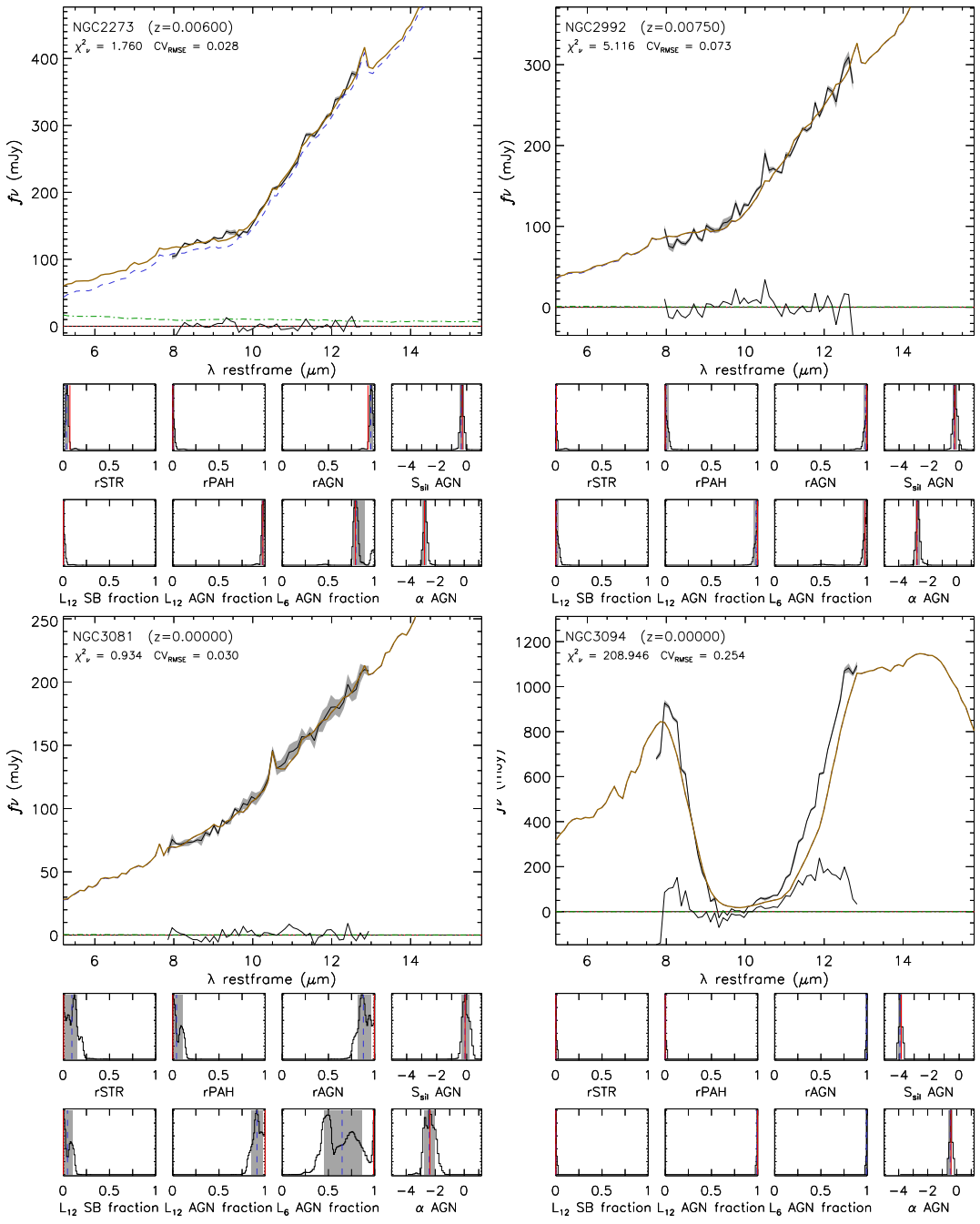
NGC2273 (z=0.00600)
χ^2_ν = 1.760 CV_{RMSE} = 0.028
NGC2992 (z=0.00750)
χ^2_ν = 5.116 CV_{RMSE} = 0.073
NGC3081 (z=0.00000)
χ^2_ν = 0.934 CV_{RMSE} = 0.030
NGC3094 (z=0.00000)
χ^2_ν = 208.946 CV_{RMSE} = 0.254
fν (mJy)
λ restframe (μm)
rSTR
rPAH
rAGN
S_{sil} AGN
L_{12} SB fraction
L_{12} AGN fraction
L_6 AGN fraction
α AGN

FIGURE A.1

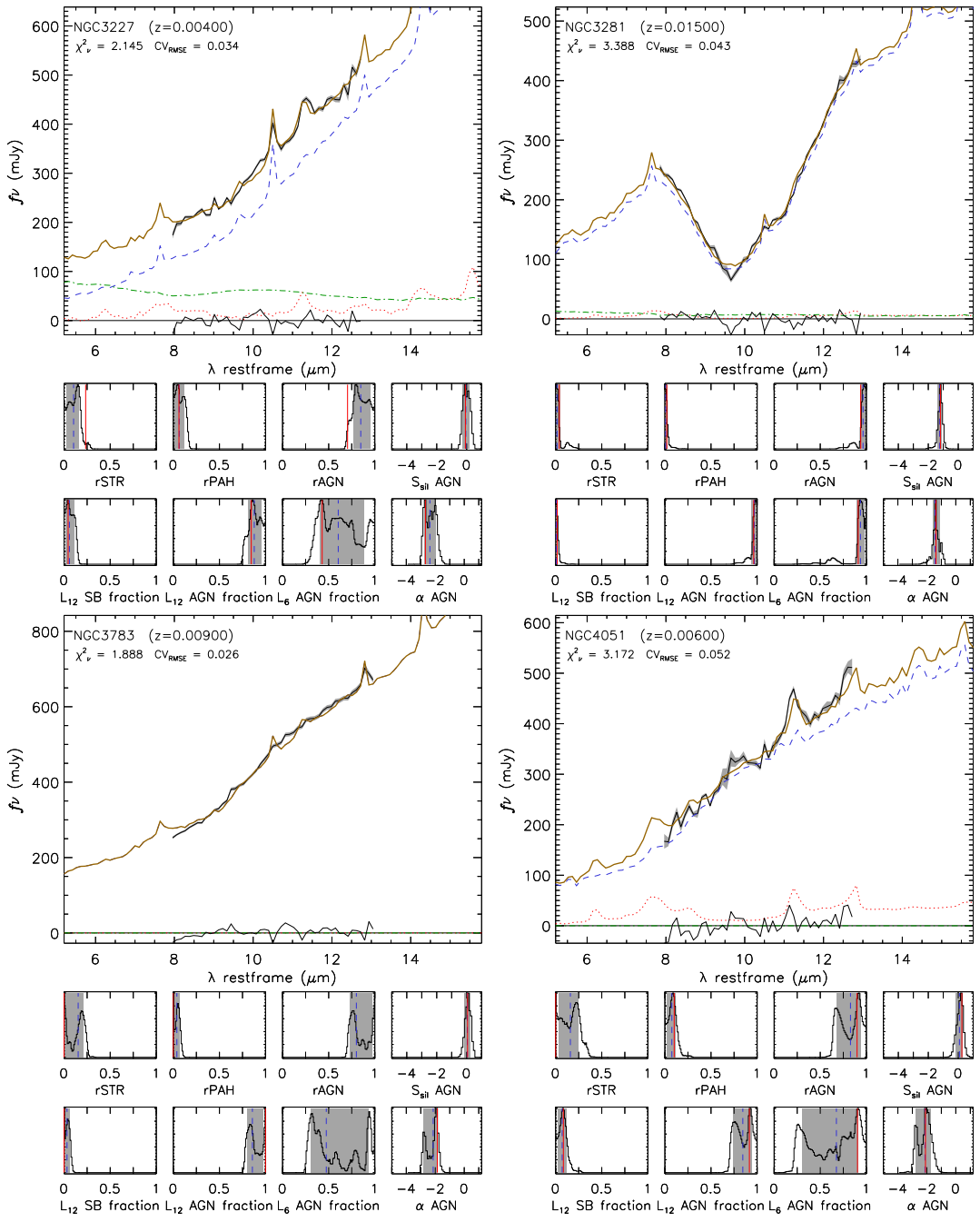
NGC3227 (z=0.00400)
χ^2_ν = 2.145 CV_{RMSE} = 0.034
NGC3281 (z=0.01500)
χ^2_ν = 3.388 CV_{RMSE} = 0.043
NGC3783 (z=0.00900)
χ^2_ν = 1.888 CV_{RMSE} = 0.026
NGC4051 (z=0.00600)
χ^2_ν = 3.172 CV_{RMSE} = 0.052
fν (mJy)
λ restframe (μm)
rSTR
rPAH
rAGN
S_{sil} AGN
L_{12} SB fraction
L_{12} AGN fraction
L_6 AGN fraction
α AGN

FIGURE A.1

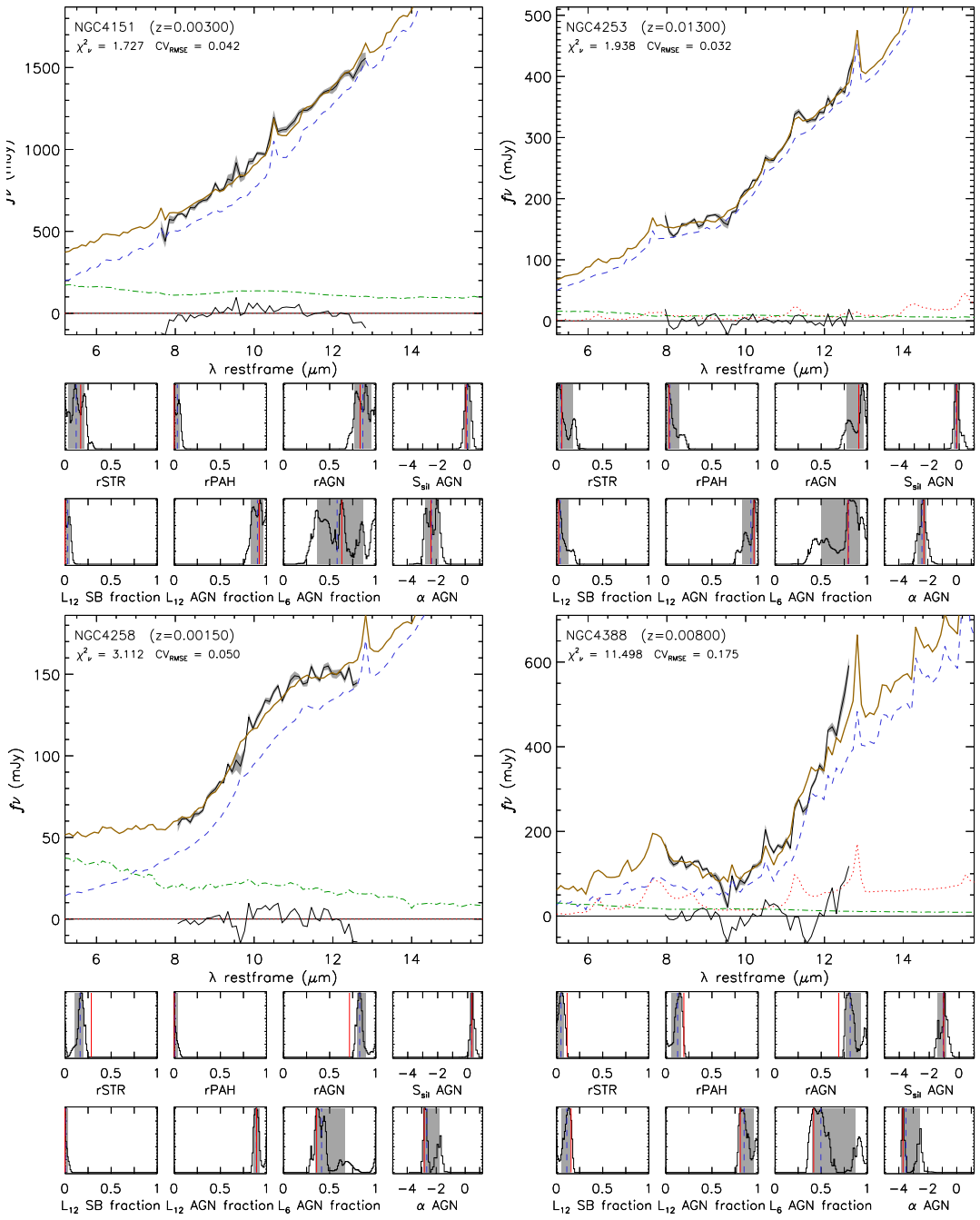
NGC4151 (z=0.00300)
χ^2_ν = 1.727 CV_{RMSE} = 0.042
NGC4253 (z=0.01300)
χ^2_ν = 1.938 CV_{RMSE} = 0.032
NGC4258 (z=0.00150)
χ^2_ν = 3.112 CV_{RMSE} = 0.050
NGC4388 (z=0.00800)
χ^2_ν = 11.498 CV_{RMSE} = 0.175
fν (mJy)
λ restframe (μm)
rSTR
rPAH
rAGN
S_{sil} AGN
L_{12} SB fraction
L_{12} AGN fraction
L_6 AGN fraction
α AGN

FIGURE A.1

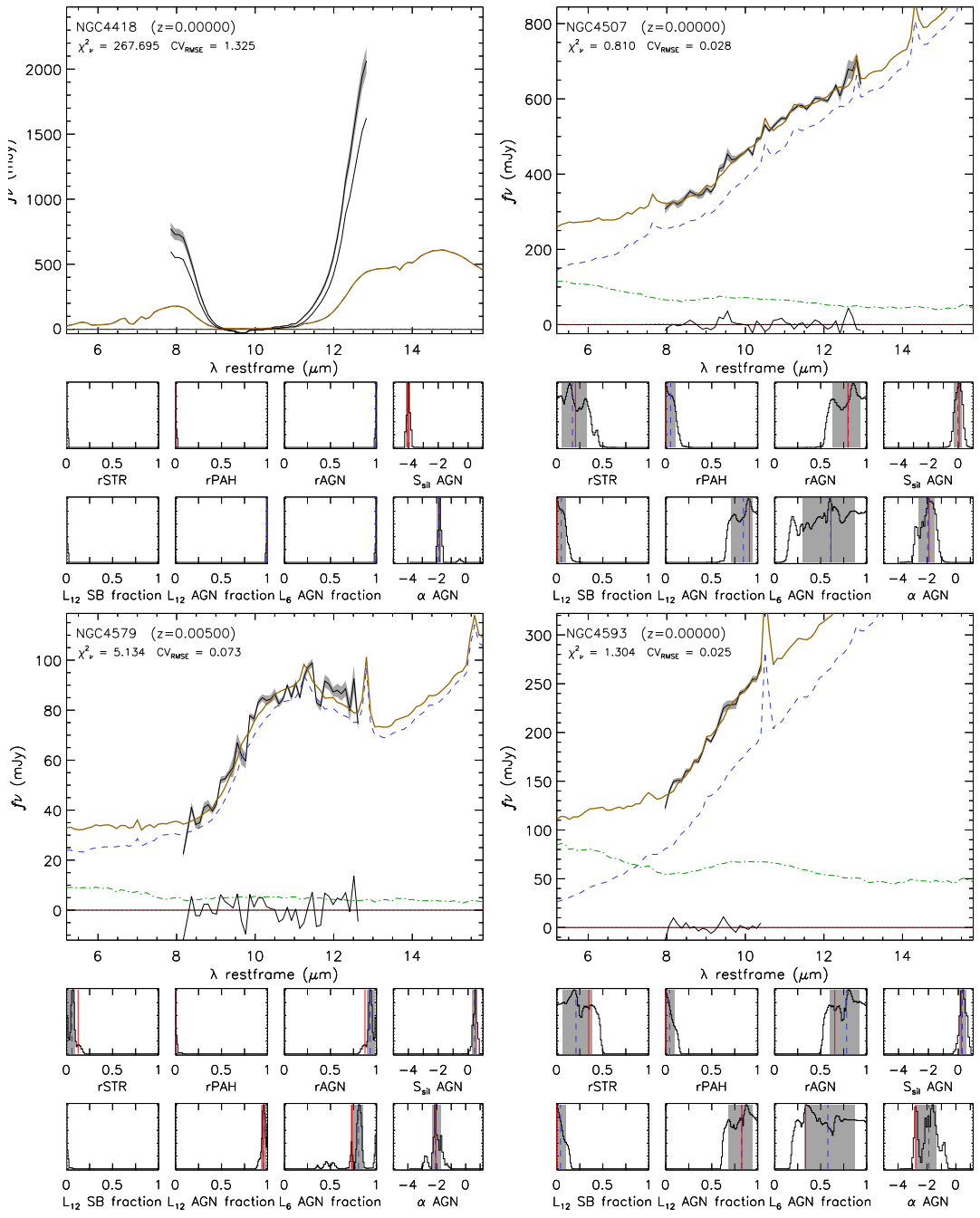
NGC4418 (z=0.00000)
χ^2_ν = 267.695 CV_{RMSE} = 1.325
NGC4507 (z=0.00000)
χ^2_ν = 0.810 CV_{RMSE} = 0.028
NGC4579 (z=0.00500)
χ^2_ν = 5.134 CV_{RMSE} = 0.073
NGC4593 (z=0.00000)
χ^2_ν = 1.304 CV_{RMSE} = 0.025
fν (mJy)
λ restframe (μm)
rSTR
rPAH
rAGN
S_{sil} AGN
L_{12} SB fraction
L_{12} AGN fraction
L_6 AGN fraction
α AGN

FIGURE A.1

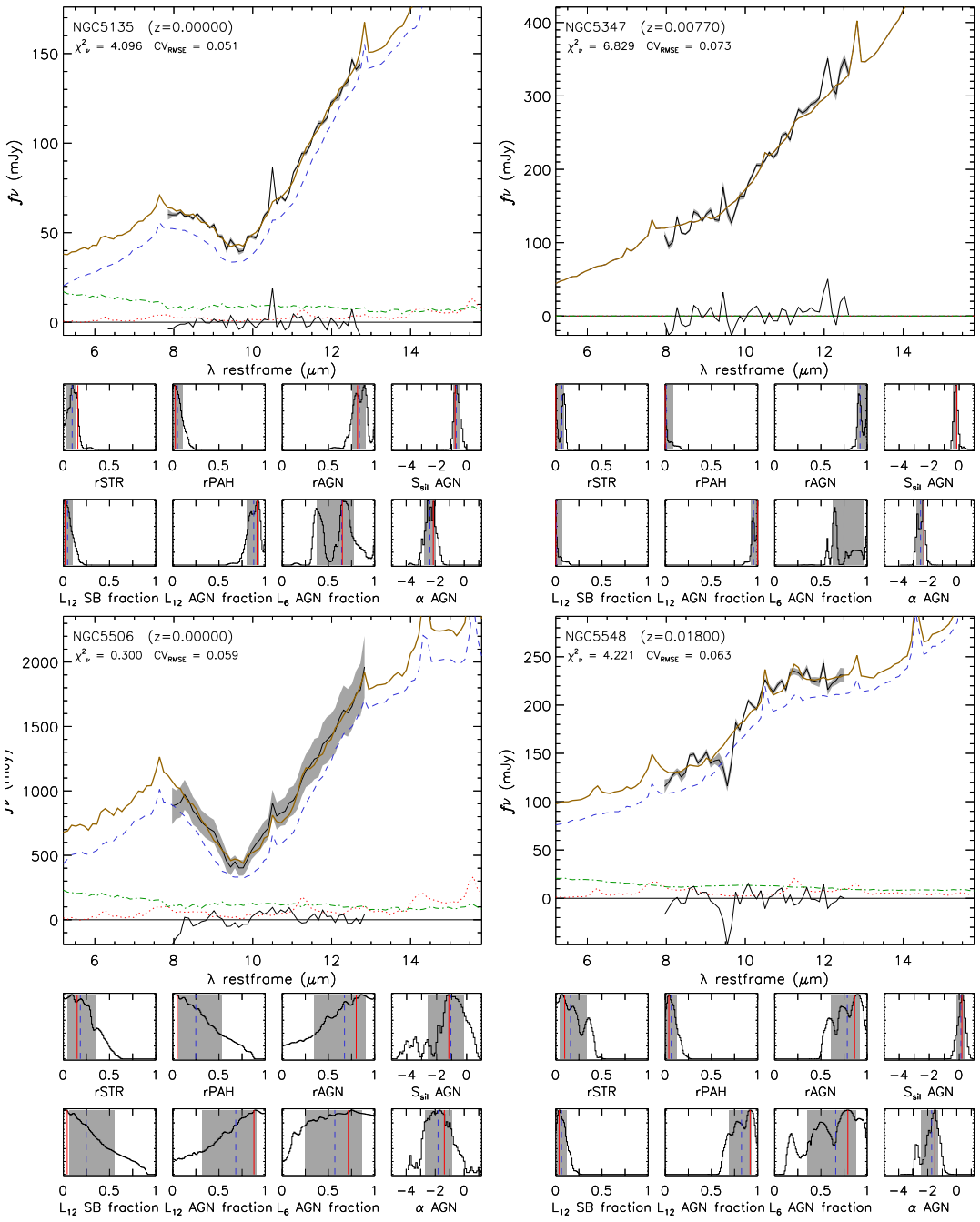
NGC5135 (z=0.00000)
χ^2_ν = 4.096 CV_{RMSE} = 0.051
NGC5347 (z=0.00770)
χ^2_ν = 6.829 CV_{RMSE} = 0.073
NGC5506 (z=0.00000)
χ^2_ν = 0.300 CV_{RMSE} = 0.059
NGC5548 (z=0.01800)
χ^2_ν = 4.221 CV_{RMSE} = 0.063
fν (mJy)
λ restframe (μm)
rSTR
rPAH
rAGN
S_{sil} AGN
L_{12} SB fraction
L_{12} AGN fraction
L_6 AGN fraction
α AGN

FIGURE A.1

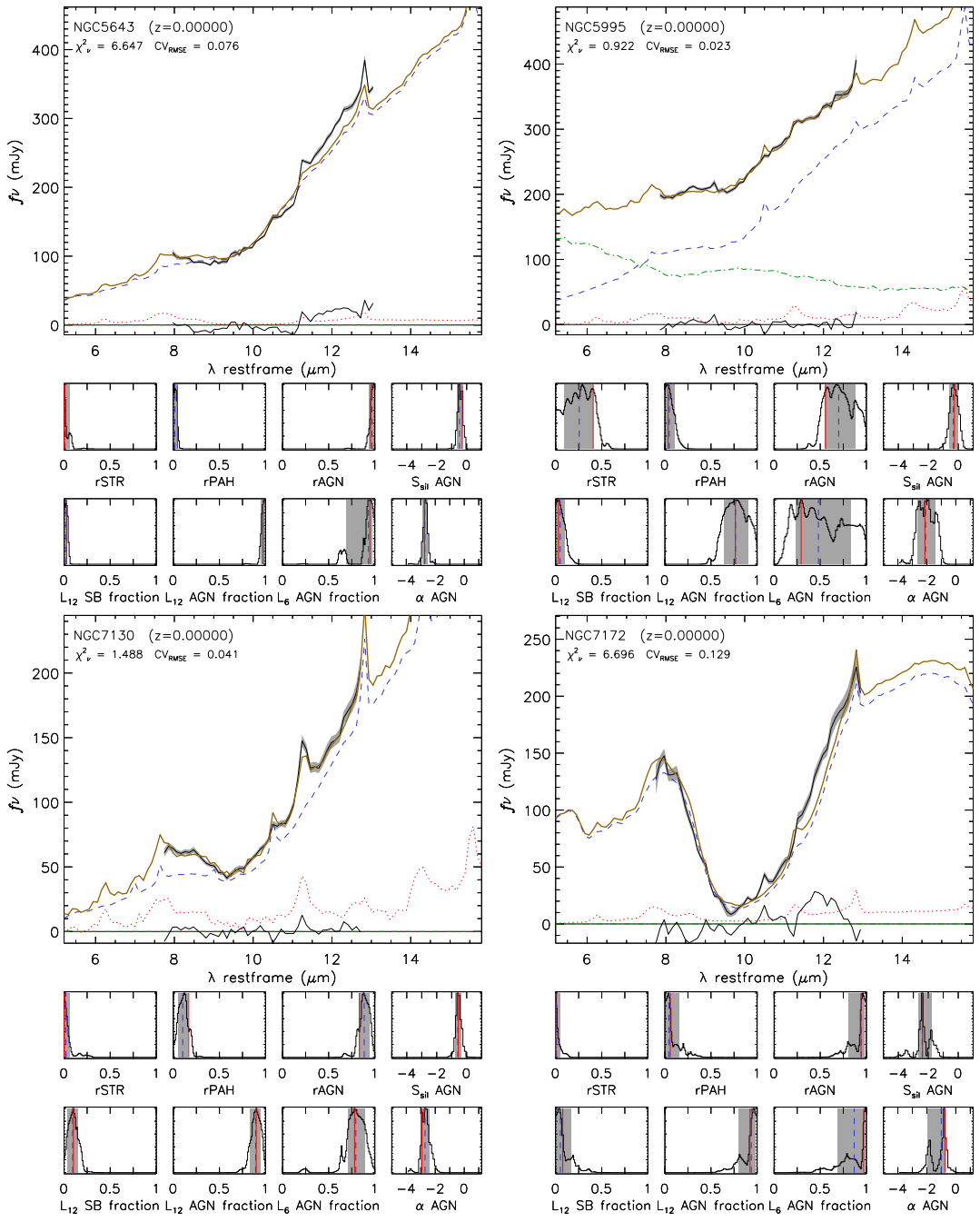
NGC5643 (z=0.00000)
χ^2_ν = 6.647 CV_{RMSE} = 0.076
NGC5995 (z=0.00000)
χ^2_ν = 0.922 CV_{RMSE} = 0.023
NGC7130 (z=0.00000)
χ^2_ν = 1.488 CV_{RMSE} = 0.041
NGC7172 (z=0.00000)
χ^2_ν = 6.696 CV_{RMSE} = 0.129
fν (mJy)
λ restframe (μm)
rSTR
rPAH
rAGN
S_{sil} AGN
L_{12} SB fraction
L_{12} AGN fraction
L_6 AGN fraction
α AGN

FIGURE A.1

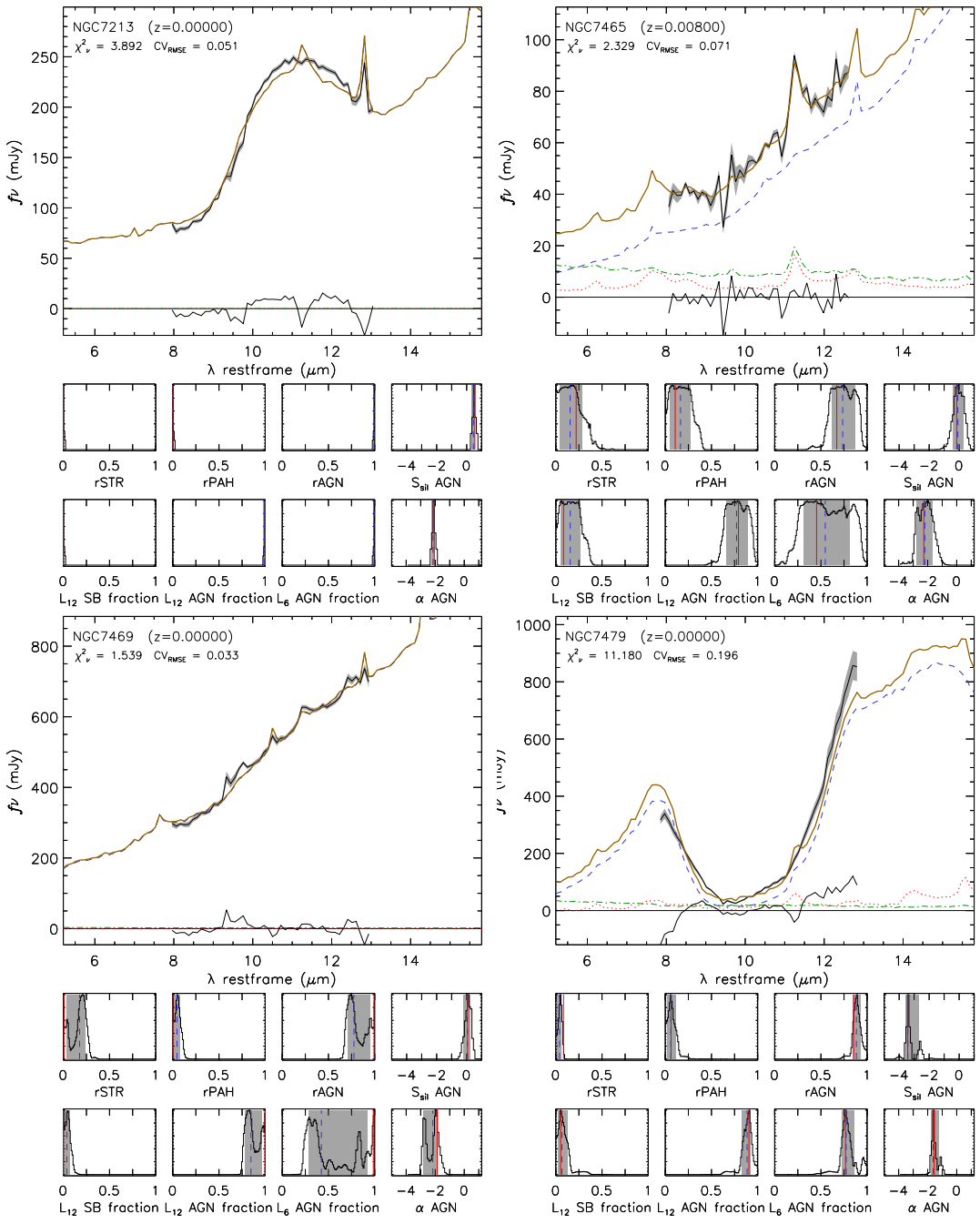
NGC7213 (z=0.00000)
χ^2_ν = 3.892 CV_{RMSE} = 0.051
NGC7465 (z=0.00800)
χ^2_ν = 2.329 CV_{RMSE} = 0.071
NGC7469 (z=0.00000)
χ^2_ν = 1.539 CV_{RMSE} = 0.033
NGC7479 (z=0.00000)
χ^2_ν = 11.180 CV_{RMSE} = 0.196
fν (mJy)
λ restframe (μm)
rSTR
rPAH
rAGN
S_{sil} AGN
L_{12} SB fraction
L_{12} AGN fraction
L_6 AGN fraction
α AGN

FIGURE A.1

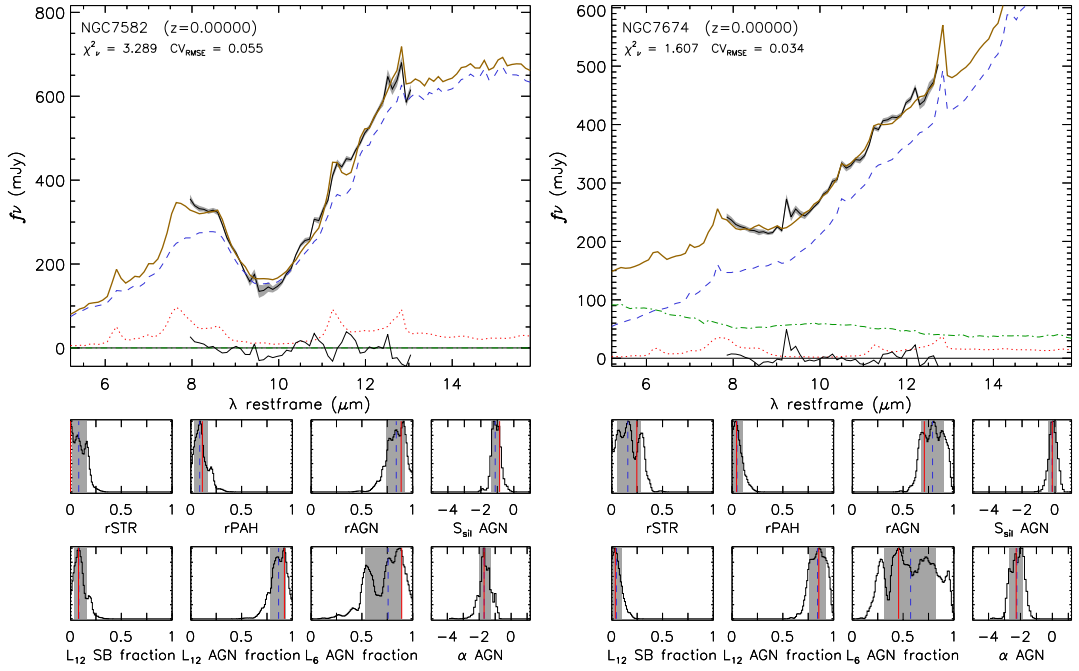
NGC7582 (z=0.00000)
χ^2_ν = 3.289 CV_{RMSE} = 0.055
NGC7674 (z=0.00000)
χ^2_ν = 1.607 CV_{RMSE} = 0.034
fν (mJy)
λ restframe (μm)
rSTR
rPAH
rAGN
S_{sil} AGN
L_{12} SB fraction
L_{12} AGN fraction
L_6 AGN fraction
α AGN

FIGURE A.1

References

Alexander, D. M., Bauer, F. E., Brandt, W. N., Schneider, D. P., Hornschemeier, A. E., Vignali, C., Barger, A. J., Broos, P. S., Cowie, L. L., Garmire, G. P., Townsley, L. K., Bautz, M. W., Chartas, G., and Sargent, W. L. W.: 2003, *AJ* **126**, 539

Alexander, D. M. and Hickox, R. C.: 2012, *New A Rev.* **56**, 93

Alonso-Herrero, A., Esquej, P., Roche, P. F., Ramos Almeida, C., González-Martín, O., Packham, C., Levenson, N. A., Mason, R. E., Hernán-Caballero, A., Pereira-Santaella, M., Alvarez, C., Aretxaga, I., López-Rodríguez, E., Colina, L., Díaz-Santos, T., Imanishi, M., Rodríguez Espinosa, J. M., and Perlman, E.: 2016a, *MNRAS* **455**, 563

Alonso-Herrero, A., Pereira-Santaella, M., Rieke, G. H., and Rigopoulou, D.: 2012a, *ApJ* **744**, 2

Alonso-Herrero, A., Pérez-González, P. G., Alexander, D. M., Rieke, G. H., Rigopoulou, D., Le Floc'h, E., Barmby, P., Papovich, C., Rigby, J. R., Bauer, F. E., Brandt, W. N., Egami, E., Willner, S. P., Dole, H., and Huang, J.-S.: 2006, *ApJ* **640**, 167

Alonso-Herrero, A., Poulton, R., Roche, P. F., Hernán-Caballero, A., Aretxaga, I., Martínez-Paredes, M., Ramos Almeida, C., Pereira-Santaella, M., Díaz-Santos, T., Levenson, N. A., Packham, C., Colina, L., Esquej, P., González-Martín, O., Ichikawa, K., Imanishi, M., Rodríguez Espinosa, J. M., and Telesco, C.: 2016b, *MNRAS* **463**, 2405

Alonso-Herrero, A., Quillen, A. C., Rieke, G. H., Ivanov, V. D., and Efstathiou, A.: 2003, *AJ* **126**, 81

Alonso-Herrero, A., Quillen, A. C., Simpson, C., Efstathiou, A., and Ward, M. J.: 2001, *AJ* **121**, 1369

Alonso-Herrero, A., Ramos Almeida, C., Esquej, P., Roche, P. F., Hernán-Caballero, A., Hönig, S. F., González-Martín, O., Aretxaga, I., Mason, R. E., Packham, C., Levenson, N. A., Rodríguez Espinosa, J. M., Siebenmorgen, R., Pereira-Santaella, M., Díaz-Santos, T., Colina, L., Alvarez, C., and Telesco, C. M.: 2014, *MNRAS* **443**, 2766

Alonso-Herrero, A., Ramos Almeida, C., Mason, R., Asensio Ramos, A., Roche, P. F., Levenson, N. A., Elitzur, M., Packham, C., Rodríguez Espinosa, J. M., Young, S., Díaz-Santos, T., and Pérez-García, A. M.: 2011, *ApJ* **736**, 82

Alonso-Herrero, A., Sánchez-Portal, M., Ramos Almeida, C., Pereira-Santaella, M., Esquej, P., García-Burillo, S., Castillo, M., González-Martín, O., Levenson, N., Hatziminaoglou, E., Acosta-Pulido, J. A., González-Serrano, J. I., Pović, M., Packham, C., and Pérez-García, A. M.: 2012b, *MNRAS* **425**, 311

Antonucci, R.: 1993, *ARA&A* **31**, 473

Antonucci, R. R. J. and Miller, J. S.: 1985, *ApJ* **297**, 621

Appleton, P. N., Fadda, D. T., Marleau, F. R., Frayer, D. T., Helou, G., Condon, J. J., Choi, P. I., Yan, L., Lacy, M., Wilson, G., Armus, L., Chapman, S. C., Fang, F., Heinrichson, I., Im, M., Jannuzi, B. T., Storrie-Lombardi, L. J., Shupe, D., Soifer, B. T., Squires, G., and Teplitz, H. I.: 2004, *ApJS* **154**, 147

Asmus, D., Gandhi, P., Hönig, S. F., Smette, A., and Duschl, W. J.: 2015, *MNRAS* **454**, 766

Asmus, D., Hönig, S. F., Gandhi, P., Smette, A., and Duschl, W. J.: 2014, *MNRAS* **439**, 1648

Assef, R. J., Stern, D., Kochanek, C. S., Blain, A. W., Brodwin, M., Brown, M. J. I., Donoso, E., Eisenhardt, P. R. M., Jannuzi, B. T., Jarrett, T. H., Stanford, S. A., Tsai, C.-W., Wu, J., and Yan, L.: 2013, *ApJ* **772**, 26

Baldwin, J. A., Phillips, M. M., and Terlevich, R.: 1981, *PASP* **93**, 5

Balestra, I., Mainieri, V., Popesso, P., Dickinson, M., Nonino, M., Rosati, P., Teimoorinia, H., Vanzella, E., Cristiani, S., Cesarsky, C., Fosbury, R. A. E., Kuntschner, H., and Rettura, A.: 2010, *A&A* **512**, A12

Bauer, F. E., Alexander, D. M., Brandt, W. N., Schneider, D. P., Treister, E., Hornschemeier, A. E., and Garmire, G. P.: 2004, *AJ* **128**, 2048

Beckmann, V., Soldi, S., Ricci, C., Alfonso-Garzón, J., Courvoisier, T. J.-L., Domingo, A., Gehrels, N., Lubiński, P., Mas-Hesse, J. M., and Zdziarski, A. A.: 2009, *A&A* **505**, 417

Beckwith, S. V. W., Stiavelli, M., Koekemoer, A. M., Caldwell, J. A. R., Ferguson, H. C., Hook, R., Lucas, R. A., Bergeron, L. E., Corbin, M., Jogee, S., Panagia, N., Robberto, M., Royle, P., Somerville, R. S., and Sosey, M.: 2006, *AJ* **132**, 1729

Bendo, G. J., Boselli, A., Dariush, A., Pohlen, M., Roussel, H., Sauvage, M., Smith, M. W. L., Wilson, C. D., Baes, M., Cooray, A., Clements, D. L., Cortese, L., Foyle, K., Galametz, M., Gomez, H. L., Lebouteiller, V., Lu, N., Madden, S. C., Mentuch, E., O'Halloran, B., Page, M. J., Remy, A., Schulz, B., and Spinoglio, L.: 2012, *MNRAS* **419**, 1833

Bertin, E. and Arnouts, S.: 1996, *A&AS* **117**, 393

Bianchi, S., Corral, A., Panessa, F., Barcons, X., Matt, G., Bassani, L., Carrera, F. J., and Jiménez-Bailón, E.: 2008, *MNRAS* **385**, 195

Bradt, H. V., Burke, B. F., Canizares, C. R., Greenfield, P. E., Kelley, R. L., McClintock, J. E., van Paradijs, J., and Koski, A. T.: 1978, *ApJ* **226**, L111

Brandt, W. N. and Hasinger, G.: 2005, *ARA&A* **43**, 827

Brightman, M. and Nandra, K.: 2011, *MNRAS* **413**, 1206

Burtscher, L., Meisenheimer, K., Tristram, K. R. W., Jaffe, W., Hönig, S. F., Davies, R. I., Kishimoto, M., Pott, J.-U., Röttgering, H., Schartmann, M., Weigelt, G., and Wolf, S.: 2013, *A&A* **558**, A149

Calzetti, D., Wu, S.-Y., Hong, S., Kennicutt, R. C., Lee, J. C., Dale, D. A., Engelbracht, C. W., van Zee, L., Draine, B. T., Hao, C.-N., Gordon, K. D., Moustakas, J., Murphy, E. J., Regan, M., Begum, A., Block, M., Dalcanton, J., Funes, J., Gil de Paz, A., Johnson, B., Sakai, S., Skillman, E., Walter, F., Weisz, D., Williams, B., and Wu, Y.: 2010, *ApJ* **714**, 1256

Cardamone, C. N., Urry, C. M., Damen, M., van Dokkum, P., Treister, E., Labbé, I., Virani, S. N., Lira, P., and Gawiser, E.: 2008, *ApJ* **680**, 130

Cardamone, C. N., van Dokkum, P. G., Urry, C. M., Taniguchi, Y., Gawiser, E., Brammer, G., Taylor, E., Damen, M., Treister, E., Cobb, B. E., Bond, N., Schawinski, K., Lira, P., Murayama, T., Saito, T., and Sumikawa, K.: 2010, *ApJS* **189**, 270

Chary, R. and Elbaz, D.: 2001, *ApJ* **556**, 562

Cohen, S. H., Ryan, Jr., R. E., Straughn, A. N., Hathi, N. P., Windhorst, R. A., Koekemoer, A. M., Pirzkal, N., Xu, C., Mobasher, B., Malhotra, S., Strolger, L.-G., and Rhoads, J. E.: 2006, *ApJ* **639**, 731

Condon, J. J.: 1992, *ARA&A* **30**, 575

Contini, T., Considere, S., and Davoust, E.: 1998, *A&AS* **130**, 285

Corral, A., Della Ceca, R., Caccianiga, A., Severgnini, P., Brunner, H., Carrera, F. J., Page, M. J., and Schwope, A. D.: 2011, *A&A* **530**, A42

Dale, D. A., Aniano, G., Engelbracht, C. W., Hinz, J. L., Krause, O., Montiel, E. J., Roussel, H., Appleton, P. N., Armus, L., Beirão, P., Bolatto, A. D., Brandl, B. R., Calzetti, D., Crocker, A. F., Croxall, K. V., Draine, B. T., Galametz, M., Gordon, K. D., Groves, B. A., Hao, C.-N., Helou, G., Hunt, L. K., Johnson, B. D., Kennicutt, R. C., Koda, J., Leroy, A. K., Li, Y., Meidt, S. E., Miller, A. E., Murphy, E. J., Rahman, N., Rix, H.-W., Sandstrom, K. M., Sauvage, M., Schinnerer, E., Skibba, R. A., Smith, J.-D. T., Tabatabaei, F. S., Walter, F., Wilson, C. D., Wolfire, M. G., and Zibetti, S.: 2012, *ApJ* **745**, 95

Dale, D. A. and Helou, G.: 2002, *ApJ* **576**, 159

De Buizer, J. and Fisher, R.: 2005, in H. U. Käufl, R. Siebenmorgen, and A. Moorwood (eds.), *High Resolution Infrared Spectroscopy in Astronomy*, pp 84–87

de Graauw, T., Helmich, F. P., Phillips, T. G., Stutzki, J., Caux, E., Whyborn, N. D., Dieleman, P., Roelfsema, P. R., Aarts, H., Assendorp, R., Bachiller, R., Baechtold, W., Barcia, A., Beintema, D. A., Belitsky, V., Benz, A. O., Bieber, R., Boogert, A., Borys, C., Bumble, B., Caïs, P., Caris, M., Cerulli-Irelli, P., Chattopadhyay, G., Cherednichenko, S., Ciechanowicz, M., Coeur-Joly, O., Comito, C., Cros, A., de Jonge, A., de Lange, G., Delforges, B., Delorme, Y., den Boggende, T., Desbat, J.-M., Diez-González, C., di Giorgio, A. M., Dubbeldam, L., Edwards, K., Eggens, M., Erickson, N., Evers, J., Fich, M., Finn, T., Franke, B., Gaier, T., Gal, C., Gao, J. R., Gallego, J.-D., Gauffre, S., Gill, J. J., Glenz, S., Golstein, H., Goulooze, H., Gunsing, T., Güsten, R., Hartogh, P., Hatch, W. A., Higgins, R., Honingh, E. C., Huisman, R., Jackson, B. D., Jacobs, H., Jacobs, K., Jarchow, C., Javadi, H., Jellema, W., Justen, M., Karpov, A., Kasemann, C., Kawamura, J., Keizer, G., Kester, D., Klapwijk, T. M., Klein, T., Kollberg, E., Kooi, J., Kooiman, P.-P., Kopf, B., Krause, M., Krieg, J.-M., Kramer, C., Kruizenga, B., Kuhn, T., Laauwen, W., Lai, R., Larsson, B., Leduc, H. G., Leinz, C., Lin, R. H., Liseau, R., Liu, G. S., Loose, A., López-Fernandez, I., Lord, S., Luinge, W., Marston, A., Martín-Pintado, J., Maestrini, A., Maiwald, F. W., McCoey, C., Mehdi, I., Megej, A., Melchior, M., Meinsma, L.,

Merkel, H., Michalska, M., Monstein, C., Moratschke, D., Morris, P., Muller, H., Murphy, J. A., Naber, A., Natale, E., Nowosielski, W., Nuzzolo, F., Olberg, M., Olbrich, M., Orfei, R., Orleanski, P., Ossenkopf, V., Peacock, T., Pearson, J. C., Peron, I., Phillip-May, S., Piazzo, L., Planesas, P., Rataj, M., Ravera, L., Risacher, C., Salez, M., Samoska, L. A., Saraceno, P., Schieder, R., Schlecht, E., Schlöder, F., Schmülling, F., Schultz, M., Schuster, K., Siebertz, O., Smit, H., Szczerba, R., Shipman, R., Steinmetz, E., Stern, J. A., Stokroos, M., Teipen, R., Teyssier, D., Tils, T., Trappe, N., van Baaren, C., van Leeuwen, B.-J., van de Stadt, H., Visser, H., Wildeman, K. J., Wafelbakker, C. K., Ward, J. S., Wesselius, P., Wild, W., Wulff, S., Wunsch, H.-J., Tielens, X., Zaal, P., Zirath, H., Zmuidzinas, J., and Zwart, F.: 2010, *A&A* **518**, L6

de Vaucouleurs, G., de Vaucouleurs, A., Corwin, Jr., H. G., Buta, R. J., Paturel, G., and Fouque, P.: 1991, *S&T* **82**, 621

Del Moro, A., Alexander, D. M., Mullaney, J. R., Daddi, E., Pannella, M., Bauer, F. E., Pope, A., Dickinson, M., Elbaz, D., Barthel, P. D., Garrett, M. A., Brandt, W. N., Charmandaris, V., Chary, R. R., Dasyra, K., Gilli, R., Hickox, R. C., Hwang, H. S., Ivison, R. J., Juneau, S., Le Floc'h, E., Luo, B., Morrison, G. E., Rovilos, E., Sargent, M. T., and Xue, Y. Q.: 2013, *A&A* **549**, A59

Diamond-Stanic, A. M. and Rieke, G. H.: 2012, *ApJ* **746**, 168

Díaz-Santos, T., Alonso-Herrero, A., Colina, L., Packham, C., Levenson, N. A., Pereira-Santaella, M., Roche, P. F., and Telesco, C. M.: 2010, *ApJ* **711**, 328

Doe, S., Nguyen, D., Stawarz, C., Refsdal, B., Siemiginowska, A., Burke, D., Evans, I., Evans, J., McDowell, J., Houck, J., and Nowak, M.: 2007, in R. A. Shaw, F. Hill, and D. J. Bell (eds.), *Astronomical Data Analysis Software and Systems XVI*, Vol. 376 of *Astronomical Society of the Pacific Conference Series*, p. 543

Donley, J. L., Koekemoer, A. M., Brusa, M., Capak, P., Cardamone, C. N., Civano, F., Ilbert, O., Impey, C. D., Kartaltepe, J. S., Miyaji, T., Salvato, M., Sanders, D. B., Trump, J. R., and Zamorani, G.: 2012, *ApJ* **748**, 142

Donley, J. L., Rieke, G. H., Pérez-González, P. G., and Barro, G.: 2008, *ApJ* **687**, 111

Donley, J. L., Rieke, G. H., Pérez-González, P. G., Rigby, J. R., and Alonso-Herrero, A.: 2007, *ApJ* **660**, 167

Donley, J. L., Rieke, G. H., Rigby, J. R., and Pérez-González, P. G.: 2005, *ApJ* **634**, 169

Efstathiou, A. and Rowan-Robinson, M.: 1995, *MNRAS* **273**, 649

Elitzur, M.: 2007, in L. C. Ho and J.-W. Wang (eds.), *The Central Engine of Active Galactic Nuclei*, Vol. 373 of *Astronomical Society of the Pacific Conference Series*, p. 415

Elitzur, M.: 2012, *ApJ* **747**, L33

Elitzur, M. and Shlosman, I.: 2006, *ApJ* **648**, L101

Esquej, P., Alonso-Herrero, A., González-Martín, O., Hönig, S. F., Hernán-Caballero, A., Roche, P., Ramos Almeida, C., Mason, R. E., Díaz-Santos, T., Levenson, N. A., Aretxaga, I., Rodríguez Espinosa, J. M., and Packham, C.: 2014, *ApJ* **780**, 86

Evans, A. S., Becklin, E. E., Scoville, N. Z., Neugebauer, G., Soifer, B. T., Matthews, K., Ressler, M., Werner, M., and Rieke, M.: 2003, *AJ* **125**, 2341

Fanaroff, B. L. and Riley, J. M.: 1974, *MNRAS* **167**, 31P

Fazio, G. G., Hora, J. L., Allen, L. E., Ashby, M. L. N., Barmby, P., Deutsch, L. K., Huang, J.-S., Kleiner, S., Marengo, M., Megeath, S. T., Melnick, G. J., Pahre, M. A., Patten, B. M., Polizotti, J., Smith, H. A., Taylor, R. S., Wang, Z., Willner, S. P., Hoffmann, W. F., Pipher, J. L., Forrest, W. J., McMurty, C. W., McCreight, C. R., McKelvey, M. E., McMurray, R. E., Koch, D. G., Moseley, S. H., Arendt, R. G., Mentzell, J. E., Marx, C. T., Losch, P., Mayman, P., Eichhorn, W., Krebs, D., Jhabvala, M., Gezari, D. Y., Fixsen, D. J., Flores, J., Shakoorzadeh, K., Jungo, R., Hakun, C., Workman, L., Karpati, G., Kichak, R., Whitley, R., Mann, S., Tollestrup, E. V., Eisenhardt, P., Stern, D., Gorjian, V., Bhattacharya, B., Carey, S., Nelson, B. O., Glaccum, W. J., Lacy, M., Lowrance, P. J., Laine, S., Reach, W. T., Stauffer, J. A., Surace, J. A., Wilson, G., Wright, E. L., Hoffman, A., Domingo, G., and Cohen, M.: 2004, *ApJS* **154**, 10

Feltre, A., Hatziminaoglou, E., Fritz, J., and Franceschini, A.: 2012, *MNRAS* **426**, 120

Freeman, P., Doe, S., and Siemiginowska, A.: 2001, in J.-L. Starck and F. D. Murtagh (eds.), *Astronomical Data Analysis*, Vol. 4477 of *Proc. SPIE*, pp 76–87

Fritz, J., Franceschini, A., and Hatziminaoglou, E.: 2006, *MNRAS* **366**, 767

Galametz, M., Kennicutt, R. C., Albrecht, M., Aniano, G., Armus, L., Bertoldi, F., Calzetti, D., Crocker, A. F., Croxall, K. V., Dale, D. A., Donovan Meyer, J., Draine, B. T., Engelbracht, C. W., Hinz, J. L., Roussel, H., Skibba, R. A., Tabatabaei, F. S., Walter, F., Weiss, A., Wilson, C. D., and Wolfire, M. G.: 2012, *MNRAS* **425**, 763

Gandhi, P., Horst, H., Smette, A., Hönig, S., Comastri, A., Gilli, R., Vignali, C., and Duschl, W.: 2009, *A&A* **502**, 457

García-Bernete, I., Ramos Almeida, C., Acosta-Pulido, J. A., Alonso-Herrero, A., González-Martín, O., Hernán-Caballero, A., Pereira-Santaella, M., Levenson, N. A., Packham, C., Perlman, E. S., Ichikawa, K., Esquej, P., and Díaz-Santos, T.: 2016, *MNRAS* **463**, 3531

García-Bernete, I., Ramos Almeida, C., Acosta-Pulido, J. A., Alonso-Herrero, A., Sánchez-Portal, M., Castillo, M., Pereira-Santaella, M., Esquej, P., González-Martín, O., Díaz-Santos, T., Roche, P., Fisher, S., Pović, M., Pérez García, A. M., Valtchanov, I., Packham, C., and Levenson, N. A.: 2015, *MNRAS* **449**, 1309

García-Burillo, S., Combes, F., Ramos Almeida, C., Usero, A., Krips, M., Alonso-Herrero, A., Aalto, S., Casasola, V., Hunt, L. K., Martín, S., Viti, S., Colina, L., Costagliola, F., Eckart, A., Fuente, A., Henkel, C., Márquez, I., Neri, R., Schinnerer, E., Tacconi, L. J., and van der Werf, P. P.: 2016, *ApJ* **823**, L12

García-González, J., Alonso-Herrero, A., Hernán-Caballero, A., Pereira-Santaella, M., Ramos-Almeida, C., Acosta-Pulido, J. A., Díaz-Santos, T., Esquej, P., González-Martín, O., Ichikawa, K., López-Rodríguez, E., Povic, M., Roche, P. F., and Sánchez-Portal, M.: 2016, *MNRAS* **458**, 4512

García-González, J., Alonso-Herrero, A., Pérez-González, P. G., Hernán-Caballero, A., Sarajedini, V. L., and Villar, V.: 2015, *MNRAS* **446**, 3199

Giacconi, R., Rosati, P., Tozzi, P., Nonino, M., Hasinger, G., Norman, C., Bergeron, J., Borgani, S., Gilli, R., Gilmozzi, R., and Zheng, W.: 2001, *ApJ* **551**, 624

Giavalisco, M., Ferguson, H. C., Koekemoer, A. M., Dickinson, M., Alexander, D. M., Bauer, F. E., Bergeron, J., Biagetti, C., Brandt, W. N., Casertano, S., Cesarsky, C., Chatzichristou, E., Conselice, C., Cristiani, S., Da Costa, L., Dahlen, T., de Mello, D., Eisenhardt, P., Erben, T., Fall, S. M., Fassnacht, C., Fosbury, R., Fruchter, A., Gardner, J. P., Grogin, N., Hook, R. N., Hornschemeier, A. E., Idzi, R., Jogee, S., Kretchmer, C., Laidler, V., Lee, K. S., Livio, M., Lucas, R., Madau, P., Mobasher, B., Moustakas, L. A., Nonino, M., Padovani, P., Papovich, C., Park, Y., Ravindranath, S., Renzini, A., Richardson, M., Riess, A., Rosati, P., Schirmer, M., Schreier, E., Somerville, R. S., Spinrad, H., Stern, D., Stiavelli, M., Strolger, L., Urry, C. M., Vandame, B., Williams, R., and Wolf, C.: 2004, *ApJ* **600**, L93

Gilli, R., Comastri, A., and Hasinger, G.: 2007, *A&A* **463**, 79

Glass, I. S.: 2004, *MNRAS* **350**, 1049

Glasse, A. C., Atad-Ettedgui, E. I., and Harris, J. W.: 1997, in A. L. Ardeberg (ed.), *Optical Telescopes of Today and Tomorrow*, Vol. 2871 of *Proc. SPIE*, pp 1197–1203

González-Martín, O., Díaz-González, D., Acosta-Pulido, J. A., Masegosa, J., Papadakis, I. E., Rodríguez-Espinosa, J. M., Márquez, I., and Hernández-García, L.: 2014, *A&A* **567**, A92

González-Martín, O., Masegosa, J., Márquez, I., Guainazzi, M., and Jiménez-Bailón, E.: 2009, *A&A* **506**, 1107

González-Martín, O., Masegosa, J., Márquez, I., Rodríguez-Espinosa, J. M., Acosta-Pulido, J. A., Ramos Almeida, C., Dultzin, D., Hernández-García, L., Ruschel-Dutra, D., and Alonso-Herrero, A.: 2015, *A&A* **578**, A74

González-Martín, O., Rodríguez-Espinosa, J. M., Díaz-Santos, T., Packham, C., Alonso-Herrero, A., Esquej, P., Ramos Almeida, C., Mason, R., and Telesco, C.: 2013, *A&A* **553**, A35

Goulding, A. D., Alexander, D. M., Bauer, F. E., Forman, W. R., Hickox, R. C., Jones, C., Mullaney, J. R., and Trichas, M.: 2012, *ApJ* **755**, 5

Granato, G. L. and Danese, L.: 1994, *MNRAS* **268**, 235

Grazian, A., Fontana, A., de Santis, C., Nonino, M., Salimbeni, S., Giallongo, E., Cristiani, S., Gallozzi, S., and Vanzella, E.: 2006, *A&A* **449**, 951

Griffin, M. J., Abergel, A., Abreu, A., Ade, P. A. R., André, P., Augueres, J.-L., Babbedge, T., Bae, Y., Baillie, T., Baluteau, J.-P., Barlow, M. J., Bendo, G., Benielli, D., Bock, J. J., Bonhomme, P., Brisbin, D., Brockley-Blatt, C., Caldwell, M., Cara, C., Castro-Rodriguez, N., Cerulli, R., Chanial, P., Chen, S., Clark, E., Clements, D. L., Clerc, L., Coker, J., Communal, D., Conversi, L., Cox, P., Crumb, D., Cunningham, C., Daly, F., Davis, G. R., de Antoni, P., Delderfield, J., Devin, N., di Giorgio, A., Didschuns, I., Dohlen, K., Donati, M., Dowell, A., Dowell, C. D., Duband, L., Dumaye, L., Emery, R. J., Ferlet, M., Ferrand, D., Fontignie, J., Fox, M., Franceschini, A., Frerking, M., Fulton, T., Garcia, J., Gastaud, R., Gear, W. K., Glenn, J., Goizel, A., Griffin, D. K., Grundy, T., Guest, S., Guillemet, L., Hargrave, P. C., Harwit, M., Hastings, P., Hatziminaoglou, E., Herman, M., Hinde, B., Hristov, V., Huang, M., Imhof, P., Isaak, K. J., Israelsson, U., Ivison, R. J., Jennings, D., Kiernan, B., King, K. J., Lange, A. E., Latter, W., Laurent, G., Laurent, P., Leeks, S. J., Lellouch, E., Levenson, L., Li, B., Li, J., Lilienthal, J., Lim, T., Liu, S. J., Lu, N., Madden, S., Mainetti, G., Marliani, P., McKay, D., Mercier, K., Molinari, S., Morris, H., Moseley, H., Mulder, J., Mur, M., Naylor, D. A., Nguyen, H., O'Halloran, B., Oliver, S., Olofsson, G., Olofsson, H.-G., Orfei, R., Page, M. J., Pain, I., Panuzzo, P.,

Papageorgiou, A., Parks, G., Parr-Burman, P., Pearce, A., Pearson, C., Pérez-Fournon, I., Pinsard, F., Pisano, G., Podosek, J., Pohlen, M., Polehampton, E. T., Pouliquen, D., Rigopoulou, D., Rizzo, D., Roseboom, I. G., Roussel, H., Rowan-Robinson, M., Rownd, B., Saraceno, P., Sauvage, M., Savage, R., Savini, G., Sawyer, E., Scharmberg, C., Schmitt, D., Schneider, N., Schulz, B., Schwartz, A., Shafer, R., Shupe, D. L., Sibthorpe, B., Sidher, S., Smith, A., Smith, A. J., Smith, D., Spencer, L., Stobie, B., Sudiwala, R., Sukhatme, K., Surace, C., Stevens, J. A., Swinyard, B. M., Trichas, M., Tourette, T., Triou, H., Tseng, S., Tucker, C., Turner, A., Vaccari, M., Valtchanov, I., Vigroux, L., Virique, E., Voellmer, G., Walker, H., Ward, R., Waskett, T., Weilert, M., Wesson, R., White, G. J., Whitehouse, N., Wilson, C. D., Winter, B., Woodcraft, A. L., Wright, G. S., Xu, C. K., Zavagno, A., Zemcov, M., Zhang, L., and Zonca, E.: 2010, *A&A* **518**, L3

Hao, H., Elvis, M., Civano, F., Lanzuisi, G., Brusa, M., Lusso, E., Zamorani, G., Comastri, A., Bongiorno, A., Impey, C. D., Koekemoer, A. M., Le Floc'h, E., Salvato, M., Sanders, D., Trump, J. R., and Vignali, C.: 2010, *ApJ* **724**, L59

Häring, N. and Rix, H.-W.: 2004, *ApJ* **604**, L89

Hatziminaoglou, E., Hernán-Caballero, A., Feltre, A., and Piñol Ferrer, N.: 2015, *ApJ* **803**, 110

Hatziminaoglou, E., Omont, A., Stevens, J. A., Amblard, A., Arumugam, V., Auld, R., Aussel, H., Babbedge, T., Blain, A., Bock, J., Boselli, A., Buat, V., Burgarella, D., Castro-Rodríguez, N., Cava, A., Chanial, P., Clements, D. L., Conley, A., Conversi, L., Cooray, A., Dowell, C. D., Dwek, E., Dye, S., Eales, S., Elbaz, D., Farrah, D., Fox, M., Franceschini, A., Gear, W., Glenn, J., González Solares, E. A., Griffin, M., Halpern, M., Ibar, E., Isaak, K., Ivison, R. J., Lagache, G., Levenson, L., Lu, N., Madden, S., Maffei, B., Mainetti, G., Marchetti, L., Mortier, A. M. J., Nguyen, H. T., O'Halloran, B., Oliver, S. J., Page, M. J., Panuzzo, P., Papageorgiou, A., Pearson, C. P., Pérez-Fournon, I., Pohlen, M., Rawlings, J. I., Rigopoulou, D., Rizzo, D., Roseboom, I. G., Rowan-Robinson, M., Sanchez Portal, M., Schulz, B., Scott, D., Seymour, N., Shupe, D. L., Smith, A. J., Symeonidis, M., Trichas, M., Tugwell, K. E., Vaccari, M., Valtchanov, I., Vigroux, L., Wang, L., Ward, R., Wright, G., Xu, C. K., and Zemcov, M.: 2010, *A&A* **518**, L33

Heckman, T. M.: 1980, *A&A* **87**, 152

Helou, G., Soifer, B. T., and Rowan-Robinson, M.: 1985, *ApJ* **298**, L7

Hernán-Caballero, A., Alonso-Herrero, A., Hatziminaoglou, E., Spoon, H. W. W., Ramos Almeida, C., Díaz Santos, T., Hönig, S. F., González-Martín, O., and Esquej, P.: 2015, *ApJ* **803**, 109

Hernán-Caballero, A. and Hatziminaoglou, E.: 2011, *MNRAS* **414**, 500

Hernán-Caballero, A., Pérez-Fournon, I., Hatziminaoglou, E., Afonso-Luis, A., Rowan-Robinson, M., Rigopoulou, D., Farrah, D., Lonsdale, C. J., Babbedge, T., Clements, D., Serjeant, S., Pozzi, F., Vaccari, M., Montenegro-Montes, F. M., Valtchanov, I., González-Solares, E., Oliver, S., Shupe, D., Gruppioni, C., Vila-Vilaró, B., Lari, C., and La Franca, F.: 2009, *MNRAS* **395**, 1695

Hernán-Caballero, A., Spoon, H. W. W., Lebouteiller, V., Rupke, D. S. N., and Barry, D. P.: 2016, *MNRAS* **455**, 1796

Hickox, R. C., Jones, C., Forman, W. R., Murray, S. S., Kochanek, C. S., Eisenstein, D., Jannuzi, B. T., Dey, A., Brown, M. J. I., Stern, D., Eisenhardt, P. R., Gorjian, V., Brodwin, M., Narayan, R., Cool, R. J., Kenter, A., Caldwell, N., and Anderson, M. E.: 2009, *ApJ* **696**, 891

Hickox, R. C., Mullaney, J. R., Alexander, D. M., Chen, C.-T. J., Civano, F. M., Goulding, A. D., and Hainline, K. N.: 2014, *ApJ* **782**, 9

Ho, L. C., Filippenko, A. V., and Sargent, W. L. W.: 1997, *ApJS* **112**, 315

Hoenig, S. F.: 2013, *ArXiv e-prints*

Hönig, S. F., Beckert, T., Ohnaka, K., and Weigelt, G.: 2006, *A&A* **452**, 459

Hönig, S. F. and Kishimoto, M.: 2010, *A&A* **523**, A27

Hönig, S. F. and Kishimoto, M.: 2011, *A&A* **534**, A121

Hönig, S. F., Kishimoto, M., Gandhi, P., Smette, A., Asmus, D., Duschl, W., Polletta, M., and Weigelt, G.: 2010, *A&A* **515**, A23

Hopkins, A. M. and Beacom, J. F.: 2006, *ApJ* **651**, 142

Houck, J. R., Roellig, T. L., van Cleve, J., Forrest, W. J., Herter, T., Lawrence, C. R., Matthews, K., Reitsema, H. J., Soifer, B. T., Watson, D. M., Weedman, D., Huisjen, M., Troeltzsch, J., Barry, D. J., Bernard-Salas, J., Blacken, C. E., Brandl, B. R., Charmandaris, V., Devost, D., Gull, G. E., Hall, P., Henderson, C. P., Higdon, S. J. U., Pirger, B. E., Schoenwald, J., Sloan, G. C., Uchida, K. I., Appleton, P. N., Armus, L., Burgdorf, M. J., Fajardo-Acosta, S. B., Grillmair, C. J., Ingalls, J. G., Morris, P. W., and Teplitz, H. I.: 2004, *ApJS* **154**, 18

Ichikawa, K., Packham, C., Ramos Almeida, C., Asensio Ramos, A., Alonso-Herrero, A., González-Martín, O., Lopez-Rodriguez, E., Ueda, Y., Díaz-Santos, T., Elitzur, M., Hönig, S. F., Imanishi, M., Levenson, N. A., Mason, R. E., Perlman, E. S., and Alsip, C. D.: 2015, *ApJ* **803**, 57

Ivison, R. J., Magnelli, B., Ibar, E., Andreani, P., Elbaz, D., Altieri, B., Amblard, A., Arumugam, V., Auld, R., Aussel, H., Babbedge, T., Berta, S., Blain, A., Bock, J., Bongiovanni, A., Boselli, A., Buat, V., Burgarella, D., Castro-Rodríguez, N., Cava, A., Cepa, J., Chanial, P., Cimatti, A., Cirasuolo, M., Clements, D. L., Conley, A., Conversi, L., Cooray, A., Daddi, E., Dominguez, H., Dowell, C. D., Dwek, E., Eales, S., Farrah, D., Förster Schreiber, N., Fox, M., Franceschini, A., Gear, W., Genzel, R., Glenn, J., Griffin, M., Gruppioni, C., Halpern, M., Hatziminaoglou, E., Isaak, K., Lagache, G., Levenson, L., Lu, N., Lutz, D., Madden, S., Maffei, B., Magdis, G., Mainetti, G., Maiolino, R., Marchetti, L., Morrison, G. E., Mortier, A. M. J., Nguyen, H. T., Nordon, R., O'Halloran, B., Oliver, S. J., Omont, A., Owen, F. N., Page, M. J., Panuzzo, P., Papageorgiou, A., Pearson, C. P., Pérez-Fournon, I., Pérez García, A. M., Poglitsch, A., Pohlen, M., Popesso, P., Pozzi, F., Rawlings, J. I., Raymond, G., Rigopoulou, D., Riguccini, L., Rizzo, D., Rodighiero, G., Roseboom, I. G., Rowan-Robinson, M., Saintonge, A., Sanchez Portal, M., Santini, P., Schulz, B., Scott, D., Seymour, N., Shao, L., Shupe, D. L., Smith, A. J., Stevens, J. A., Sturm, E., Symeonidis, M., Tacconi, L., Trichas, M., Tugwell, K. E., Vaccari, M., Valtchanov, I., Vieira, J., Vigroux, L., Wang, L., Ward, R., Wright, G., Xu, C. K., and Zemcov, M.: 2010, *A&A* **518**, L31

Kauffmann, G., Heckman, T. M., Tremonti, C., Brinchmann, J., Charlot, S., White, S. D. M., Ridgway, S. E., Brinkmann, J., Fukugita, M., Hall, P. B., Ivezić, Ž., Richards, G. T., and Schneider, D. P.: 2003, *MNRAS* **346**, 1055

Kewley, L. J., Heisler, C. A., Dopita, M. A., and Lumsden, S.: 2001, *ApJS* **132**, 37

Khachikian, E. Y. and Weedman, D. W.: 1974, *ApJ* **192**, 581

Klesman, A. and Sarajedini, V.: 2007, *ApJ* **665**, 225

Koratkar, A. and Blaes, O.: 1999, *PASP* **111**, 1

Kormendy, J. and Richstone, D.: 1995, *ARA&A* **33**, 581

Kozłowski, S., Kochanek, C. S., Stern, D., Ashby, M. L. N., Assef, R. J., Bock, J. J., Borys, C., Brand, K., Brodwin, M., Brown, M. J. I., Cool, R., Cooray, A., Croft, S., Dey, A., Eisenhardt, P. R., Gonzalez, A., Gorjian, V., Griffith, R., Grogin, N., Ivison, R., Jacob, J., Jannuzi, B. T., Mainzer, A., Moustakas, L., Röttgering, H., Seymour, N., Smith, H. A., Stanford, S. A., Stauffer, J. R., Sullivan, I. S., van Breugel, W., Willner, S. P., and Wright, E. L.: 2010, *ApJ* **716**, 530

Krabbe, A., Böker, T., and Maiolino, R.: 2001, *ApJ* **557**, 626

Krolik, J. H. and Begelman, M. C.: 1988, *ApJ* **329**, 702

Kroupa, P.: 2001, *MNRAS* **322**, 231

Lacy, M., Ridgway, S. E., Gates, E. L., Nielsen, D. M., Petric, A. O., Sajina, A., Urrutia, T., Cox Drews, S., Harrison, C., Seymour, N., and Storrie-Lombardi, L. J.: 2013, *ApJS* **208**, 24

Lacy, M., Storrie-Lombardi, L. J., Sajina, A., Appleton, P. N., Armus, L., Chapman, S. C., Choi, P. I., Fadda, D., Fang, F., Frayer, D. T., Heinrichsen, I., Helou, G., Im, M., Marleau, F. R., Masci, F., Shupe, D. L., Soifer, B. T., Surace, J., Teplitz, H. I., Wilson, G., and Yan, L.: 2004, *ApJS* **154**, 166

Lagage, P. O., Pel, J. W., Authier, M., Belorgey, J., Claret, A., Doucet, C., Dubreuil, D., Durand, G., Elswijk, E., Girardot, P., Käufl, H. U., Kroes, G., Lortholary, M., Lussignol, Y., Marchesi, M., Pantin, E., Peletier, R., Pirard, J.-F., Pragt, J., Rio, Y., Schoenmaker, T., Siebenmorgen, R., Silber, A., Smette, A., Sterzik, M., and Veyssiere, C.: 2004, *The Messenger* **117**, 12

Laurent, O., Mirabel, I. F., Charmandaris, V., Gallais, P., Madden, S. C., Sauvage, M., Vigroux, L., and Cesarsky, C.: 2000, *A&A* **359**, 887

Le Fèvre, O., Vettolani, G., Paltani, S., Tresse, L., Zamorani, G., Le Brun, V., Moreau, C., Bottini, D., Maccagni, D., Picat, J. P., Scaramella, R., Scodeggio, M., Zanichelli, A., Adami, C., Arnouts, S., Bardelli, S., Bolzonella, M., Cappi, A., Charlot, S., Contini, T., Foucaud, S., Franzetti, P., Garilli, B., Gavignaud, I., Guzzo, L., Ilbert, O., Iovino, A., McCracken, H. J., Mancini, D., Marano, B., Marinoni, C., Mathez, G., Mazure, A., Meneux, B., Merighi, R., Pellò, R., Pollo, A., Pozzetti, L., Radovich, M., Zucca, E., Arnaboldi, M., Bondi, M., Bongiorno, A., Busarello, G., Ciliegi, P., Gregorini, L., Mellier, Y., Merluzzi, P., Ripepi, V., and Rizzo, D.: 2004, *A&A* **428**, 1043

Lebouteiller, V., Barry, D. J., Goes, C., Sloan, G. C., Spoon, H. W. W., Weedman, D. W., Bernard-Salas, J., and Houck, J. R.: 2015, *ApJS* **218**, 21

Lebouteiller, V., Barry, D. J., Spoon, H. W. W., Bernard-Salas, J., Sloan, G. C., Houck, J. R., and Weedman, D. W.: 2011, *ApJS* **196**, 8

Lehmer, B. D., Brandt, W. N., Alexander, D. M., Bauer, F. E., Schneider, D. P., Tozzi, P., Bergeron, J., Garmire, G. P., Giacconi, R., Gilli, R., Hasinger, G., Hornschemeier, A. E., Koekemoer, A. M., Mainieri, V., Miyaji, T., Nonino, M., Rosati, P., Silverman, J. D., Szokoly, G., and Vignali, C.: 2005, *ApJS* **161**, 21

Lehmer, B. D., Brandt, W. N., Alexander, D. M., Bell, E. F., Hornschemeier, A. E., McIntosh, D. H., Bauer, F. E., Gilli, R., Mainieri, V., Schneider, D. P., Silverman, J. D., Steffen, A. T., Tozzi, P., and Wolf, C.: 2008, *ApJ* **681**, 1163

Levenson, N. A., Radomski, J. T., Packham, C., Mason, R. E., Schaefer, J. J., and Telesco, C. M.: 2009, *ApJ* **703**, 390

Levenson, N. A., Sirocky, M. M., Hao, L., Spoon, H. W. W., Marshall, J. A., Elitzur, M., and Houck, J. R.: 2007, *ApJ* **654**, L45

Li, A. and Draine, B. T.: 2001, *ApJ* **554**, 778

Li, Y., Calzetti, D., Kennicutt, R. C., Hong, S., Engelbracht, C. W., Dale, D. A., and Moustakas, J.: 2010, *ApJ* **725**, 677

Li, Y., Crocker, A. F., Calzetti, D., Wilson, C. D., Kennicutt, R. C., Murphy, E. J., Brandl, B. R., Draine, B. T., Galametz, M., Johnson, B. D., Armus, L., Gordon, K. D., Croxall, K., Dale, D. A., Engelbracht, C. W., Groves, B., Hao, C.-N., Helou, G., Hinz, J., Hunt, L. K., Krause, O., Roussel, H., Sauvage, M., and Smith, J. D. T.: 2013, *ApJ* **768**, 180

Lira, P., Videla, L., Wu, Y., Alonso-Herrero, A., Alexander, D. M., and Ward, M.: 2013, *ApJ* **764**, 159

Luo, B., Brandt, W. N., Xue, Y. Q., Alexander, D. M., Brusa, M., Bauer, F. E., Comastri, A., Fabian, A. C., Gilli, R., Lehmer, B. D., Rafferty, D. A., Schneider, D. P., and Vignali, C.: 2011, *ApJ* **740**, 37

Lutz, D., Maiolino, R., Spoon, H. W. W., and Moorwood, A. F. M.: 2004, *A&A* **418**, 465

Magorrian, J., Tremaine, S., Richstone, D., Bender, R., Bower, G., Dressler, A., Faber, S. M., Gebhardt, K., Green, R., Grillmair, C., Kormendy, J., and Lauer, T.: 1998, *AJ* **115**, 2285

Mainieri, V., Kellermann, K. I., Fomalont, E. B., Miller, N., Padovani, P., Rosati, P., Shaver, P., Silverman, J., Tozzi, P., Bergeron, J., Hasinger, G., Norman, C., and Popesso, P.: 2008, *ApJS* **179**, 95

Maiolino, R. and Rieke, G. H.: 1995, *ApJ* **454**, 95

Malizia, A., Bassani, L., Bazzano, A., Bird, A. J., Masetti, N., Panessa, F., Stephen, J. B., and Ubertini, P.: 2012, *MNRAS* **426**, 1750

Marconi, A. and Hunt, L. K.: 2003, *ApJ* **589**, L21

Marinucci, A., Bianchi, S., Nicastro, F., Matt, G., and Goulding, A. D.: 2012, *ApJ* **748**, 130

Martínez-Paredes, M., Aretxaga, I., Alonso-Herrero, A., González-Martín, O., Lopéz-Rodríguez, E., Ramos Almeida, C., Asensio Ramos, A., Diaz Santos, T., Elitzur, M., Esquej, P., Hernan-Caballero, A., Ichikawa, K., Nikutta, R., Packham, C., Pereira-Santaella, M., and Telesco, C.: 2017, *ArXiv e-prints*

Mason, R. E., Lopez-Rodriguez, E., Packham, C., Alonso-Herrero, A., Levenson, N. A., Radomski, J., Ramos Almeida, C., Colina, L., Elitzur, M., Aretxaga, I., Roche, P. F., and Oi, N.: 2012, *AJ* **144**, 11

Mateos, S., Alonso-Herrero, A., Carrera, F. J., Blain, A., Severgnini, P., Caccianiga, A., and Ruiz, A.: 2013, *MNRAS* **434**, 941

Mateos, S., Alonso-Herrero, A., Carrera, F. J., Blain, A., Watson, M. G., Barcons, X., Braito, V., Severgnini, P., Donley, J. L., and Stern, D.: 2012, *MNRAS* **426**, 3271

Mateos, S., Barcons, X., Carrera, F. J., Ceballos, M. T., Caccianiga, A., Lamer, G., Maccacaro, T., Page, M. J., Schwope, A., and Watson, M. G.: 2005, *A&A* **433**, 855

Mateos, S., Carrera, F. J., Alonso-Herrero, A., Hernán-Caballero, A., Barcons, X., Asensio Ramos, A., Watson, M. G., Blain, A., Caccianiga, A., Ballo, L., Braito, V., and Ramos Almeida, C.: 2016, *ApJ* **819**, 166

Mateos, S., Carrera, F. J., Alonso-Herrero, A., Rovilos, E., Hernán-Caballero, A., Barcons, X., Blain, A., Caccianiga, A., Della Ceca, R., and Severgnini, P.: 2015, *MNRAS* **449**, 1422

Meléndez, M., Mushotzky, R. F., Shimizu, T. T., Barger, A. J., and Cowie, L. L.: 2014, *ApJ* **794**, 152

Mignoli, M., Cimatti, A., Zamorani, G., Pozzetti, L., Daddi, E., Renzini, A., Broadhurst, T., Cristiani, S., D'Odorico, S., Fontana, A., Giallongo, E., Gilmozzi, R., Menci, N., and Saracco, P.: 2005, *A&A* **437**, 883

Miller, N. A., Bonzini, M., Fomalont, E. B., Kellermann, K. I., Mainieri, V., Padovani, P., Rosati, P., Tozzi, P., and Vattakunnel, S.: 2013, *ApJS* **205**, 13

Mooley, K. P., Frail, D. A., Ofek, E. O., Miller, N. A., Kulkarni, S. R., and Horesh, A.: 2013, *ApJ* **768**, 165

Moorwood, A. F. M., Lutz, D., Oliva, E., Marconi, A., Netzer, H., Genzel, R., Sturm, E., and de Graauw, T.: 1996, *A&A* **315**, L109

Mor, R., Netzer, H., and Elitzur, M.: 2009, *ApJ* **705**, 298

Moran, E. C., Barth, A. J., Kay, L. E., and Filippenko, A. V.: 2000, *ApJ* **540**, L73

Moran, E. C., Filippenko, A. V., and Chornock, R.: 2002, *ApJ* **579**, L71

Moustakas, J., Kennicutt, Jr., R. C., Tremonti, C. A., Dale, D. A., Smith, J.-D. T., and Calzetti, D.: 2010, *ApJS* **190**, 233

Mullaney, J. R., Alexander, D. M., Goulding, A. D., and Hickox, R. C.: 2011, *MNRAS* **414**, 1082

Mushotzky, R. F., Shimizu, T. T., Meléndez, M., and Koss, M.: 2014, *ApJ* **781**, L34

Nenkova, M., Sirocky, M. M., Ivezić, Ž., and Elitzur, M.: 2008a, *ApJ* **685**, 147

Nenkova, M., Sirocky, M. M., Nikutta, R., Ivezić, Ž., and Elitzur, M.: 2008b, *ApJ* **685**, 160

Netzer, H.: 1987, *MNRAS* **225**, 55

Neugebauer, G. and Matthews, K.: 1999, *AJ* **118**, 35

Nikutta, R., Elitzur, M., and Lacy, M.: 2009, *ApJ* **707**, 1550

Noll, S., Burgarella, D., Giovannoli, E., Buat, V., Marcillac, D., and Muñoz-Mateos, J. C.: 2009, *A&A* **507**, 1793

Osterbrock, D. E.: 1977, *ApJ* **215**, 733

Osterbrock, D. E. and Martel, A.: 1993, *ApJ* **414**, 552

Ott, S.: 2010, in Y. Mizumoto, K.-I. Morita, and M. Ohishi (eds.), *Astronomical Data Analysis Software and Systems XIX*, Vol. 434 of *Astronomical Society of the Pacific Conference Series*, p. 139

Packham, C., Telesco, C. M., Hough, J. H., and Ftaclas, C.: 2005, in A. M. Hidalgo-Gámez, J. J. González, J. M. Rodríguez Espinosa, and S. Torres-Peimbert (eds.), *Revista Mexicana de Astronomia y Astrofisica Conference Series*, Vol. 24 of *Revista Mexicana de Astronomia y Astrofisica, vol. 27*, pp 7–12

Paolillo, M., Schreier, E. J., Giacconi, R., Koekemoer, A. M., and Grogin, N. A.: 2004, *ApJ* **611**, 93

Pappa, A., Georgantopoulos, I., Stewart, G. C., and Zezas, A. L.: 2001, *MNRAS* **326**, 995

Peeters, E., Spoon, H. W. W., and Tielens, A. G. G. M.: 2004, *ApJ* **613**, 986

Pereyra, N. A., Vanden Berk, D. E., Turnshek, D. A., Hillier, D. J., Wilhite, B. C., Kron, R. G., Schneider, D. P., and Brinkmann, J.: 2006, *ApJ* **642**, 87

Perez Garcia, A. M., Rodriguez Espinosa, J. M., and Santolaya Rey, A. E.: 1998, *ApJ* **500**, 685

Pérez-González, P. G., Rieke, G. H., Egami, E., Alonso-Herrero, A., Dole, H., Papovich, C., Blaylock, M., Jones, J., Rieke, M., Rigby, J., Barmby, P., Fazio, G. G., Huang, J., and Martin, C.: 2005, *ApJ* **630**, 82

Pérez-González, P. G., Rieke, G. H., Villar, V., Barro, G., Blaylock, M., Egami, E., Gallego, J., Gil de Paz, A., Pascual, S., Zamorano, J., and Donley, J. L.: 2008, *ApJ* **675**, 234

Petric, A. O., Ho, L. C., Flagey, N. J. M., and Scoville, N. Z.: 2015, *ApJS* **219**, 22

Phillips, M. M., Charles, P. A., and Baldwin, J. A.: 1983, *ApJ* **266**, 485

Phinney, E. S.: 1989, in F. Meyer (ed.), *NATO Advanced Science Institutes (ASI) Series C*, Vol. 290 of *NATO Advanced Science Institutes (ASI) Series C*, p. 457

Pier, E. A. and Krolik, J. H.: 1992, *ApJ* **401**, 99

Pilbratt, G. L., Riedinger, J. R., Passvogel, T., Crone, G., Doyle, D., Gageur, U., Heras, A. M., Jewell, C., Metcalfe, L., Ott, S., and Schmidt, M.: 2010, *A&A* **518**, L1

Poglitsch, A., Waelkens, C., Geis, N., Feuchtgruber, H., Vandenbussche, B., Rodriguez, L., Krause, O., Renotte, E., van Hoof, C., Saraceno, P., Cepa, J., Kerschbaum, F., Agnèse, P., Ali, B., Altieri, B., Andreani, P., Augueres, J.-L., Balog, Z., Barl, L., Bauer, O. H., Belbachir, N., Benedettini, M., Billot, N., Boulade, O., Bischof, H., Blommaert, J., Callut, E., Cara, C., Cerulli, R., Cesarsky, D., Contursi, A., Creten, Y., De Meester, W., Doublier, V., Doumayrou, E., Duband, L., Exter, K., Genzel, R., Gillis, J.-M., Grözinger, U., Henning, T., Herreros, J., Huygen, R., Inguscio, M., Jakob, G., Jamar, C., Jean, C., de Jong, J., Katterloher, R., Kiss, C., Klaas, U., Lemke, D., Lutz, D., Madden, S., Marquet, B., Martignac, J., Mazy, A., Merken, P., Montfort, F., Morbidelli, L., Müller, T., Nielbock, M., Okumura, K., Orfei, R., Ottensamer, R., Pezzuto, S., Popesso, P., Putzeys, J., Regibo, S., Reveret, V., Royer, P., Sauvage, M., Schreiber, J., Stegmaier, J., Schmitt, D., Schubert, J., Sturm, E., Thiel, M., Tofani, G., Vavrek, R., Wetzstein, M., Wieprecht, E., and Wiezorrek, E.: 2010, *A&A* **518**, L2

Polletta, M., Bassani, L., Malaguti, G., Palumbo, G. G. C., and Caroli, E.: 1996, *ApJS* **106**, 399

Ramos Almeida, C., Alonso-Herrero, A., Esquej, P., González-Martín, O., Riffel, R. A., García-Bernete, I., Rodríguez Espinosa, J. M., Packham, C., Levenson, N. A., Roche, P., Díaz-Santos, T., Aretxaga, I., and Álvarez, C.: 2014a, *MNRAS* **445**, 1130

Ramos Almeida, C., Alonso-Herrero, A., Levenson, N. A., Asensio Ramos, A., Rodríguez Espinosa, J. M., González-Martín, O., Packham, C., and Martínez, M.: 2014b, *MNRAS* **439**, 3847

Ramos Almeida, C., Levenson, N. A., Alonso-Herrero, A., Asensio Ramos, A., Rodríguez Espinosa, J. M., Pérez García, A. M., Packham, C., Mason, R., Radomski, J. T., and Díaz-Santos, T.: 2011a, *ApJ* **731**, 92

Ramos Almeida, C., Martínez González, M. J., Asensio Ramos, A., Acosta-Pulido, J. A., Hönig, S. F., Alonso-Herrero, A., Tadhunter, C. N., and González-Martín, O.: 2016, *MNRAS* **461**, 1387

Ramos Almeida, C., Sánchez-Portal, M., Pérez García, A. M., Acosta-Pulido, J. A., Castillo, M., Asensio Ramos, A., González-Serrano, J. I., Alonso-Herrero, A., Rodríguez Espinosa, J. M., Hatziminaoglou, E., Coia, D., Valtchanov, I., Pović, M., Esquej, P., Packham, C., and Altieri, B.: 2011b, *MNRAS* **417**, L46

Reunanen, J., Kotilainen, J. K., and Prieto, M. A.: 2002, *MNRAS* **331**, 154

Rieke, G. H.: 1978, *ApJ* **226**, 550

Rieke, G. H., Young, E. T., Engelbracht, C. W., Kelly, D. M., Low, F. J., Haller, E. E., Beeman, J. W., Gordon, K. D., Stansberry, J. A., Misselt, K. A., Cadien, J., Morrison, J. E., Rivlis, G., Latter, W. B., Noriega-Crespo, A., Padgett, D. L., Stapelfeldt, K. R., Hines, D. C., Egami, E., Muzerolle, J., Alonso-Herrero, A., Blaylock, M., Dole, H., Hinz, J. L., Le Floc'h, E., Papovich, C., Pérez-González, P. G., Smith, P. S., Su, K. Y. L., Bennett, L., Frayer, D. T., Henderson, D., Lu, N., Masci, F., Pesenson, M., Rebull, L., Rho, J., Keene, J., Stolovy, S., Wachter, S., Wheaton, W., Werner, M. W., and Richards, P. L.: 2004, *ApJS* **154**, 25

Risaliti, G., Elvis, M., and Nicastro, F.: 2002, *ApJ* **571**, 234

Roche, P. F., Alonso-Herrero, A., and Gonzalez-Martin, O.: 2015, *MNRAS* **449**, 2598

Roche, P. F., Packham, C., Aitken, D. K., and Mason, R. E.: 2007, *MNRAS* **375**, 99

Roche, P. F., Packham, C., Telesco, C. M., Radomski, J. T., Alonso-Herrero, A., Aitken, D. K., Colina, L., and Perlman, E.: 2006, *MNRAS* **367**, 1689

Rodríguez Espinosa, J. M. and Pérez García, A. M.: 1997, *ApJ* **487**, L33

Rodriguez Espinosa, J. M., Rudy, R. J., and Jones, B.: 1987, *ApJ* **312**, 555

Roussel, H.: 2013, *PASP* **125**, 1126

Sajina, A., Yan, L., Armus, L., Choi, P., Fadda, D., Helou, G., and Spoon, H.: 2007, *ApJ* **664**, 713

Sales, D. A., Pastoriza, M. G., Riffel, R., and Winge, C.: 2013, *MNRAS* **429**, 2634

Sales, D. A., Pastoriza, M. G., Riffel, R., Winge, C., Rodríguez-Ardila, A., and Carciofi, A. C.: 2011, *ApJ* **738**, 109

Sánchez-Portal, M., Castillo-Fraile, M., Ramos Almeida, C., Esquej, P., Alonso-Herrero, A., Pérez García, A. M., Acosta-Pulido, J., Altieri, B., Bongiovanni, A., Castro-Cerón, J. M., Cepa, J., Coia, D., Conversi, L., Fritz, J., González-Serrano, J. I., Hatziminaoglou, E., Pović, M., Rodríguez Espinosa, J. M., and Valtchanov, I.: 2013, in J. C. Guirado, L. M. Lara, V. Quilis, and J. Gorgas (eds.), *Highlights of Spanish Astrophysics VII*, pp 392–398

Sandage, A. and Tammann, G. A.: 1987, *A revised Shapley-Ames Catalog of bright galaxies*

Sarajedini, V. L., Gilliland, R. L., and Kasm, C.: 2003, *ApJ* **599**, 173

Sarajedini, V. L., Koo, D. C., Klesman, A. J., Laird, E. S., Perez Gonzalez, P. G., and Mozena, M.: 2011, *ApJ* **731**, 97

Schartmann, M., Meisenheimer, K., Camenzind, M., Wolf, S., and Henning, T.: 2005, *A&A* **437**, 861

Schartmann, M., Meisenheimer, K., Camenzind, M., Wolf, S., Tristram, K. R. W., and Henning, T.: 2008, *A&A* **482**, 67

Schmidt, M.: 1963, *Nature* **197**, 1040

Schmidt, M. and Green, R. F.: 1983, *ApJ* **269**, 352

Schulz, H., Komossa, S., Schmitz, C., and Mücke, A.: 1999, *A&A* **346**, 764

Seyfert, C. K.: 1943, *ApJ* **97**, 28

Shi, Y., Rieke, G. H., Hines, D. C., Gorjian, V., Werner, M. W., Cleary, K., Low, F. J., Smith, P. S., and Bouwman, J.: 2006, *ApJ* **653**, 127

Shimizu, T. T., Meléndez, M., Mushotzky, R. F., Koss, M. J., Barger, A. J., and Cowie, L. L.: 2016, *MNRAS* **456**, 3335

Siebenmorgen, R., Heymann, F., and Efstathiou, A.: 2015, *A&A* **583**, A120

Silverman, J. D., Mainieri, V., Salvato, M., Hasinger, G., Bergeron, J., Capak, P., Szokoly, G., Finoguenov, A., Gilli, R., Rosati, P., Tozzi, P., Vignali, C., Alexander, D. M., Brandt, W. N., Lehmer, B. D., Luo, B., Rafferty, D., Xue, Y. Q., Balestra, I., Bauer, F. E., Brusa, M., Comastri, A., Kartaltepe, J., Koekemoer, A. M., Miyaji, T., Schneider, D. P., Treister, E., Wisotski, L., and Schramm, M.: 2010, *ApJS* **191**, 124

Sirocky, M. M., Levenson, N. A., Elitzur, M., Spoon, H. W. W., and Armus, L.: 2008, *ApJ* **678**, 729

Skibba, R. A., Engelbracht, C. W., Dale, D., Hinz, J., Zibetti, S., Crocker, A., Groves, B., Hunt, L., Johnson, B. D., Meidt, S., Murphy, E., Appleton, P., Armus, L., Bolatto, A., Brandl, B., Calzetti, D., Croxall, K., Galametz, M., Gordon, K. D., Kennicutt, R. C., Koda, J., Krause, O., Montiel, E., Rix, H.-W., Roussel, H., Sandstrom, K., Sauvage, M., Schinnerer, E., Smith, J. D., Walter, F., Wilson, C. D., and Wolfire, M.: 2011, *ApJ* **738**, 89

Spinoglio, L., Andreani, P., and Malkan, M. A.: 2002, *ApJ* **572**, 105

Spinoglio, L., Malkan, M. A., Rush, B., Carrasco, L., and Recillas-Cruz, E.: 1995, *ApJ* **453**, 616

Spoon, H. W. W., Marshall, J. A., Houck, J. R., Elitzur, M., Hao, L., Armus, L., Brandl, B. R., and Charmandaris, V.: 2007, *ApJ* **654**, L49

Stalevski, M., Fritz, J., Baes, M., Nakos, T., and Popović, L. Č.: 2012, *MNRAS* **420**, 2756

Stasińska, G., Cid Fernandes, R., Mateus, A., Sodré, L., and Asari, N. V.: 2006, *MNRAS* **371**, 972

Stern, D., Assef, R. J., Benford, D. J., Blain, A., Cutri, R., Dey, A., Eisenhardt, P., Griffith, R. L., Jarrett, T. H., Lake, S., Masci, F., Petty, S., Stanford, S. A., Tsai, C.-W., Wright, E. L., Yan, L., Harrison, F., and Madsen, K.: 2012, *ApJ* **753**, 30

Stern, D., Eisenhardt, P., Gorjian, V., Kochanek, C. S., Caldwell, N., Eisenstein, D., Brodwin, M., Brown, M. J. I., Cool, R., Dey, A., Green, P., Jannuzi, B. T., Murray, S. S., Pahre, M. A., and Willner, S. P.: 2005, *ApJ* **631**, 163

Strolger, L.-G., Riess, A. G., Dahlen, T., Livio, M., Panagia, N., Challis, P., Tonry, J. L., Filippenko, A. V., Chornock, R., Ferguson, H., Koekemoer, A., Mobasher, B., Dickinson, M., Giavalisco, M., Casertano, S., Hook, R., Blondin, S., Leibundgut, B., Nonino, M., Rosati, P., Spinrad, H., Steidel, C. C., Stern, D., Garnavich, P. M., Matheson, T., Grogin, N., Hornschemeier, A., Kretchmer, C., Laidler, V. G., Lee, K., Lucas, R., de Mello, D., Moustakas, L. A., Ravindranath, S., Richardson, M., and Taylor, E.: 2004, *ApJ* **613**, 200

Telesco, C. M., Ciardi, D., French, J., Ftaclas, C., Hanna, K. T., Hon, D. B., Hough, J. H., Julian, J., Julian, R., Kidger, M., Packham, C. C., Pina, R. K., Varosi, F., and Sellar, R. G.: 2003, in M. Iye and A. F. M. Moorwood (eds.), *Instrument Design and Performance for Optical/Infrared Ground-based Telescopes*, Vol. 4841 of *Proc. SPIE*, pp 913–922

Telesco, C. M., Pina, R. K., Hanna, K. T., Julian, J. A., Hon, D. B., and Kisko, T. M.: 1998, in A. M. Fowler (ed.), *Infrared Astronomical Instrumentation*, Vol. 3354 of *Proc. SPIE*, pp 534–544

Thompson, G. D., Levenson, N. A., Uddin, S. A., and Sirocky, M. M.: 2009, *ApJ* **697**, 182

Tozzi, P., Gilli, R., Mainieri, V., Norman, C., Risaliti, G., Rosati, P., Bergeron, J., Borgani, S., Giacconi, R., Hasinger, G., Nonino, M., Streblyanska, A., Szokoly, G., Wang, J. X., and Zheng, W.: 2006, *A&A* **451**, 457

Tran, H. D.: 2001, *ApJ* **554**, L19

Tran, H. D.: 2003, *ApJ* **583**, 632

Tran, Q. D., Lutz, D., Genzel, R., Rigopoulou, D., Spoon, H. W. W., Sturm, E., Gerin, M., Hines, D. C., Moorwood, A. F. M., Sanders, D. B., Scoville, N., Taniguchi, Y., and Ward, M.: 2001, *ApJ* **552**, 527

Trevese, D., Boutsia, K., Vagnetti, F., Cappellaro, E., and Puccetti, S.: 2008, *A&A* **488**, 73

Trevese, D., Kron, R. G., Majewski, S. R., Bershady, M. A., and Koo, D. C.: 1994, *ApJ* **433**, 494

Trippe, M. L., Crenshaw, D. M., Deo, R. P., Dietrich, M., Kraemer, S. B., Rafter, S. E., and Turner, T. J.: 2010, *ApJ* **725**, 1749

Tueller, J., Baumgartner, W. H., Markwardt, C. B., Skinner, G. K., Mushotzky, R. F., Ajello, M., Barthelmy, S., Beardmore, A., Brandt, W. N., Burrows, D., Chincarini, G., Campana, S., Cummings, J., Cusumano, G., Evans, P., Fenimore, E., Gehrels, N., Godet, O., Grupe, D., Holland, S., Kennea, J., Krimm, H. A., Koss, M.,

Moretti, A., Mukai, K., Osborne, J. P., Okajima, T., Pagani, C., Page, K., Palmer, D., Parsons, A., Schneider, D. P., Sakamoto, T., Sambruna, R., Sato, G., Stamatikos, M., Stroh, M., Ukwata, T., and Winter, L.: 2010, *ApJS* **186**, 378

Tueller, J., Mushotzky, R. F., Barthelmy, S., Cannizzo, J. K., Gehrels, N., Markwardt, C. B., Skinner, G. K., and Winter, L. M.: 2008, *ApJ* **681**, 113

Ulrich, M.-H., Maraschi, L., and Urry, C. M.: 1997, *ARA&A* **35**, 445

Urry, C. M. and Padovani, P.: 1995, *PASP* **107**, 803

Veilleux, S. and Osterbrock, D. E.: 1987, *ApJS* **63**, 295

Vernet, J., Dekker, H., D'Odorico, S., Kaper, L., Kjaergaard, P., Hammer, F., Randich, S., Zerbi, F., Groot, P. J., Hjorth, J., Guinouard, I., Navarro, R., Adolfse, T., Albers, P. W., Amans, J.-P., Andersen, J. J., Andersen, M. I., Binetruy, P., Bristow, P., Castillo, R., Chemla, F., Christensen, L., Conconi, P., Conzelmann, R., Dam, J., de Caprio, V., de Ugarte Postigo, A., Delabre, B., di Marcantonio, P., Downing, M., Elswijk, E., Finger, G., Fischer, G., Flores, H., François, P., Goldoni, P., Guglielmi, L., Haigron, R., Hanenburg, H., Hendriks, I., Horrobin, M., Horville, D., Jessen, N. C., Kerber, F., Kern, L., Kiekebusch, M., Kleszcz, P., Klougart, J., Kragt, J., Larsen, H. H., Lizon, J.-L., Lucuix, C., Mainieri, V., Manuputy, R., Martayan, C., Mason, E., Mazzoleni, R., Michaelsen, N., Modigliani, A., Moehler, S., Møller, P., Norup Sørensen, A., Nørregaard, P., Péroux, C., Patat, F., Pena, E., Pragt, J., Reinero, C., Rigal, F., Riva, M., Roelfsema, R., Royer, F., Sacco, G., Santin, P., Schoenmaker, T., Spano, P., Sweers, E., Ter Horst, R., Tintori, M., Tromp, N., van Dael, P., van der Vliet, H., Venema, L., Vidali, M., Vinther, J., Vola, P., Winters, R., Wistisen, D., Wulterkens, G., and Zacchei, A.: 2011, *A&A* **536**, A105

Véron-Cetty, M.-P. and Véron, P.: 2006, *A&A* **455**, 773

Véron-Cetty, M.-P. and Véron, P.: 2010a, *A&A* **518**, A10

Véron-Cetty, M.-P. and Véron, P.: 2010b, *A&A* **518**, A10

Villforth, C., Koekemoer, A. M., and Grogin, N. A.: 2010, *ApJ* **723**, 737

Villforth, C., Sarajedini, V., and Koekemoer, A.: 2012, *MNRAS* **426**, 360

Ward, M. J., Blanco, P. R., Wilson, A. S., and Nishida, M.: 1991, *ApJ* **382**, 115

Werner, M. W., Roellig, T. L., Low, F. J., Rieke, G. H., Rieke, M., Hoffmann, W. F., Young, E., Houck, J. R., Brandl, B., Fazio, G. G., Hora, J. L., Gehrz, R. D., Helou, G., Soifer, B. T., Stauffer, J., Keene, J., Eisenhardt, P., Gallagher, D., Gautier, T. N., Irace, W., Lawrence, C. R., Simmons, L., Van Cleve, J. E., Jura, M., Wright, E. L., and Cruikshank, D. P.: 2004, *ApJS* **154**, 1

Williams, R. E., Blacker, B., Dickinson, M., Dixon, W. V. D., Ferguson, H. C., Fruchter, A. S., Giavalisco, M., Gilliland, R. L., Heyer, I., Katsanis, R., Levay, Z., Lucas, R. A., McElroy, D. B., Petro, L., Postman, M., Adorf, H.-M., and Hook, R.: 1996, *AJ* **112**, 1335

Wolf, C., Meisenheimer, K., Kleinheinrich, M., Borch, A., Dye, S., Gray, M., Wisotzki, L., Bell, E. F., Rix, H.-W., Cimatti, A., Hasinger, G., and Szokoly, G.: 2004, *A&A* **421**, 913

Xue, Y. Q., Luo, B., Brandt, W. N., Bauer, F. E., Lehmer, B. D., Broos, P. S., Schneider, D. P., Alexander, D. M., Brusa, M., Comastri, A., Fabian, A. C., Gilli, R., Hasinger, G., Hornschemeier, A. E., Koekemoer, A., Liu, T., Mainieri, V., Paolillo, M., Rafferty, D. A., Rosati, P., Shemmer, O., Silverman, J. D., Smail, I., Tozzi, P., and Vignali, C.: 2011, *ApJS* **195**, 10

Young, M., Brandt, W. N., Xue, Y. Q., Paolillo, M., Alexander, D. M., Bauer, F. E., Lehmer, B. D., Luo, B., Shemmer, O., Schneider, D. P., and Vignali, C.: 2012, *ApJ* **748**, 124

Young, S., Packham, C., Mason, R. E., Radomski, J. T., and Telesco, C. M.: 2007, *MNRAS* **378**, 888